CENTRO DE INVESTIGACIÓN Y DE ESTUDIOS AVANZADOS
DEL INSTITUTO POLITÉCNICO NACIONAL

UNIDAD ZACATENCO
DEPARTAMENTO DE FÍSICA

"Búsqueda de nueva física a través de fenomenología de neutrinos y modelos teóricos"

Tesis que presenta

Gonzalo Sánchez García

para obtener el Grado de

Doctor en Ciencias

en la Especialidad de

Física

Director de tesis: Dr. Omar Gustavo Miranda Romagnoli

Ciudad de México Agosto, 2022

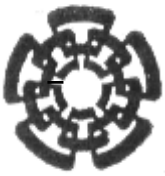

CENTER FOR RESEARCH AND ADVANCED STUDIES OF THE NATIONAL POLYTECHNIC INSTITUTE

PHYSICS DEPARTMENT

"Searching for new physics through neutrino phenomenology and theoretical models"

by

Gonzalo Sánchez García

In order to obtain the

Doctor of Science

degree, speciality in

Physics

Advisor: Ph. D. Omar Gustavo Miranda Romagnoli

Mexico City August, 2022

Agradecimientos

A mi asesor, Omar Miranda, por sus enseñanzas, su tiempo y su paciencia durante estos años. Gracias por aceptarme como su alumno y confiar en mi para realizar este trabajo.

A mi mamá, mi papá y mi hermana por acompañarme durante este largo camino. Gracias por todo el apoyo, sin ustedes esto no hubiera sido posible.

A mis colaboradores Alfredo Galindo, José Valle, Dimitris Papoulias y Diego Aristizabal. Muchas gracias por las muy interesantes discusiones y las oportunidades que me han dado.

A mis sinodales Ivan Heredia, Pablo Roig, Abdel Pérez, David Fernández y Eduardo Peinado. Muchas gracias por sus valiosos comentarios.

A mis amigos Abraham, Jesús, César, Alfredo, Jorge, Gabriela y Gustavo, mis amigos desde hace tantos años y que siempre me han acompañado.

A mis amigos y compañeros Horacio, Pedro, Omar, Marcela, Marco y Giovany, por todos esos momentos compartidos durante la maestría y el doctorado.

Al CINVESTAV por darme una gran formación académica.

Al CONACYT por respaldar mis estudios de doctorado bajo el número de beca 614309.

Este trabajo ha sido apoyado en parte por el proyecto CONACYT A1-S-23238.

Abstract

Since the discovery of neutrino oscillations, a prove that neutrinos are massive, there has been a strong effort to find new physics through the neutrino sector of particle physics. In this thesis, we study several well-motivated scenarios of physics beyond the Standard Model, both from a theoretical as well as from a phenomenological point of view. That is the case of non-standard interactions (NSI) or a non-zero neutrino magnetic moment. We discuss the expected size of the NSI induced from the type II seesaw mechanism, where charged scalars are introduced to the theory. From a phenomenological point of view, we mainly study the process of Coherent Elastic Neutrino-Nucleus Scattering (CEvNS). We discuss how this process is useful to perform tests of the SM, to study nuclear physics, and to constrain NSI parameters. Our analyses consider current data, and also explore the sensitivities from future experiments, including a proposal to measure CEvNS by using isotopically enriched detectors. We also study the theory of neutrino electromagnetic properties, and the sensitivities that are expected through the process of CEvNS from solar neutrinos in future Dark Matter detectors.

Resumen

A partir del descubrimiento de las oscilaciones de neutrinos ha habido un gran esfuerzo para encontrar señales de nueva física a través del sector de neutrinos de la física de partículas. En este trabajo estudiamos diversos escenarios de física más allá del Modelo Estándar desde una perspectiva teórica y fenomenológica. Nos enfocaremos en el formalismo de interacciones no estándar de neutrinos (NSI) y en el momento magnético del neutrino. Estudiaremos la magnitud de los acoplamientos NSI inducidos por el mecanismo seesaw tipo II, mediante el cual se introducen escalares cargados en la teoría. Desde el punto de vista fenomenológico, estudiaremos el proceso de dispersión elástica coherente neutrino-núcleo (CEvNS). Discutiremos cómo este proceso puede ser útill para realizar pruebas al Modelo Estándar, física nuclear y parámetros NSI. Nuestros análisis incluyen datos actuales, así como expectativas a futuro, incluyendo una propuesta de utilizar un arreglo de isótopos de germanio para medir CEvNS. Finalmente, estudiaremos el momento magnético del neutrino y la sensibilidad a este parámetro que se espera mediante detectores de Materia Oscura.

Contents

Chapter 1

Introduction

The main goal of Particle Physics is to study the matter and its interactions at the most fundamental level. Now we know that, at this level, the matter is formed of elementary particles, defined as those that do not have an internal structure and which can interact by one or more of the four known forces: gravity and electromagnetic interactions, which we are familiar with; the weak force, which is responsible for particle decays, and the strong force, responsible of keeping nuclei together. Examples of elementary particles are electrons and the up and down quarks which are common matter constituents. In addition, we also have one of the most intriguing elementary particles, which is the main topic of this work: neutrinos. Discovered in 1956 [1, 2], these particles play an essential role in the study and understanding of weak interactions. Neutrinos are sometimes called *ghost* particles since, although they can be produced in large amounts, they hardly ever interact with matter, making it very difficult for us to probe their intrinsic properties.

From a historical perspective, we have faced many theoretical and experimental issues in understanding and describing the interactions between particles. It was in the 1960s and the 1970s that the theory that we use today to describe interactions started being widely accepted and adopted in its current form. We call this theory the Standard Model (SM) of particle physics, and it has been tested innumerable times since 1978, becoming one of the most precise theories we have today. However, it still lacks to explain for some observed phenomena. For instance, years ago, it was widely believed that neutrinos were massless. There were strong theoretical and experimental motivations to think so, and, in fact, the SM was constructed under this assumption. However, the observation of a phenomenon called neutrino oscillations, which we will describe in chapter 3, corroborated that this was not the case and that there are at least two massive neutrinos. Observations like this have opened the window to the search for

new physics. These are exciting news for us as particle physicists since there are still many issues that remain unanswered in the study of neutrinos.

Throughout this thesis, we will address different questions. What Standard Model tests and new physics probes can be studied through neutrino interactions? What sensitivity can we reach with current and future experimental data? What is the neutrino mass nature? We will be interested in probing new physics beyond the SM through different processes that involve neutrinos scattering off electrons and nuclei. Indeed, the process of neutrino-electron scattering is one of the pioneers in the study of neutrinos. In contrast, in the case of nuclei scattering, we will study the process of Coherent Elastic Neutrino-Nucleus Scattering, which was recently observed for the first time in 2017.

As examples of new physics scenarios, we will study two different approaches: the theory and phenomenology of what we call Non-Standard Interactions (NSI) and the description of neutrino electromagnetic properties. Within the NSI formalism, the effects of new physics are contained in coupling constants parametrizing interactions that are not allowed in the SM. We will see that interactions like these can naturally arise from theoretical models that intend to explain, for instance, the origin of the neutrino mass. In other words, NSI parameters have different interpretations depending on the specific model under consideration and allow for a general study of new physics beyond the SM. Setting bounds to these parameters through the analysis of experimental data can give information on fundamental theoretical parameters, such as the mass of new mediators or the strength of an interaction. Regarding electromagnetic properties, it is well known that neutrinos have no electric charge within the SM. However, electromagnetic couplings appear in SM extensions where massive neutrinos are considered. In particular, we will study the theoretical description and the sensitivity of different experiments to the effective neutrino magnetic moment, which has different forms when expressed in terms of fundamental parameters, depending on the nature of neutrino masses.

How do we test a theory involving particles that we can not even see? Basically, we first need to produce the desired particles, make them interact with other particles, and confirm that the theory matches the observed results to a certain degree. In general, particle sources can be classified into three main groups: cosmic rays, which are particles coming from outer space, including solar neutrinos; then we have nuclear reactors, where, as the name suggests, particles are produced as a byproduct of induced nuclear reactions; and last but not least, we can also produce particle beams in linear and circular accelerators to make them collide and produce other particles. Once particles

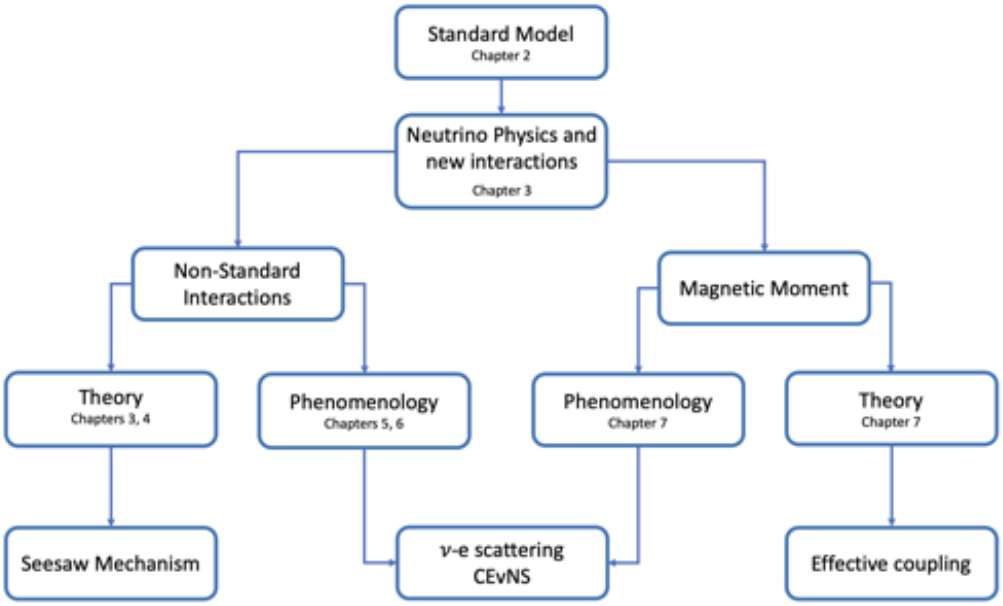

Figure 1.1: Structure of this thesis.

are produced we need to detect them. Depending on the nature of the particle, there are also different ways to do so. For instance, we can detect particles by tracking the signal they leave when traveling through a detector and we can use photomultiplier tubes to measure photons produced due to the interaction. For our main analyses, we will use solar, reactor, and accelerator sources and we will briefly describe how these neutrinos have been detected.

In Fig. 1.1, we present the structure of the thesis. In chapter 2, we introduce an overview of the SM. In chapter 3 our attention is turned to neutrino physics by describing the current picture of neutrinos within the SM and introducing the concept of neutrino masses and the NSI formalism. In chapter 4, we discuss one of the neutrino mass generation models, called the type II Seesaw mechanism, and we will see how this theory relates to NSI. In chapters 5 and 6, we study the phenomenology of NSI for neutrino interactions with nuclei. In chapter 5, we focus on the results obtained from current data, while in chapter 6, we analyze the expectations from future experiments. At the same time, we propose a different approach to measure these interactions that is viable with current technology. Chapter 7 focuses on the theory and phenomenology of neutrino electromagnetic properties. Finally, chapter 8 gives the conclusions and perspectives for neutrino physics.

Chapter 2

The Standard Model of Particle Physics

This work aims to study the phenomenology of parameters that account for physics beyond the SM. As we will see, these parameters can be related to new gauge mediators and may result from the manifestation of the origin of neutrino masses at low energies, just as the Fermi theory of beta decay describes a low energy manifestation of the SM. In order to explore these underlying physics, we first give a brief review of the main ideas that were used to develop the SM as a gauge field theory [3, 4, 5] and how the concept of *symmetry* is essential for the description of interactions between particles. We have referred to the SM as a *gauge field theory* since, within this formalism, particles are described by fields. On the other hand, *gauge* theories are those based on local symmetries of an underlying Lagrangian that dictate the interactions between particles. The set of symmetries has a group mathematical structure whose elements act on a representation of the group. In the particular case of the SM, the Lagrangian of the theory is written in terms of the matter fermion fields, and the elements of the symmetry group act on different representations of these fermions, which are accommodated in a convenient way so that the theory reproduces experimental observations. A consequence of gauge invariance is the existence of vector fields, which we refer to as gauge fields, and which will mediate the different forces between fermion fields. Apart from determining the form of the interactions, the chosen gauge symmetry group also fixes the number of gauge bosons, which corresponds to the number of generators of the group. It is worth mentioning that the SM also has a chiral character. In general, a free Dirac fermion field ψ can be decomposed as the sum of two independent components, ψ_L and ψ_R, called left and right-handed chiralities, respectively. Different experiments have shown that the W boson, responsible for what we will define as charged current weak interactions,

only couples to fermions with left-handed chiralities. This means that the SM needs to be constructed in a way such that left and right-handed particles behave differently under the symmetry group.

We may wonder why we use gauge theories to describe particles and their interactions. The reason is simple: because it works. The first hint indicating that gauge theories can be used in particle physics came from the description of quantum electrodynamics (QED), a gauge theory based on the abelian $U(1)$ symmetry group with only one generator, whose associated gauge boson can be identified with the photon. In addition, Noether's theorem states that for each symmetry, there is an associated conserved quantity. For QED, the corresponding symmetry group is responsible for current conservation. After the discovery of the weak and the strong forces, it was in 1954 that Yang and Mills [6] proposed the idea of generalizing the concept of gauge invariance to non-abelian groups. This generalization allowed for introducing more gauge fields, which were necessary for the description of strong and weak interactions. Neutrinos are not sensitive to the strong force, so we will focus only on the description of electroweak interactions in the following section.

2.1 Electroweak interactions

For the construction of the theory, we first need to choose the gauge symmetry group. It turns out that the groups $SU(3)$, $SU(2)$, and $SU(1)$ have eight, three, and one generator, respectively, which coincides with the number of mediators needed for the description of the three different forces described by the SM: eight gluons for the strong force, three bosons for the weak force, and one photon for the electromagnetic interactions. This suggests the $SU(3)_C \times SU(2)_L \times U(1)_Y$ group as a plausible election for our symmetry group[1], where the subscripts make reference to color charge (C), left-handed chirality (L), and weak hypercharge (Y). Within the SM, the color group is unbroken, which allows us to separately study the electroweak interactions, and from now on, we will focus on the $SU(2)_L \times U(1)_Y$ sector, which will be essential for the description of neutrinos.

Once the gauge symmetry group is fixed, then the fermions need to be accommodated in convenient representations such that the interactions and the corresponding phenomenology consistent with experiments are reproduced. Fermions can be classified in two different groups: leptons are those which do not interact by the strong force,

[1]Historically, SU(2) was proposed for the description of weak interactions before the Z boson was discovered.

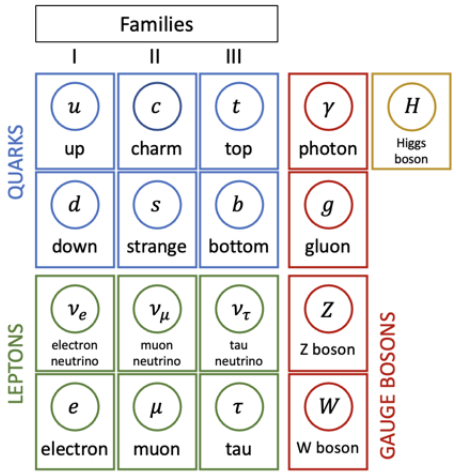

Figure 2.1: Fundamental particles of the SM.

while quarks are those that interact by the strong force through the color charge. Leptons are in addition classified in neutrinos and charged leptons, while quarks are divided in up-type and down-type quarks. The number of fundamental fermions is dictated by the experiments and until now we have three copies of each fermion type, called families, which are summarized in the first three columns of Fig. 2.1. As charged leptons we have the electron (e), the muon (μ), and the tau (τ), each with its corresponding neutrino, denoted as ν_e, ν_μ, and ν_τ, respectively. The up-type quarks are the up (u), charm, (c), and the top (t), while the down-type quarks are the down (d), strange (s), and bottom (b) [7].

As we have mentioned, within the SM the left and right-handed chiralities of a field ψ behave differently. These components can be obtained through the projection operators, defined such that:

$$\psi_L = P_L\psi = \frac{1-\gamma^5}{2}\psi, \qquad \psi_R = P_R\psi = \frac{1+\gamma^5}{2}\psi, \tag{2.1}$$

with γ^5 a 4×4 matrix called the chirality matrix. This distinction is important since, among many representation possibilities, the one that reproduces the correct phenomenology of interactions is that where left-handed chiral fields are taken as weak isospin doublets. In the case of leptons, we denote the doublets:

$$L_{eL} = \begin{pmatrix} \nu_{eL} \\ e_L \end{pmatrix}, \qquad L_{\mu L} = \begin{pmatrix} \nu_{\mu L} \\ \mu_L \end{pmatrix}, \qquad L_{\tau L} = \begin{pmatrix} \nu_{\tau L} \\ \tau_L \end{pmatrix}. \tag{2.2}$$

		I	I_3	Y	Q
Lepton doublet	ν_{eL}	1/2	1/2	-1	0
	e_L	1/2	-1/2	-1	-1
Lepton singlet	e_R	0	0	-2	-1
Quark doublet	u_L	1/2	1/2	1/3	2/3
	d_L	1/2	-1/2	1/3	-1/3
Quark singlets	u_R	0	0	4/3	2/3
	d_R	0	0	-2/3	-1/3
Higgs doublet	$\Phi^+(x)$	1/2	1/2	1	1
	$\Phi^0(x)$	1/2	-1/2	1	0

Table 2.1: Quantum numbers for leptons, quarks, and the scalar sector of the SM. We show the values for weak isospin (I), the corresponding third component (I_3), weak hypercharge (Y), and electric charge (Q) [8].

And for quarks we define:

$$Q_{1L} = \begin{pmatrix} u_L \\ d_L \end{pmatrix}, \qquad Q_{2L} = \begin{pmatrix} c_L \\ s_L \end{pmatrix}, \qquad Q_{3L} = \begin{pmatrix} t_L \\ b_L \end{pmatrix}. \tag{2.3}$$

The right-handed chiral components of charged leptons and quarks are taken as singlets under the $SU(2)$ gauge group:

$$e_R, \quad \mu_R, \quad \tau_R, \quad u_R, \quad d_R, \quad c_R, \quad s_R, \quad t_R, \quad b_R. \tag{2.4}$$

Since only left-handed components are observed for neutrinos, then the SM does not include their corresponding right-handed counterparts, an assumption that leads to a zero mass for these particles. For charged leptons and quarks, it will be sometimes useful to follow the notation:

$$\ell_{eX} = e_X, \qquad \ell_{\mu X} = \mu_X, \qquad \ell_{\tau X} = \tau_X, \tag{2.5}$$

$$q^U_{uX} = u_X, \qquad q^U_{cL} = c_X, \qquad q^U_{tX} = t_X, \tag{2.6}$$

$$q^D_{dX} = d_X, \qquad q^D_{sX} = s_X, \qquad q^D_{bX} = b_X, \tag{2.7}$$

with $X = L, R$ denoting the two different chiralities. Once the fermion content is set, we need to construct a Lagrangian that is locally invariant under the symmetry gauge group. First, we need to specify the transformation for lepton doublets and singlets. In general, any element of a group can be parametrized by the group generators and a set

of local parameters. For our particular case of interest, an element of $SU(2)_L \times U(1)_Y$ can be represented by the local parameters $\theta_\alpha(x)$ (with $\alpha = 1, 2, 3$) and $\eta(x)$, such that [8]

$$U(\theta_\alpha(x), \eta(x)) = \exp\left(i\theta_\alpha(x) I_\alpha + i\eta(x)\frac{Y}{2}\right), \tag{2.8}$$

where I_α (with $\alpha = 1, 2, 3$) are the generators of $SU(2)$. These generators have a matrix representation which is not unique but needs to be fixed. We use the convention:

$$I_\alpha = \frac{\tau_\alpha}{2} \qquad (\alpha = 1, 2, 3), \tag{2.9}$$

with τ_α the Pauli matrices. On the other hand, the quantity Y accounts for the action of the $U(1)$ abelian group, which will be fixed for each fermion chiral field through the Gell-Mann-Nishijima relation:

$$Q = I_3 + \frac{Y}{2}, \tag{2.10}$$

where I_3 is the corresponding isospin component, and Q refers to the electric charge. The quantum numbers for each particle are summarized in Table 2.1.

The Lagrangian of the theory should also contain kinetic terms for the fermion fields, which involve factors of the form $\partial_\mu \psi$. It turns out that terms like these are not gauge invariant when we apply the transformation in Eq. (2.8). However we can recover gauge invariance by introducing a *covariant* derivative, which consists on adding to the derivative a boson field for each group generator. Then, we introduce the boson fields W^a_μ ($a = 1, 2, 3$) and B_μ such that we define the covariant derivative:

$$D_\mu = \partial_\mu + igW^a_\mu I_a + ig' B_\mu \frac{Y}{2}, \tag{2.11}$$

where g, and g' are coupling constants associated to the symmetry groups $SU(2)_L$ and $U(1)_Y$, respectively. Now a locally gauge invariant Lagrangian can be constructed if the covariant derivative and the introduced boson fields transform as [8]:

$$D_\mu \to D'_\mu(x) = U(\theta_\alpha(x), \eta(x)) D_\mu U^{-1}(\theta_\alpha(x), \eta(x)), \tag{2.12}$$

$$A_\mu \cdot I \to A'_\mu \cdot I = U(\theta_\alpha(x), \eta(x)) \left(A_\mu \cdot I - i/g\ \partial_\mu\right) U^{-1}(\theta_\alpha(x), \eta(x)), \tag{2.13}$$

$$B_\mu \frac{Y}{2} \to B'_\mu \frac{Y}{2} = U(\theta_\alpha(x), \eta(x)) \left(B_\mu \frac{Y}{2} - i/g'\ \partial_\mu\right) U^{-1}(\theta_\alpha(x), \eta(x)). \tag{2.14}$$

For simplicity, we consider for the moment just the first family of fermion fields. Then,

the Lagrangian that is locally invariant under the defined transformations reads

$$\mathcal{L} = i\left(\overline{L_{eL}}\not{D}L_{eL} + \overline{e_R}\not{D}e_R\right) + i\left(\overline{Q_{1L}}\not{D}Q_{1L} + \overline{u_R}\not{D}u_R + \overline{d_R}\not{D}d_R\right), \tag{2.15}$$

where we have used the notation $\not{D} = \gamma^\mu D_\mu$, with γ^μ the Dirac matrices, and the bar notation indicates $\overline{\psi} = \psi^\dagger\gamma^0$. The Lagrangian in Eq. (2.15) is now gauge invariant and gives rise to interactions between fermions and gauge bosons. This can be seen by using the explicit form of the covariant derivative. Then, omitting the kinetic terms, we get the interaction Lagrangian $\mathcal{L}_I$:

$$\begin{aligned}\mathcal{L}_I = \; & -\frac{1}{2}\overline{L_{eL}}\left(g\not{W}^a\tau_a - g'\not{B}\right)L_{eL} + g'\overline{e_R}\not{B}e_R \\ & -\frac{1}{2}\overline{Q_{1L}}\left(g\not{W}^a\tau_a + \frac{1}{3}g'\not{B}\right)Q_{1L} - \frac{2}{3}g'\overline{u_R}\not{B}u_R + \frac{1}{3}g'\overline{d_R}\not{B}d_R.\end{aligned} \tag{2.16}$$

For the leptonic part, the first line in Eq. (2.16), we get the explicit form

$$\mathcal{L}_{I,L} = -\frac{1}{2}\begin{pmatrix}\overline{\nu_{eL}} & \overline{e_L}\end{pmatrix}\begin{pmatrix} g\not{W}^3 - g'\not{B} & g(\not{W}^1 - i\not{W}^2) \\ g(\not{W}^1 + i\not{W}^2) & -g\not{W}^3 - g'\not{B}\end{pmatrix}\begin{pmatrix}\nu_{eL} \\ e_L\end{pmatrix} + g'\overline{e_R}\not{B}e_R. \tag{2.17}$$

From this equation we can distinguish two different interactions, a charged current interaction (CC), given by the off-diagonal terms of Eq. (2.17), and a neutral current interaction (NC), characterized by the diagonal terms in the same equation together with the remaining last term. We then define the field $W_\mu = (W_\mu^1 - iW_\mu^2)/\sqrt{2}$ so the charged current interaction Lagrangian reads:

$$\mathcal{L}_{I,L}^{CC} = -\frac{g}{2\sqrt{2}}j_{W,L}^\mu W_\mu + \text{h.c.}, \tag{2.18}$$

where h.c. refers to the hermitian conjugate, and we have defined the leptonic charged current, $j_{W,L}^\mu$, as

$$j_{W,L}^\mu = \overline{\nu_e}\gamma^\mu(1-\gamma^5)e = 2\overline{\nu_{eL}}\gamma^\mu e_L. \tag{2.19}$$

The charged current is given its name since the interacting fermions differ by one charge unit. Equation (2.18) explicitly shows the coupling of left-handed leptons to what we have defined as the W boson. This is in accordance with experimental observations, where only left-handed fields participate in charged current interactions. In general, interactions between particles can be illustrated by what we call Feynman diagrams. These are graphical representations of interactions and their strength. The Feynman diagram corresponding to the CC weak interaction is depicted in Fig. 2.2, where, as

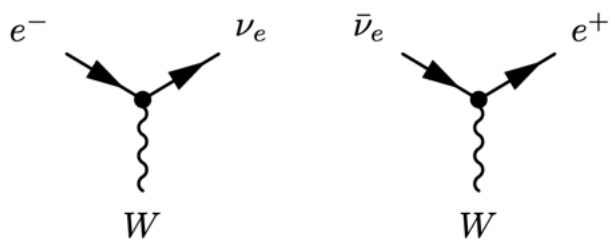

Figure 2.2: Feynman diagrams for the SM lepton charged current.

a general rule, fermions are represented by straight lines, and gauge bosons by curvy lines. The first diagram in Fig. 2.2 corresponds to the first term in Eq. (2.18), while the second diagram corresponds to the hermitian conjugate. When accounting for three lepton families, Eq. (2.19) needs to be generalized by adding equivalent terms to the electron CC but for muon and tau fields.

Now we focus on the NC part of the Lagrangian in Eq. (2.17). Expanding the diagonal terms in this equation, we get

$$\mathcal{L}_{I,L}^{NC} = -\frac{1}{2}\left(\overline{\nu_{eL}}(g\cancel{W^3} - g'\cancel{B})\nu_{eL} - \overline{e_L}(g\cancel{W^3} + g'\cancel{B})e_L - 2g'e_R\cancel{B}e_R\right). \tag{2.20}$$

The *neutral current* character makes reference to the fact that the fermions involved in the interaction are of the same kind and have the same electric charge. At this point we should remember that the general theory must reproduce an interaction Lagrangian that describes the electromagnetic interactions. As a reminder, the QED Lagrangian predicts an interaction between the electron (or any charged lepton) and the photon of the form

$$\mathcal{L}_{I,L}^{\gamma} = -q_e j_{\gamma,L}^{\mu} A_{\mu}, \tag{2.21}$$

where A_μ is the electromagnetic field, q_e is the absolute value of the elementary electric charge, and $j_{\gamma,L}^{\mu}$ is the electromagnetic current

$$j_{\gamma,L}^{\mu} = -\overline{e}\gamma^{\mu}e. \tag{2.22}$$

The problem with the Lagrangian in Eq. (2.20) is that both the W_μ^3 and B_μ fields couple to the neutrino fields when g' and g are different form zero. This forbids us from identifying any of the gauge fields with the photon, since it is experimentally observed that photons do not couple to neutrinos, which are neutral particles. To fix this, we can use a unitary matrix to perform a rotation of the fields W_μ^3 and B_μ. By defining

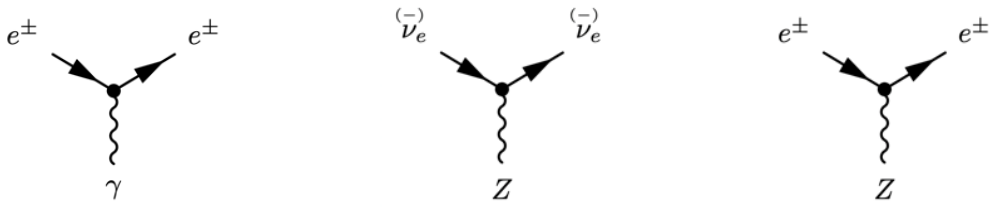

Figure 2.3: Left panel: Feynman diagram for the coupling of charged leptons with the photon. Right panel: Feynman diagram for the coupling of neutrinos and charged leptons to the Z boson.

the resulting fields A_μ and Z_μ, we get

$$\begin{pmatrix} A_\mu \\ Z_\mu \end{pmatrix} = \begin{pmatrix} \cos\theta_W & \sin\theta_W \\ -\sin\theta_W & \cos\theta_W \end{pmatrix} \begin{pmatrix} B_\mu \\ W^3_\mu \end{pmatrix}, \tag{2.23}$$

with θ_W the only constant needed to parameterize a 2×2 unitary matrix. Within the frame of the SM, this *constant* (actually, its value depends on the energy scale) is called the *weak mixing angle*. In terms of the rotated fields, Eq. (2.20) reads

$$\begin{aligned} \mathcal{L}^{NC}_{I,L} = \; & -\frac{1}{2}\{\overline{\nu_{eL}}(g\cos\theta_W + g'\sin\theta_W)\not{Z}\nu_{eL} - \overline{e_L}(g\cos\theta_W - g'\sin\theta_W)\not{Z}e_L\} \\ & -\frac{1}{2}\{\overline{\nu_{eL}}(g\sin\theta_W - g'\cos\theta_W)\not{A}\nu_{eL} - \overline{e_L}(g\sin\theta_W + g'\cos\theta_W)\not{A}e_L\} \\ & - g'\overline{e_R}\sin\theta_W\not{Z}e_R + g'\overline{e_R}\cos\theta_W\not{A}e_R. \end{aligned} \tag{2.24}$$

From the second line in the last expression, we can now identify the field A_μ with the electromagnetic field if we set the condition

$$g\sin\theta_W = g'\cos\theta_W. \tag{2.25}$$

This way, the first term in the second line of Eq. (2.24) vanishes and we ensure that the A_μ field does not couple to neutrinos for g and g' different from zero. Moreover, we ensure that A_μ couples to the left and right chiralities of charged fermions with the same strength, a second characteristic that the photon field satisfies. Notice from Eq. (2.25) that the weak mixing angle does not represent another free parameter of the theory, since now it depends on the gauge coupling constants. It is common to write the NC Lagrangian in terms of the weak mixing angle instead of the coupling constant g', so we get the form

$$\begin{aligned} \mathcal{L}^{NC}_{I,L} = \; & -\frac{g}{2\cos\theta_W}(\overline{\nu_{eL}}\not{Z}\nu_{eL} - (1-2\sin^2\theta_W)\overline{e_L}\not{Z}e_L + 2\sin^2\theta_W\overline{e_R}\not{Z}e_R) \\ & + g\sin\theta_W\bar{e}\not{A}e. \end{aligned} \tag{2.26}$$

Now the last term in Eq. (2.26) has the exact form of that in Eq. (2.21), which strengthens our previous statement of identifying A_μ as the electromagnetic field. As this term has to give us the correct coupling of charged fermions to the photon, we further set the condition

$$g \sin\theta_W = q_e, \qquad\qquad g' \cos\theta_W = q_e. \tag{2.27}$$

The Feynman diagram representing the coupling of charged fermions with the photon is illustrated in the left panel of Fig. 2.3. In addition, from the last conditions we can obtain the relation between the coupling constants g, g', and the fundamental charge q_e:

$$\frac{1}{g^2} + \frac{1}{g'^2} = \frac{1}{q_e^2}. \tag{2.28}$$

Regarding the coupling of fermion fields to what we defined as the Z_μ boson, we can write the first line of Eq. (2.26) in the form

$$\mathcal{L}^Z_{I,L} = -\frac{g}{2\cos\theta_W} j^\mu_{Z,L} Z_\mu, \tag{2.29}$$

where we have defined the weak neutral current

$$j^\mu_{Z,L} = 2g^\nu_L \overline{\nu_{eL}} \gamma^\mu \nu_{eL} + 2g^\ell_L \overline{e_L} \gamma^\mu e_L + 2g^\ell_R \overline{e_R} \gamma^\mu e_R, \tag{2.30}$$

with the values of g^ν_L, g^ℓ_L, and g^ℓ_R given in Table 2.2. Notice from the table that these constants are the same for each of the three lepton families and, for this reason, we say that there is a *universality* of the weak force. Equivalently, we can write the weak neutral current in terms of the fields ν_e and $e = e_L + e_R$:

$$j^\mu_{Z,L} = \overline{\nu_e} \gamma^\mu (g^\nu_V - g^\nu_A \gamma^5) \nu_e + \overline{e} \gamma^\mu (g^l_V - g^l_A \gamma^5) e. \tag{2.31}$$

Where we have used the vector coupling constant $g^\nu_V = g^\nu_L + g^\nu_R$, and the axial coupling constant $g^\nu_A = g^\nu_L - g^\nu_R$, which values are also given in Table 2.2. The Feynman diagrams corresponding to the interactions in Eq. (2.31) are illustrated in the central and right panels of Fig. 2.3. Again, we can generalize the currents defined in Eqs. (2.30) and (2.31) to the case of three families by adding the corresponding terms for muon and tau fields. Notice that the Z_μ boson has a particular behavior when compared to the other gauge bosons. In contrast to the W_μ boson, it couples to both left and right-handed chiralites, while in contrast to the photon, it does so with different strengths, both properties being a consequence of the mixing of the original gauge fields.

Fermion (f)		g_L^f	g_R^f	g_V^f	g_A^f
ν	$(\nu_e, \nu_\mu, \nu_\tau)$	$\frac{1}{2}$	0	$\frac{1}{2}$	$\frac{1}{2}$
ℓ	(e, μ, τ)	$-\frac{1}{2} + \sin^2\theta_W$	$\sin^2\theta_W$	$-\frac{1}{2} + 2\sin^2\theta_W$	$-\frac{1}{2}$
q^U	(u, c, t)	$\frac{1}{2} - \frac{2}{3}\sin^2\theta_W$	$-\frac{2}{3}\sin^2\theta_W$	$\frac{1}{2} - \frac{4}{3}\sin^2\theta_W$	$\frac{1}{2}$
q^D	(d, s, b)	$-\frac{1}{2} + \frac{1}{3}\sin^2\theta_W$	$\frac{1}{3}\sin^2\theta_W$	$-\frac{1}{2} + \frac{2}{3}\sin^2\theta_W$	$-\frac{1}{2}$

Table 2.2: Neutral current left, right, vector, and axial couplings for leptons and quarks.

Until now, we have studied the interaction terms for the leptonic sector of the SM. We can then follow the same procedure to obtain the corresponding expressions for the quark sector. By doing so, from the second line of the interaction invariant Lagrangian in Eq. (2.16), we end up with a CC Lagrangian of the form

$$\mathcal{L}_{I,Q}^{CC} = -\frac{g}{2\sqrt{2}} j_{W,Q}^{\mu} W_{\mu} + \text{h.c.}, \tag{2.32}$$

with the corresponding weak quark charged current:

$$j_{W,Q}^{\mu} = \overline{u}\gamma^{\mu}(1-\gamma^5)d = 2\overline{u_L}\gamma^{\mu}d_L, \tag{2.33}$$

which can be also generalized to the case of three families. In the case of neutral currents, the main difference between lepton and quark sectors is that, for the latter, we have terms including the coupling of the original gauge boson, B_μ, to *up*-type quarks, which correspond to the doublet components with the largest I_3 value. However, after rotating the neutral boson fields, we end up again with an interaction Lagrangian of the form

$$\mathcal{L}_{I,Q}^{Z} = -\frac{g}{2\cos\theta_W} j_{Z,Q}^{\mu} Z_{\mu}, \tag{2.34}$$

with the quark weak neutral current

$$j_{Z,Q}^{\mu} = 2g_L^u \overline{u_L}\gamma^{\mu}u_L + 2g_R^u \overline{u_R}\gamma^{\mu}u_R + 2g_L^d \overline{d_L}\gamma^{\mu}d_L + 2g_R^d \overline{d_R}\gamma^{\mu}d_R. \tag{2.35}$$

The values of g_X^u and g_X^u are given in Table 2.2. Again, we can define the corresponding axial and vector couplings to write the neutral current in the form:

$$j_{Z,Q}^{\mu} = \overline{u}\gamma^{\mu}(g_V^u - g_A^u\gamma^5)u + \overline{d}\gamma^{\mu}(g_V^d - g_A^d\gamma^5)d. \tag{2.36}$$

As seen in Table 2.2, the couplings for leptons and quarks are different, which is a consequence of the fractional electric charge of quarks, which translates into different

couplings between the original gauge bosons and the d_L, d_R, and u_R fields. Finally, from the neutral part of the quark interaction Lagrangian, we also have an electromagnetic interaction for quarks, with the same form as in the leptonic case, but with a current of the form

$$j^{\mu}_{\gamma,Q} = \frac{2}{3}\overline{u}\gamma^{\mu}u - \frac{1}{3}\overline{d}\gamma^{\mu}d. \tag{2.37}$$

From the above discussion, we now have a description of interactions between particles that is consistent with experimental data and that reproduces the correct phenomenology. Notice that kinetic terms for fermions are also included when expanding the covariant derivatives. However, there is an important thing that is missing. So far, the Lagrangian does not include mass terms for any of the particles. These need to be included since, except for the photon, all the observed particles in nature are massive. Particle mass terms in the Lagrangian can be interpreted as the coupling between left and right chiralities of a given field. Forthis purpose, it would be enough to add terms of the form

$$m_f\overline{f}f = m_f\overline{f_L}f_R + m_f\overline{f_R}f_L, \tag{2.38}$$

with f a generic field and m_f its corresponding mass. In practice, this can not be done directly by hand since left and right-handed fields transform in different ways under the considered gauge group. Hence, terms like that in Eq. (2.38) are not gauge invariant. To introduce them in a consistent way, we will need to add scalar fields to the theory, which we discuss in the next section.

2.2 How do particles acquire their mass?

As we have seen, the introduction of mass terms for fermions and gauge bosons would spoil gauge invariance. However, we can add these terms by *hiding* the symmetry of the theory through what we call the Higgs mechanism [9, 10]. The idea is to introduce a complex scalar doublet of the form

$$\Phi = \begin{pmatrix} \Phi^+ \\ \Phi^0 \end{pmatrix}, \tag{2.39}$$

with quantum numbers as given in Table 2.1. This way, the most general gauge invariant Lagrangian for the scalar sector under $SU(2)_L \times U(1)_Y$ will be

$$\mathcal{L}_H = (D_\mu\Phi)^\dagger(D^\mu\Phi) - m_\Phi^2\Phi^\dagger\Phi - \frac{\lambda}{4}(\Phi^\dagger\Phi)^2, \tag{2.40}$$

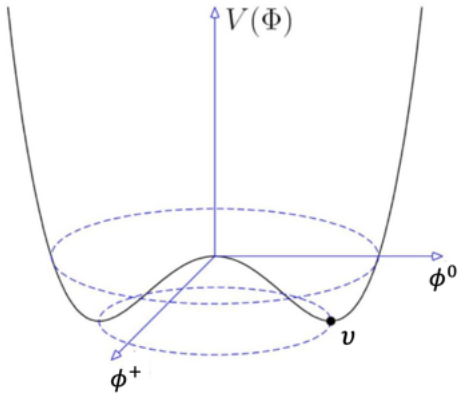

Figure 2.4: Standard Model Higgs potential.

where we assume $m_\Phi^2 < 0$, and $\lambda > 0$. The second and third terms in the last expression are the Higgs potential. We see that this potential has a minimum whenever Φ satisfies the condition

$$|\Phi|^2 \equiv \frac{v_\Phi^2}{2} = -\frac{m_\Phi^2}{\lambda}. \tag{2.41}$$

Since $m_\Phi^2 < 0$, then there are infinite possibilities to fulfill this condition as we can see from the potential in Fig. 2.4. In Quantum Field Theory, the minimum of the potential, v_Φ, corresponds to the vacuum, the state of minimum energy. However, only neutral fields can have a non-zero value in vacuum, which we call vacuum expectation value (vev). Then, we take the direction of non-zero vev in the ϕ^0 direction:

$$\langle \Phi \rangle = \frac{1}{\sqrt{2}} \begin{pmatrix} 0 \\ v_\Phi \end{pmatrix}. \tag{2.42}$$

The action of taking a particular direction for the minimum energy state is called *spontaneous symmetry breaking*, and we say that the neutral component of the scalar field induces a vev, v_Φ. We can now expand the neutral component $\phi^0(x)$ around this minimum and express the Higgs doublet as:

$$\Phi(x) = \frac{1}{\sqrt{2}} \exp\left(\frac{i}{2v_\Phi}\xi_a(x)\tau_a\right) \begin{pmatrix} 0 \\ v_\Phi + H(x) \end{pmatrix}, \tag{2.43}$$

with $\xi_a(x)$ complex fields and $H(x)$ a real field that we call the Higgs field. We can now exploit the gauge invariance of the theory to perform a convenient transformation $U(-\xi_a(x)/v_\Phi, 0)$, with U defined in Eq. (2.8), such that we rotate out the fields $\xi_a(x)$

and we are left with

$$\Phi(x) = \frac{1}{\sqrt{2}} \begin{pmatrix} 0 \\ v_\Phi + H(x) \end{pmatrix}. \tag{2.44}$$

When using $\Phi(x)$ as in Eq. (2.44) we refer to the *unitary gauge*, and substituting in Eq. (2.40) we get

$$\begin{aligned} \mathcal{L}_H = \; & \frac{1}{2}(\partial H)^2 - \frac{\lambda v_\Phi^2}{4} H^2 - \frac{\lambda v_\Phi}{4} H^3 - \frac{\lambda}{16} H^4 + \frac{g^2 v_\Phi}{2} W_\mu^\dagger W^\mu H + \frac{g^2 v_\Phi}{4\cos^2(\theta_W)} Z_\mu Z^\mu H \\ & + \frac{g^2}{4} W_\mu^\dagger W^\mu H^2 + \frac{g^2}{8\cos^2(\theta_W)} Z_\mu Z^\mu H^2 + \frac{g^2 v_\Phi^2}{4} W_\mu^\dagger W^\mu + \frac{g^2 v_\Phi^2}{8\cos^2(\theta_W)} Z_\mu Z^\mu. \end{aligned} \tag{2.45}$$

The first two terms in Eq. (2.45) represent a kinetic and a mass term for the Higgs field, respectively. Then we have trilinear an quartic self interactions of H. The next four terms are trilinear couplings of the Higgs field with gauge bosons. The most interesting part of Eq. (2.45) comes from the last two terms, where we can identify mass terms for the W and Z bosons, respectively. We see that the unitary gauge allows us to see the physical particle content of the theory.

Now we focus on generating mass terms for fermions. First, notice that the SM symmetry group allows us to add invariant terms to the Lagrangian of the theory by coupling the scalar doublet to fermion fields. For instance, in the lepton sector, for the general case of three families, we can generate the term

$$\mathcal{L}_{H,L} = -\sum_{\alpha,\beta} Y'^{\ell}_{\alpha\beta} \overline{L'_{\alpha L}} \Phi \ell'_{\beta L} + \text{h.c.}, \tag{2.46}$$

where $\alpha, \beta = e, \mu, \tau$, and we have used primed fields to denote the original massless fermion fields. Couplings as those in the previous equation are known as Yukawa couplings and Y' is the Yukawa coupling matrix, which is in general a complex matrix. Again, to see the physical content of the theory, we can use the unitary gauge for Φ, ending up with

$$\mathcal{L}_{H,L} = -\frac{1}{\sqrt{2}} \sum_{\alpha,\beta} Y'^{\ell}_{\alpha\beta} \overline{\ell'_{\alpha L}} \ell'_{\beta R} H - \frac{v_\Phi}{\sqrt{2}} \sum_{\alpha,\beta} Y'^{\ell}_{\alpha\beta} \overline{\ell'_{\alpha L}} \ell'_{\beta R} + \text{h.c.} \tag{2.47}$$

The first term in the previous equation gives trilinear couplings between charged leptons and the Higgs field. The second term, in addition, represents the coupling between left and right-handed fields as that in Eq. (2.38). However, these include couplings between different fields so we can not identify these terms with definite mass states. To fix this,

it will be useful to accommodate the Lagrangian in matrix form and use the notation:

$$\ell'_L = \begin{pmatrix} e'_L \\ \mu'_L \\ \tau'_L \end{pmatrix}, \qquad \nu'_L = \begin{pmatrix} \nu'_{eL} \\ \nu'_{\mu L} \\ \nu'_{\tau L} \end{pmatrix}, \qquad q'^U_L = \begin{pmatrix} u'_L \\ c'_L \\ t'_L \end{pmatrix}, \qquad q'^D_L = \begin{pmatrix} d'_L \\ s'_L \\ b'_L \end{pmatrix}, \tag{2.48}$$

and similarly for right-handed chiralities. It is very important to understand the meaning of the different notations. Equations (2.2) and (2.3) denote doublets of $SU(2)$. In contrast, the definitions in Eq. (2.48) denote column matrices with no transformation rules, these are matrices defined just to simplify the Lagrangian notation. Using this definition, we can express Eq. (2.47) in a matrix form:

$$\mathcal{L}_{H,L} = -\left(\frac{v_\Phi + H}{\sqrt{2}}\right) \overline{\ell'_L} Y'^{\ell} \ell'_R + \text{h.c.} \tag{2.49}$$

Now, in general, a complex matrix can be diagonalized by a biunitary transformation [8], which means that there exist two unitary matrices, which we denote as V^ℓ_L, and V^ℓ_R, such that

$$V^{\ell\dagger}_L Y'^{\ell} V^\ell_R = Y^\ell = \text{diag}(y_1, y_2, y_3), \tag{2.50}$$

with Y^ℓ a diagonal matrix and y_α real [11]. If we define now

$$\ell_L = V^{\ell\dagger}_L \ell'_L = \begin{pmatrix} e_L \\ \mu_L \\ \tau_L \end{pmatrix}, \tag{2.51}$$

and similarly for right-handed fields, then, after diagonalizing Y'^{ℓ} in Eq. (2.49), and using $\ell_\alpha = \ell_{\alpha L} + \ell_{\alpha R}$, we end up with

$$\mathcal{L}_{H,L} = -\left(\frac{v_\Phi + H}{\sqrt{2}}\right) \overline{\ell_L} Y^\ell \ell_R + \text{h.c.} = -\frac{1}{\sqrt{2}} \sum_\alpha y^\ell_\alpha \overline{\ell_\alpha} \ell_\alpha H - \frac{v_\Phi}{\sqrt{2}} \sum_\alpha y^\ell_\alpha \overline{\ell_\alpha} \ell_\alpha. \tag{2.52}$$

The first term in the previous equation represents a coupling of the Higgs field to lepton fields, and the corresponding Feynman diagram is illustrated in Fig. 2.5. Notice that, as a general rule, scalar fields in Feynman diagrams are depicted with dashed lines. The second term in Eq. (2.52) can now be identified with a mass term for leptons since it now couples leptons only of the same flavor. Then, unprimed fields, such as those in Eq. (2.51), denote states with definite mass. We see that the Higgs field provides a mathematically consistent manner to incorporate lepton masses into the theory.

Now we want to see what happens to the charged and neutral current interactions

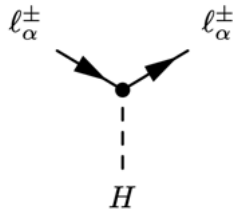

Figure 2.5: Feynman diagram for the SM coupling of the charged leptons with the Higgs field.

when using the definite mass fields. Rotating the charged lepton fields in Eq. (2.19), we have

$$j^\mu_{W,L} = 2\overline{\nu'_L}\gamma^\mu V_L^\ell \ell_L. \tag{2.53}$$

However, we are free to redefine the neutrino flavor fields as $\nu_L = V_L^{\ell\dagger}\nu'_L$ and the charged current keeps the original form. In the case of neutral current, it also preserves its form due to the unitarity of the rotating matrices, a phenomenon which is called the GIM mechanism [12].

In a similar way, we can also generate masses for the quark sector. For the case of down-type quarks, we can add a term to the Lagrangian that has the same shape as that used for charged leptons. However, here we also have to generate masses for the up-type quarks. Then, the most general invariant term needed for the quark sector will be of the form

$$\mathcal{L}_{H,Q} = -\sum_{\alpha\beta} Y'^D_{\alpha\beta}\overline{Q'_{\alpha L}}\Phi q'^D_{\beta R} - \sum_{\alpha\beta} Y'^U_{\alpha\beta}\overline{Q'_{\alpha L}}\tilde{\Phi} q'^U_{\beta R}, \tag{2.54}$$

where $\tilde{\Phi} = i\tau_2\Phi^*$. Using the unitary gauge, and expressing the result in the matrix notation introduced in Eq. (2.48), we have

$$\mathcal{L}_{H,Q} = -\left(\frac{v_\Phi + H}{\sqrt{2}}\right)\left[\overline{q'^D_L}Y'^D q'^D_R + \overline{q'^U_L}Y'^U q'^U_R\right]. \tag{2.55}$$

The two matrices $Y'^{D,U}$ can be diagonalized by biunitary transformations as in Eq. (2.50), by replacing $\ell \to D, U$ to indicate that the rotation matrices are different for each type of fermions. After diagonalizing, we get a Lagrangian in terms of the massive states (unprimed fields):

$$\begin{aligned}\mathcal{L}_{H,Q} &= -\left(\frac{v_\Phi + H}{\sqrt{2}}\right)\left[\overline{q^D_L}Y^D q^D_R + \overline{q^U_L}Y^U q^U_R\right] \\ &= -\sum_\alpha \frac{y^D_\alpha v_\Phi}{\sqrt{2}}\overline{q^D_\alpha}q^D_\alpha - \sum_\alpha \frac{y^U_\alpha v_\Phi}{\sqrt{2}}\overline{q^U_\alpha}q^U_\alpha - \sum_\alpha \frac{y^D_\alpha}{\sqrt{2}}\overline{q^D_\alpha}q^D_\alpha H - \sum_\alpha \frac{y^U_\alpha}{\sqrt{2}}\overline{q^U_\alpha}q^U_\alpha H.\end{aligned} \tag{2.56}$$

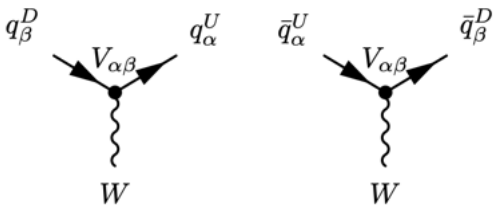

Figure 2.6: Feynman diagram for the SM quark charged current after considering mixing effects.

The first two terms of the second line represent mass terms for the case of down and up type quarks, respectively, while the third and fourth terms correspond to the coupling of these particles to the Higgs field. Now, if we substitute the definite mass states in the neutral current in Eq. (2.36), then, this current will have again the same form as with the original fields because of the GIM mechanism. However, there is a difference in the case of charged current when compared to the lepton sector. Rotating the corresponding fields in Eq. (2.33), we have

$$j^\mu_{W,Q} = 2\overline{q_L^U} V \gamma^\mu q_L^D, \tag{2.57}$$

where we have defined the product $V = V_L^{U\dagger} V_L^D$. The matrix V is known in the literature as the CKM matrix. In contrast to the lepton sector, here we do not have the freedom of redefining the up type quark fields, and the couplings of the quark fermion fields to the W gauge boson are weighted by the elements of V, as illustrated in the Feynman diagrams of Fig. 2.6. We will be more interested in a similar effect when considering neutrino masses as an extension of the SM, where we will have an analogue matrix to the CKM one.

In summary, to create an SM-like theory, the following steps are needed:

- Choose the gauge group which determines the interaction-mediating fields.
- Choose the primary fermions to underlie the model and the representations of the gauge group in which the fermions are placed.
- Write the globally invariant Lagrangian for the model and the corresponding locally invariant Lagrangian.
- Introduce an appropriate number of multiplets of scalar as well as of interaction terms of these multiplets with the fermions to obtain massive particles through spontaneous symmetry breaking.
- Specify the final composition of the model.

Any other gauge theory attempting to incorporate new physics should follow the previous steps to give a complete description of particles and their interactions.

2.3 Effective CC and NC Lagrangians

So far, we have seen that within the SM, fermions couple to gauge bosons through neutral and charged currents. The advantage of using Feynman diagrams is that we can then join them to describe many observed processes. For instance, the charged current contribution to a scattering process of the form $f_1 + f_3 \to f_2 + f_4$ is illustrated in the left diagram of Fig. 2.7. External lines represent the initial and final fermion states, while internal lines account for particles that *mediate* the interaction. Physically, we say that the fermions interact by exchanging a W boson. The main goal of Feynman diagrams is to provide a simple tool to calculate event amplitudes, which eventually account for the probability of an event to be observed. To this end we can follow the well known Feynman rules. Following these rules, we can take, for instance, the $\nu_e + e^- \to \nu_e + e^-$ process. Then, the amplitude associated to the diagram in Fig. 2.7 reads [8]

$$\begin{aligned}\mathcal{A} = \ & \overline{u}(p_2)\left(-i\frac{g}{2\sqrt{2}}\gamma^\mu\left(1-\gamma^5\right)\right)u(p_1)\left[i\frac{-g_{\mu\nu}+p_\mu p_\nu/M_W^2}{q^2-M_W^2}\right]\times \\ & \times\,\overline{u}(p_4)\left(-i\frac{g}{2\sqrt{2}}\gamma^\nu\left(1-\gamma^5\right)\right)u(p_3),\end{aligned} \tag{2.58}$$

where $u(p_i)$ are the Dirac spinors corresponding to each particle of momentum p_i, q is the momentum transfer, and $g_{\mu\nu}$ is the metric tensor. In general, most of the processes that we measure are at relatively low energies below the scale of the W mass. In this case, the term between square brackets in Eq. (2.58), which contains the information of the boson propagator, can be approximated to $ig_{\mu\nu}/M_W^2$, with M_W the mass of the W boson. Then, we can arrange some terms and we get the amplitude:

$$\mathcal{A} = -i\frac{g^2}{8M_W^2}\overline{u}(p_2)\gamma^\mu\left(1-\gamma^5\right)u(p_1)\overline{u}(p_4)\gamma_\mu\left(1-\gamma^5\right)u(p_3). \tag{2.59}$$

By using this approximation, we say that we have *integrated out* the degrees of freedom of the W gauge boson. For convenience, we now define the Fermi constant, G_F, so that

$$\frac{G_F}{\sqrt{2}} = \frac{g^2}{8M_W^2}, \tag{2.60}$$

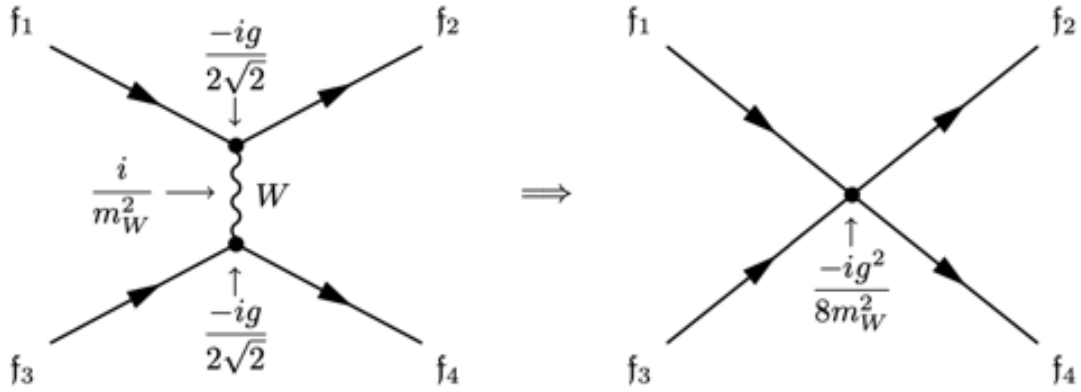

Figure 2.7: Neutrino-electron scattering charged current interaction reduced to point four-fermion interaction.

and the amplitude for charged current neutrino-electron scattering now reads

$$\mathcal{A} = -i\frac{G_F}{\sqrt{2}}\overline{u}(p_2)\gamma^\mu\left(1-\gamma^5\right)u(p_1)\overline{u}(p_4)\gamma_\mu\left(1-\gamma^5\right)u(p_3). \tag{2.61}$$

Notice that the information about the W boson is now thoroughly contained in G_F. In fact, the amplitude in Eq. (2.61) is only written in terms of the initial and final fermion states, which can be obtained from an effective Lagrangian that couples the charged currents involved in the process with an strength parametrized by the Fermi constant:

$$\mathcal{L}_{\text{eff}}^{CC} = -\frac{G_F}{\sqrt{2}}\overline{\nu_e}\gamma^\mu(1-\gamma^5)e\overline{e}\gamma_\mu(1-\gamma^5)\nu_e. \tag{2.62}$$

The corresponding Feynman diagram is illustrated in the right diagram of Fig. 2.7. Notice that the W boson mediated interaction has been now reduced to a four-fermion point interaction. In terms of the projection operators, the effective Lagrangian can be written as

$$\mathcal{L}_{\text{eff}}^{CC} = -2\sqrt{2}G_F\overline{\nu_e}\gamma^\mu P_L e\overline{e}\gamma_\mu P_L\nu_e. \tag{2.63}$$

Similarly, we can analyze the case of a NC contribution to a process of the form $f_{1i} + f_{2i} \to f_{1f} + f_{2f}$, as illustrated in the left Feynman diagram of Fig. 2.8. Taking again the particular case $\nu_e + e^- \to \nu_e + e^-$, we have an amplitude of the form [8]

$$\begin{aligned}\mathcal{A} =& \overline{u}(p_{1f})\left(-i\frac{g}{2\cos\theta_W}\gamma^\mu\left(g_V^\nu - g_A^\nu\gamma^5\right)\right)u(p_{1i})\left[i\frac{-g_{\mu\nu}+p_\mu p_\nu/M_Z^2}{q^2-M_Z^2}\right]\times \\ &\times\,\overline{u}(p_{2f})\left(-i\frac{g}{2\cos\theta_W}\gamma_\mu\left(g_V^e - g_A^e\gamma^5\right)\right)u(p_{2i}).\end{aligned} \tag{2.64}$$

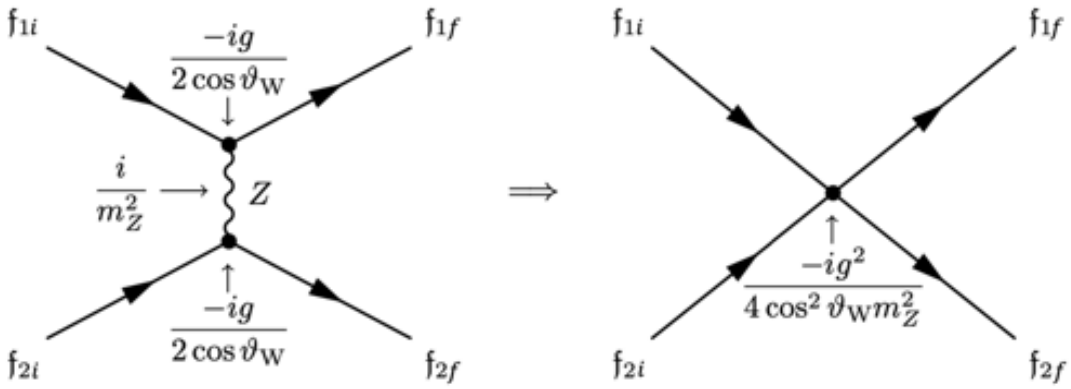

Figure 2.8: Neutrino-electron scattering neutral current interaction reduced to point four-fermion interaction.

Again, we can approximate the quantity between square brackets to $ig_{\mu\nu}/M_Z^2$, and using the relation $M_W = M_Z \cos\theta_W$, we can express

$$\mathcal{A} = -i\frac{2G_F}{\sqrt{2}}\overline{u}(p_{1f})\gamma^\mu\left(g_V^\nu - g_A^\nu\gamma^5\right)u(p_{1i})\overline{u}(p_{2f})\gamma_\mu\left(g_V^e - g_A^e\gamma^5\right)u(p_{2i}). \tag{2.65}$$

We can now follow a similar approach to that of the charged current and obtain the amplitude in the previous equation from an effective Lagrangian of the form

$$\mathcal{L}_{\text{eff}}^{NC} = -\frac{2G_F}{\sqrt{2}}\overline{\nu}_e\gamma^\mu\left(g_V^\nu - g_A^\nu\gamma^5\right)\nu_e\overline{e}\gamma_\mu\left(g_V^e - g_A^e\gamma^5\right)e. \tag{2.66}$$

The resulting Feynman diagram is illustrated in the right diagram of Fig. 2.8, where we can see that the original diagram has been again reduced to a four fermion point interaction. Using $g_V = g_L + g_R$, $g_A = g_L - g_R$, and the fact that for neutrinos $g_L^\nu = 1/2$, and $g_R^\nu = 0$, we have

$$\mathcal{L}_{\text{eff}}^{NC} = -2\sqrt{2}G_F\overline{\nu}_e\gamma^\mu P_L\nu_e\overline{e}\gamma_\mu g_L^f P_L e - 2\sqrt{2}G_F\overline{\nu}_e\gamma^\mu P_L\nu_e\overline{e}\gamma_\mu g_R^f P_R e. \tag{2.67}$$

We can generalize the Lagrangian in Eq. (2.67) for a neutral current interaction of a neutrino of flavor $\alpha = e, \mu, \tau$ with a fermion f:

$$\mathcal{L}_{eff}^{NC} = -2\sqrt{2}G_F\overline{\nu_\alpha}\gamma^\mu P_L\nu_\alpha\overline{f}\gamma_\mu g_X^f P_X f. \tag{2.68}$$

In general, f represents any charged lepton or quark, but we will be particularly interested in the interaction of neutrinos with common matter, which means that we

will take the case where $f = e, u, d$. In Eq. (2.68), $X = R, L$ is the chirality, and the values of g_X^f are given in Table 2.2. Notice that the SM effective NC Lagrangian in Eq. (2.68) satisfies the following important properties:

- The strength of the interaction is independent of the neutrino flavor, a property that is known as the *universality* of the weak force.
- It does not allow for neutrino flavor transitions between the initial and the final states.

This will be important when we introduce the concept of Non-Standard Interactions (NSI) in the following chapter, a type of interactions that will be widely studied in the remainder of this work.

Chapter 3

Neutrino Physics

Now that we know the fundamental concepts of the SM, we will focus our attention on the study of neutrinos and their interactions. Historically, the existence of the neutrino was theoretically proposed by Pauli in 1930 [13] as a solution for energy conservation in the process of beta decay. By that time, it had been observed that several nuclei, like ^{40}K and ^{3}H, could decay through a reaction of the type

$$A \to B + e^{-}, \tag{3.1}$$

with A and B nuclei that differ in one charge unit. If this was the case, the energy conservation laws dictate that the energy of the emitted electron should have a fixed value, determined by the masses of the involved particles:

$$E = \frac{m_A^2 - m_B^2 + m_e^2}{2m_A}. \tag{3.2}$$

However, experimental observations indicated that the electrons were detected with a continuous energy spectrum as that shown in Fig. 3.1. Such an spectrum could be explained if more particles were involved in the process, which motivated Pauli to propose the emission of a third particle along with the nucleus and the electron. This new particle was eventually called *neutrino*. To preserve charge conservation, this particle had to be neutral, which until now we know is true, and given the shape of the spectrum, it had to be massless, which now we know it is not. Years later, in 1933, Fermi took this idea and presented his theory of beta decay [14], explaining the nucleus decay as a result of a neutron conversion into a proton by the simultaneous emission of

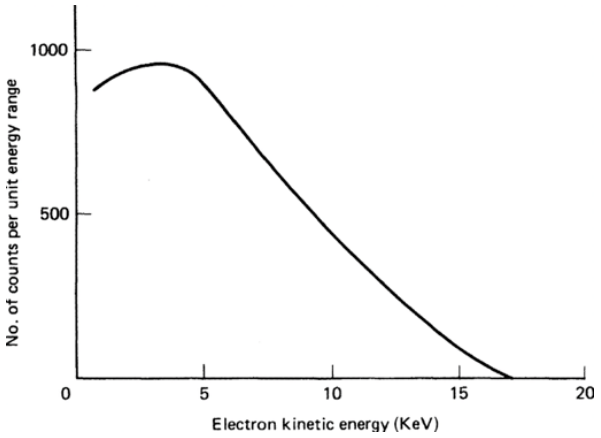

Figure 3.1: Neutrino energy spectrum observed for beta decay [7].

an electron and what we now know as anti-neutrino:

$$n \to p^+ + e^- + \overline{\nu}. \tag{3.3}$$

The experimental evidence of the existence of the neutrino was observed in the mid-1950s at the Savannah River nuclear reactor [1], where Cowan and Reines observed the inverse reaction of Eq. (3.3), that is

$$\overline{\nu} + p^+ \to n + e^+. \tag{3.4}$$

Similar observations lead to the conclusion that neutrinos also participate in reactions that involve the decay of particles as pions and muons. For years, it was thought that it was the same neutrino the one involved in all the reactions. However, in 1962, an experiment was carried out in Brookheaven by Lederman, Schwartz, and Steinberger, where they observed the reaction [15]

$$\overline{\nu} + p^+ \to \mu^+ + n. \tag{3.5}$$

In contrast, there was no evidence of the reaction:

$$\overline{\nu} + p^+ \to e^+ + n. \tag{3.6}$$

If there was only one neutrino type, then both reactions should occur at the same rate. This experiment represented clear evidence that there were at least two different types of neutrinos, each associated with the flavor of the charged lepton involved in the production reaction. Years later, in 1975, the τ lepton was discovered [16], and

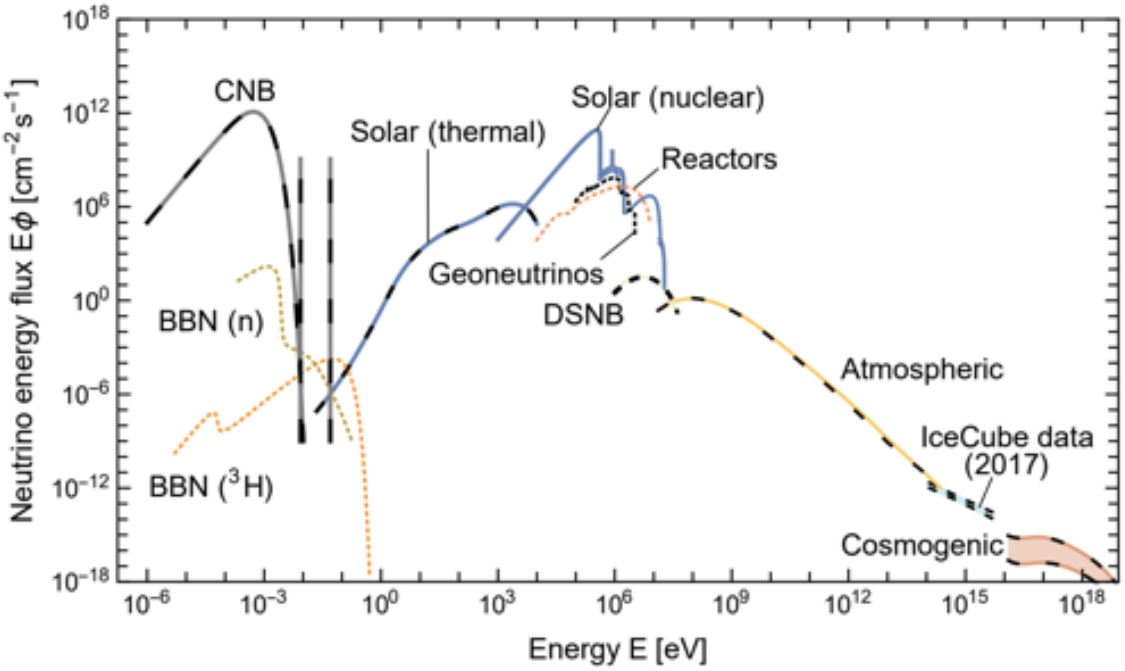

Figure 3.2: Neutrino energy spectrum on earth. Image taken from [18].

its corresponding neutrino was observed by the DONUT experiment at Fermilab in 2000 [17], completing the three neutrino picture that we have today.

In this chapter, we present a general picture of neutrino physics. We begin by discussing some of the main sources of neutrinos, each with its corresponding spectrum and flux. Then, we will focus on how neutrinos interact with electrons and nuclei within the SM picture. In addition, we discuss the theory of what we call neutrino oscillations, and we introduce the current status of the parameters that result from this phenomenon. Then, we present two different mechanisms by which neutrinos can acquire their mass, and finally, we will introduce the concept of non-standard interactions, which phenomenology will be studied in detail in the next chapters.

3.1 Neutrino sources

A unique property of neutrinos is that their different sources cover an extremely large range of energies that goes from μeV (cosmological sources), to the highest neutrino energy ever detected by IceCube, with an energy of PeV (10^{15} eV) [19], which is believed to have an origin from active galactic nuclei. We summarize in Fig. 3.2 all the neutrino sources present on Earth [18]. The different spectra cover astrophysical sources such as solar and cosmological measurements, neutrinos naturally produced on Earth such as

atmospheric and geoneutrinos, and artificial sources that include reactor and accelerator neutrinos. The spectra in the figure are summed over the three flavors, so oscillation effects, which we will discuss later, do not affect the presented distribution. Solid lines refer to neutrino sources, while dashed lines refer to anti-neutrino sources. For instance, the solar spectrum is completely made of electron neutrinos, while reactor sources are of electron anti-neutrinos. In the case of atmospheric neutrinos, produced by the collision of particles from outer space with nuclei in the atmosphere, we have the production of both neutrinos and anti-neutrinos. Cosmogenic neutrinos are predicted sources which have not been observed yet, but different experiments aim to get the first measurements in the upcoming years. In the next subsections we discuss the three main sources of neutrinos that will be used in this work; which are solar, accelerator, and reactor neutrinos.

3.1.1 Terrestrial neutrino experiments

Terrestrial neutrino experiments include those like reactor and accelerator neutrinos, which are artificially created in the laboratory. Regarding reactor sources, a small fraction of the energy produced at thermal power plants is released in the form of anti-neutrinos, which result from the decay of fission products inside the reactor. In this case, the anti-neutrinos are produced by the beta decay of neutron-rich elements. The main contribution to the flux comes from the decay of four elements with different average proportions: ^{235}U (56%), ^{239}Pu (30%), ^{238}U (8%), and ^{241}Pu (6%). It is true that these percentages vary with time as the fuel inside the reactor is burnt, but they represent an average relation within the operation time. Each of the fission events releases around 200 MeV of energy, producing on average 6 anti-neutrinos in the range of a few MeV. As a consequence, a total of 2×10^{20} s^{-1} neutrinos are produced per GW of thermal power. Indeed, this large flux allowed for the first experimental observation of neutrinos by Cowan and Reines in the Savannah River nuclear power plant [1]. Usually, the detection of these anti-neutrinos is done by an inverse beta decay process

$$\overline{\nu}_e + p \rightarrow n + e^+. \tag{3.7}$$

As a two body process, the energies of the involved particles are well determined. Then, considering the initial proton at rest, we have the relation

$$E_\nu = E_e + T_n + m_n - m_p \approx E_e + 1.293\text{MeV}, \tag{3.8}$$

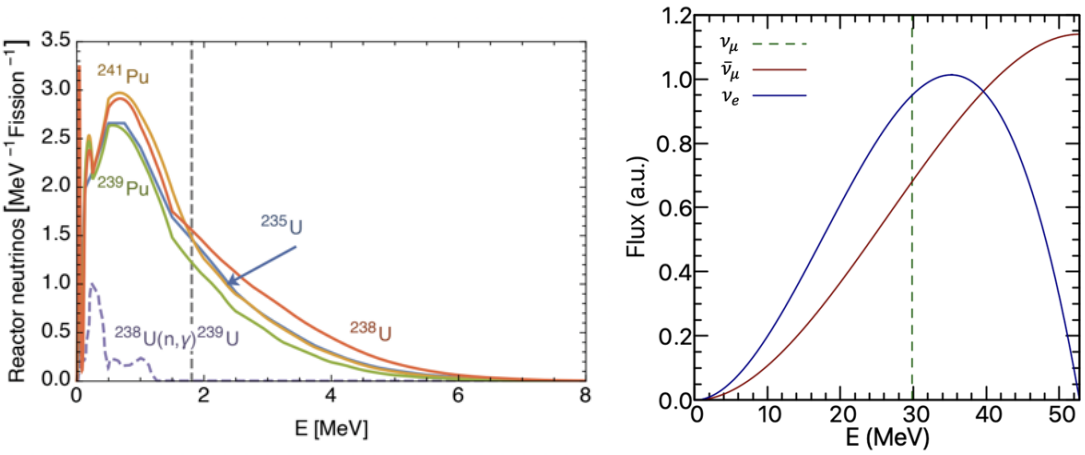

Figure 3.3: Left panel: Reactor anti-neutrino spectrum for the Hubber model; dashed distribution corresponds to neutron capture contribution [18]. Right panel: Typical normalized neutrino spectra for π-DAR sources.

where E_e is the energy of the positron and T_n is the kinetic energy of the final neutron, which we can neglect since it is very small. The anti-neutrino spectrum can be obtained by measuring the positron spectrum for each fission line and using Eq. (3.8). Since 2011, the standard references for these measurements above 2 MeV are those performed separately by Muller [20] and Huber [21]. We show in the left panel of Fig. 3.3 the different spectra for the four fission lines. The vertical dashed line in the figure shows a neutrino energy threshold of $E_\nu \approx 1.8$ MeV. Below this energy regime, neutrinos are also produced in the fission lines but they do not have enough energy to undergo the inverse beta decay reaction given in Eq. (3.7). For energies below this threshold, there is also a contribution to the anti-neutrino flux coming from neutron captures during the fission process, which is very difficult to model. Therefore there are a lot of uncertainties in the reactor flux below $E_\nu \approx 1.8$ MeV.

A second type of terrestrial human-made neutrinos are those coming from accelerator sources, on which neutrinos are produced by the decay of pions, kaons, or muons, which are produced as a byproduct of the collision of a high energy proton beam into a nuclear target. They can be classified in two main different groups:

Pion Decay In Flight (π-DIF): In this case, a high energy proton beam collides with a target, usually made of low density materials like beryllium or graphite. As a result of the interaction, there is a production of high energy pions and kaons, which have enough energy to leave the target material before being stopped. As charged particles, these mesons can then be focalized inside a magnetic tunnel with a length of about 100 m, where the mesons decay. Depending on the polarity of the magnets, they can guide only positively or negatively charged particles, and we can have the

production of pure muon neutrinos, or anti-neutrinos, respectively, through the decay channels:

$$\pi^+, K^+ \rightarrow \mu^+ + \nu_\mu, \tag{3.9}$$

$$\pi^-, K^- \rightarrow \mu^- + \overline{\nu}_\mu. \tag{3.10}$$

The energy of these neutrinos depends on the energy of the original proton beam and can be as large as a few GeV.

Pion Decay At Rest (π-DAR): In this case, neutrinos are also produced by smashing a proton beam into a target material. In contrast to π-DIF neutrinos, here the proton beam has a lower energy and the target is a high density material so that the resulting pions are stopped inside it. Most of the negatively charged pions are absorbed by nuclei, while the positively charged pions decay at rest through the decay channel in Eq. (3.9). The neutrinos produced at this step are usually called *prompt* neutrinos and have a definite energy determined by the kinematics of a two body decay, with $E_{\nu_\mu} \approx 29$ MeV. On the other hand, the resulting positively charged muons also decay at rest within the material, this time through the reaction

$$\mu^+ \rightarrow e^+ + \nu_e + \overline{\nu}_\mu. \tag{3.11}$$

Here, the decay channel is a three body process, and the two produced neutrinos, called *delayed* neutrinos, do not have a fixed energy. Rather, they have a spectrum, which can be analytically obtained by energy conservation laws [7]. The three contributions to the neutrino flux for π-DAR sources are shown in the right panel of Fig. 3.3. Spallation neutron sources, which we will study in detail in the remaining of this work, fall in this category of neutrino sources.

3.1.2 Solar neutrinos

Astrophysical neutrino sources include those that are produced within star cores. In this section, we particularly focus on the description of neutrinos coming from stars like the Sun. Inside a star core, neutrinos are produced by a variety of thermonuclear fusion processes that release energy. The main channels of neutrino production in the Sun are the *pp* chain and the CNO cycle. The different paths by which neutrinos are produced in both cases are illustrated in the two panels of Fig. 3.4. Regardless of the mechanism, the basic process summarizes to the conversion of four protons and two

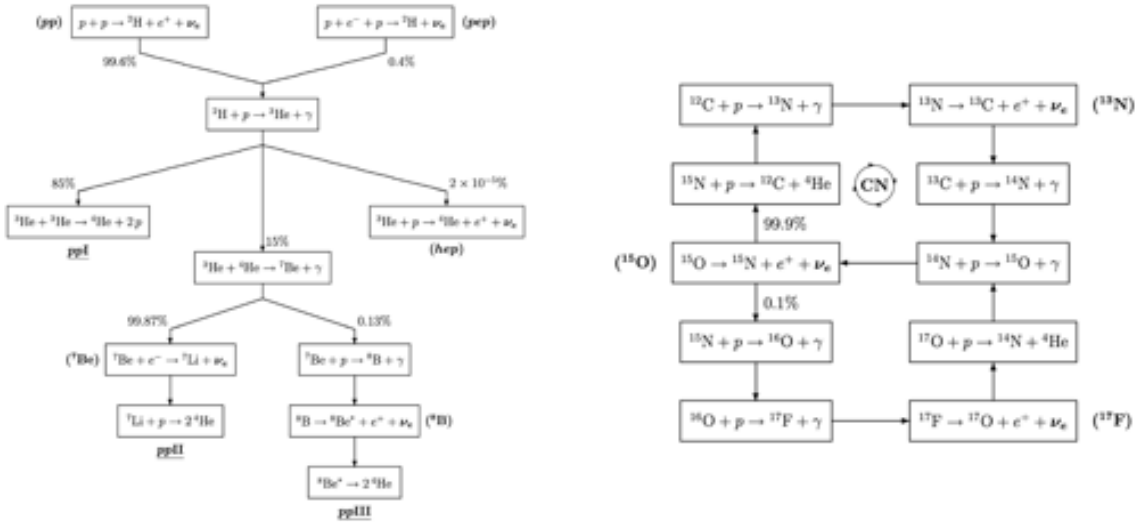

Figure 3.4: Electron neutrino production within the Sun core through the *pp* chain (left panel), and the CNO cycle (right panel) [8].

electrons into neutrinos and, after a line is complete, we have the conversion

$$4p + 2e^- \rightarrow^4 \mathrm{He} + 2\nu_e + Q, \tag{3.12}$$

where $Q \approx 26.7$ MeV is energy released either in the form of photons or as kinetic energy of neutrinos throughout the process and, in consequence, the spectrum of solar neutrinos must be below this limit.

The basis of neutrino production inside the Sun is the *pp* fusion, which results in the production of He nuclei. In a classical mechanics picture, the fusion process within a star like the Sun would not be possible for two particles of the same sign charge because the electric Coulomb potential is dominant over the strong force for distances above an average nucleus of radius R_N. To undergo fusion, a particle should need enough energy to overpass this Coulomb *barrier*; otherwise, the same sign particles would be repelled, as illustrated in the left panel of Fig. 3.5. For a proton-proton interaction, the Coulomb barrier is of around 550 keV, while the mean energy of the protons inside the Sun is about 1.5 keV, so in principle, the reaction would not be possible. However, under a quantum mechanics picture, there is a probability for the protons to overcome the barrier through quantum tunneling [22]. The same argument is valid for each step of the *pp* chain and the CNO cycle, allowing for the fusion process and the production of neutrinos. The resulting fluxes are shown in the right panel of Fig. 3.5.

The solar neutrino fluxes strongly depend on the specific model considered to describe different solar properties. These models require to reproduce the current values

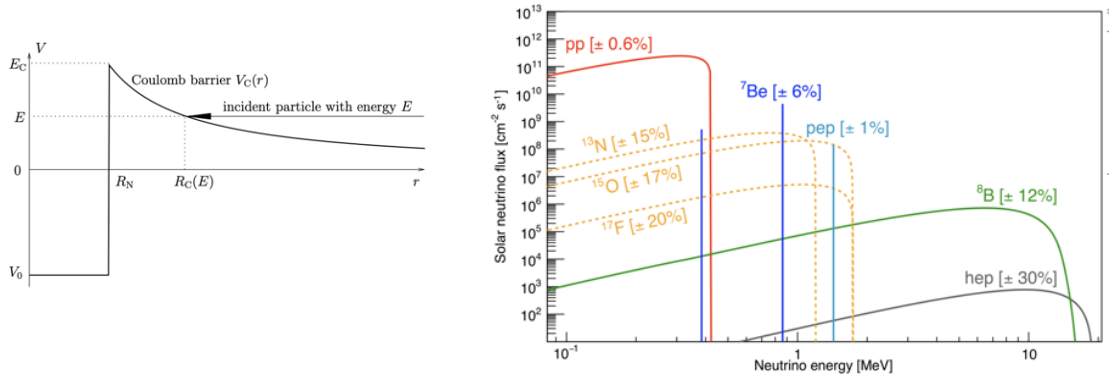

Figure 3.5: Left panel: Coulomb barrier that forbids neutrino production in a classical mechanics picture [8]. Right panel: Solar neutrino spectra for the GS98 model [8].

of luminosity, solar radius, as well as the ratio of heavy elements relative to the H abundance in the surface of the Sun. Also, a specific solar model can be tested through measurements coming from helioseismology, such as sound speed profile, the depth of the outer-most layer of the solar interior (the convective zone), and the abundance of He at the surface. A model constructed with the best available physics and input data is called a Solar Standard Model. Two of the most widely accepted models in the determination of the neutrino fluxes are the BSB05(GS98) and the BSB05(AGS05) models from Bahcall's group [23], which differ on the adopted input of heavy elements abundance in the Sun. The GS98 model uses the *old* heavy elements abundances from Ref. [24], while the AGS05 uses the *new* abundances in Ref. [25]. Although these *new* measurements are more precise, they are in disagreement with helioseismological observations, in contrast to the *old* measurements, which are in excellent agreement. Currently, there is not an agreement on the origin of this discrepancy, which is referred to as the *solar abundance problem*. The flux for each neutrino line is given in Table 3.1 for the two different models. Since there is a better agreement with helioseismological observations, we will consider the GS98 model for the computations in this work, which are those illustrated in Fig. 3.5.

3.2 Neutrino interactions in the Standard Model

It has been explained that neutrinos interact with other particles through the weak force, which means that they interact by exchanging W and Z bosons. As we have seen, there are different decay processes, like the beta and the muon decay, in which neutrinos are involved. However, we are also interested in processes where neutrinos scatter with other particles. That is the case, for instance of neutrino-electron elastic

Line	BSB05 (GS98)	BSB05 (AGS05)
$\Phi_{pp}/10^{10}$	5.99	6.06
$\Phi_{pep}/10^{8}$	1.42	1.45
$\Phi_{hep}/10^{3}$	7.93	8.25
$\Phi_{Be}/10^{9}$	4.84	4.34
$\Phi_{B}/10^{6}$	5.69	4.51
$\Phi_{N}/10^{8}$	3.05	2.00
$\Phi_{O}/10^{8}$	2.31	1.44
$\Phi_{F}/10^{6}$	5.83	3.25

Table 3.1: Solar neutrino flux in units of $\mathrm{cm}^{-2}\mathrm{s}^{-1}$ for the GS98 and AGS05 models.

scattering, and the scattering of neutrinos with nuclei, which will be of interest for our work and that we describe below.

3.2.1 Neutrino-electron elastic scattering

This process makes reference to an interaction of the form

$$\nu_\alpha + e^- \to \nu_\alpha + e^- \qquad (\alpha = e, \mu, \tau). \tag{3.13}$$

The *elastic* character of this interaction comes from the fact that the initial and final particles are the same, and hence, the effect of the interaction is a redistribution of the energy and momentum of the involved particles. Being a pure leptonic process, and because of the clear abundance of electrons in matter, an interaction as that in Eq. (3.13) is one of the most studied and well known weak processes. For incoming electron neutrinos, there are two contributions to the process, one from charged current, mediated by a W boson, and one from neutral current, mediated by a Z boson, as illustrated in the Feynman diagrams of Fig. 3.6. In contrast, for an incoming muon or tau neutrino, the charged current contribution is not present and the process is only mediated by the neutral current contribution in the right diagram of Fig. 3.6. For low energy experiments, as is the case for reactor and solar neutrinos, among other sources, gauge bosons can be integrated out, which allows us to describe the interaction through effective Lagrangians as those presented in section 2.3. Explicitly, for an incoming ν_e, the charged and neutral current contributions for this process are, respectively:

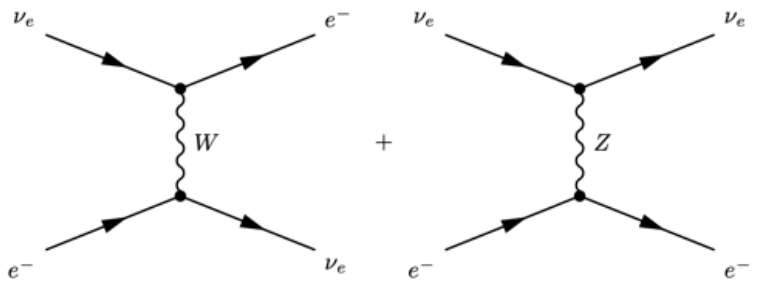

Figure 3.6: Feynman diagrams representing charged and neutral current contributions to neutrino-electron scattering.

$$\mathcal{L}_{eff}^{CC} = -\frac{G_F}{\sqrt{2}} \left[\overline{\nu_e}\gamma^\rho(1-\gamma^5)e\right] \left[\overline{e}\gamma_\rho(1-\gamma^5)\nu_e\right], \tag{3.14}$$

and

$$\mathcal{L}_{eff}^{NC} = -\frac{G_F}{\sqrt{2}} \left[\overline{\nu_e}\gamma^\rho(1-\gamma^5)\nu_e\right] \left[\overline{e}\gamma_\rho(g_V^l - g_A^l\gamma^5)e\right]. \tag{3.15}$$

Now, because of the properties of gamma matrices, it has been proven that interactions of the form of Eqs. (3.14) and (3.15) can in general be expressed in terms of other gamma matrices by exchanging two of the involved fields. These relations are known as Fierz Transformations [26], and are widely used in scattering processes to simplify some calculations. In particular, for a V-A four fermion interaction, we have the transformation

$$\left[\overline{\psi_1}\gamma^\rho(1-\gamma^5)\psi_2\right] \left[\overline{\psi_3}\gamma_\rho(1-\gamma^5)\psi_4\right] = \left[\overline{\psi_1}\gamma^\rho(1-\gamma^5)\psi_4\right] \left[\overline{\psi_3}\gamma_\rho(1-\gamma^5)\psi_2\right], \tag{3.16}$$

with ψ_i fermionic fields. Notice that in this case the matrix products remain the same, but there is an exchange between the fields labeled as ψ_2 and ψ_4. Then, we can exchange the electron and neutrino fields in Eq. (3.14) so that the charged and neutral currents have the same form. This way, for an incoming electron neutrino, the scattering is

	ν_e	$\overline{\nu_e}$	$\nu_{\mu,\tau}$	$\overline{\nu_{\mu,\tau}}$
g_1	$\frac{1}{2} + \sin^2\theta_W$	$\sin^2\theta_W$	$-\frac{1}{2} + \sin^2\theta_W$	$\sin^2\theta_W$
g_2	$\sin^2\theta_W$	$\frac{1}{2} + \sin^2\theta_W$	$\sin^2\theta_W$	$-\frac{1}{2} + \sin^2\theta_W$

Table 3.2: Neutrino-electron scattering SM couplings.

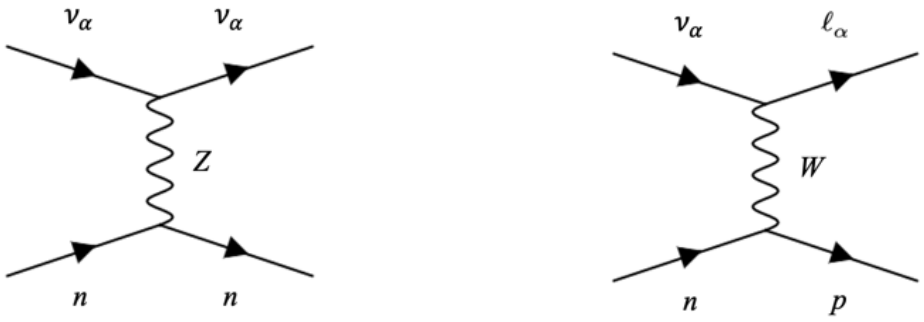

Figure 3.7: Standard Model interaction between a neutrino and a nucleon through neutral current (left) and charged current (right).

described by the effective neutral current form Lagrangian:

$$\mathcal{L}_{eff}^{NC} = -\frac{G_F}{\sqrt{2}} \left[\overline{\nu_e}\gamma^\rho(1-\gamma^5)\nu_e\right] \left[\overline{e}\gamma_\rho((1+g_V^\ell) - (1+g_A^\ell)\gamma^5)e\right]. \tag{3.17}$$

In the case of an incoming muon or tau neutrino, the interaction Lagrangian is only given by Eq. (3.15). We see that both Lagrangians in Eqs. (3.15) and (3.17) have the same form. Then, their contributions to the total cross-section can be added and in general we have [8]

$$\frac{\mathrm{d}\sigma}{\mathrm{d}T}(E_\nu, T) = \frac{2G_F^2 m_e}{\pi}\left[g_1^2 + g_2^2\left(1 - \frac{T}{E_\nu}\right)^2 - g_1 g_2 \frac{m_e T}{E_\nu^2}\right], \tag{3.18}$$

with m_e the mass of the electron, T its recoil energy, and E_ν the energy of the incoming neutrino. The values of g_1 and g_2 depend on the flavor of the incoming neutrino or anti-neutrino and are given in Table 3.2. As we will see, the introduction of NSI will modify the constants involved in the SM cross-section.

3.2.2 Coherent Elastic Neutrino-Nucleus Scattering

At tree level, neutrinos can interact with composite particles, like nucleons, by two different processes. The first one is carried on by a neutral current, which is characterized by a purely kinematic interaction and has a neutral Z boson as a mediator. In this case, particles before and after the interaction are the same but with different energies. On the second type of process, the interaction is given through a charged current, so it is mediated by $W^\pm$ bosons, and particles before and after the interaction may be different. Both processes are illustrated in Fig. 3.7 for a neutrino-neutron interaction.

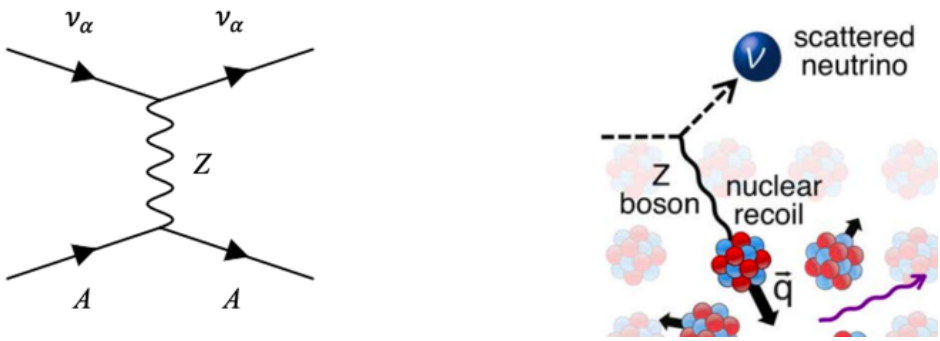

Figure 3.8: Left panel: Feynman diagram for the process of CEvNS. Right panel: Kinematic effects resulting from the CEvNS interaction. Image taken from [27].

The cross-section for this type of processes is different depending on the energy of the incident neutrino. For small energies, below 100 MeV, the dominant term of the interaction corresponds to that of the neutral current. If the neutrino's energy increases, then the interaction is dominated by the charged current and the probability for the nucleon to remain intact decreases.

Within the SM, neutrinos can also interact with an entire nucleus. In this case, the analysis turns out to be more difficult due to the internal structure of the nucleus, considered as a set of individual nucleons. We distinguish again different types of processes, but we will focus on the case of Coherent Elastic Neutrino-Nucleus Scattering (CEvNS), theoretically proposed by Freedman in 1974 [28]. After the interaction, the initial and final state of the nucleus is the same, and we have a process of the form

$$\nu_\alpha + A(Z,N) \rightarrow \nu_\alpha + A(Z,N), \tag{3.19}$$

where A stands for a nucleus with Z protons and N neutrons. The CEvNS interaction is a neutral current process, which means that, at tree level, it is mediated by a Z boson, as illustrated in the Feynman diagram on the left panel of Fig. 3.8. As a result of the interaction, there is a redistribution of the energies of the involved particles so the nucleus acquires a small kinetic recoil energy, T, determined by the momentum transfer $q^2 = 2MT$, with M the mass of the nucleus. The interaction process is depicted in the right panel of Fig. 3.8. The *coherent* character of CEvNS comes from the fact that, under certain conditions, the individual scattering amplitudes from all nucleons add up coherently to contribute to the total cross-section. This is achieved when the magnitude of the momentum transfer to the nucleus is negligible compared with the inverse of the nucleus radius, which is only true for relatively low energy neutrinos. This

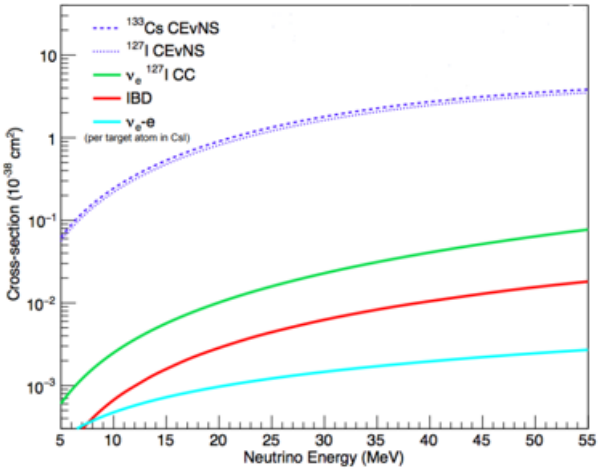

Figure 3.9: Comparison between total CEvNS cross-section and other neutrino processes in a low energy regime [27].

can be explained from a quantum mechanics picture. For a low energy neutrino, there is an associated de Broglie wavelength that is much larger than the dimensions of an average nucleus. In that case, the neutrino can not distinguish the internal scatterers of the nucleus individually, and the contributions from each nucleon to the process add up coherently. For larger energies, the associated wavelength of the neutrino is comparable to the nucleus dimensions, and the coherence effect is lost since now the neutrino distinguishes the internal structure of the nucleus.

The main advantage of CEvNS, when compared to other processes involving neutrinos, comes from its relatively large cross-section, which is given by [29, 30]

$$\left(\frac{d\sigma}{dT}\right)^{\text{coh}}_{\text{SM}} = \frac{G_F^2 M}{\pi}\left[1 - \frac{MT}{2E_\nu^2}\right][Z g_V^p F_Z^V(q^2) + N g_V^n F_N^V(q^2)]^2, \tag{3.20}$$

where $g_V^p = 1/2 - 2\sin^2\theta_W$ and $g_V^n = -1/2$ are the SM vector coupling constants, M is the mass of the nucleus, E_ν is the incoming neutrino energy, and T is the nucleus recoil energy. Notice that, within the SM, $|g_V^p| << |g_V^n|$. Therefore, there is an enhancement of the CEvNS cross-section that effectively goes as the squared number of neutrons, N^2, of the target material, which is a consequence of the coherent character of the interaction described above. As a result, the CEvNS interaction is dominant at low energies when compared to other processes, as can be seen in Fig. 3.9, where we show the cross-section of a neutrino with a Cs and I nuclei. Notice that in the range that goes from five to some tens of MeV, the CEvNS cross-section is around two orders of magnitude larger than the neutrino-electron scattering and the inverse beta decay cross-sections. In principle, this should make the CEvNS process relatively easier to measure; however, the kinetic

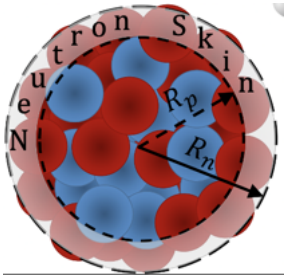

Figure 3.10: Schematic representation of proton and neutron root mean square (rms) radius [34].

recoil energy of the nucleus, which is measured on an experiment, is very small, and for current technologies it can be very difficult to reach the necessary thresholds. In addition, systematic uncertainties regarding the description of the internal structure of the nucleus (see below) make this measurement a challenging task. Fortunately, the COHERENT collaboration reported the first measurement of the process of CEvNS in 2017 by using a CsI based detector. We will discuss this experiment in detail in the following chapter.

Since axial contributions to the process are negligible [31], the cross-section in Eq. (3.20) applies for both neutrinos and anti neutrinos. In addition, the expression is flavor independent, with small corrections that have no significant impact for current experimental sensitivities [32]. Equation (3.20) also depends on the vector nuclear form factors $F^V_{Z,N}(q^2)$, which were introduced in Ref. [33] to mathematically account for the coherent structure of the cross-section in nucleus scattering. These form factors correspond to the Fourier transform of the nucleus distribution. In a general analysis, the form factors are different for protons and neutrons, and they are specially important at a higher momentum transfer. The main characteristic of these functions is that they are normalized to unity for $q^2 = 0$, or equivalently for $T = 0$, and vanish at a large momentum transfer, which is consistent with the coherency conditions already discussed.

Depending on the considered nucleus distribution, we can find in the literature many different models to describe the proton and neutron form factors. Here we will mainly consider two approximations. First we have the symmetrized Fermi distribution, which results in a form factor of the form

$$F_X^{SF}\left(q^2\right) = \frac{3}{qc\left((qc)^2 + (\pi qa)^2\right)}\left(\frac{\pi qa}{\sinh\left(\pi qa\right)}\right)\left(\frac{\pi qa\sin\left(qc\right)}{\tanh\left(\pi qa\right)} - qc\cos\left(qc\right)\right), \quad (3.21)$$

where X represents Z or N and $q^2 = 2MT$. The parameter a quantifies the surface

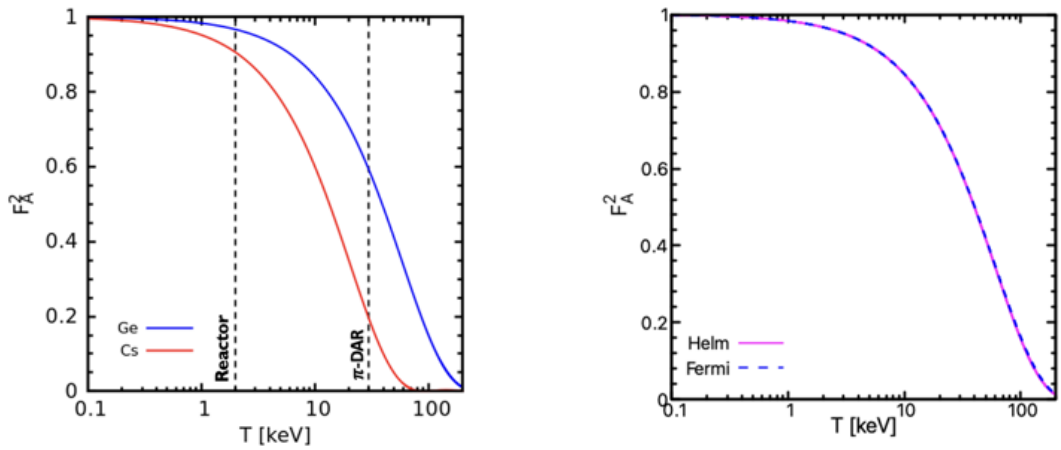

Figure 3.11: Left panel: Neutron form factor for Cs and Ge using the Helm parametrization. Vertical dashed lines show average maximum nuclear recoil energy for neutrinos from reactor and π-DAR sources. Right panel: Comparison between SF and Helm form factors for a Ge nucleus.

thickness, defined as the width of the region in which the nuclear density falls from 90% to 10% of the central density [35]. On the other hand, the parameter c is related to what we call the nucleon rms radius, R_A:

$$R_A^2 = \frac{3}{5}c^2 + \frac{7}{5}(\pi a)^2. \tag{3.22}$$

The proton and neutron rms radii, illustrated in Fig. 3.10, represent the average radius within which the corresponding nucleon is confined inside the nucleus.

We illustrate in the left panel of Fig. 3.11 the neutron form factor for a Cs and a Ge nuclei as a function of the nuclear recoil energy. The more energetic a neutrino is, the larger the kinetic energy that it can transfer to a nucleus. Hence, the impact of the form factor will depend on the neutrino source. The vertical dashed lines in Fig. 3.11 represent the maximum T that neutrinos from reactors and π-DAR sources can give to an average nuclear target. We conclude that the impact of the form factor will be significant for π-DAR sources, but can be well approximated to unity in the case of reactor neutrinos. This will be important for further analyses on which we will study how the combination of experiments with different neutrino sources can be used to constrain parameters that describe physics beyond the SM and nuclear physics.

As a second parametrization, we have the Helm form factor, which is given by

$$F_X^{Helm}(q^2) = 3\frac{j_1(qR_0)}{qR_0}e^{\frac{-q^2s^2}{2}}, \tag{3.23}$$

where $j_1(x)$ is the spherical Bessel function of order one, and R_0 is the box radius. This parameter is also related to the nucleon rms radius by

$$R_A^2 = \frac{3}{5}R_0^2 + 3s^2. \tag{3.24}$$

Here the constant s quantifies the surface thickness. Any of the two parametrizations presented here can be used to describe the form factors. In fact, we show in the right panel of Fig. 3.11 a comparison between the Symmetrized Fermi and Helm form factors for a Ge nucleus. As we can see, they are almost equal in the range of interest, being the maximum difference between their values below 1%. As a result, regarding the chosen form factor, all of the observables considered in this work turn to be model independent, and we will follow the convention of considering the Symmetrized Fermi distribution for protons and the Helm one for the case of neutrons.

Experimentally, the proton rms radius can be studied through electromagnetic interactions, and there have been measurements of this parameter for many nuclei. In contrast, the neutron rms radius is more difficult to study due to the lack of charge of the neutron and for most nuclei we only have theoretical predictions. However, the CEvNS process can be used to study the neutron rms radius through its cross-section dependence on nuclear form factors [36].

3.3 Neutrino oscillations

The SM in its original form can explain different phenomena with great accuracy. However, there are different experimental observations that can not be explained within this theory. For instance, we have the case of solar neutrinos, atmospheric neutrinos, and long baseline neutrino experiments. One of the most known mismatches came in the case of solar neutrinos through what we call the Solar Neutrino Problem. In summary, different experiments measuring the solar neutrino flux were having a considerable deficit when comparing their results with theoretical predictions. Today we know that this deficit can be explained if neutrinos change their flavor during their propagation, a phenomenon called neutrino oscillations. Through this mechanism, a neutrino that was created, for instance, as an electron state, has a probability of being measured as a muon or a tau neutrino state. Here we give a brief review of the Solar Neutrino Problem to motivate the idea of neutrino oscillations.

Historically, the Homestake Experiment (South Dakota, USA) was the first one to ever measure solar neutrinos in 1968 [37]. This was done with a Cl detector, through

the charged current reaction

$$\nu_e + {}^{37}\mathrm{Cl} \rightarrow e^- + {}^{37}\mathrm{Ar}. \tag{3.25}$$

The experiment was sensitive only to electron neutrino interactions from the ^{8}B flux (see Fig. 3.5), and the events were measured by extracting the resulting Ar atoms by radiochemical processes, with a reported efficiency of 90%. In addition, the experiment was expected to measure less events than the theoretical prediction because it was known that many of the Ar atoms would decay before being extracted. However, the discrepancy was far from the expected, and the collaboration reported an event rate of around 0.3 when compared to theoretical calculations. This result represented the first hint of a neutrino deficit for solar neutrinos.

After the Homestake experiment observations, the GALLEX detector (Gran Sasso, Italy), was designed in 1991 to measure solar neutrinos [38], this time by means of a detector based on Ga, through the reaction

$$\nu_e + {}^{71}\mathrm{Ga} \rightarrow e^- + {}^{71}\mathrm{Ge}. \tag{3.26}$$

This detector was sensitive mainly to neutrinos from the *pp*, ^{8}B, and ^{7}Be lines. As in the Homestake experiment, the events were counted by extracting the Ge nuclei by radiochemical methods, and the efficiency was tested with a Cr source to be sure that the experiment was working properly. Despite all the efforts, eventually, it was also reported around a 0.5 event rate when compared to theoretical predictions. The GNO experiment, its successor, reported similar results [39]. Independently from the GALLEX experiment, the SAGE detector (Russia) was another gallium-based experiment [40], built in 1990, that intended to measure solar neutrinos through the reaction in Eq. (3.26). The efficiency of the experiment was also tested with a Cr source, but it also reported a rate of around 0.5 when compared to the theoretical prediction, which confirmed the GALLEX-GNO measurement.

Another experiment that intended to measure solar neutrinos was the Kamiokande experiment (Kamioka, Japan) in 1986 [41]. In contrast to the other experiments, this detector was made of pure water, and was able to measure neutrinos in real time by the Cherenkov radiation that resulted from the final state electrons in the reaction

$$\nu_\alpha + e^- \rightarrow \nu_\alpha + e^-. \tag{3.27}$$

Although this reaction is sensitive to all active neutrino flavors, the detector was mainly

sensitive to electron neutrinos since its cross-section is around six times larger than that for muon and tau neutrinos. The experiment was only sensitive to the ^{8}B line, and it also reported a deficit of 0.5 when compared to the SM prediction. The upgrade of this experiment is Super-Kamiokande, which reported similar results [42].

What all these experiments had in common was that they were mainly sensitive to electron neutrinos. It was the SNO experiment (Ontario, Canada) the one that eventually overcame this issue [43]. This experiment consisted of a detector made of heavy water (D_2O), where neutrinos from the ^{8}B line were also detected by the trace left from Cherenkov radiation. In addition to interactions of the form in Eq. (3.27), the experiment was also sensitive to the reaction channels [44]:

$$\text{CC:} \quad \nu_e + d \to p + p + e^-, \tag{3.28}$$

$$\text{NC:} \quad \nu_\alpha + d \to p + n + \nu_\alpha, \tag{3.29}$$

with d denoting the deuterium in heavy water. The neutral current reaction in Eq. (3.29) allowed for the measurement of the three neutrino flavors, reporting a rate of 0.8 when compared to theoretical predictions, which is consistent, after accounting for the different uncertainties, with the hypothesis of flavor transitions during neutrino propagation. This represented one of the final proofs for neutrino oscillations as the solution to the solar neutrino problem. As an interesting fact, neutrino oscillations were proposed in 1957 by Pontecorvo [45] in analogy to the observed oscillations of K^0 hadrons. By that time, the only known neutrino was the electron neutrino. Therefore, Pontecorvo originally proposed transitions between a neutrino and an anti-neutrino. However, by 1967 the muon neutrino had already been observed, and it was in that year that he predicted the solar neutrino problem as a consequence of oscillations of electron neutrinos to either a muon neutrino or a hypothetical sterile neutrino state [46].

From the theoretical point of view, oscillations are only possible if neutrino interaction states are different from propagation states. In the standard theory of neutrino oscillations, a neutrino of flavor α is created as a result of charged current interactions. Then, within a quantum mechanical approach, this flavor state $|\nu_\alpha\rangle$ can be represented as a linear combination of three massive states $|\nu_k\rangle$:

$$|\nu_\alpha\rangle = \sum_{k=1,2,3} U^*_{\alpha k}|\nu_k\rangle \quad \Leftrightarrow \quad |\nu_k\rangle = \sum_{\alpha=e,\mu,\tau} U_{\alpha k}|\nu_\alpha\rangle, \tag{3.30}$$

where U is a unitary matrix, and the two basis are orthonormal. The above massive states are solutions of the free Hamiltonian $\mathcal{H}$, which means that they obey the

Schröedinger equation:

$$\mathcal{H}|\nu_k\rangle = E_k|\nu_k\rangle, \tag{3.31}$$

with $E_k = \sqrt{p^2 + m_k^2}$ the energy of the massive states, and we are assuming that these states carry the same momentum p. As a solution to the Schröedinger equation, the mass states evolve in time as plane waves in the form $|\nu_k(t)\rangle = \exp(-iE_k t)|\nu_k\rangle$, which combined with the right hand expression in Eq. (3.30), gives

$$|\nu_\alpha(t)\rangle = \sum_\beta \left(\sum_k U^*_{\alpha k} e^{-iE_k t} U_{\beta k} \right) |\nu_\beta\rangle. \tag{3.32}$$

This last equation shows that the neutrino state at a time t becomes a superposition of the different neutrino flavor states. Then, the probability of finding the neutrino on a flavor state $|\nu_\beta\rangle$ is given by

$$P_{\nu_\alpha \to \nu_\beta} = |\langle \nu_\beta | \nu_\alpha(t)\rangle|^2 = \sum_{k,j} U^*_{\alpha k} U_{\beta k} U_{\alpha j} U^*_{\beta j} e^{i(E_k - E_j)t}. \tag{3.33}$$

For ultrarelativistic neutrinos, which has been the case for currently detected neutrinos since their masses are tiny, we have $E_k \approx E + m_k^2/2E$, with E the neutrino energy neglecting the mass contribution. In addition, in this approximation, where we use natural units, we can use $t \approx L$, with L the distance traveled by the massive states. Then, Eq. (3.33) can be expressed as

$$P_{\nu_\alpha \to \nu_\beta} = \sum_{k,j} U^*_{\alpha k} U_{\beta k} U_{\alpha j} U^*_{\beta j} e^{i\frac{\Delta m^2_{kj} L}{2E}}. \tag{3.34}$$

The anti-neutrino case can be obtained in a similar way and the corresponding expression is given by taking the conjugate of Eq. (3.34), that is

$$P_{\overline{\nu_\alpha} \to \overline{\nu_\beta}} = \sum_{k,j} U_{\alpha k} U^*_{\beta k} U^*_{\alpha j} U_{\beta j} e^{-i\frac{\Delta m^2_{kj} L}{2E}}. \tag{3.35}$$

From Eqs. (3.34) and (3.35) , we can see that the oscillation probability is only sensitive to neutrino squared mass differences. As we will see, oscillation data gives us information about these squared mass differences, but we do not know the correct sign of Δm^2_{32}. Then, there is the question of what is the correct mass ordering of neutrinos. We refer to the Normal Ordering (NO) and to the Inverted Ordering (IO) of neutrino mass when we consider ν_1 and ν_3 as the lightest neutrino, respectively. Both scenarios

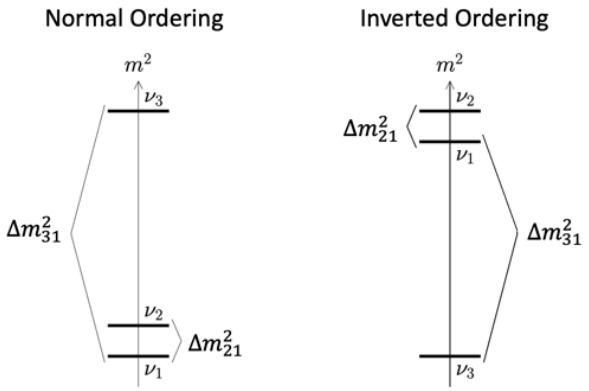

Figure 3.12: Neutrino mass pattern in the Normal Ordering (left) and Inverted Ordering (right).

are illustrated in Fig. 3.12.

3.4 Oscillations in matter

The theory of neutrino oscillations in vacuum during their propagation from the sun to the earth seemed to be a good explanation for the Solar Neutrino Problem. If this was the correct explanation, it was expected a seasonal variation on the solar neutrino flux since the distance between the earth and the sun changes significantly throughout the year. However, not significant variations were observed, and this hypothesis was disfavored. A solution was given in 1978 by L. Wolfenstein [47], who proposed that neutrino flavor transitions were enhanced by matter effects during neutrino propagation within the sun, which we briefly summarize.

When neutrinos propagate in matter, they experience an effective potential that modifies their evolution equation. In principle, it is well known that neutrinos barely interact with matter so we may wonder how they even notice the surrounding matter when they propagate in a medium. The answer comes from the process of neutrino-electron *coherent* elastic forward scattering, depicted in Fig. 3.13 for the case of neutral current interactions. As described in section 3.2.1, for a neutrino elastic collision, there is a rearrangement of the momenta of the involved particles. When the momentum of the initial and final neutrino are different, then the cross-section involved in the process is very small since the neutrino interacts with only one particle. However, when a neutrino propagates in matter, they can interact with the surrounding particles with no momentum exchange. In this case, we ignore the particle with which the neutrino interacts, so we need to sum up *coherently* the contributions from all the particles of the medium, which in regular matter are mainly protons, electrons, and neutrons. This

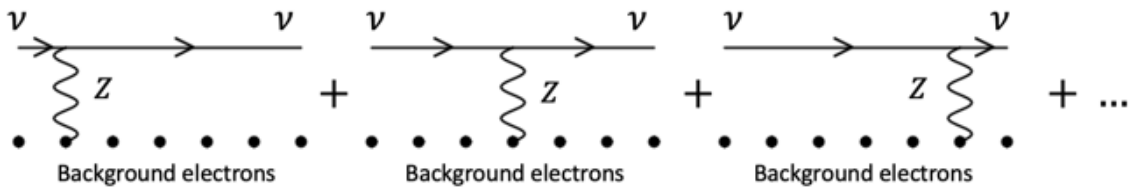

Figure 3.13: Neutral current contribution for neutrino-electron coherent elastic forward scattering in a medium.

way, the cross-section of the process is enhanced and becomes the dominant process for neutrino interactions in a medium. This process is analogous to a refraction index for a photon propagating through a medium. In general, both charged and neutral current interactions can contribute to the coherent forward scattering. Then, assuming neutral matter, the potential that a neutrino ν_α feels during the propagation in matter is given by[1] [8]

$$V_\alpha = \sqrt{2} G_F \left(N_e \delta_{\alpha e} - \frac{1}{2} N_n \right), \tag{3.36}$$

with N_n the density of neutrons and N_e the density of electrons, which is the same as that of protons for neutral matter. The physical meaning of V_α is that of a potential energy of ultra-relativistic left-handed neutrinos of flavor α propagating through a medium. This potential needs to be included in the evolution equation of neutrinos. Then, denoting the amplitude of $\nu_\alpha \to \nu_\beta$ transitions as $\psi_{\alpha\beta}(x) = \langle \nu_\beta | \nu_\alpha(x) \rangle$, the evolution equation for this amplitude in the matrix form reads

$$i \frac{\mathrm{d}}{\mathrm{d}x} \Psi_\alpha = \frac{1}{2E} \left(U M^2 U^\dagger + A \right) \Psi_\alpha, \tag{3.37}$$

where we have used the matrix notation:

$$\Psi_\alpha = \begin{pmatrix} \psi_{\alpha e} \\ \psi_{\alpha \mu} \\ \psi_{\alpha \tau} \end{pmatrix}, \qquad M^2 = \begin{pmatrix} 0 & 0 & 0 \\ 0 & \Delta m^2_{12} & 0 \\ 0 & 0 & \Delta m^2_{13} \end{pmatrix}, \qquad A = \begin{pmatrix} A_{CC} & 0 & 0 \\ 0 & 0 & 0 \\ 0 & 0 & 0 \end{pmatrix}, \tag{3.38}$$

with $A_{CC} = 2\sqrt{2} E G_F N_e$. The expression in Eq. (3.37) represents a Schrodinger-like equation, with the Hamiltonian, in the flavor basis, $\mathcal{H}_\mathrm{F} = (2E)^{-1} \left(U M^2 U^\dagger + A \right)$. There is an interesting effect when we consider matter effects, which enhances the oscillation probability. To illustrate the general concept, we consider the case of two neutrino mix-

[1] In neutral matter the density of protons and neutrons is the same. Hence, the neutral current contribution to V_α of protons is canceled by the neutral current contribution of electrons.

ing, which, as we will see, ends up being an excellent approximation for solar neutrinos. Denoting by θ and Δm^2 the mixing angle and the squared mass difference in vacuum for two neutrino mixing, respectively, and after removing common phases, Eq. (3.37) explicitly reads

$$i\frac{\mathrm{d}}{\mathrm{d}x}\begin{pmatrix}\psi_{ee}\\ \psi_{e\mu}\end{pmatrix} = \frac{1}{4E}\begin{pmatrix}-\Delta m^2\cos 2\theta + 2A_{CC} & \Delta m^2\sin 2\theta\\ \Delta m^2\sin 2\theta & \Delta m^2\cos 2\theta\end{pmatrix}\begin{pmatrix}\psi_{ee}\\ \psi_{e\mu}\end{pmatrix}. \tag{3.39}$$

The Hamiltonian matrix in Eq. (3.39) can then be diagonalized by a unitary transformation U_M of the form

$$U_M = \begin{pmatrix}\cos\theta_M & \sin\theta_M\\ -\sin\theta_M & \cos\theta_M\end{pmatrix}, \tag{3.40}$$

with θ_M the weak mixing angle in matter. The unitary transformation is such that

$$U_M^T\mathcal{H}_F U_M = \mathcal{H}_M = \frac{1}{4E}\mathrm{diag}\left(-\Delta m_M^2, \Delta m_M^2\right). \tag{3.41}$$

Being Δm_M^2 the squared mass difference in matter, and $\mathcal{H}_M$ denotes the Hamiltonian in the mass basis. In terms of their vacuum counterparts, the matter parameters are given by

$$\Delta m_M^2 = \sqrt{\left(\Delta m^2\cos 2\theta - A_{CC}\right)^2 + \left(\Delta m_M^2\sin 2\theta\right)^2}, \tag{3.42}$$

$$\tan 2\theta_M = \frac{\tan 2\theta}{1 - \frac{A_{CC}}{\Delta m^2\cos 2\theta}}. \tag{3.43}$$

Notice from Eq. (3.43), that there is a resonance for $A_{CC} = \Delta m^2\cos 2\theta$, where the mixing angle in matter is $\pi/4$, leading to a maximal neutrino mixing. This is the so-called MSW effect [48]. In normal matter, A_{CC} is positive and from Eq. (3.43) we see that a resonant condition can exist only if $\theta < \pi/4$. Therefore, the oscillation probability behaves differently in matter than it does in vacuum, where the probability is symmetric under $\theta \to \pi/2 - \theta$. If possible, the resonance condition can be achieved if the electron density satisfies

$$(N_e)_{res} = \frac{\Delta m^2\cos 2\theta}{2\sqrt{2}G_F E}. \tag{3.44}$$

In the case of antineutrinos, there is a change of sign in A_{cc}, and hence, there can only be a resonance if $\theta > \pi/4$. This means that there can only be a resonance either for neutrinos or for antineutrinos, but not for both.

If the propagation medium has a constant density, it is hard to find the conditions

for resonance. However, if the matter density is variable, then we can find a region where the resonance is satisfied, opening the possibility to enhance transitions between states. To explain this, we consider the rotation of the flavor fields:

$$\begin{pmatrix}\nu_e\\ \nu_\mu\end{pmatrix} = \begin{pmatrix}\cos\theta_M & \sin\theta_M\\ -\sin\theta_M & \cos\theta_M\end{pmatrix}\begin{pmatrix}\nu_1^M\\ \nu_2^M\end{pmatrix} \quad \Rightarrow \quad \begin{pmatrix}\psi_{ee}\\ \psi_{e\mu}\end{pmatrix} = \begin{pmatrix}\cos\theta_M & \sin\theta_M\\ -\sin\theta_M & \cos\theta_M\end{pmatrix}\begin{pmatrix}\phi_{e1}\\ \phi_{e2}\end{pmatrix}. \tag{3.45}$$

The ν_i^M fields can be interpreted as the *effective neutrino mass* eigenstates in matter, and $\phi_{ei} = \langle\nu_e|\nu_i^M\rangle$ is the amplitude of ν_e in the effective mass basis. Expressing Eq. (3.39) in terms of the new rotated fields probabilities:

$$i\frac{\mathrm{d}}{\mathrm{d}x}\begin{pmatrix}\phi_{e1}\\ \phi_{e2}\end{pmatrix} = \frac{1}{4E}\begin{pmatrix}-\Delta m_M^2 & -4Ei\frac{\mathrm{d}\theta_M}{\mathrm{d}x}\\ 4Ei\frac{\mathrm{d}\theta_M}{\mathrm{d}x} & \Delta m_M^2\end{pmatrix}\begin{pmatrix}\phi_{e1}\\ \phi_{e2}\end{pmatrix}. \tag{3.46}$$

In general, the effective mass eigenstates vary with time and, just as flavor fields, there can be transitions between them. Then, the amplitudes ϕ_{ei} also vary in time. However, if the non-diagonal terms in Eq. (3.46) are negligible, then there will be no transitions between effective matter states and the effect on the amplitude will be a phase factor with respect to the initial amplitude. This is called the adiabatic approximation, and the details about the conditions that need to be satisfied for this approximation can be found in Ref. [8]. The most important feature of this approximation is that in this case the survival probability will depend only on the initial effective mixing angle, that is, on the angle at the point where the neutrino was produced:

$$P^{\text{adiab}}_{\nu_e\to\nu_e} = \frac{1}{2} + \frac{1}{2}\cos 2\theta_M \cos 2\theta. \tag{3.47}$$

We will use this approximation in chapter 7 to study neutrino electromagnetic properties with solar neutrinos.

3.5 Massive neutrinos

The observation of neutrino oscillations has provided a definite proof that at least two of the neutrinos are massive. However, questions like what is the absolute neutrino mass scale, what is the correct mass hierarchy, and what is the origin of their so tiny masses, are still open. Since neutrinos are considered massless within the SM, then the theory needs to be extended so that we account for their little masses. To do so, we first need to know that, in contrast to the other elementary fermions, neutrinos have

no electric charge and, in consequence, the fields describing these particles can have a Dirac or a Majorana nature. For Dirac fermions, particles and anti-particles correspond to different states, while in the case of Majorana fields both particle and anti-particle correspond to the same state. Here we summarize how Dirac or Majorana terms for neutrino masses can be added to the SM Lagrangian.

Dirac masses: In this case, we can generate neutrino masses with the same Higgs mechanism that gives masses to the other fermions. This can be done by the introduction right-handed neutrinos $\nu_{\alpha R}$. A theory that only adds these states is called a minimal extension of the SM because we are only adding right-handed states to the existing neutrino fields. However, these right-handed neutrino states are not observed to participate in weak interactions, so they must be added as singlets under the $SU(2)_L \times U(1)_Y$ gauge group. In consequence, they are not sensitive to any forces other than gravity, and they are called sterile states. To generate Dirac masses with the new introduced right-handed fields, we only have to replicate the mechanism used in section 2.2 to generate the masses of up-type quarks. That is, we add to the Lagrangian a Yukawa-type interaction of the form

$$\mathcal{L}_{\rm D}^{\rm mass} = -\sum_{\alpha,\beta} Y'^{\ell}_{\alpha\beta} \overline{L_{\alpha L}} \Phi \ell'^{D}_{\beta R} - \sum_{\alpha,\beta} Y'^{\nu}_{\alpha\beta} \overline{L_{\alpha L}} \widetilde{\Phi} \nu'_{\beta R}, \tag{3.48}$$

where $\alpha, \beta = e, \mu, \tau$ and Y'^{ν} is a completely general complex matrix of Yukawa couplings. After spontaneous symmetry breaking, and using the unitary norm, we can write the previous equation in the form

$$\mathcal{L}_{\rm D}^{\rm mass} = -\left(\frac{v_\Phi + H}{\sqrt{2}}\right)\left(\overline{\ell'_L} Y'^{\ell} \ell'_R + \overline{\nu'_L} Y'^{\nu} \nu'_R\right) + \text{h.c.}, \tag{3.49}$$

where we have used the matrix notation introduced in Eq. (2.48), adding the right-handed neutrinos $\nu'_R = \begin{pmatrix} \nu'_{eR} & \nu'_{\mu R} & \nu'_{\tau R} \end{pmatrix}^T$. Each of the Yukawa matrices in the previous equation can be diagonalized by a biunitary transformation. For Y'^{ℓ} we use the same matrices as in Eq. (2.50), when we introduced the Higgs mechanism, and for Y'^{ν} we use the unitary matrices V_L^ν and V_R^ν, such that

$$V_L^{\nu\dagger} Y'^{\nu} V_R^{\nu} = Y^{\nu}, \tag{3.50}$$

with $Y^\nu = \text{diag}(y_1^\nu, y_2^\nu, y_3^\nu)$ a diagonal real matrix. We now define the neutrino massive

chiral states:

$$n_L = V_L^{\nu\dagger}\nu_L^{'} = \begin{pmatrix} \nu_{1L} \\ \nu_{2L} \\ \nu_{3L} \end{pmatrix}, \tag{3.51}$$

with a similar expression for ν_R states. By substituting the last two equations in the Dirac masses Lagrangian (Eq. (3.49)) and using $\nu = \nu_L + \nu_R$, we get the diagonalized Lagrangian:

$$\mathcal{L}_{\rm D}^{\rm mass} = -\sum_\alpha \frac{y_\alpha^\ell v_\Phi}{\sqrt{2}}\overline{\ell_\alpha}\ell_\alpha - \sum_k \frac{y_k^\nu v_\Phi}{\sqrt{2}}\overline{\nu_k}\nu_k - \sum_\alpha \frac{y_\alpha^\ell}{\sqrt{2}}\overline{\ell_\alpha}\ell_\alpha H - \sum_k \frac{y_k^\nu}{\sqrt{2}}\overline{\nu_k}\nu_k H. \tag{3.52}$$

From the second term in this equation we can identify the Dirac neutrino masses with the form

$$m_k = \frac{y_k^\nu v_\Phi}{\sqrt{2}}. \tag{3.53}$$

We see that, as in the case of the other fermions, the masses of Dirac neutrinos are proportional to v_Φ, and the smallness of their masses is not explained. Also, the last term in Eq. (3.52) represents the coupling of neutrinos to the SM Higgs field, which is expected since in this case they acquire their mass through the same mechanism as the other fermions. It is interesting to see the effect that the introduction of massive neutrinos has for the interaction with other fermions. In the case of charged current, we have

$$j_{W,L}^\rho = 2\overline{\nu_L'}\gamma^\rho \ell_L' = 2\overline{n_L}V_L^{\nu\dagger}V_L^\ell\gamma^\rho\ell_L. \tag{3.54}$$

The matrix $U \equiv V_L^{\nu\dagger}V_L^\ell$ is the lepton sector analogue of the CKM matrix defined for quarks. This matrix is usually called the PMNS matrix, and we can write the charged current in the form

$$j_{W,L}^\rho = 2\overline{n_L}U^\dagger\gamma^\rho\ell_L. \tag{3.55}$$

In the case of the neutral current, the GIM mechanism is preserved given the unitarity of V_L^ν and V_L^ℓ. This can be noticed from the definition of the massive states

$$j_{W,L}^\rho = 2g_\ell^\nu\overline{\nu_L'}\gamma^\rho\nu_L' = 2g_\ell^\nu\overline{n_L}V_L^{\nu\dagger}V_L^\nu\gamma^\rho n_L = 2g_\ell^\nu\overline{n_L}\gamma^\rho n_L, \tag{3.56}$$

and the neutral current has the same form in the mass basis as in the flavor basis. There are two important comments regarding neutrino mixing. First, it is useful to define the neutrino flavor states as

$$\nu_L = Un_L. \tag{3.57}$$

In this way, the neutrino charged current in Eq. (3.55) has the same form as that in the SM. In contrast to the quark sector, this can be done in cases where the effects of the neutrino masses are neglected. Otherwise, we need to use the charged current in terms of neutrino mass states. Secondly, the mixing in the lepton sector is given to neutrinos since the charged leptons can be distinguished by their mass. In contrast, we cannot distinguish neutrinos by measuring their mass, but only by the charged lepton involved in their production process.

Majorana masses: To understand the concept of Majorana masses, we need to remember that, in general, we can write a fermion field ψ as the sum of two independent chiral fields $\psi = \psi_L + \psi_R$, each with two independent components. Also, we know that a fermion field is described by the Dirac equation $(i\gamma^\mu \partial_\mu - m)\,\psi = 0$. Then, expressing ψ in terms of the chiral fields we have:

$$i\gamma^\mu \partial_\mu \psi_L = m\psi_R, \tag{3.58}$$

$$i\gamma^\mu \partial_\mu \psi_R = m\psi_L. \tag{3.59}$$

In the case of a massless fermion, the system in Eqs. (3.58) and (3.59) is decoupled, and the field can be thoroughly described by two degrees of freedom. Within the SM this is the case of neutrino fields, but we now know that neutrinos are massive. However, Majorana realized that also neutral massive fields can be described by two degrees of freedom if we assume ψ_L and ψ_R are not independent [49]. Indeed, we can take the relation

$$\psi_R = C\overline{\psi_L}^T, \tag{3.60}$$

with C the charge conjugation operator, which transforms particle states into anti-particle states. Notice that this represents a valid choice since, defined in this way, the field ψ_R is actually a right-handed field. We can see this by applying the P_L projection operator, which satisfies $P_L(C\overline{\psi_L}^T) = 0$. Then, if the condition in Eq. (3.60) is satisfied, the two Eqs. (3.58) and (3.59) are the same, so the particle can be described with only one independent field ψ_L. Then, by denoting $\psi_L^C = C\overline{\psi_L}^T$, a Majorana fermion field can be written as

$$\psi = \psi_L + \psi_L^C, \tag{3.61}$$

which represents the Majorana condition for a fermion field. In general, it can be shown that under the C operation, a field transforms as $\psi \to \psi^C$ and vice versa. Then, from Eq. (3.61), we can see that a Majorana field is the same as its anti-particle field. This means that only neutral particles, like neutrinos, can be Majorana fields. It is true

that in general we can also write the field ψ_L in terms of ψ_R but, within the SM, the left-handed neutrino fields are those that participate in weak interactions and we take the convention of writing the field in terms of ψ_L. From the condition in Eq. (3.61), the Majorana mass Lagrangian takes the form

$$\mathcal{L}^M_{\text{mass}} = -m\left(\overline{\nu^C_L}\nu_L + \nu_L\overline{\nu^C_L}\right) = -m\left(-\nu_L^T C^\dagger \nu_L + \overline{\nu_L} C \overline{\nu_L}^T\right), \tag{3.62}$$

where the notation defined above Eq. (3.61) was used. It is important to mention that a Lagrangian as that in Eq. (3.62) is not allowed within the symmetries of the SM. In fact, Weinberg [50] showed that the lowest energy dimension operator constructed with SM fields that can generate a Majorana mass Lagrangian, without spoiling gauge symmetry, is the dimension five operator:

$$\mathcal{L}_5 = \frac{\kappa}{\mathcal{M}}\left(L_L^T \tau_2 \Phi\right) C^\dagger \left(\Phi^T \tau_2 L_L\right) + \text{h.c.} \tag{3.63}$$

In this Lagrangian, κ is a dimensionless coupling constant and $\mathcal{M}$ is a constant with dimensions of mass that is introduced for a correct renormalizability of the theory, which needs the operator to be of dimension four at most. In this sense, the Majorana mass terms would result as a low energy manifestation of a more general theory than the SM, that is valid above the electro weak scale, just as the Fermi theory of the beta decay is a low energy manifestation of the SM theory. After spontaneous symmetry breaking, and using the unitary norm, the operator in Eq. (3.63) gives the Lagrangian term

$$\mathcal{L}^M_{\text{mass}} = -\frac{\kappa v_\Phi^2}{2\mathcal{M}}\left(-\nu_L^T C^\dagger \nu_L + \overline{\nu_L} C \overline{\nu_L}^T\right), \tag{3.64}$$

where we can identify the mass given by $m = \kappa v_\Phi^2/2\mathcal{M}$. Another notable difference when considering Majorana neutrinos comes in the case of neutrino mixing. If we consider three Majorana neutrinos, then we can construct the Majorana mass term

$$\mathcal{L}^M_{mass} = \nu_L^{\prime T} C^\dagger M_L \nu'_L + \text{h.c.} \tag{3.65}$$

Here M_L is a symmetric complex matrix, in contrast to the Dirac case, where the matrix was completely general. In consequence, the matrix M_L can be diagonalized with only one unitary matrix V_L^ν through the transformation

$$V_L^{\nu T} M_L V_L^\nu = M = \text{diag}(m_1, m_2, m_3), \tag{3.66}$$

with m_k real. Then, we can use the same transformation between the primed fields and

the mass fields as in Eq. (3.51), and defining $\nu_k = \nu_{kL} + \nu_{kL}^C$, we end up with the mass Lagrangian for three Majorana neutrinos

$$\mathcal{L}^M = \sum_{k=1}^{3} m_k \overline{\nu_{kL}^C} \nu_{kL} + \text{H.c.} = -\sum_{k=1}^{3} m_k \overline{\nu_k} \nu_k. \tag{3.67}$$

With the applied rotation, we can write the charged current as in Eq. (3.54) by defining $U = V_L^{\ell\dagger} V_L^{\nu}$, and we end up again with

$$j_{W,L}^{\rho} = 2\overline{n_L} U^{\dagger} \gamma^{\rho} \ell_L. \tag{3.68}$$

Then, if we define the flavor fields as in Eq. (3.57), we again have a charged current with the same form as in the SM. From the previous discussion, it would be interpreted that the matrices U in Eqs. (3.55) and (3.68) are the same. However, this is not the case, and the difference does not come from the charged current interaction. Instead, it has to do with the origin of the mass terms for neutrinos and whether or not these terms are invariant over a transformation of the form

$$\nu_{kL} \to e^{i\varphi_k} \nu_{kL}. \tag{3.69}$$

In general, a 3×3 complex matrix can be parametrized by three mixing angles and six phases. For Dirac neutrino masses, the mass Lagrangian in Eq. (3.52) is invariant under a transformation of the form in Eq. (3.69), and we can eliminate five of the non-physical phases with a proper transformation choice. We denote the remaining phase as δ and it is called the Dirac phase. In contrast, the Majorana mass Lagrangian in Eq. (3.64) is not invariant under this transformation. Hence, we can only eliminate three of the non physical phases. The remaining two extra phases, denoted as α_2 and α_3, can be factored out in a diagonal matrix of phases:

$$U^M = \text{diag}\left\{1, e^{i\alpha_2}, e^{i\alpha_3}\right\}, \tag{3.70}$$

Then, if we denote U^D the *Dirac* mixing matrix, parametrized by three mixing angles and the δ phase, we can in general write

$$U = U^D U^M \quad \Rightarrow \quad U_{\beta k} = U_{\beta k}^D e^{i\alpha_k}. \tag{3.71}$$

With no summation over the k index. In this way, the Dirac mixing matrix can be obtained using Eq. (3.71) with $U^M = I$, while the Majorana mixing matrix by taking

U^M as in Eq. (3.70). Notice that the quartic products of U elements in the oscillation probability in Eq. (3.34) are invariant over the transformation $U_{\alpha k} \to e^{i\psi_\alpha} U_{\alpha k} e^{i\phi_\alpha}$, which means, according to Eq. (3.71), that oscillations are not sensitive to Majorana phases.

Many parametrizations are given in the literature for U^D. In this work we will use the convention adopted by the Particle Data Group (PDG), where we denote the three mixing angles as θ_{12}, θ_{13}, and θ_{23}, and the physical Dirac CP phase as δ, so we express [51]

$$U^D = \begin{pmatrix} c_{12}c_{13} & s_{12}s_{13} & s_{13}e^{-i\delta} \\ -s_{12}c_{23} - c_{12}s_{23}s_{13}e^{i\delta} & c_{12}c_{23} - s_{12}s_{23}s_{13}e^{i\delta} & s_{23}c_{13} \\ s_{12}s_{23} - c_{12}c_{23}s_{13}e^{i\delta} & -c_{12}s_{23} - s_{12}c_{23}s_{13}e^{i\delta} & c_{23}c_{13} \end{pmatrix}, \tag{3.72}$$

where $c_{ij} = \cos\theta_{ij}$ and $s_{ij} = \sin\theta_{ij}$. As we will see, different experiments are sensitive to different parameters of the mixing matrix.

Another characteristic of the Majorana mass Lagrangian in Eq. (3.64) is that, in contrast to the Dirac case, it is not invariant to a global transformation of the form

$$\nu_{kL} \to e^{i\varphi}\nu_{kL} \qquad (k = 1, 2, 3), \tag{3.73}$$

where we are using the same phase for the three different massive neutrinos. It can be shown that this implies a non-conservation of the total lepton flavor number, a quantity that is conserved within the SM. This leads to the possibility of observing the process of neutrinoless double beta decay, in which two neutrons simultaneously decay, producing two electrons and two protons with no neutrinos in the final state. The process is illustrated in Fig. 3.14 and it represents one of the most promising ways to prove, if it is the case, a Majorana nature for neutrinos.

Apart from the parametrization for the U matrix adopted by the PDG, we can find in the literature another paramterization that is more suitable for the study of Majorana neutrinos. This is called the symmetric parametrization, and it has the form [52]

$$U = \begin{pmatrix} c_{12}c_{13} & s_{12}s_{13}e^{-i\phi_{12}} & s_{13}e^{-i\phi_{13}} \\ -s_{12}c_{23}e^{i\phi_{12}} - c_{12}s_{23}s_{13}e^{-i(\phi_{23}-\phi_{13})} & c_{12}c_{23} - s_{12}s_{23}s_{13}e^{-i(\phi_{12}+\phi_{23}-\phi_{13})} & s_{23}c_{13}e^{-i\phi_{23}} \\ s_{12}s_{23}e^{i(\phi_{12}+\phi_{23})} - c_{12}c_{23}s_{13}e^{i\phi_{13}} & -c_{12}s_{23}e^{i\phi_{23}} - s_{12}c_{23}s_{13}e^{-i(\phi_{12}-\phi_{13})} & c_{23}c_{13} \end{pmatrix}. \tag{3.74}$$

Here the physical CP phases are ϕ_{12}, ϕ_{13}, and ϕ_{23}. Notice that the number of free parameters has not changed with respect to the PDG parametrization. The δ CP

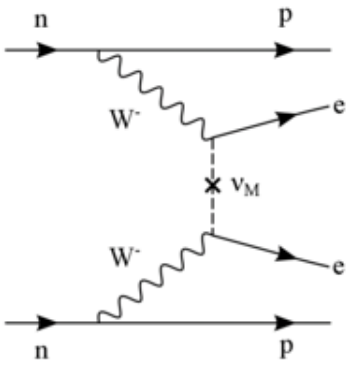

Figure 3.14: Feynman diagram for neutrinoless double beta decay process.

phase in Eq. (3.72) is related to the phases in Eq. (3.74) through [52]

$$\delta = \phi_{13} - \phi_{12} - \phi_{23}. \tag{3.75}$$

In fact, the symmetric parametrization provides a cleaner picture of CP processes that are thoroughly a consequence of Majorana phases. For instance, the effective mass parameter that characterizes the amplitude of the neutrinoless double beta decay, illustrated in Fig. 3.14, is given by [52]

$$\langle m \rangle = \left| \sum_j U_{ej}^2 m_j \right|. \tag{3.76}$$

In the PDG parametrization, considering Majorana phases, this amplitude reads

$$\langle m \rangle = \left| c_{12}^2 c_{13}^2 m_1 + s_{12}^2 c_{13}^2 m_2 e^{2i\alpha_2} + s_{13}^2 m_3 e^{2i(\delta+\alpha_3)} \right|. \tag{3.77}$$

Since neutrinoless double beta decay is a process related to Majorana neutrinos, we would expect the phase δ not to be present in this expression. However, in terms of the symmetric parametrization, as given in Eq. (3.74), we have

$$\langle m \rangle = \left| c_{12}^2 c_{13}^2 m_1 + s_{12}^2 c_{13}^2 m_2 e^{2i\phi_{12}} + s_{13}^2 m_3 e^{2i\phi_{13}} \right|. \tag{3.78}$$

In this way, we see that the symmetrical parametrization provides a transparent description in which only two phases appear in the effective mass parameter, as it should. These two phases represent precisely the CP violating Majorana phases.

Parameter	Best fit	1σ range	2σ range	3σ range
Δm^2_{21} $[10^{-5}\text{eV}^2]$	7.50	7.30 - 7.72	7.12 - 7.93	6.94 - 8.14
$\lvert\Delta m^2_{31}\rvert$ $[10^{-3}\text{eV}^2]$ (NO)	2.55	2.51 - 2.57	2.49 - 2.60	2.47 - 2.63
$\lvert\Delta m^2_{31}\rvert$ $[10^{-3}\text{eV}^2]$ (IO)	2.45	2.42 - 2. 47	2.39 - 2.50	2.37 - 2.53
$\sin^2\theta_{12}/10^{-1}$	3.18	3.02 - 3.34	2.86 - 3.52	2.71 - 3.69
$\sin^2\theta_{23}/10^{-1}$ (NO)	5.74	5.60 - 5.88	5.41 - 5.99	4.34 - 6.10
$\sin^2\theta_{23}/10^{-1}$ (IO)	5.78	5.61 - 5.88	5.41 - 5.98	4.33 - 6.08
$\sin^2\theta_{13}/10^{-2}$ (NO)	2.200	2.138 - 2.269	2.069 - 2.337	2.000 - 2.405
$\sin^2\theta_{13}/10^{-2}$ (IO)	2.225	2.155 - 2.289	2.086 - 2.356	2.018 - 2.424
δ/π (NO)	1.08	0.96 - 1.21	0.84 - 1.42	0.71 - 1.99
δ/π (IO)	1.58	1.42 - 1.73	1.26 - 1.85	1.11 - 1.96

Table 3.3: Status of oscillation parameters from global analyses [53] for NO and IO of neutrino mass hierarchy.

3.6 Status of neutrino oscillation parameters

From the previous sections we know that neutrino oscillations are only sensitive to the U^D matrix elements. Then, the physical parameters in neutrino oscillations are the three mixing angles, the δ CP phase, and the squared mass differences Δm^2_{21} and Δm^2_{31}. The current picture includes robust experimental constraints for the case of θ_{12}, θ_{13}, and Δm^2_{21}. However, many of the main questions of neutrino physics remain in this sector. Here are some of the things that we still do not know:

- Robust constraints for the δ CP phase.
- Whether θ_{23} is below or above $\pi/4$.
- The correct sign of Δm^2_{31}.
- The absolute scale of the neutrino mass.

According to the ratio L/E, neutrino oscillation experiments can be divided in four different groups: solar neutrino experiments, short baseline reactor experiments, atmospheric experiments, and long baseline accelerator experiments. We summarize the current constraints for oscillation parameters in Table 3.3 [53], which are obtained from global analyses.

Solar neutrino experiments are sensitive to the $(\sin^2\theta_{12}, \Delta m^2_{21})$ parameter space. The global analyses of solar neutrinos include data from the radiochemical experiments

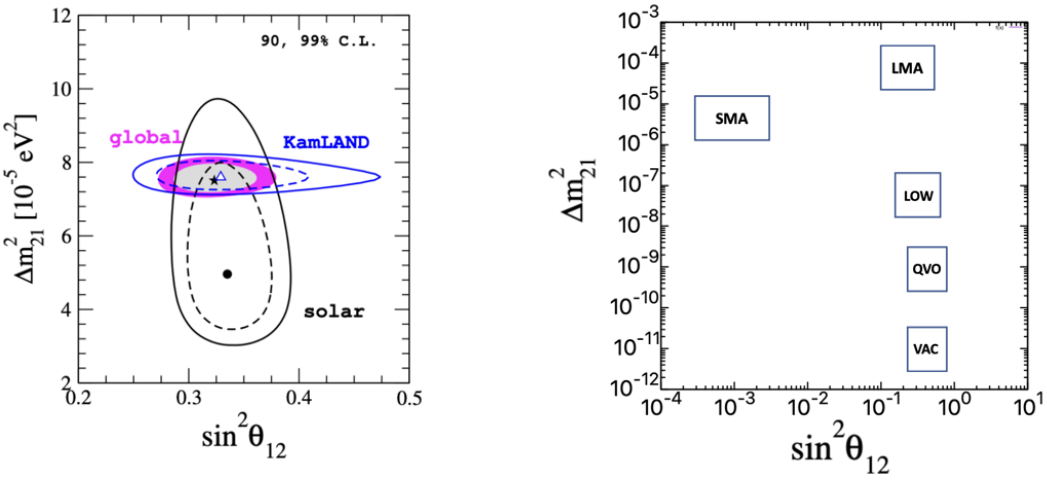

Figure 3.15: Left panel: Black and blue contours show the allowed values for oscillation parameters for solar neutrinos and KamLAND experiment, respectively, at 90% (dashed lines) and 99% (solid lines) C. L. Colored regions show the results for combined global analyses at 90% (gray) and 99% (magenta) C. L. Image taken from [57]. Right panel: Different regions in the $(\sin^2\theta_{12}, \Delta m^2_{21})$ parameter space.

described in the previous section, as well as data from BOREXINO [54], and Super Kamiokande [55]. Since it is sensitive to the same parameters, global analyses in this channel also include data from KamLAND [56], which is a reactor experiment. The 90% C. L. regions for these experiments, together with a combined analysis are shown in the left panel of Fig. 3.15 [53]. Historically, different regions in the parameter space were proposed to solve the solar neutrino problem. These are shown in the right panel of Fig. 3.15, where we distinguish five regions: the Small Mixing Angle (SMA), the Large Mixing Angle (LMA), the low Δm^2_{21} (LOW), the quasi-vacuum-oscillations (QVO), and the vacuum oscillations (VAC) regions. In the case of SMA, LMA, and LOW regions, matter effects are the most relevant for neutrino oscillations to a different degree. For QVO, both matter and vacuum effects are important, while for VAC, matter effects are negligible, and vacuum effects are responsible for oscillations. From the results in the left panel of Fig. 3.15, we conclude that current global data favors an LMA solution for neutrino oscillations.

The group of short baseline reactors is mainly sensitive to the mixing angle θ_{13}. They now have greater power than old reactors, and most of these experiments were developed with multiple same kind detectors located at different distances from the reactor, which enhanced the total measured number of events. The data for global analyses comes from detectors as Daya Bay [58], RENO [59], and Double Chooz [60], all of them favoring a non-zero value of θ_{13}. Actually, this non-zero value helps to reconcile the tension between solar data and KamLAND.

Atmospheric neutrino experiments are sensitive to the parameter space $(\sin^2\theta_{23}, \Delta m^2_{31})$.

The first observation of the atmospheric neutrino flux was done by the Super-Kamiokande collaboration, which reported a dependence of the observed number of events on the zenith angle [61]. This represented a clear signature of neutrino oscillations because it was observed that neutrinos from below the detector, which traveled the longest distance, were less than those coming from the upper direction. The reported data was consistent with the theory of neutrino oscillations and shows a small preference for $\theta_{23} > \pi/4$ and a normal mass ordering. Current global analyses also include data from the ANTARES [62], and Ice Cube DeepCore [63] experiments, first intended to measure very high energy neutrinos, but eventually adapted for atmospheric neutrino energies. Their results are consistent with Super-Kamiokande observations.

Finally, long baseline accelerator neutrino experiments have been analyzed to confirm oscillations of muon neutrinos, which means that these experiments are also sensitive to the $(\sin^2\theta_{23}, \Delta m^2_{31})$ parameter space. For global analyses we have the measurements of T2K [64] (initially KEK experiment), MINOS [65], and NOνA [66], all of which show consistent results with neutrino oscillations. In the case of T2K, the analysis shows a preference for maximal mixing ($\theta_{23} \approx \pi/4$), while NO$\nu$A and MINOS favor the case below maximal mixing. In addition, since accelerators are a source of muon neutrinos and anti-neutrinos, experiments like T2K have provided a mild sensitivity to the δ CP phase.

3.7 Non-Standard neutrino Interactions

As we have mentioned, the phenomenon of neutrino oscillations represents a clear evidence that the SM is not complete and that neutrinos can give special hints in the search for new physics. Indeed, there has been a lot of interest in modeling different extensions of the SM to explain, for instance, the neutrino mass pattern. A useful phenomenological approach is that of Non-Standard Interactions (NSI), which can affect the production, propagation, and detection of neutrinos. In the low energy regime, these interactions can be formulated by an effective four-fermion Lagrangian. In general, there are two different types of NSI considered in the literature. The charged current interactions, described by

$$\mathcal{L}_{\mathrm{CC-NSI}} = -2\sqrt{2}G_F\overline{\nu}_\alpha\gamma^\mu\mathcal{P}_L\ell_\beta\overline{f'}\gamma_\mu\mathcal{P}_X\epsilon^{ff'X}_{\alpha\beta}f \tag{3.79}$$

and the neutral current NSI, which is of the form

$$\mathcal{L}_{\text{NC}-\text{NSI}} = -2\sqrt{2}G_F\overline{\nu}_\alpha\gamma^\mu\mathcal{P}_L\nu_\beta\overline{f}\gamma_\mu\mathcal{P}_X\epsilon^{fX}_{\alpha\beta}f, \tag{3.80}$$

where P_L and P_R denotes the projection operators. Here, f and f' stand for charged fermions. The strength of the interactions is measured by the parameters $\varepsilon^{fX}_{\alpha\beta}$ (with $X = L, R$) and we have factorized G_F for convenience. We are interested in neutrino interactions with matter, so we will mainly consider the case of neutral current interactions of neutrinos with electrons and with *up* and *down* quarks. The subscripts α and β run over the three lepton flavors e, μ, τ, and there are two main differences when comparing the effective NSI Lagrangians in Eqs. (3.79) and (3.80) with those predicted by the SM and discussed in section 2.3. First, we see that when $\alpha = \beta$, Eq. (3.80) allows for interactions with different strengths depending on the neutrino flavor. This contrasts with the SM, where there is a universality of the weak force and, for this reason, we refer to such parameters as non-universal NSI. In addition, we also parametrize interactions with $\alpha \neq \beta$, where the incident neutrino flavor is different from the final state. These are called flavor-changing NSI. In the limit $\varepsilon^{fX}_{\alpha\beta} \to 0$ we recover the SM, while the case $\varepsilon^{fX}_{\alpha\beta} \approx 1$ corresponds to new interactions that are comparable to the weak interactions scale. We do not expect these couplings to be of order larger than 1 since in that case they would be dominant when compared to the SM interactions. Instead, they are proposed as small deviations from the SM predictions.

The effects of NSI can be present in neutrino production, propagation, and detection. In the case of neutrino propagation, they modify the potential to which neutrinos are sensitive when traveling through matter. By considering NSI, the small tension between solar and KAMLand results can be solved [57]. However, it also opens the window for degeneracy in the determination of the θ_{12} parameter [57]. For simplicity, we can explain this from a perspective of a two neutrino picture. In the case of standard oscillations, the equation describing neutrino propagation was given in Eq. (3.39). Then, we concluded that matter effects could be considered by using an effective mass squared difference and an effective weak mixing angle, which in terms of the vacuum parameters can be written:

$$\cos 2\theta_M = \frac{\Delta m^2 \cos 2\theta - 2\sqrt{2}EG_FN_e}{\sqrt{\left(\Delta m^2 \cos 2\theta - 2\sqrt{2}EG_FN_e\right)^2 + \left(\Delta m^2 \sin 2\theta\right)^2}}. \tag{3.81}$$

On the other hand, in the adiabatic approximation, the flavor survival probability can

be expressed in the form

$$P(\nu_e \to \nu_e) = \frac{1}{2}\left(1 + \cos 2\theta \cos 2\theta_m\right). \tag{3.82}$$

According to experimental observations, the deficit in solar neutrino experiments requires a probability $P(\nu_e \to \nu_e) < 0.5$, which is not possible for $\cos 2\theta < 0$ since, from Eq. (3.81), we would also have $\cos 2\theta_m < 0$ and the second term between parenthesis in Eq. (3.82) would be positive. For this case, it is enough to consider the parameter space $0 < \theta < \pi/4$. Instead, if we consider the presence of NSI, then, by following Ref. [67], we need to add the corresponding contribution to the SM Hamiltonian, that is

$$\mathcal{H}_{\rm NSI} = \sqrt{2} G_F N_d \begin{pmatrix} 0 & \varepsilon \\ \varepsilon & \varepsilon' \end{pmatrix}, \tag{3.83}$$

with N_d the density of d quarks in the propagation medium. The effective parameters $\epsilon = -\sin\theta_{23}(\epsilon^{dL}_{e\tau} + \epsilon^{dR}_{e\tau})$ and $\epsilon' = \sin\theta^2_{23}(\epsilon^{dL}_{\tau\tau} + \epsilon^{dR}_{\tau\tau}) - (\epsilon^{dL}_{ee} + \epsilon^{dR}_{ee})$ account for the NSI effects. Again, diagonalizing the complete Hamiltonian $\mathcal{H} = \mathcal{H}_F + \mathcal{H}_{\rm NSI}$, we get the mixing angle in matter:

$$\cos 2\theta^{\rm NSI}_M = \frac{\Delta m^2 \cos 2\theta - 2\sqrt{2} E G_F \left(N_e - \epsilon' N_d\right)}{\sqrt{\left(\Delta m^2 \cos 2\theta - 2\sqrt{2} E G_F \left(N_e - \epsilon' N_d\right)\right)^2 + \left(\Delta m^2 \sin 2\theta + 4\sqrt{2} E G_F \epsilon N_d\right)^2}}, \tag{3.84}$$

which means that the product $\cos 2\theta \cos 2\theta_m$ in Eq. (3.82) can be negative for $\cos 2\theta < 0$, and the experimental data would be consistent for $0 < \theta < \pi/2$. We can see that the introduction of NSI results in a degeneration in the mixing angle. This region was first studied in Ref. [67] and is called the LMA-D solution. Experiments like KamLAND are not able to disentangle this degeneracy since they are not sensitive to matter effects.

The presence of NSI not only affects neutrino propagation, but they can also have a measurable effect in the production and detection of neutrinos. For instance, if we account the effects of NSI in neutrino electron-scattering, then the cross-section for an incoming electron neutrino reads

$$\begin{aligned}\frac{d\sigma(E_\nu, T)}{dT} = \frac{2G_F^2 m_e}{\pi} \Bigg\{ &(g_L + \varepsilon^{eL}_{ee})^2 + \sum_{\alpha \neq e} \left|\varepsilon^{eL}_{\alpha e}\right|^2 + \left((g_R + \varepsilon^{eR}_{ee})^2 + \sum_{\alpha \neq e} \left|\varepsilon^{eR}_{\alpha e}\right|^2\right) \left(1 - \frac{T}{E_\nu}\right)^2 \\ &- \left((g_L + \varepsilon^{eL}_{ee})(g_R + \varepsilon^{eR}_{ee}) + \sum_{\alpha \neq e} \left|\varepsilon^{eL}_{\alpha e}\right| \left|\varepsilon^{eR}_{\alpha e}\right|\right) \frac{m_e T}{E_\nu^2} \Bigg\},\end{aligned} \tag{3.85}$$

NSI	Bound	Experiment	Reference
ϵ_{ee}^{eL}	(-0.021, 0.052)	Solar + KamLAND	[68]
$\epsilon_{\tau\tau}^{eL}$	(-0.120, 0.060)	Solar + KamLAND	[68]
$\epsilon_{\tau\tau}^{eR}$	(-0.990, 0.230)	Solar + KamLAND	[68]
$\epsilon_{\mu\tau}^{eV}$	(-0.035, 0.018)	Atmospheric	[69]
$\epsilon_{\mu\tau}^{dV}$	(-0.0067, 0.0081)	IceCube	[70]
ϵ_{ee}^{dL}	(-0.3, 0.3)	CHARM	[71]
ϵ_{ee}^{dR}	(-0.6, 0.5)	CHARM	[71]
$\epsilon_{e\tau}^{qL}$	(-0.5, 0.5)	CHARM	[71]
$\epsilon_{e\tau}^{qR}$	(-0.5, 0.5)	CHARM	[71]
$\epsilon_{e\tau}^{eR}$	(-0.19, 0.19)	TEXONO	[72]

Table 3.4: Current NSI bounds from experiments with different neutrino sources and detection technologies [57]. We have used the notation $\varepsilon_{\alpha\beta}^{fV} = \varepsilon_{\alpha\beta}^{fL} + \varepsilon_{\alpha\beta}^{fR}$ and $q = u, d$.

with similar expressions for the case of an incoming muon or tau neutrino. We summarize in Table 3.4 the NSI constraints given by different experiments when considering only one parameter to be different from zero. For instance, the combination of Super-Kamiokande and KamLAND, and the Borexino detector separately, can give constraints to the non-universal parameters ϵ_{ee}^{eX} and $\epsilon_{\tau\tau}^{eX}$. Constraints to parameters involving initial muon neutrinos can be obtained through atmospheric neutrinos. Data from Super-Kamiokande has given strong constraints for $\epsilon_{\mu\tau}^{dV}$ and $\epsilon_{\mu\mu}^{dV}$, which result from the fact that the presence of these couplings downgrade the consistency of neutrino oscillations with the deficit observed for atmospheric neutrinos. In addition, data from the DeepCore experiment (IceCube collaboration), which has been able to measure neutrinos down to 5 GeV, has been used to set more robust constraints in the flavor changing parameter $\epsilon_{\mu\tau}^{dV}$. Regarding short base-line experiments, several constraints have been obtained from accelerator based neutrinos such as LSND and CHARM, the latter being sensitive to neutrino-nucleus scattering. Also, short base-line reactor experiments like TEXONO have been used to set bounds on NSI parameters, which are shown in Table 3.4.

In further analyses, we will also use data from current and future experiments that are sensitive to the CEvNS process to set constraints on many of the NSI parameters.

In this case, the cross-section after including those contributions reads [31]

$$\frac{\mathrm{d}\sigma}{\mathrm{d}T}\left(E_\nu, T\right) \simeq \frac{G_F^2 M}{\pi}\left(1-\frac{MT}{2E_\nu^2}\right)\left\{\left[Z\left(g_V^p + 2\varepsilon_{ee}^{uV} + \varepsilon_{ee}^{dV}\right)F_Z^V(q^2) + N\left(g_V^n + \varepsilon_{ee}^{uV} + 2\varepsilon_{ee}^{dV}\right)F_N^V(q^2)\right]^2 + \sum_\alpha\left[Z\left(2\varepsilon_{\alpha e}^{uV} + \varepsilon_{\alpha e}^{dV}\right)F_Z^V(q^2) + N\left(\varepsilon_{\alpha e}^{uV} + 2\varepsilon_{\alpha e}^{dV}\right)F_N^V(q^2)\right]^2\right\}, \tag{3.86}$$

where we have assumed an incoming electron neutrino and we have used the notation

$$\varepsilon_{\alpha\beta}^{fV} = \varepsilon_{\alpha\beta}^{fL} + \varepsilon_{\alpha\beta}^{fR}. \tag{3.87}$$

The corresponding cross-section for a muon source can be directly obtained by replacing the index $e \leftrightarrow \mu$ in Eq. (3.86). As we will see, the introduction of NSI parameters brings degeneracies not only for oscillation parameters, but also for other fundamental parameters of weak interactions. We will study how different experimental arrays can help to remove such degeneracies.

Chapter 4

Neutrino mass generation models and NSI

As we have seen, the discovery of neutrino oscillations is a clear evidence that at least two neutrinos have a non-zero mass, which implies that the SM is not complete. Many theories that intend to explain the origin of neutrino masses have in common that they naturally give rise to effective couplings with the same form as the NSI Lagrangians given in Eqs. (3.79) and (3.80). This allows us to interpret NSI parameters in terms of the fundamental quantities of a theory such as the mass of a new mediator, an scalar induced vev, or even as Yukawa-like couplings. In this chapter, we study the theory and phenomenology of a particular model that gives rise to these NSI couplings.

One of the most promising neutrino mass generation models is the seesaw mechanism, by which neutrinos acquire their tiny masses through the exchange of heavy leptons or scalar bosons. Among the most common seesaw schemes, we distinguish three main variations: the Type I, where heavy right-handed neutrino fields are introduced, the Type II [1], where an scalar triplet is introduced, and the Type III, where charged leptons are responsible for the neutrino mass generation. All of these schemes are most generally formulated in a way that they respect the $SU(2)_L \times U(1)_Y$ symmetry group of the SM [73]. Here we focus our discussion on the type II seesaw mechanism. In this model, we introduce a triplet scalar Δ that is invariant over the $SU(2)_L$ gauge group, with hypercharge $Y_\Delta = 2$. In its matrix form, we denote

$$\Delta = \begin{pmatrix} \Delta^+/\sqrt{2} & \Delta^{++} \\ \Delta^0 & -\Delta^+/\sqrt{2} \end{pmatrix}, \tag{4.1}$$

[1] Because of its simplicity, the seesaw mechanism with charged scalars was originally called the type I seesaw mechanism

with Δ^{++}, Δ^{+}, and Δ^{0} complex fields. The scalar triplet can couple to the SM fields as long as any added operator is invariant under the SM symmetries, and only if it is of dimension four, which ensures that we keep the renormalizability of the theory. Under these conditions, the most general Lagrangian that can be added to the theory is of the form

$$\mathcal{L}_{\text{type II}} = \left[iY_{\Delta\alpha\beta}L_{\alpha}^{T}C^{-1}\tau_2\Delta L_{\beta} + \text{h.c.}\right] + \left(D_{\mu}\Delta\right)^{\dagger}\left(D^{\mu}\Delta\right) - V(\Phi,\Delta), \tag{4.2}$$

where C is the charge conjugate operator. The first term in the previous equation can be identified as a Yukawa-type coupling and Y_{Δ} is the associated Yukawa matrix, which is complex and symmetric [74]. The second term corresponds to the scalar triplet kinetic operator, with D_{μ} a covariant derivative, and the last term is the potential associated to the scalar fields. In its most general form, we have

$$\begin{aligned} V(\Phi,\Delta) = &- m_{\Phi}^{2}\Phi^{\dagger}\Phi + \frac{\lambda}{4}(\Phi^{\dagger}\Phi)^{2} + M_{\Delta}^{2}\text{Tr}\left[\Delta^{\dagger}\Delta\right] + \lambda_2\left[\text{Tr}\Delta^{\dagger}\Delta\right]^{2} + \lambda_3\text{Tr}\left[\Delta^{\dagger}\Delta\right]^{2} \\ &+ \left[\mu\Phi^{T}i\sigma_2\Delta^{\dagger}\Phi + \text{h.c.}\right] + \lambda_1(\Phi^{\dagger}\Phi)\text{Tr}\left[\Delta^{\dagger}\Delta\right] + \lambda_4\Phi^{\dagger}\Delta\Delta^{\dagger}\Phi, \end{aligned} \tag{4.3}$$

with the first two terms corresponding to the SM Higgs potential, and the λ_i are dimensionless coupling constants. Since the triplet Δ is assigned a lepton number $L = 2$, then the term proportional to μ represents the only source of lepton number violation. Once the scalar triplet is introduced, the number of degrees of freedom does not allow us to have a graphical representation of the potential as in the case of the SM. However, the conditions for the potential to be bounded from below, which is necessary to have a stable minimum, have been studied in Ref. [75]. In analogy to the SM Higgs potential, the neutral components of the scalar doublet and triplet can induce a vacuum expectation value, which we denote as v_{Φ} and v_{Δ}, respectively. Then, after spontaneous symmetry breaking, we separate the real and complex components of these fields

$$\Delta = \frac{1}{\sqrt{2}}\begin{pmatrix} \Delta^{+} & \sqrt{2}\Delta^{++} \\ v_{\Delta} + h_{\Delta} + i\eta_{\Delta} & -\Delta^{+} \end{pmatrix}, \qquad \Phi = \frac{1}{\sqrt{2}}\begin{pmatrix} \sqrt{2}\Phi^{+} \\ v + h_{\Phi} + i\eta_{\Phi} \end{pmatrix}, \tag{4.4}$$

with $h_{\Delta}, \eta_{\Delta}, h_{\Phi}$, and η_{Φ} real fields. Minimization of the potential in Eq. (4.3), in terms of the fields in Eq. (4.4), leads to the relations

$$M_{\Delta}^{2} = \frac{v_{\Phi}^{2}\mu}{\sqrt{2}v_{\Delta}} - \frac{1}{2}\left[2v_{\Delta}^{2}(\lambda_2+\lambda_3) + v_{\Phi}^{2}(\lambda_1+\lambda_4)\right], \tag{4.5}$$

$$m_{\Phi}^{2} = \frac{1}{2}\left[\frac{v_{\Phi}^{2}\lambda}{2} + v_{\Delta}^{2}(\lambda_1+\lambda_4) - 2\sqrt{2}\mu v_{\Delta}\right]. \tag{4.6}$$

Since we expect the scale of new physics to be larger than the electroweak scale, we can assume $v_\phi << M_\Delta$. Then, solving Eq. (4.5) for v_Δ, and keeping only terms of $\mathcal{O}(v_\Phi^2/M_\Delta^2)$, we have:

$$v_\Delta \approx \frac{\mu v_\Phi^2}{\sqrt{2}M_\Delta^2}. \tag{4.7}$$

From this expression, we see that a small vev v_Δ can be induced by either a small μ, a large M_Δ, or a combination of both. In fact, a small coupling μ is in agreement with the t'Hooft's naturalness argument, which states that, at a given energy scale, a quantity is allowed to be small only if the system becomes more symmetrical when the referred quantity vanishes [76]. In the specific case of the type II seesaw, the system becomes more symmetrical in the sense that in the limit $\mu \to 0$ we recover lepton number conservation. Then, it is expected to have a very small μ.

From the definitions in Eq. (4.4), we see that the theory has now 10 degrees of freedom from the scalar sector; three of them are used to generate gauge boson masses, and only seven remain as physical fields. Now, expanding the potential in Eq. (4.3), we can see that there are mixed terms that does not allow us to identify definite masses for the fields in Eq. (4.4). Then, in analogy with the lepton and quark sectors, we need to arrange the fields into a matrix form and diagonalize the resulting mass matrix. After performing this procedure, we get the following physical fields:

- A doubly charged Higgs field, H^{++}, which coincides with the field Δ^{++}, and with mass
$$m_{H^{++}}^2 = M_\Delta^2 - v_\Delta^2\lambda_3 - \frac{\lambda_4}{2}v_\Phi^2. \tag{4.8}$$

- A singly charged field, $H^\pm$, that is a mixture of the fields $\Phi^\pm$ and $\Delta^\pm$, with mass
$$m_{H^+}^2 = \left(M_\Delta^2 - \frac{\lambda_4}{4}v_\Phi^2\right)\left(1 + \frac{2v_\Delta^2}{v_\Phi^2}\right). \tag{4.9}$$

- A CP odd scalar field, A^0, that is a mixture of η_Δ and η_ϕ, with mass
$$m_{A^0}^2 = M_\Delta^2\left(1 + \frac{4v_\Delta^2}{v_\Phi^2}\right). \tag{4.10}$$

- A SM Higgs-like field, h, that is a mixture of h_Δ and h_ϕ, with mass
$$m_h^2 = \frac{1}{2}[A + C - \sqrt{(A-C)^2 + 4B^2}]. \tag{4.11}$$

- A heavy Higgs boson field, H^0, that is also a mixture of h_Δ and h_ϕ, with mass

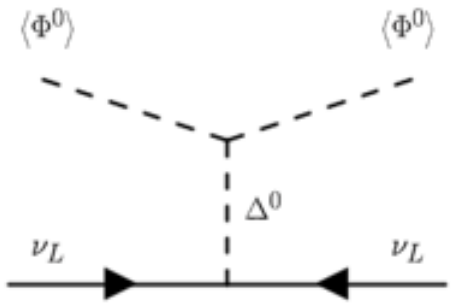

Figure 4.1: Feynman diagram for neutrino mass generation within the type II seesaw mechanism.

$$m^2_{H^0} = \frac{1}{2}[A + C + \sqrt{(A-C)^2 + 4B^2}]. \tag{4.12}$$

Where the parameters A, B, and C satisfy:

$$A = \frac{\lambda}{2}v^2_\Phi, \;\; B = v_\Phi(-\sqrt{2}\mu + (\lambda_1+\lambda_4)v_\Delta), \;\; C = M^2_\Delta + 2(\lambda_2+\lambda_3)v^2_\Delta. \tag{4.13}$$

Within the singly charged sector, the mixture is determined by a mixing angle $\beta^\pm$ that at first order satisfies $\tan\beta^\pm = \sqrt{2}v_\Delta/v_\Phi \approx 0$. Then, in the case $v_\Delta << v_\Phi$ we can safely consider $H^\pm \approx \Delta^\pm$. In addition, the masses of the physical scalar bosons in this limit can be approximated to the form:

$$m^2_{H^{\pm\pm}} \simeq M^2_\Delta - \frac{\lambda_4}{2}v^2_\Phi, \;\; m^2_{H^\pm} \simeq M^2_\Delta - \frac{\lambda_4}{4}v^2_\Phi, \;\; m^2_h \simeq 2\lambda v^2_\Phi, \;\; \text{and} \;\; m^2_{H^0} \approx m^2_{A^0} \simeq M^2_\Delta. \tag{4.14}$$

Notice that the mass splitting of the triplet comes from the quartic coupling constant λ_4, which is expected to be small because a relatively large value of this coupling at the electroweak scale can become non-perturbative at high energies, even below the Planck scale.

Now that we understand the physical masses of the scalars involved in the theory, we can study the origin of neutrino masses. After spontaneous symmetry breaking, the first term in Eq. (4.2) induces a neutrino Majorana mass term of the form

$$\mathcal{L}_{\text{Majorana}} = \overline{\nu^c_{\alpha L}} m_{\alpha\beta}\nu_{\beta L} + \text{h.c.}, \tag{4.15}$$

where the flavor basis matrix $m_{\alpha\beta}$ is given in terms of the Yukawa couplings:

$$m_{\alpha\beta} \equiv (Y_\Delta)_{\alpha\beta}\frac{v_\Delta}{\sqrt{2}}. \tag{4.16}$$

The Feynman diagram responsible for neutrino masses through this mechanism is illustrated in Fig. 4.1. The neutrino fields $\nu_{\alpha L}$ in Eq. (4.15) are flavor states; in order to have neutrino fields with definite mass, we diagonalize the matrix $m_{\alpha\beta}$ by rotating the flavor fields to the mass states ν_i with definite masses m_i. This can be done with the unitary transformation U, getting the result

$$m = U^* \text{diag}(m_1, m_2, m_3) U^\dagger. \tag{4.17}$$

As we have seen, the matrix U depends on three mixing angles θ_{12}, θ_{13}, and θ_{23}, one "Dirac" CP phase δ, and two CP Majorana phases, which we denote α_2, and α_3. In addition, we know that oscillation data from solar and long base-line neutrinos provide tight restrictions on the determination of the allowed neutrino mass and mixing parameters. These restrictions apply to any model that intends to explain the mass origin of neutrinos, like the type II seesaw mechanism. If this is the mechanism responsible of neutrino mass generation, then Eq. (4.17) must be satisfied and we can use oscillation data to determine the allowed regions for each matrix element. The blue regions in the panels of Fig. 4.2 show the allowed values for each matrix element, as a function of m_1, that are consistent with oscillation data in the normal ordering scheme, where m_1 is precisely the lightest neutrino mass. To generate these regions, we perform a scan over the oscillation parameters at their 3σ ranges, consistent with the global analyses as reported in Ref. [53] and summarized in Table 3.3. In the case of the Majorana phases, we allow them to take values between the whole range of $[0, 2\pi)$. In the different panels, we show the region corresponding to a neutrino mass in a range from 10^{-4} to 1 eV. However, we also show shaded bands that correspond to mass values that are ruled out from different measurements. Cosmological observations give the vertical regions ruled out from Barion Acoustic Oscillations (BAO) [79], and from Cosmic Microwave Background (CMB) alone [80]. These observations give constraints to the sum of the three neutrino masses, and we have used the best fit values of the squared mass differences to give an approximate constraint to the lightest neutrino mass. Another way to set constraints to neutrino masses is by measuring the endpoint of the energy spectrum of an electron emitted through beta decay, which endpoint is shifted for massive neutrinos. In this case, the most robust constraint comes from the latest measurement of KATRIN experiment [81], which measures the tail of the spectrum of the tritium beta decay. Again, this experiment constrains a parameter that depends on the three neutrino masses, and the approximate limit for the lightest neutrino is indicated as the remaining vertical shaded region in the different panels of Fig. 4.2.

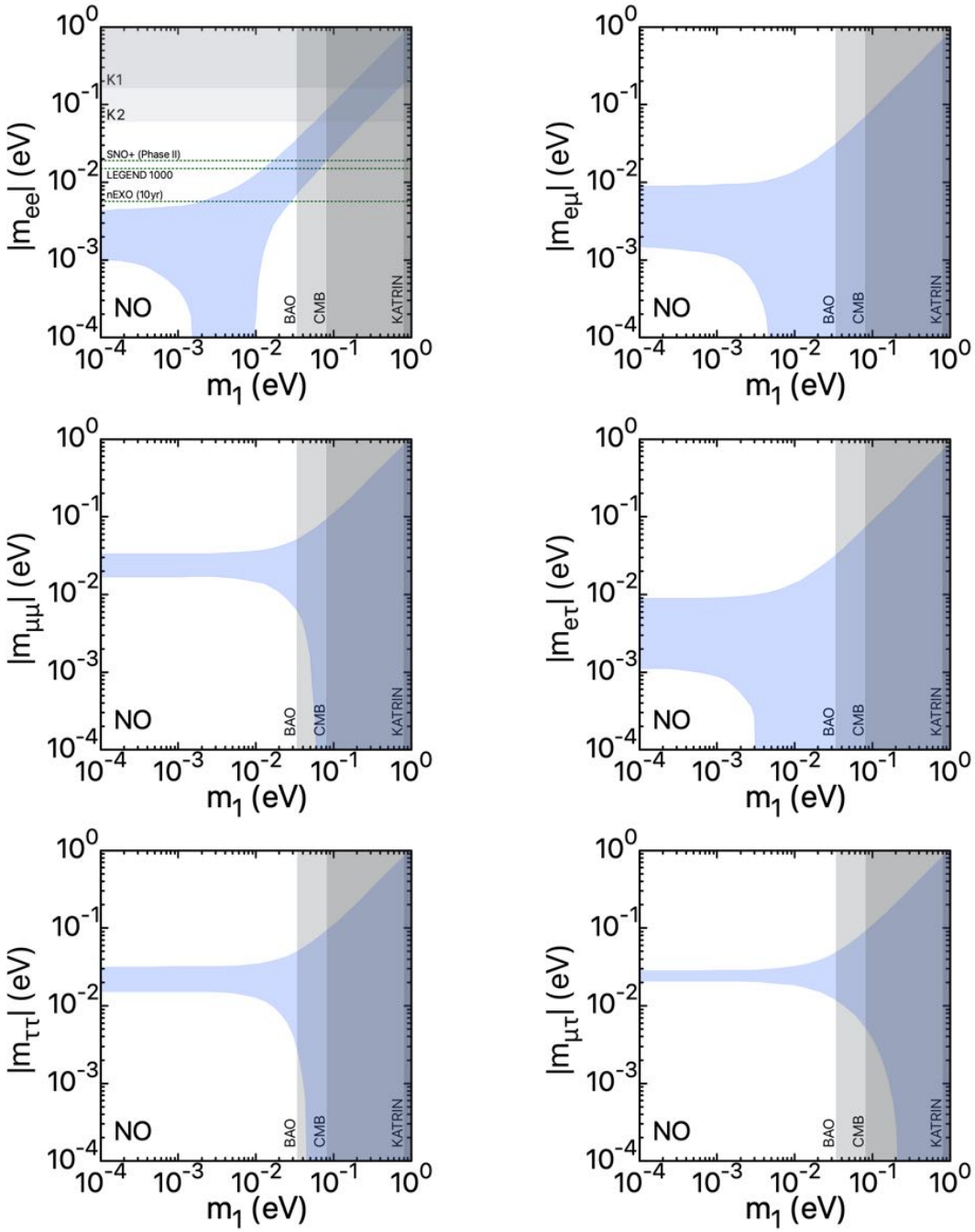

Figure 4.2: Blue regions represent the allowed neutrino mass matrix element magnitudes, $|m_{\alpha\beta}|$, as a function of m_1, for normal ordering (**NO**) of neutrino mass [77]. Oscillation parameters are taken within their 3σ limits as reported in [53]. The vertical shaded regions illustrate the m_1 upper limits from KATRIN and cosmological observations. The $|m_{ee}|$ panel coincides with the effective mass from neutrinoless double beta decay $\langle m_{\beta\beta}\rangle$, where the shaded horizontal bands are excluded by KAMLAND-Zen [78] and dotted lines correspond to future experimental sensitivities.

The panel corresponding to $|m_{ee}|$ in Fig. 4.2 also has another physical meaning because it coincides with the neutrinoless double beta decay amplitude for Majorana neutrinos, which is given by

$$\langle m_{\beta\beta}\rangle = \left|\sum_{j=1}^{3} U_{ej}^2 m_j\right| = |m_{ee}|. \tag{4.18}$$

Horizontal shaded regions in the corresponding panel refer to the current KamLAND-zen upper limits for $\langle m_{\beta\beta}\rangle$ [78], each obtained under different assumptions for the nuclear matrix elements in the search for neutrinoless double beta decay. The horizontal dashed lines show the sensitivity that future experiments SNO+ [82], LEGEND 1000 [83], and nEXO [84] will reach. Clearly, these limits are only valid for the $|m_{ee}|$ case, but they have a direct impact on the upper bounds for the lightest neutrino mass. Notice from the first panel in Fig. 4.2, that there are some combinations of values that result on a vanishing amplitude $\langle m_{\beta\beta}\rangle = |m_{ee}|$. This is an effect of a destructive interference between the Majorana phases, which is characteristic of the NO scheme. The same effect can be noticed on the other panels of the figure. Therefore, it is possible to have combinations of parameters for which one or more of the $|m_{\alpha\beta}|$ vanish, while the others take relatively large values.

We perform a similar analysis for the case of the IO scheme, which corresponding regions are shown in the panels of Fig. 4.3. Here, the lightest neutrino mass corresponds to m_3 and the panel corresponding to $|m_{ee}|$ has still the same physical meaning as in the case of NO. However, notice that in this case there are no combinations of phases that allow for a cancellation of the amplitude $\langle m_{\beta\beta}\rangle = |m_{ee}|$, a feature that can be exploited with future sensitivities to determine the nature of the neutrino mass.

4.1 NSI from type II seesaw model

So far, we have discussed the terms of the type II seesaw Lagrangian that produce Majorana mass terms for neutrinos. Now, we focus on the terms that are responsible of introducing NSI in the form of the neutral current Lagrangian given in Eq. (3.80). Again, after spontaneous symmetry breaking, the first term in Eq. (4.2) gives terms of the form

$$\mathcal{L}_{\Delta^\pm} = \sqrt{2} Y_{\Delta\alpha\beta} \nu_{L\alpha}^T C \ell_{L\beta} \Delta^+ + \text{h.c.}. \tag{4.19}$$

We show the corresponding Feynman diagram in the left panel of Fig. 4.4. At low energies, we can integrate out the degrees of freedom of the heavy $\Delta^\pm \approx H^\pm$, giving as

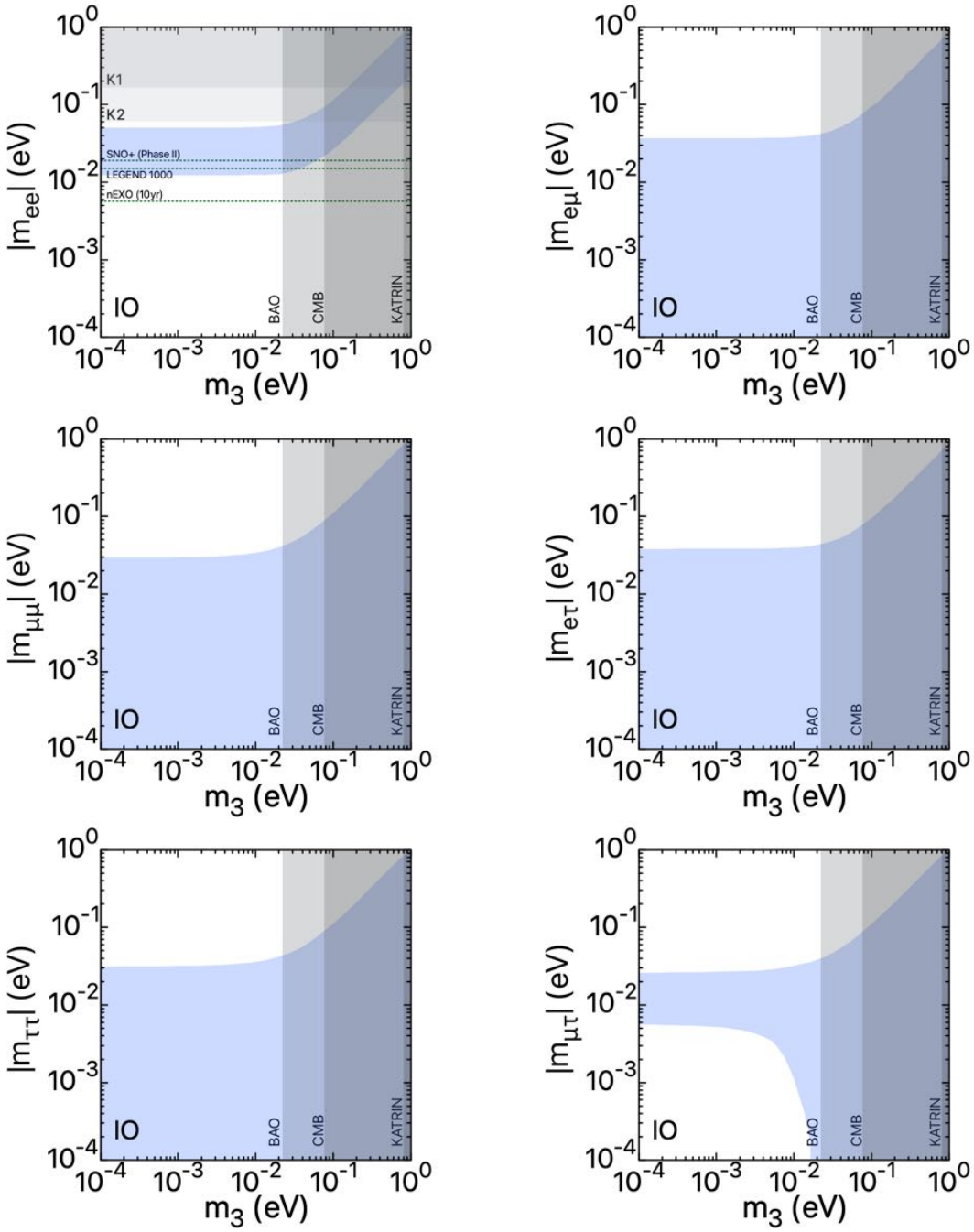

Figure 4.3: Blue regions represent the allowed neutrino mass matrix element magnitudes, $|m_{\alpha\beta}|$, as a function of m_3, for inverted ordering (**IO**) of neutrino mass [77]. Oscillation parameters are taken within their 3σ limits as reported in [53]. The vertical shaded regions illustrate the m_3 upper limits from KATRIN and cosmological observations. The $|m_{ee}|$ panel coincides with the effective mass from neutrinoless double beta decay $\langle m_{\beta\beta}\rangle$, where shaded horizontal bands are excluded by KAMLAND-Zen [78] and dotted lines correspond to future experimental sensitivities.

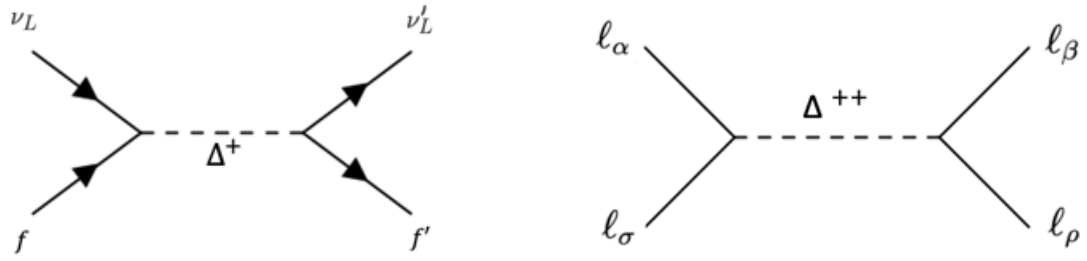

Figure 4.4: Left panel: Feynman diagram responsible for NSI mediated by the singly charged Higgs. Right panel: Feynman diagram illustrating the contribution from doubly charged Higgs to three lepton decays at tree level.

a result

$$\mathcal{L} \supset -\frac{Y_{\alpha\alpha'}Y^*_{\beta\beta'}}{2m^2_{H^\pm}}\overline{\nu^c_\alpha}(1-\gamma^5)\ell_{\alpha'}\overline{\ell_{\beta'}}(1+\gamma^5)\nu^c_\beta. \tag{4.20}$$

Then, we can Fierz transform the previous Lagrangian to get the vector-form interaction[2]

$$\mathcal{L} \supset -\frac{Y_{\alpha\alpha'}Y^*_{\beta\beta'}}{4m^2_{H^\pm}}\overline{\nu^c_\alpha}\gamma^\mu(1+\gamma^5)\nu^c_\beta\overline{\ell_{\beta'}}\gamma_\mu(1-\gamma^5)\ell_{\alpha'}. \tag{4.21}$$

Using different properties of the C operator and the γ^μ matrices, we can express the previous result in the form

$$\mathcal{L} \supset -\frac{Y_{\Delta\alpha\alpha'}Y^*_{\Delta\beta\beta'}}{m^2_{H^\pm}}\overline{\nu_\beta}\gamma^\mu P_L\nu_\alpha\overline{\ell_{\beta'}}\gamma_\mu P_L\ell_{\alpha'}, \tag{4.22}$$

where we have used $P_L = (1-\gamma^5)/2$. In the particular case where $\ell_{\beta'} = \ell_{\alpha'} \equiv \ell$, with ℓ a charged fermion, this expression has the same form as that given in Eq. (3.80) for neutral current NSI by identifying

$$\epsilon^{\ell L}_{\alpha\beta} = -\frac{Y^*_{\Delta\alpha\ell}Y_{\Delta\beta\ell}}{2\sqrt{2}G_F M^2_\Delta}, \tag{4.23}$$

where we have taken the limit $m^2_{H^\pm} \approx M^2_\Delta$. Equation (4.23) illustrates an example of how NSI can be translated into fundamental parameters of a specific theory. Here, the NSI are in terms of the Yukawa couplings and the mass of the charged scalar. As we have seen, several experimental bounds currently exist for NSI as those in Eq. (4.23), which are obtained through neutrino-electron scattering experiments (see Table 3.4).

[2]We used the identity $-2\left[\overline{\psi_1}(1-\gamma^5)\psi_2\right]\left[\overline{\psi_3}(1+\gamma^5)\psi_4\right] = \left[\overline{\psi_1}\gamma^\mu(1+\gamma^5)\psi_4\right]\left[\overline{\psi_3}\gamma_\mu(1-\gamma^5)\psi_2\right]$.

4.2 NSI consistent with LFV limits

For the particular case of the type II seesaw, the introduction of charged scalars allows for Lepton Flavor Violation (LFV) processes [85], which are characterized by a non conservation of the lepton family number in transitions between e, μ, and τ states. These processes are forbidden within the SM, and they include rare decays such as $\mu \to e\gamma$, and three lepton decays like $\mu \to 3e$. Experimentally, LFV processes have not been observed yet, but they are somehow expected after the confirmation of neutrino oscillations and, regardless of their theoretical origin, their search is still active at particle colliders. In this section, we study how current bounds on LFV processes can give information about the expected size of the NSI if the type II seesaw is responsible for neutrino masses. We will determine whether the expected size of NSI, consistent with LFV limits, are below the experimental bounds given in Table 3.4, where we have NSI bounds of order 10^{-1} and, in some cases, of order 10^{-2}.

We begin by presenting the possible LFV processes allowed by the type II seesaw mechanism. For instance, three lepton decays are possible at tree level by considering the Feynman diagram on the right panel of Fig. 4.4. The branching ratio (BR) for processes like these have been computed in different references, showing a dependency on the Yukawa couplings and the masses of the scalar mediators. In the case of a muon decaying to three electrons we have [85]

$$BR(\mu \to eee) = \frac{1}{G_F^2} \frac{\left|(Y_\Delta^\dagger)_{ee}(Y_\Delta)_{\mu e}\right|^2}{m_{H^{++}}^4}, \tag{4.24}$$

with similar expressions for other three-lepton decays such as $\tau \to 3e$ or $\tau \to \mu ee$. Another case of interest are processes of the type $\ell_\alpha \to \ell_\beta \gamma$, which are possible at a quantum loop level through the exchange of a charged scalar and a lepton. The left and central diagrams in Fig. 4.5 show the contribution to this process from the doubly charged scalar, where there is also an exchange of a charged lepton. The right panel of the same figure corresponds to the contribution from the singly charged scalar, for which we also have the exchange of a Majorana neutrino. After considering these three contributions, the branching ratio for the process $\mu \to e\gamma$ is given by [85]

$$BR(\mu \to e\gamma) \approx \frac{\alpha}{192\pi} \frac{\left|(Y_\Delta^\dagger Y_\Delta)_{e\mu}\right|^2}{G_F^2} \left(\frac{1}{m_{H^+}^2} + \frac{8}{m_{H^{++}}^2}\right)^2, \tag{4.25}$$

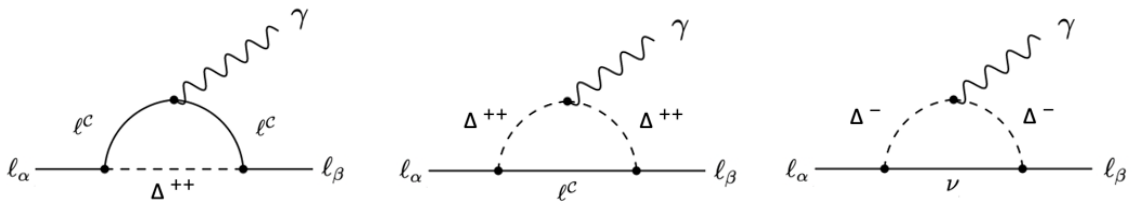

Figure 4.5: Feynman diagrams illustrating the contribution from singly charged and doubly charged Higgs to flavor lepton violation processes at one loop order.

with similar expressions for the other decays like $\tau \to e\gamma$ and $\tau \to \mu\gamma$. These processes have been experimentally studied within different collaborations. In particular, τ decays have been recently studied at τ factories like BaBar [86]. Theoretical expressions like Eqs. (4.24) and (4.25), together with the experimental limits for each branching ratio, can be used to set constraints for Yukawa couplings and charged scalar masses of the type II seesaw. We summarize in Table 4.1 the current experimental status for the different decays, with the branching ratios adapted from Ref. [87][3]. For the limits in the last column we have assumed $m^2_{H^{\pm\pm}} \approx m^2_{H^{\pm}} \approx M^2_\Delta$. Notice from the table that three lepton decays can be useful to constrain the product of Yukawa coupling pairs, while the other decays are sensitive to the sum of three of such pairs. As we have seen, such Yukawa coupling products are also present in the NSI expressions, which means that we can set bounds for the expected NSI signals from the type II seesaw by using experimental LFV limits. To see this, we determine the maximum NSI of each type that is consistent with the limits given in the last column of Table 4.1. For instance, in the case of the diagonal parameter ε^{eL}_{ee}, we take the modulus of Eq. (4.23), for $\alpha = \beta = e$, and we express the Yukawa couplings in terms of the flavor matrix elements through Eq. (4.16), giving the relation

$$\frac{|m_{ee}|^2}{\sqrt{2}G_F} = |\varepsilon^{eL}_{ee}|\, M^2_\Delta v^2_\Delta. \tag{4.26}$$

On the other hand, we can also express the Yukawa couplings on the third column of Table 4.1 in terms of the corresponding mass matrix elements. In this way, we get inequalities that depend on LFV limits and that also involve the product $M_\Delta v_\Delta$. For instance, from the $\mu \to e\gamma$ process (first row on the table), we have

$$\frac{|m^\dagger m|_{e\mu}}{G_F} < L_1\, M^2_\Delta v^2_\Delta, \tag{4.27}$$

[3]There is an updated value of $\mathrm{BR}(\tau \to \mu\gamma) < 4.2\times10^{-8}$ from Belle II [88] that does not significantly modify our results.

Processes	Experimental limits on BR	Bounds on $G_F^{-1}M_\Delta^{-2}Y_\Delta^2$
$\mu \to e\gamma$	$\text{BR} < 4.2 \times 10^{-13}$	$G_F^{-1}M_\Delta^{-2}\lvert Y_\Delta^\dagger Y_\Delta\rvert_{e\mu} < 2.1 \times 10^{-5} = L_1$
$\mu \to 3e$	$\text{BR} < 1.0 \times 10^{-12}$	$G_F^{-1}M_\Delta^{-2}\lvert Y_\Delta^\dagger\rvert_{\mu e}\lvert Y_\Delta\rvert_{ee} < 2.0 \times 10^{-6} = L_2$
$\tau \to 3e$	$\text{BR} < 2.7 \times 10^{-8}$	$G_F^{-1}M_\Delta^{-2}\lvert Y_\Delta^\dagger\rvert_{\tau e}\lvert Y_\Delta\rvert_{ee} < 7.9 \times 10^{-4} = L_3$
$\tau \to e^+e^-\mu^-$	$\text{BR} < 1.8 \times 10^{-8}$	$G_F^{-1}M_\Delta^{-2}\lvert Y_\Delta^\dagger\rvert_{\tau e}\lvert Y_\Delta\rvert_{e\mu} < 4.5 \times 10^{-4} = L_4$
$\tau \to e\gamma$	$\text{BR} < 3.3 \times 10^{-8}$	$G_F^{-1}M_\Delta^{-2}\lvert Y_\Delta^\dagger Y_\Delta\rvert_{e\tau} < 1.4 \times 10^{-2} = L_5$
$\tau \to \mu\gamma$	$\text{BR} < 4.4 \times 10^{-8}$	$G_F^{-1}M_\Delta^{-2}\lvert Y_\Delta^\dagger Y_\Delta\rvert_{\mu\tau} < 1.6 \times 10^{-2} = L_6$
$\tau \to \mu^+\mu^-e^-$	$\text{BR} < 2.7 \times 10^{-8}$	$G_F^{-1}M_\Delta^{-2}\lvert Y_\Delta^\dagger\rvert_{\tau\mu}\lvert Y_\Delta\rvert_{\mu e} < 5.6 \times 10^{-4} = L_7$
$\tau \to e^+\mu^-\mu^-$	$\text{BR} < 1.7 \times 10^{-8}$	$G_F^{-1}M_\Delta^{-2}\lvert Y_\Delta^\dagger\rvert_{\tau e}\lvert Y_\Delta\rvert_{\mu\mu} < 6.3 \times 10^{-4} = L_8$
$\tau \to \mu^+e^-e^-$	$\text{BR} < 1.5 \times 10^{-8}$	$G_F^{-1}M_\Delta^{-2}\lvert Y_\Delta^\dagger\rvert_{\tau\mu}\lvert Y_\Delta\rvert_{ee} < 5.9 \times 10^{-4} = L_9$
$\tau \to 3\mu$	$\text{BR} < 2.1 \times 10^{-8}$	$G_F^{-1}M_\Delta^{-2}\lvert Y_\Delta^\dagger\rvert_{\tau\mu}\lvert Y_\Delta\rvert_{\mu\mu} < 6.9 \times 10^{-4} = L_{10}$

Table 4.1: Constraints from LFV processes on the Yukawa coupling matrix Y_Δ. Experimental limits on the branching ratios (BR) are taken from Ref. [51], and the bounds on $G_F^{-1}M_\Delta^{-2}Y_\Delta^2$, L_i, are adapted from Ref. [87].

where L_1 is the corresponding limit indicated in the third column of the same table. Using the previous two equations to eliminate the product $M_\Delta v_\Delta$, and repeating the process for the ten different limits, we get expressions of the form:

$$\frac{|m^\dagger m|_{\alpha\beta}}{|m_{ee}|^2} < \frac{L_i}{2\sqrt{2}\ |\varepsilon_{ee}^{eL}|} \qquad (i = 1, 3, 4), \tag{4.28}$$

$$\frac{|m^\dagger|_{\alpha\beta}|m|_{\sigma\rho}}{|m_{ee}|^2} < \frac{L_i}{2\sqrt{2}\ |\varepsilon_{ee}^{eL}|} \qquad (i \neq 1, 3, 4). \tag{4.29}$$

Now, we want to determine the maximum value of $|\varepsilon_{ee}^{eL}|$ that can satisfy the ten Eqs. in (4.28) and (4.29). To do so, notice that the left hand side in each of the equations depends only on different $|m_{\alpha\beta}|$, which as we know from Eq. (4.17), are a function of parameters obtained from oscillation data. We perform a scan over the matrix elements by generating random numbers for the oscillation parameters between their

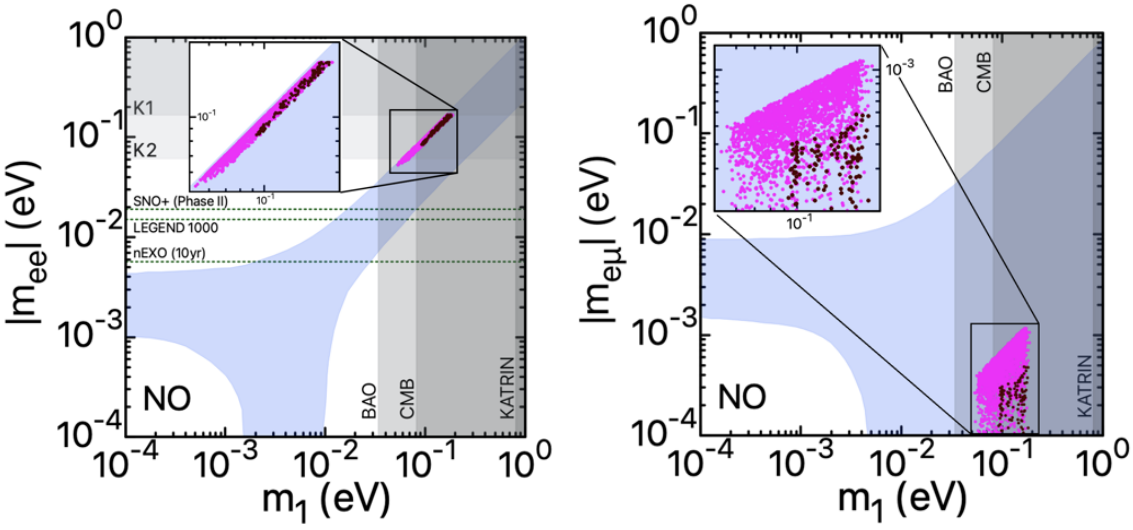

Figure 4.6: Blue regions represent the allowed neutrino mass matrix element magnitudes $|m_{ee}|$ (left) and $|m_{e\mu}|$ (right) as a function of m_1 for normal neutrino mass ordering (**NO**). Oscillation parameters are taken within their 3σ limits as reported in [53]. The vertical shaded regions illustrate the m_1 upper limits from KATRIN and cosmological observations. The left panel coincides with the effective mass from neutrinoless double beta decay $\langle m_{\beta\beta}\rangle$ and the shaded horizontal bands are excluded by KAMLAND-Zen [78], while dotted lines correspond to future sensitivities. Magenta dots represent the regions where the corresponding matrix elements satisfy the LFV limits and allow for $|\varepsilon^{eL}_{ee}| > 1\times10^{-4}$. Brown dots represent the analogue for $|\varepsilon^{eL}_{e\tau}|$ [77].

3σ ranges shown in Table 3.3 for the NO scheme. For each combination, we vary the value of $|\varepsilon^{eL}_{ee}|$ until we find the maximum for which the ten inequalities in Eqs. (4.28) and (4.29) are satisfied. This gives us the strength of the NSI that is consistent with both oscillation data and LFV constraints. No combinations of parameters were found such that they allow for an $|\varepsilon^{eL}_{ee}|$ of order 10^{-3} or larger. However, there were several combinations that allowed for an NSI of order 10^{-4} and, after performing the scan, we found $|\varepsilon^{eL}_{ee}| < 8\times10^{-4}$. Magenta dots in Fig. 4.6 show the region in the parameter space, as a function of m_1, for which we found $|\varepsilon^{eL}_{ee}|$ of order 10^{-4}. The panels in the figure give a perspective of the relation between the flavor mass matrix entries that need to be satisfied in order to have an NSI of this order. Notice that the difference between $|m_{ee}|$ (left) and $|m_{e\mu}|$ (right) should be of around one order of magnitude, which is mainly a consequence of the tight experimental bound for the process $\mu \to 3e$, which depends on the product $|m_{ee}||m_{e\mu}|$, as seen in Table 4.1. The vertical and horizontal shaded regions, as well as the dotted lines in the left panel follow the same notation as that in Fig. 4.2. We followed a similar procedure to look for the largest possible value of the other non-universal NSI, with the results summarized in Table 4.2. In all cases, we see that the maximum expected NSI parameters are below the current experimental

NSI	Explicit Form	Estimated Limit (**NO**)	Estimated Limit (**IO**)
$\lvert\epsilon^{eL}_{ee}\rvert$	$(2\sqrt{2}G_F)^{-1}M_\Delta^{-2}\lvert Y^*_{\Delta ee}Y_{\Delta ee}\rvert$	$< 8.0\times10^{-4}$	$< 8.0\times10^{-4}$
$\lvert\epsilon^{eL}_{e\mu}\rvert$	$(2\sqrt{2}G_F)^{-1}M_\Delta^{-2}\lvert Y^*_{\Delta ee}Y_{\Delta \mu e}\rvert$	$< 7.0\times10^{-7}$	$< 7.0\times10^{-7}$
$\lvert\epsilon^{eL}_{e\tau}\rvert$	$(2\sqrt{2}G_F)^{-1}M_\Delta^{-2}\lvert Y^*_{\Delta ee}Y_{\Delta \tau e}\rvert$	$< 2.0\times10^{-4}$	$< 2.1\times10^{-4}$
$\lvert\epsilon^{eL}_{\mu\mu}\rvert$	$(2\sqrt{2}G_F)^{-1}M_\Delta^{-2}\lvert Y^*_{\Delta \mu e}Y_{\Delta \mu e}\rvert$	$< 6.8\times10^{-6}$	$< 2.5\times10^{-6}$
$\lvert\epsilon^{eL}_{\mu\tau}\rvert$	$(2\sqrt{2}G_F)^{-1}M_\Delta^{-2}\lvert Y^*_{\Delta \mu e}Y_{\Delta \tau e}\rvert$	$< 4.8\times10^{-6}$	$< 2.5\times10^{-6}$
$\lvert\epsilon^{eL}_{\tau\tau}\rvert$	$(2\sqrt{2}G_F)^{-1}M_\Delta^{-2}\lvert Y^*_{\Delta \tau e}Y_{\Delta \tau e}\rvert$	$< 9.5\times10^{-5}$	$< 9.9\times10^{-5}$

Table 4.2: Constraints on NSI parameters consistent with LFV processes in the type II seesaw mechanism [77].

limits, which are of order 10^{-2} at least.

For the analysis of flavor changing NSI, we again look for inequalities that depend on the flavor matrix elements. For instance, in the case of $|\varepsilon^{eL}_{\tau e}|$ we get the conditions:

$$\frac{|m^\dagger m|_{\alpha\beta}}{|m_{e\tau}||m_{ee}|} < \frac{L_i}{2\sqrt{2}\ |\varepsilon^{eL}_{\tau e}|} \qquad (i = 1, 3, 4), \tag{4.30}$$

$$\frac{|m^\dagger|_{\alpha\beta}|m|_{\sigma\rho}}{|m_{e\tau}||m_{ee}|} < \frac{L_i}{2\sqrt{2}\ |\varepsilon^{eL}_{\tau e}|} \qquad (i \neq 1, 3, 4). \tag{4.31}$$

We again generate random numbers for oscillation parameters under the NO scheme, and we look for the maximum value of the NSI for which conditions (4.30) and (4.31) are satisfied. In this case we found $|\varepsilon^{eL}_{\tau e}| < 2.0\times10^{-4}$. The parameter space region for which we have a flavor changing NSI of order 10^{-4} is shown as brown dots in the two panels of Fig. 4.6. Notice that, again, the rate between $|m_{ee}|$ (left) and $|m_{e\mu}|$ (right) should be of around one order of magnitude. Similar regions can be directly obtained for the other matrix entries and the results for the other flavor changing NSI are shown in the third column of Table 4.2.

Apart from setting bounds to the expected NSI from the type II seesaw, we can use the information from the previous analysis to see what values of M_Δ and v_Δ can reproduce a desired order of the NSI. First, notice that for fixed values of $|\varepsilon^{eL}_{ee}|$ and $|m_{ee}|$, there can be infinite combinations of M_Δ and v_Δ that satisfy Eq. (4.26). On the other hand, for each dot in the magenta region in Fig. 4.6, which translates into a value for $|m_{ee}|$, it is possible to find a fixed NSI consistent with LFV limits, such that

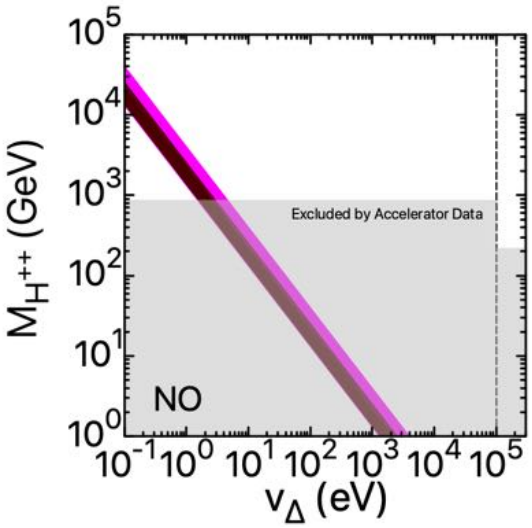

Figure 4.7: Magenta region shows the combinations of M_Δ and v_Δ that allow for $|\varepsilon_{ee}^{eL}| > 1 \times 10^{-4}$ consistent with LFV limits for normal neutrino mass ordering, **NO**. The corresponding region for $|\varepsilon_{e\tau}^{eL}| > 1 \times 10^{-4}$ is shown in brown [77]. Shaded regions are excluded by collider data and the vertical dashed line corresponds to $v_\Delta = 0.1$ MeV.

$1 \times 10^{-4} < |\varepsilon_{ee}^{eL}| < 8 \times 10^{-4}$. Then, from Eq. (4.26), we can generate a curve M_Δ vs v_Δ with $|\varepsilon_{ee}^{eL}|$ of order 10^{-4}. The combination of all these curves gives the magenta region shown in Fig. 4.7. Any point inside this region represents a combination of M_Δ and v_Δ such that $|\varepsilon_{ee}^{eL}| > 1 \times 10^{-4}$. The region in brown shows the corresponding result for the case of $|\varepsilon_{e\tau}^{eL}|$. For completeness, the shaded bands in the same figure correspond to the values of M_Δ that are excluded from accelerator experimental data, where, according to different analyses, the limit depends on the value of v_Δ. This dependency arises from the fact that for small v_Δ the H^{++} mainly decays in two leptons, while for relatively large v_Δ it mainly decays to two W bosons (see section 4.3). As we can see, for $v_\Delta < 0.1$ MeV, the mass of the charged scalar is constrained to the condition $M_\Delta > 870$ GeV [89], while for the case $v_\Delta > 0.1$ the constraint is less robust and we have $M_\Delta > 220$ GeV [90].

As a final test, we can also comment on the consistency of the expected NSI with the current limits of $\mu \to e$ conversion in nuclei, another process that is forbidden within the SM but which observation would be a clear signal of new physics. Within the type II seesaw mechanism, the singly and doubly charged scalars contribute to this process.

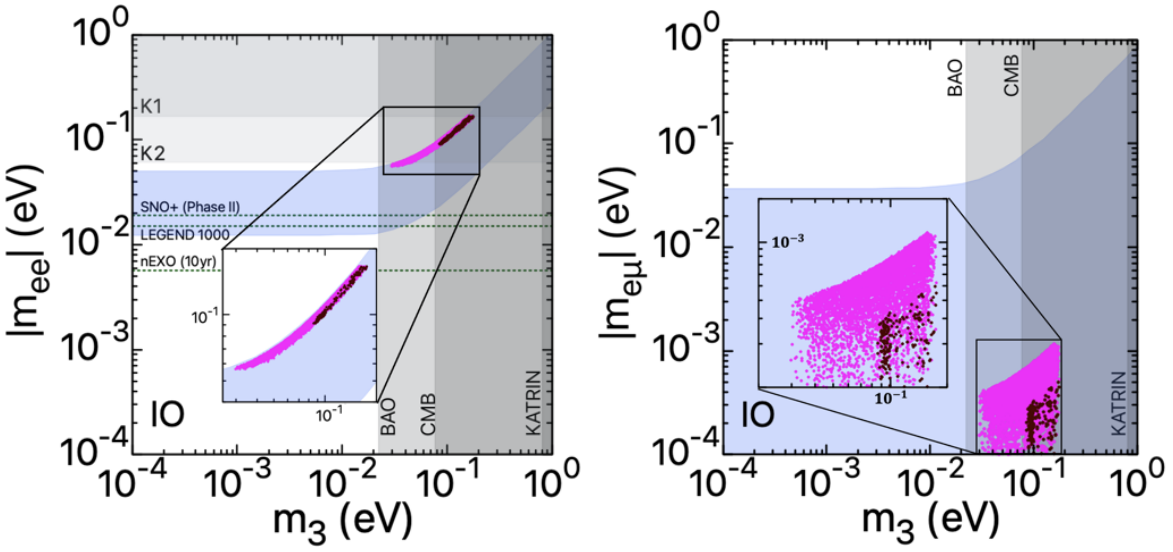

Figure 4.8: Same as Fig. 4.6 but for the case of inverted neutrino mass ordering, **IO**. Magenta dots denote the regions where the corresponding matrix elements obey LFV limits and allow for $|\varepsilon^{eL}_{ee}| > 1 \times 10^{-4}$. Brown dots show the analogue for $|\varepsilon^{eL}_{e\tau}|$ [77].

In the case of relatively light nuclei, the branching ratio is given by [91]

$$\begin{aligned} \mathrm{BR}(\mu \to e) \approx & \frac{\alpha^5}{36\pi^4}\frac{m_\mu^5}{\Gamma_{\mathrm{capt}}} Z_{\mathrm{eff}}^4 Z F^2(-m_\mu^2) \\ & \times \left| (Y_\Delta^\dagger Y_\Delta)_{e\mu} \left[\frac{5}{24 m_{H^+}^2} + \frac{1}{m_{H^{++}}^2}\right] + \frac{1}{m_{H^{++}}^2} \sum_\alpha Y^\dagger_{\Delta e\alpha} Y_{\Delta\alpha\mu} f(m_\alpha, m_{H^{++}}) \right|^2 , \end{aligned} \tag{4.32}$$

with $F(q^2)$ the nuclear form factor, m_μ the mass of the muon, α the fine structure constant, Γ_{capt} the capture rate, and Z_{eff} an effective nuclear charge. The function f has the form

$$\begin{aligned} f(m_\alpha, m_{H^{++}}) = & 4\frac{m_\alpha^2}{m_\mu^2} + \ln\left(\frac{m_\alpha^2}{m_{H^{++}}^2}\right) + \left(1 - 2\frac{m_\alpha^2}{m_\mu^2}\right)\sqrt{1 + 4\frac{m_\alpha^2}{m_\mu^2}} \\ & \times \ln\left(\frac{\sqrt{m_\mu^2 m_{H^{++}}^{-2}} + \sqrt{m_\mu^2 m_{H^{++}}^{-2} + 4 m_\alpha^2 m_{H^{++}}^{-2}}}{\sqrt{m_\mu^2 m_{H^{++}}^{-2}} - \sqrt{m_\mu^2 m_{H^{++}}^{-2} + 4 m_\alpha^2 m_{H^{++}}^{-2}}}\right) . \end{aligned} \tag{4.33}$$

We can find in the literature many experimental limits for $\mu \to e$ conversion using different nuclei such as Au, Ag, and Ti. The most stringent result comes from the SINDRUM II experiment, where an upper bound of $\mathrm{BR}(\mu \to e) < 4.2 \times 10^{-12}$ has been reported for Ti [92]. To test the consistency of the NSI bounds found here, we evaluate the BR in Eq. (4.32) using the oscillation parameters, as well as the product $v_\Delta M_\Delta$,

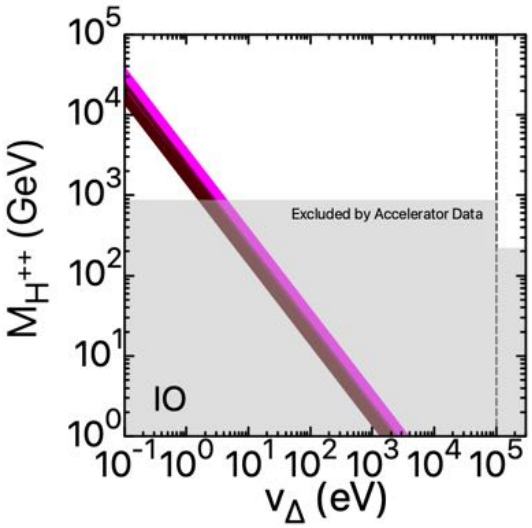

Figure 4.9: Magenta region shows the combinations of M_Δ and v_Δ that allow for $|\varepsilon_{ee}^{eL}| > 1 \times 10^{-4}$ consistent with cLFV limits for inverted neutrino mass ordering, **IO**. The corresponding region for $|\varepsilon_{e\tau}^{eL}| > 1 \times 10^{-4}$ is shown in brown [77]. Shaded regions are excluded by collider data and the vertical dashed line corresponds to $v_\Delta = 0.1$ MeV.

with $m_{H^{++}}^2 \approx m_{H^+}^2$, that reproduce NSI bounds of order 10^{-4}. In each case we get limits that are consistent with the experiment. For instance, if we take the oscillation parameters for which $|\varepsilon_{ee}^{eL}| = 8 \times 10^{-4}$, then we find a predicted branching ratio in Eq. (4.32) of $\mathrm{BR}(\mu \to e) = 1.6 \times 10^{-13}$, which is one order of magnitude below the current experimental limit from SINDRUM II. We conclude that the lepton conversion in nuclei has no impact in the determination of NSI of order 10^{-4}, which is the largest magnitude expected in the particular case of type II seesaw.

Until now, we have focused our discussion assuming the case of NO for neutrino masses. Indeed, we can perform a similar analysis for the case of IO mass hierarchy. By following the same procedure, we again found only two NSI for which we can have a strength of order 10^{-4}. The largest bound for each NSI is shown in Table 4.2. In addition, we show in Fig. 4.8 the region in parameter space for which an NSI of the referred order is allowed, this time as a function of m_3, which is the lightest neutrino mass under the IO scheme. Magenta dots in the figure show the parameter space for $|\varepsilon_{ee}^{eL}|$, while brown dots correspond to $|\varepsilon_{e\tau}^{eL}|$. Again, we can see the panels in the figure show the expected relation between $|m_{ee}|$ (left) and $|m_{e\mu}|$ (right) needed for this strength of interaction. Shaded regions and dotted lines have the same meaning as in Fig. 4.3. We also show in Fig. 4.9 the values of the product $M_\Delta v_\Delta$ that allow for an NSI of order 10^{-4} in the case of an IO of the mass hierarchy.

From this section we conclude that, in order to be consistent with LFV limits, NSI

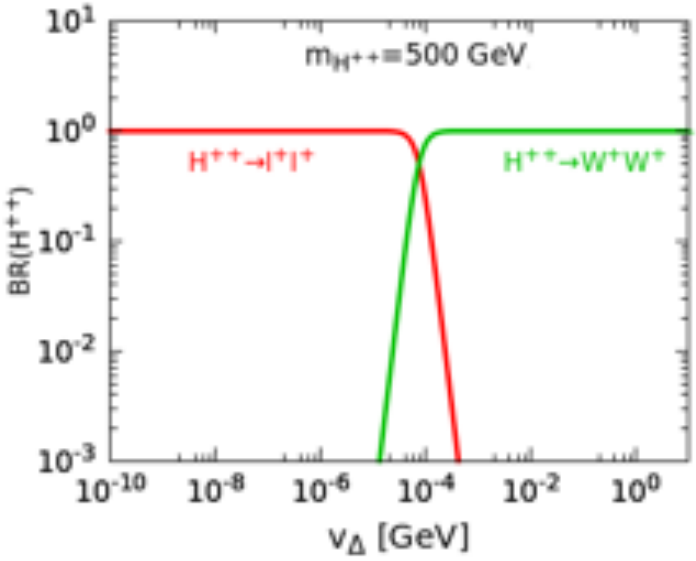

Figure 4.10: $H^{\pm\pm}$ branching ratios as a function of v_Δ for $m_{H^{\pm\pm}} = 500$ GeV. Red and green lines correspond to $H^{\pm\pm} \to \ell^\pm\ell^\pm$ and $H^{\pm\pm} \to W^\pm W^\pm$, respectively.

signals from the type II seesaw mechanism are expected to be of order 10^{-4} or less. Current experiments are far from this sensitivity, since, as we can see from Table 3.4, they can give constraints of order 10^{-1} and 10^{-2} at best. Many experimental proposals, like using Cr neutrino sources, have been considered to enhance current sensitivities, but limits will still remain far from needed to corroborate this theory as the definite mechanism for neutrino mass. However, we want to stress that, apart from NSI signals, the type II seesaw mechanism can be manifested through charged scalar decay modes. For instance, within this theory, some decay rates behave differently depending on neutrino properties that can be probed in collider physics [93], and that we briefly discuss in the following section.

4.3 Type II seesaw at colliders

For the type II seesaw mechanism, neutrino mass ordering can be probed for the v_Δ scale allowed in Fig. 4.7. To see this, let us focus on the H^{++} decay modes at colliders. In the case of $m_{H^{++}} \approx m_{H^+} \approx m_{H^0}$, the doubly charged scalar can decay into two same charge leptons or into two W^+ bosons, with decay widths [94]:

$$\Gamma(H^{\pm\pm} \to l_i^\pm l_j^\pm) = \Gamma_{l_i l_j} = \frac{m_H^{\pm\pm}}{(1+\delta_{ij})8\pi} \left| \frac{m_{ij}^\nu}{v_\Delta} \right|^2 , \tag{4.34}$$

$$\Gamma(H^{\pm\pm} \to W^{\pm}W^{\pm}) = \Gamma_{W^{\pm}W^{\pm}} = \frac{g^2 v_{\Delta}^2}{8\pi m_{H^{\pm\pm}}} \sqrt{1 - \frac{4}{r_W^2}} \left[\left(2 + (r_W/2 - 1)^2\right) \right], \quad (4.35)$$

where $r_W = m_{H^{\pm\pm}}/M_W$. In particle physics, we define the branching ratio of a given process as the decay width of the process, divided by the sum of the decay widths of all the possible decay channels. In other words, the branching ratio is a measure of the fraction of times that a process, or processes, will happen among all the possible decays. We compare in Fig. 4.10 the branching ratio of H^{++} decaying into two leptons with the corresponding one to two bosons, as a function of v_{Δ}, for $M_{H^{++}}$ fixed and using central values for oscillation parameters. Notice that the v_{Δ} region that allows for an NSI of order 10^{-4} in Fig. 4.7 falls within a range where the leptonic channel is dominant. In fact, we can see that the leptonic channel is dominant for $v_{\Delta} < 10^{-5}$ GeV, which means that under this condition, $M_{H^{++}}$ mainly decays into two leptons. In this case, the branching ratio of each two-lepton decay mode is given by

$$\mathrm{BR}(H^{++} \to \ell_{\alpha}\ell_{\beta}) = \frac{(2 - \delta_{\alpha\beta})|m_{\alpha\beta}|^2}{|m_{ee}|^2 + |m_{\mu\mu}|^2 + |m_{\tau\tau}|^2 + 2(|m_{e\mu}|^2 + |m_{e\tau}|^2 + |m_{\tau\tau}|^2)}. \quad (4.36)$$

Depending on the neutrino mass ordering, the different $|m_{\alpha\beta}|$ are determined by oscillation data. Top panels in Fig. 4.11 show a comparison of the flavor conserving ($\alpha = \beta$) branching ratios depending on the lightest neutrino mass for normal ordering (left panel), and inverted ordering (right panel) when varying oscillation parameters within their 3σ ranges. We see an evident difference between the two different hierarchies. In the case of normal ordering, the branching ratios corresponding to $\mu\mu$ and $\tau\tau$ channels are dominant for m_1 below approximately 10^{-2} eV. In contrast, for the case of inverted ordering, the ee channel is dominant in the same mass region. The above discussion suggests that H^{++} can decay to either $\mu\mu$, $\tau\tau$ (for **NO**) or ee (**IO**) with relatively large strength, depending on the ordering of the light neutrino masses. Hence, it might be possible to probe the ordering (**NO** or **IO**) by looking into the decay patterns of H^{++} to same-flavor leptonic final states. For completeness, we also show in the bottom panels of Fig. 4.11 the case of non-diagonal ($\alpha \neq \beta$) branching ratios. However, in this case both regions look very similar, with the $\mu\tau$ channel dominant and the only notable difference being the width of the allowed region for the other two channels.

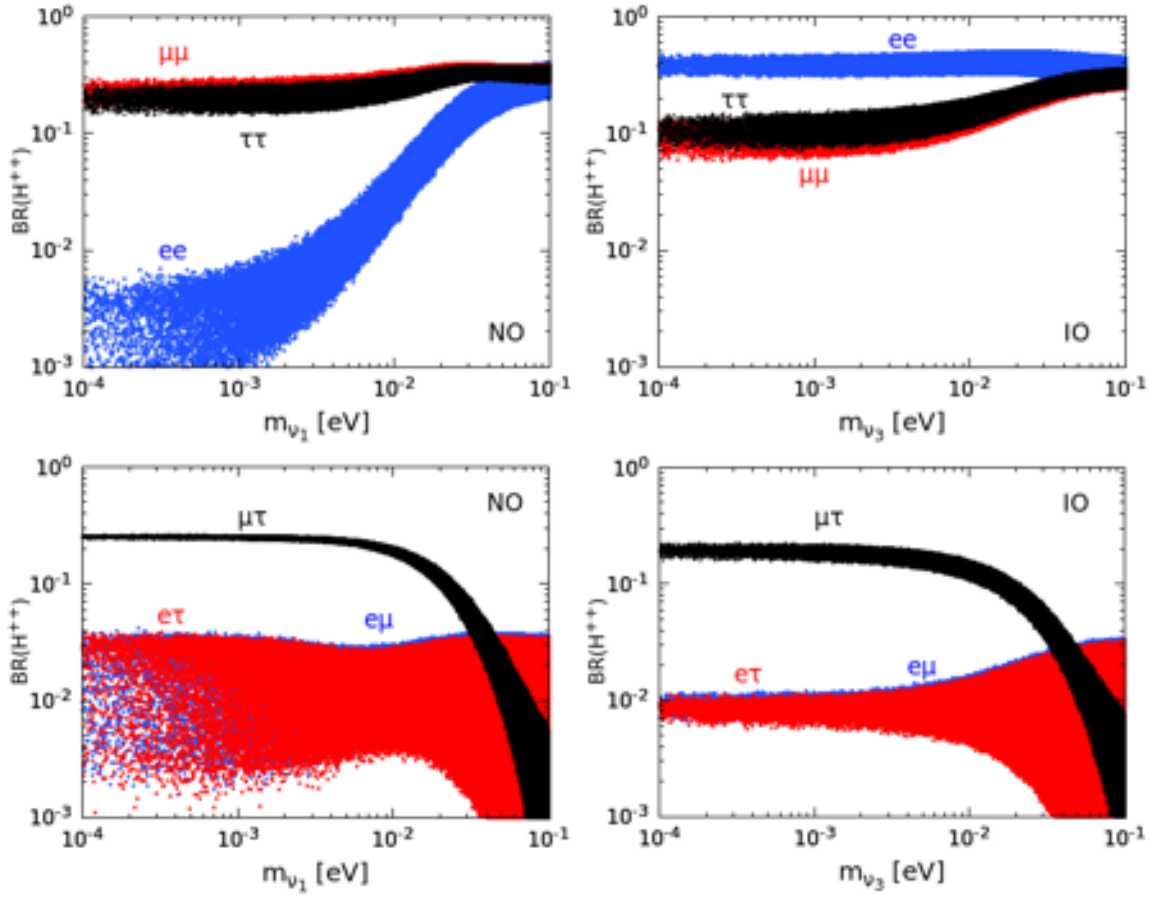

Figure 4.11: Top panels: H^{++} branching ratio to same-flavor dilepton final states as a function of the lightest neutrino mass for **NO** (left) and **IO** (right). Bottom panels: H^{++} branching ratio to two different flavor dilepton final states as a function of the lightest neutrino mass for **NO** (left), and **IO** (right)[93]. In all cases we assume $v_\Delta < 10^{-4}$ GeV and $m_{H^{\pm\pm}} = 1$ TeV, and we vary oscillation parameters within their 3σ ranges.

Chapter 5

CEvNS experiments with neutrinos from spallation neutron sources

We studied in the previous chapter how a specific theoretical model can induce interactions that can be interpreted within the NSI formalism. In particular, we focused on the NSI couplings that result from the type II seesaw mechanism in the lepton sector. However, we have seen that NSI can also be present in neutrino-quark interactions, which can be studied through processes that involve neutrino-nucleus interactions. As an example we can consider CEvNS interactions, which were introduced within the SM theory in section 3.2.2. This process is relatively new in the sense that the COHERENT collaboration reported the first experimental observation of CEvNS in 2017. This was achieved through a CsI based detector located at the Spallation Neutron Source (SNS) at Oak Ridge National Laboratory (ORNL) [27]. A few years later, in 2020, the same collaboration reported a second measurement with a 3σ significance level [95], this time by using a Liquid Argon (LAr) detector. Then, a second data set from the CsI detector run was released in 2021 [96]. In this chapter, we study the implications of these measurements in the context of the SM and NSI. We begin by using data from the experiments to constrain standard model and nuclear physics parameters. Then, we will also study different bounds that can be obtained from this process for NSI by independently analyzing data from the two different detectors. Before presenting the analysis, we start by giving a general overview of the experiment that allowed for the observation of CEvNS.

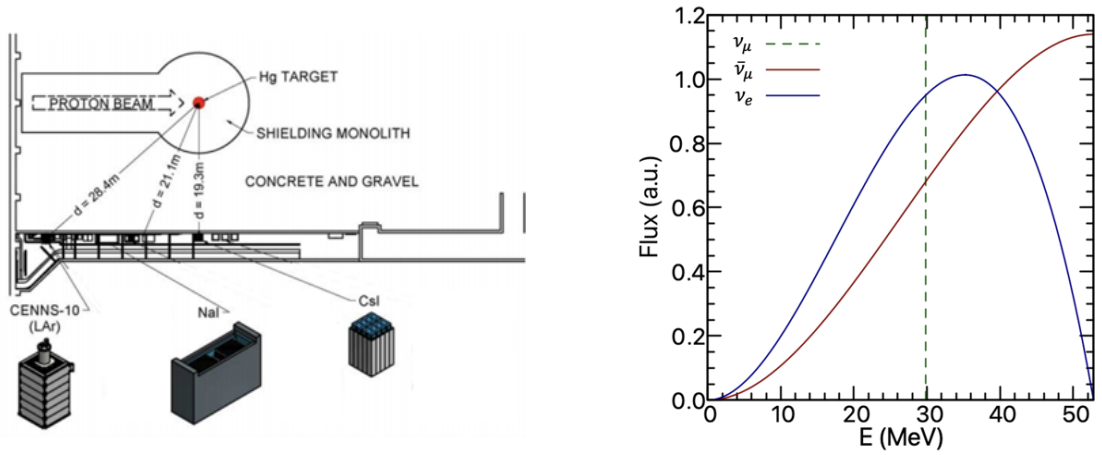

Figure 5.1: Left panel: Schematic representation of the COHERENT experiment. Image taken from [97]. Right panel: Normalized fluxes for prompt and delayed neutrinos at the SNS.

5.1 The COHERENT experiment

Neutrinos produced in π-DAR sources were discussed in section 3.1.1. Spallation Neutron Sources are a particular case of this production mechanism that offers significant advantages for the study of CEvNS. Particularly, the SNS at ORNL provides the current most intense *pulsed* neutron beam source in the world[1]. As we have seen, neutrinos from π-DAR sources are produced as a byproduct of the collision of high energy proton beams with a heavy target material. A special feature of the SNS is that the incident proton beams are *pulsed*, which means that they are produced with a certain frequency (60 Hz), and with a full Width at Half Maximum (FWHM) of 380 ns. To give some perspective, the interval between two consecutive pulses, 0.017 s, is around 4.2×10^4 times the FWHM. This plays an important role for background discrimination, and hence, for a cleaner measurement of CEvNS. For the particular case of the SNS, the pulsed proton beams hit an Hg target as sketched in the left panel of Fig. 5.1. As a result of the collision, there is a production of charged pions. Most of the negatively charged pions are captured back in the nucleus, while the π^+ decay at rest in the form $\pi^+ \to \mu^+ + \nu_\mu$, producing a mono-energetic beam of muon neutrinos, which are called *prompt* neutrinos. For a two body decay, the energies of the involved particles are fixed and can be determined directly by energy and momentum conservation. Then, the corresponding flux for *prompt* neutrinos is given by a Dirac delta distribution

$$\frac{\mathrm{dN}_{\nu_\mu}}{\mathrm{d}E} = \eta\delta\left(E - \frac{m_\pi^2 - m_\mu^2}{2m_\pi}\right). \tag{5.1}$$

[1]This may change in the following years since the European Spallation Source is currently under construction [98] and will have a significantly increased power when compared to the SNS.

Eventually, the μ^+'s also decay almost at rest, producing electrons, electron neutrinos, and muon anti-neutrinos. These two final neutrino states are jointly referred to as *delayed* neutrinos. For a three body decay, the energies of the final particles are no longer fixed, and we end up with two different spectra for the emitted neutrinos. These spectra can be analytically calculated when the decaying muon is at rest, and are given by:

$$\frac{\mathrm{dN}_{\overline{\nu}_\mu}}{\mathrm{d}E} = \eta \frac{64E^2}{m_\mu^3}\left(\frac{3}{4} - \frac{E}{m_\mu}\right), \tag{5.2}$$

$$\frac{\mathrm{dN}_{\nu_\mathrm{e}}}{\mathrm{d}E} = \eta \frac{192E^2}{m_\mu^3}\left(\frac{1}{2} - \frac{E}{m_\mu}\right). \tag{5.3}$$

Being $\eta = rN_{POT}/4\pi L^2$ a normalization factor with N_{POT} the total number of protons on target (POT), which depends on the time of exposure of the experiment; $r = 0.08$ accounts for the number of neutrinos of each flavor produced per proton on target, and L is the distance between the source and the detector. For the COHERENT experiment, detectors were located in an aisle surrounded by concrete and gravel to reduce backgrounds, as illustrated in the left panel of Fig. 5.1, where we show the actual location of the CsI and LAr detectors. The total neutrino flux on each detector is considered to be the sum of the three different contributions, which are shown in the right panel of Fig. 5.1. From the shape of the distributions, we see that neutrinos from this source have a maximum energy of around 52.8 MeV, which is small enough to still fulfill the coherence condition that is necessary for the CEvNS process.

The main advantage of using a pulsed proton beam relies on the fact that the whole process of pion and muon decays takes some tens of μs. Therefore, every event that is a candidate for CEvNS interaction has plenty of time to be detected between two pulses, and it must arrive a few microseconds after the POT trigger. Then, timing information will be crucial to discriminate between actual CEvNS and background events coming from other natural sources and cosmic rays, which are dominant for CEvNS experiments. Actually, these backgrounds, commonly known as steady-state backgrounds (SSB), are reduced in the SNS by three orders of magnitude when compared to other neutrino production mechanisms where no pulsed beams are used [99]. For SNS experiments there are two other main sources of backgrounds. First, we have the production of Beam Related Neutrons (BRN), which are neutrons produced as the result of the original proton collisions; after all, the main goal of an SNS is the production of high energy neutrons! However, only a few neutrons related to this background can cross a lead shielding that surrounds the detectors, and for many of the cases they are negligible [100]. Additionally, we have the production of Neutrino-Induced Neutrons (NIN),

which are neutrons produced at the lead shield as a result of charged and neutral current neutrino interactions with lead nuclei. As a result of this interaction, we have the production of gamma rays and neutrons, which can produce signals that can be confused with neutrino-induced events in the detector.

As for the detection process, what it is experimentally measured is the number of photoelectrons emitted as a result of the neutrino-nucleus interaction. In a general picture, the process is the following: within a scintillating material, the kinetic recoil energy originally acquired by the nucleus is transferred to the crystal lattice of the material. An event can then be detected if a scintillating agent is carried to an excited state, which eventually returns to a base state, emitting a photon that is detected through photomultiplier tubes. Ideally, the number of the emitted photoelectrons would be proportional to the initial kinetic energy of the nucleus. This is true for light target particles like electrons. However, for heavy particles, it is experimentally known that the initial kinetic energy can be *quenched*, meaning that only a fraction of the deposited energy is available for its detection as photoelectrons. This can be explained since heavier particles are more prone to release energy in the form of heat. In these cases, the number of released photoelectrons PE is given by

$$\mathrm{PE} = \mathrm{QF}(T)YT, \tag{5.4}$$

with Y the light yield, and QF a quantity defined as *quenching* factor, which accounts for the energy loss, and in general depends on the nuclear kinetic recoil energy, T, as well as in specific properties of the detector material. The quenching factor represents the fraction of kinetic recoil energy detected for the recoil of a heavy particle when compared to an incident electron of the same energy. A detailed knowledge of the QF is needed since, apart from giving the relation between the true and the observed energy, it can have a huge impact on the total number of detected events, specially if the quenched signal is near the detector threshold. This is one of the main reasons why there were more than forty years between the theoretical prediction of CEvNS and its first detection. At low energy thresholds, the quenching factor, and the form factors introduced in section 3.2.2 represent one of the main sources of systematic errors. Currently there are many efforts to reduce their systematic effects. For comparison,the first data set from the COHERENT CsI detector reported a QF contribution to systematic errors of 25%, while for the second run it was reported below 5% [96].

5.2 The analysis

Now that we know the detection mechanism, we use data from CEvNS experiments to perform tests of the SM, as well as to study new physics scenarios. For counting experiments, we compare the experimentally measured number of events with the theoretical prediction of the model under study. For this purpose, we perform a χ^2 analysis. We will use the data from the first CsI run and LAr detectors of the COHERENT collaboration to test different parameters of the SM, and we will explore the sensitivity of these experiments to NSI parameters. In addition, in following chapters we will perform similar tests, but we will focus on the sensitivity of future experiments.

In general, the number of events expected from an experiment depends on the neutrino source, as well as on the intrinsic characteristics of the detector and on the model under study. We denote this theoretical prediction by N^{th}, which is given by

$$N^{th} = \mathcal{N} \int_T A(T) dT \int_{E_{min}} dE_\nu \frac{\mathrm{d}N_\nu}{\mathrm{d}E_\nu} \frac{\mathrm{d}\sigma}{\mathrm{d}T}, \tag{5.5}$$

with $\mathrm{d}N_\nu/\mathrm{d}E_\nu$ the total neutrino flux, and $\mathrm{d}\sigma/\mathrm{d}T$ the predicted differential cross-section, which may change depending on the theoretical model considered for the computation. For instance, NSI contributions, as well as the assumption of electromagnetic properties for neutrinos introduce a different cross-section than that of the SM. The function $A(T)$ accounts for the detectors efficiency, and $\mathcal{N}$ is the number of targets within the detector that are available for scattering throughout the experimental run. This factor depends on the material density and the detectors weight, and is given by $\mathcal{N} = N_A M_{det}/M_D$, with N_A the Avogadro's number, M_{det} the mass of the detector, and M_D its molar mass. The lower limit of the T integral in Eq. (5.5) depends on the detector's threshold and the upper one on the maximum recoil energy dictated by momentum conservation laws. On the other hand, the upper limit of the integral over E_ν depends on the maximum energy of the produced neutrinos.

To compare the theoretical expectation given by Eq. (5.5) with actual experimental data, we follow the pull method, and minimize a least square function χ^2. This allows us to set bounds for different parameters at a desired confidence level (C.L.). For low statistics experiments, we can use the square function

$$\chi^2 = \sum_{i=1}^{n} \frac{\left(N_i^{exp} - (1+\alpha)N_i^{th}(X) - (1+\beta)N_i^{bg}\right)^2}{\sigma_i^2} + \frac{\alpha^2}{\sigma_\alpha^2} + \frac{\beta^2}{\sigma_\beta^2}, \tag{5.6}$$

where the index i indicates the number of data bins. N_i^{exp} corresponds to the exper-

	$\Delta\chi^2$		
Degrees of freedom	**68.39% C. L.**	**90% C. L.**	**95% C. L.**
1	1	2.71	3.84
2	2.3	4.61	5.99

Table 5.1: $\Delta\chi^2$ values for different confidence level intervals depending on the degrees of freedom.

imentally observed number of events, and N_i^{bg} are the background events, which are associated to SSB, BRN, and NIN backgrounds. On the other hand, $N_i^{th}(X)$ is the theoretical prediction for the CEvNS events, which depends on a set of parameters, X, to be tested. These parameters can be associated, for instance, to the weak mixing angle in the case of SM tests, or to non-standard interactions in the case we want to study new physics. The parameters α and β in Eq. (5.6), called *nuisance* parameters, account for normalization uncertainties for CEvNS and background measurements, respectively. Regarding the different uncertainties, σ_i^2 is the statistical variance of the i^{th} bin, while σ_α is the systematic uncertainty associated to CEvNS and σ_β the systematic uncertainty associated to backgrounds. With this method, we evaluate the χ^2 function for different values of the set of parameters under test, X, each time minimizing with respect to the nuisance parameters α and β. After doing this, there will be a minimum for the χ^2 function, which we denote as χ^2_{min}, and which gives us the best fit parameters. Then, confidence level regions for the parameter space X are determined by the combination of parameters X for which the χ^2 values lie below a certain distance $\Delta\chi^2 = \chi^2 - \chi^2_{min}$. We show in Table 5.1. the C.L. achieved for different values of $\Delta\chi^2$ [51]. These values depend on the degrees of freedom of the analysis; that is, the number of free parameters that are being tested.

Considering the neutrino flux for the SNS discussed in section 5.1, we can proceed to calculate the expected number of events in the context of the SM by using Eq. (5.5). In general, the maximum kinetic energy of the recoiling nucleus associated to this process holds the condition $T_{max}(E_\nu) = 2E_\nu^2/M$, particularly being 52.8 MeV the maximum neutrino energy for SNS neutrinos, as seen from the right panel of Fig. 5.1. So far, the COHERENT collaboration has reported CEvNS measurements with two different detectors, CsI and LAr. The efficiency function of each detector depends on the number of measured photoelectrons, or equivalently, in the nuclear recoil energy. In the case of LAr, the efficiency was given in Ref. [101] as a function of the nuclear recoil energy, while for CsI, it was given in terms of the measured photoelectrons in Ref. [102]. In this case, to perform the integral in Eq. (5.5), we need to convert the measured photoelectrons

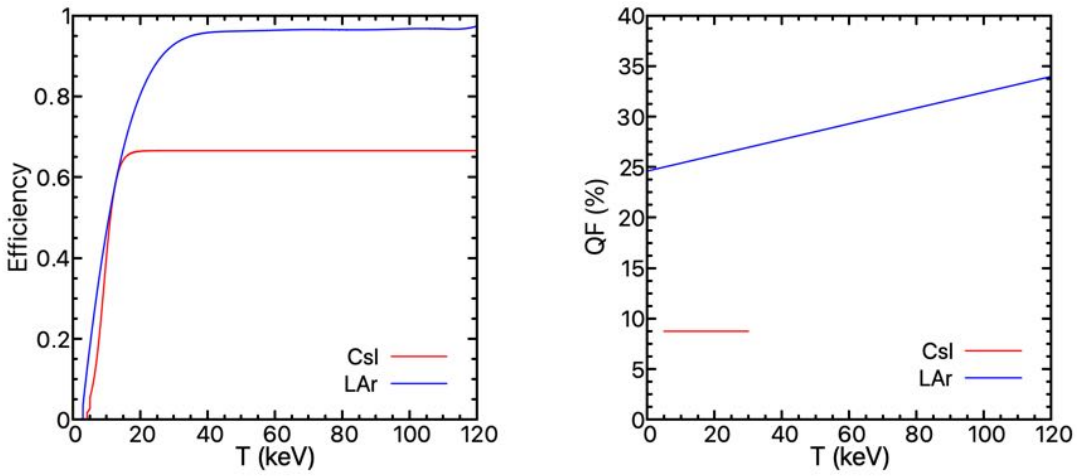

Figure 5.2: Acceptance function (left panel) and quenching factors (right panel) reported by the COHERENT collaboration for CsI and LAr detectors. The QF for CsI was only reported in the range of interest from 10 to 30 keV. Images adapted from [101, 102].

to nuclear recoil energy through Eq. (5.4). For reference, we show the efficiencies and quenching factors for both CsI and LAr detectors in the left and right panels of Fig. 5.2, respectively. Notice that in the case of CsI, the collaboration reported a constant QF for the first run, which we used for this analysis.

To calculate the SM prediction of the number of events, we use the CEvNS cross-section given in Eq. (3.20), with the weak mixing angle value at low energies, in the $\overline{\text{MS}}$ scheme, such that $\sin^2\theta_W = 0.23857(5)$ [51]. As for the form factor assumptions, we use the convention of a Symmetrized Fermi distribution for protons, and a Helm parametrization for neutrons. A list with other parameters that are relevant for the computation of the number of events in each case is given in Table 5.2. After all of these considerations, we obtain 171 and 140 predicted events for CsI and LAr, respectively. In contrast, the experimental measurements reported by the COHERENT collaboration are 136 ± 31 events for CsI [96] and 159 ± 43 for the LAr detector [101], a difference that gives room to test SM parameters and new physics scenarios. Notice that for CsI, the predicted number of events is larger than the observed result, while for the LAr

Detector	$\mathbf{M}_{det}$ **(kg)**	**L (m)**	$\mathbf{N}_{POT}$	R_p **(fm)**	R_n **(fm)**	**s (fm)**
CsI	13.9	19.3	1.76	4.81 - 4.74	5.12	0.9
LAr	24	27.5	1.37	3.14	3.36	0.9

Table 5.2: Parameters used for the computation of the predicted number of events for COHERENT CsI and LAr detectors. For CsI, the two values of R_p correspond to Cs and I, respectively, which are slightly different.

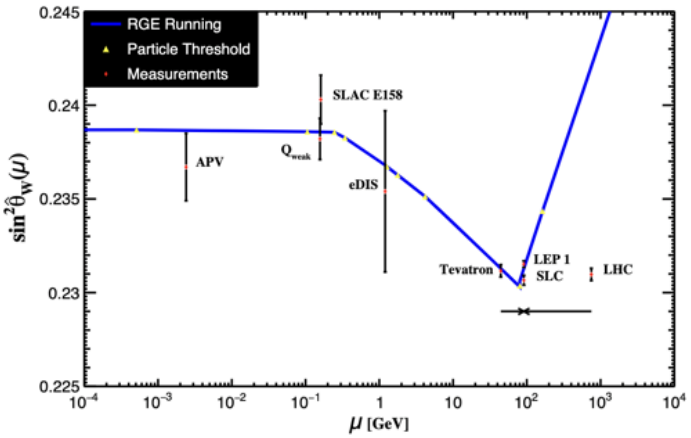

Figure 5.3: Weak mixing angle energy dependence. The blue line represents the theoretical prediction, and the dots represent different experimental measurements. Image taken from [51].

we have the opposite situation. This will be an important fact during the discussion of our results in the following subsections, where we present the implications of these measurements in the context of SM physics, nuclear physics, and NSI.

5.2.1 Sensitivity to standard parameters

We begin our discussion by testing SM and nuclear physics parameters independently. To this end, we perform the χ^2 analysis introduced in section 5.2. As we are testing SM parameters, for these computations we employ the cross-section given in Eq. (3.20) to calculate the predicted number of events. Also, it is important to highlight that for the CsI analysis we used the binned data as presented in Ref. [36], while for LAr we only used the total number of events as given in [95].

Regarding SM parameters, we study the sensitivity of the CEvNS process to the weak mixing angle value at low energies and in the $\overline{\text{MS}}$ scheme. This parameter has been widely studied with data from different experiments, and at different energy scales, as shown in Fig. 5.3. As we can see from the figure, at low energies the uncertainty is large, and any deviation from the predicted value would be a clear indicator of new physics involved in a scattering process. To perform the analysis, we vary the value of the weak mixing angle, with all the other parameters fixed, and compare the predicted events with the experimental measurement by minimizing the χ^2 function in Eq. (5.6). The different uncertainties for the analyses were extracted from Refs. [101, 102], and we use the reported values of $\sigma_\alpha = 0.25$ for CsI, and $\sigma_\alpha = 0.05$ for LAr. The results are shown in the left panel of Fig. 5.4 [103]. Notice that both detectors exhibit a displacement with respect to the current accepted value of $\sin^2\theta_W = 0.23857(5)$, each

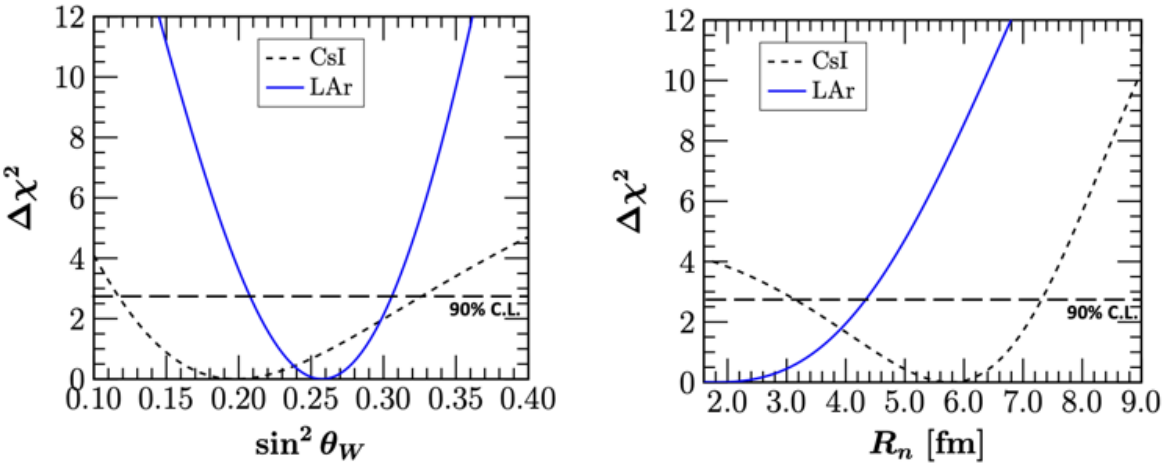

Figure 5.4: Sensitivity of COHERENT data to the weak mixing angle (left) and to the neutron rms radius (right). Solid lines show the results for the CsI detectors while the dashed lines show the results for LAr [103]. The horizontal dashed line indicates the 90% C.L. sensitivity.

of them in opposite directions. This is because one of the experiments (CsI) counted less events than the SM prediction, while the other (LAr) counted more. The improvement in the width of the constraint given by the LAr detector is remarkable, and it is a consequence of its better characterization of systematic errors when compared to the CsI case.

For the case of nuclear physics, we have seen that the CEvNS process is also sensitive to relevant nuclear parameters like the proton and neutron rms radii through the form factors present in the associated cross-section. In general, the electric charge of protons allows for a good experimental determination of R_p. However, in the case of neutrons there are many experimental limitations since electromagnetic interactions can not be used for their study. We can take advantage of the sensitivity of CEvNS to nuclear form factors to get information of the neutron rms radius, R_n, of the target material. Again, we perform a χ^2 analysis while fixing all the other parameters of the theory. The right panel in Fig. 5.4 shows the results for the neutron rms radius on each of the detection materials. Notice that the results are not directly comparable since they correspond to different elements. However, an important remark is that, given the small value of its neutron nuclear radius, for LAr we only have an upper bound for R_n. In both cases, lower values for R_n than those shown in the figure can not be tested since Eq. (3.24) puts a restriction on its minimum physical value. In the case of CsI, we have assumed the same radius for both Cs and I nuclei. The result is consistent with the measurement reported in Ref. [104] for a Pb nucleus, a heavier element than both Cs and I, and for which the authors found a value of $R_n = 5.75 \pm 0.18$ fm.

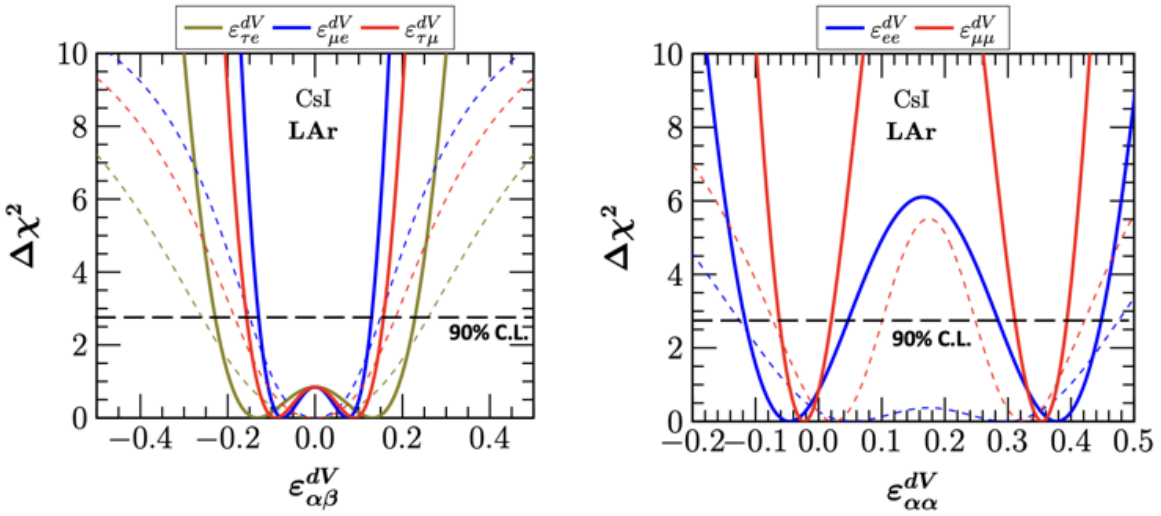

Figure 5.5: Sensitivity of the COHERENT experiments to flavor changing (left) and non-universal (right) NSI parameters. LAr results are shown as solid lines while CsI sensitivities as dashed lines [103]. The horizontal dashed line indicates the 90% C.L. sensitivity.

5.2.2 Sensitivity to NSI

Now we focus on testing the sensitivity of the COHERENT experiment to physics beyond the SM by following the NSI formalism introduced in section 3.7. To calculate the predicted number of events, we now have to consider the cross-section given in Eq. (3.86), which explicitly includes the contribution from NSI parameters. Again, we compare the theoretical prediction to the experimental results by performing a χ^2 analysis. As a first step, we only take one NSI parameter to be non-zero at a time. Since we have muon and electron neutrinos from the SNS source, and since the source to detector distance is small, then we are sensitive to all NSI except for the diagonal $\varepsilon^{fV}_{\tau\tau}$. The results for different parameters are shown in Fig. 5.5 [103]. Left panel shows the sensitivity for the case of flavor changing parameters, where we have indicated the CsI analyses with dashed lines and the corresponding results for LAr by solid lines. We can see that the allowed region for the LAr case is more constrained than that corresponding to CsI. However, the main difference between the results is the location of the minimum on each case. To explain this, notice that as we have repeatedly pointed out, the CsI experiment reported less events than the SM prediction. On the other hand, from Eq. (3.86) we can see that the contribution to the number of events from a flavor changing parameter is always positive, and in consequence, we do not have a physical manner to have less number of events than that predicted by the SM, explaining the minimum at zero. In contrast, the LAr experiment reported more events than the SM prediction, so in this case the NSI contribution adds more predicted events

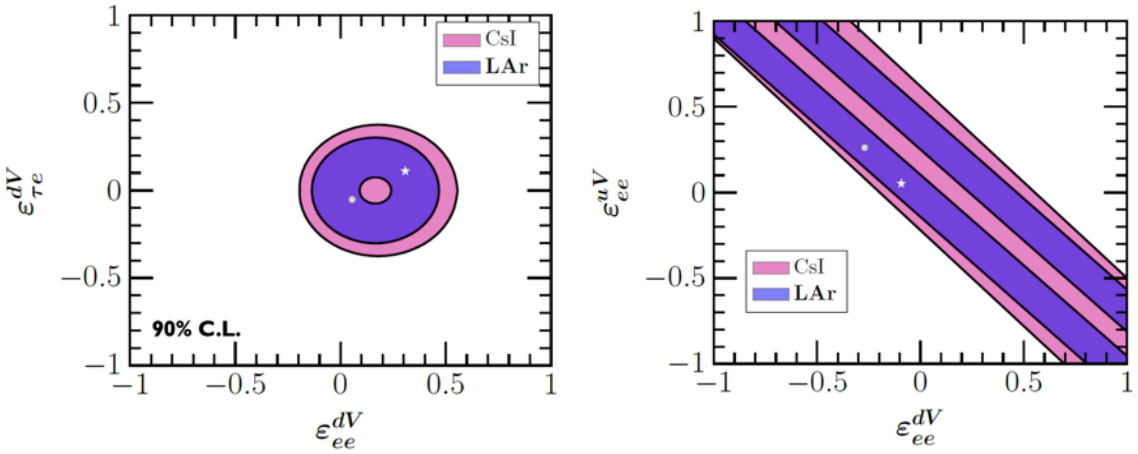

Figure 5.6: 90% C.L. allowed regions from the analysis when varying two NSI parameters at a time using CsI (magenta) and LAr (purple) data. Left panel considers the simultaneous presence of non-universal and flavor-changing NSI with d quarks, while the right panel corresponds to the case of non-universal NSI couplings with u and d quarks [103]. The dot and the star indicate the best fit point for CsI and LAr, respectively.

to match the experimental result. Therefore, the χ^2 takes its minimum value for non-zero NSI. The results for non-universal parameters are shown in the right panel of the same figure. Again, the LAr measurement gives better constraints for the parameters, and the minimum presents the expected opposite shifts as in the case of the weak mixing angle when comparing the same parameter for different detectors. The presence of two minima in this analysis is a consequence of the linear and quadratic dependence of the cross-section on the corresponding NSI parameter.

Now we go a step further and perform an equivalent analysis but assuming two NSI parameters to be different from zero at a time. As we have seen, for the case of $\varepsilon_{\alpha\mu}^{fX}$, atmospheric neutrino experiments such as Super-Kamiokande and IceCube DeepCore have already set constraints of $\mathcal{O}(10^{-2})$. Therefore, we will focus on the sensitivity of CEvNS to NSI involving e and τ flavors. Figure 5.6 shows the allowed region for two different combinations of NSI parameters at a 90% confidence level [103] for CsI (magenta) and LAr (purple). The left panel shows the allowed values in the $(\varepsilon_{ee}^{dV}, \varepsilon_{\tau e}^{dV})$ parameter space. We can see that the LAr measurement gives more robust constraints and in this case we see an allowed region delimited by an outer and an inner circle rather than a filled disk as in the CsI result. We perform a similar analysis for the $(\varepsilon_{ee}^{dV}, \varepsilon_{ee}^{uV})$ parameter space. The results are shown in the right panel of the same figure, where we can see two independent bands for the LAr case, in contrast to the single wide one obtained with the CsI data. Again, the improvement is due to the better management of systematic uncertainties for the LAr detectors. From these results we see that there

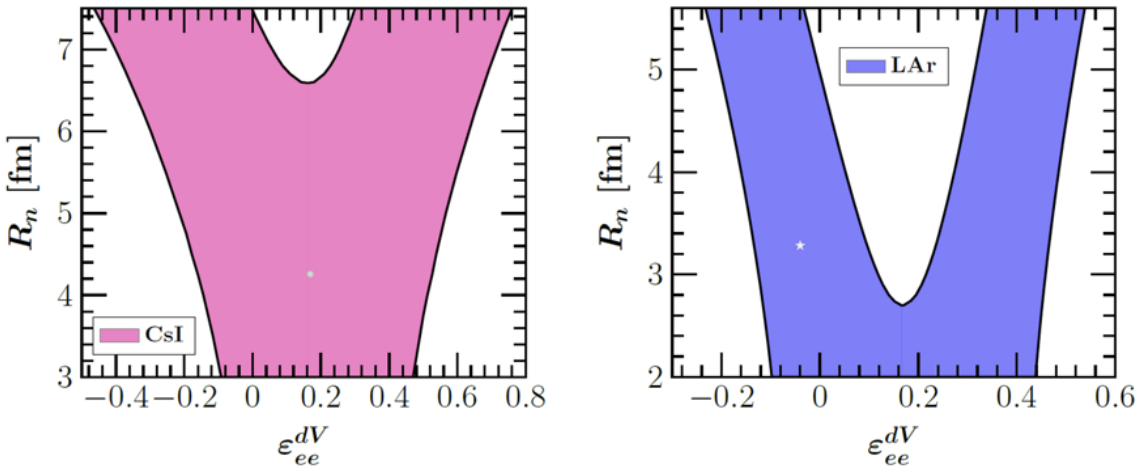

Figure 5.7: 90% C.L. allowed regions in the $(\varepsilon_{ee}^{dV}, R_n)$ parameter space for the analysis of the COHERENT data. Left panel shows the results for CsI and left panel for LAr [103]. The dot and the star indicate the best fit point for CsI and LAr, respectively.

are some degeneracies when we consider two NSI parameters at a time. In a further analysis, we will see how we can combine different future detectors in order to reduce (or even to break) these characteristic degeneracies.

At this point, we have already studied the sensitivity of the CEvNS process to SM and non-standard effects separately. Nevertheless, it is important to remark that the mismatch between the theoretical prediction and the experimental results in the two experimental observations can be due to either the presence of new physics, as well as to uncertainties in nuclear parameters. Hence, this interaction can open the window to new studies in both areas. Motivated by this, we can also perform a simultaneous analysis to constrain both the neutron rms radius and non-standard parameters at the same time. In other words, we can study the correlations between these parameters. Left panel in Fig. 5.7 shows the 90% confidence level region for the CsI detector in the $(\varepsilon_{ee}^{dV}, R_n)$ parameter space [105]. In order to get this region, we assumed a constant quenching factor as reported in Ref. [106] and shown in Fig 5.2. We can see that the obtained region is not symmetric, which again is a consequence of the mismatch between the experimental results and the theoretical prediction. Similarly, the right panel in Fig. 5.7 shows the corresponding results for the LAr detector at a 90% C.L. Again, we can not quantitatively compare the results between detectors because their target materials are of different nature and we expect them to have a different R_n. Nonetheless, we notice qualitatively similar results, the only difference being the value of R_n for which the degeneracy on the NSI is broken. In other words, the value of R_n

for which the allowed NSI values are separated in two different intervals. While for the LAr case we notice this for values around 2.6 fm, in the case of CsI the degeneracy is broken for values above 6.5 fm, a value that is not physically possible due to the expected size of the nucleus. Overall, what the results in Fig. 5.7 tell us is that, if from another experiment we can constrain one of the involved parameters alone, then we will have information about the other parameter because they are correlated. As we will see, CEvNS from nuclear reactor sources will be helpful for these analyses since, as we have mentioned, these neutrinos are on an energy regime where the effects of the nuclear form factors are not relevant for CEvNS.

Chapter 6

Expectations from future experiments

In the previous chapter, we used the results from the current measurements of CEvNS to constrain parameters like the weak mixing angle at low energies, the neutron rms radius, and NSI parameters. Currently, there are many other experiments that aim to get results from this process, each with different sources and different technologies. This has both theoretical and practical motivations. For instance, so far we only have measurements from two different target materials, which are not enough to see the characteristic N^2 dependence of the cross-section predicted by the SM (see Fig. 6.1). In addition, as we have studied, the process can be used to test different theoretical models and give a hint in the search for new physics. Regarding some applications, it has been suggested that once the CEvNS process is accurately characterized, it could be used for reactor monitoring, and to enhance nuclear security [107]. For neutrinos produced at spallation neutron sources, the most promising future experiments include the next generation detectors of the COHERENT collaboration at the SNS [108]. These include germanium detectors, a sodium iodide detector, and an upgrade of the current LAr detector to one ton of fiducial mass. Another promising experiments are those planned to run at the European Spallation Source (ESS) [109] once the facility initiates operations. As for the first half of 2022, the ESS is already under construction, and the suggested detectors include materials like cesium iodine, argon, germanium, xenon, and silicon.

In the case of neutrinos from reactor sources, the process of CEvNS has never been observed due to the very low recoil energy thresholds needed. However, a suggestive evidence of its first observation, by using a Ge detector, has been recently reported in Ref. [110]. In addition, collaborations like CONUS [111] and CONNIE [112] are still

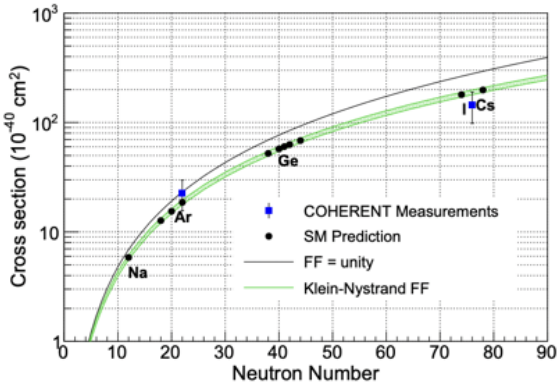

Figure 6.1: CEvNS total cross-section as a function of the number of neutrons, N, of the target material. Black line indicates a prediction when form factor is taken as unity and green line when form factor effects are considered. Black dots are the SM prediction and blue dots the current experimental measurements. Image taken from [101].

working to get this first measurement. One of the main advantages of using reactor neutrinos to measure CEvNS is that the energy regime of these neutrinos is such, that nuclear form factors do not play a significant role in the predicted number of events. However, the difficulty from these experiments relies on the fact that extremely low thresholds are needed to perform these measurements. This chapter is divided in three main sections. First, we focus on the COHERENT collaboration future detectors and we study the sensitivity that can be expected to constrain SM and NSI parameters. Then, we study how the data from future experiments that use SNS and reactor sources can be combined to give more robust constraints on certain parameters. Finally, we suggest a method that could be used to minimize the impact of systematic uncertainties by using an array of detectors of different isotopes. In this case, we also present the expected results when studying SM physics and NSI.

6.1 Future COHERENT experiments

In the following years, the COHERENT program will include a set of four detectors, each based on different materials and technologies capable of observing low-energy nuclear recoils; these include the current CsI[Na] scintillating crystal, the single-phase liquid argon detector, which will eventually have a fiducial mass of one ton, and two other experiments that are still under construction: a set of p-type point-contact Ge detectors, and an array of NaI crystals. Each detector will have a different expected threshold, baseline, and mass, all of which are summarized in Table 6.1 [97]. Following

the analysis used in the previous chapter, we now explore the sensitivity that these experiments can reach for different parameters.

6.1.1 Sensitivity to the weak mixing angle

As in the cases of CsI and LAr, we can also test the sensitivity of future COHERENT detectors to SM parameters. Specifically, we start by testing the weak mixing angle. Although the current estimates to this quantity from the recent measurements of CEvNS are not competitive, we insist on its importance because any deviation from its current accepted value can be a hint for new physics and future information from CEvNS may be relevant at very low energies. We will make the analysis by following the same procedure of minimizing the squared function given in Eq. (5.6). As we are now dealing with future experiments, we will need to make some assumptions for our χ^2 analysis, and from now on, we will consider the experimental measurement N^{exp} as that corresponding to the SM prediction.

The expected number of events, N^{th}, will be a function of $\sin^2\theta_W$, and is calculated through Eq. (5.5) by fixing all the other parameters of the theory. For the computation, we assume the same experimental running time as for the first measurement with CsI, which implies $N_{POT} = 1.76 \times 10^{23}$, and we set a source to detector distance for each case as indicated in Table 6.1. Since the experiments are still being characterized, in all cases we have considered an acceptance function given by a step function delimited by the expected threshold for each experiment [113], also given in Table 6.1. Regarding backgrounds, we have considered them to contribute with a 10% of the SM CEvNS prediction. The results are shown in Fig. 6.2, where we can see the expected allowed intervals at a 90% C.L. for Ge (left panel), Ar (central panel), and NaI (right panel). For each detector, we show four different results, each based on specific assumptions regarding systematic uncertainties for CEvNS (σ_α) and backgrounds (σ_β). We show the ideal case in which $\sigma_\alpha = \sigma_\beta = 0\%$, another with $\sigma_\alpha = 15\%$ and $\sigma_\beta = 10\%$, and

	T_{thres}	Baseline	Det. Tec.	Fid. Mass
^{133}Cs^{127}I	5 keV	19.3 m	Scintillator	14.6 kg
^{72}Ge	5 keV	22 m	HPGe PPC	10 kg
^{23}Na^{127}I	13 keV	28 m	Scintillator	2000 kg
^{40}Ar	20 keV	29 m	Liquid scintillator	1000 kg

Table 6.1: Current and future experimental setups of the COHERENT collaboration.

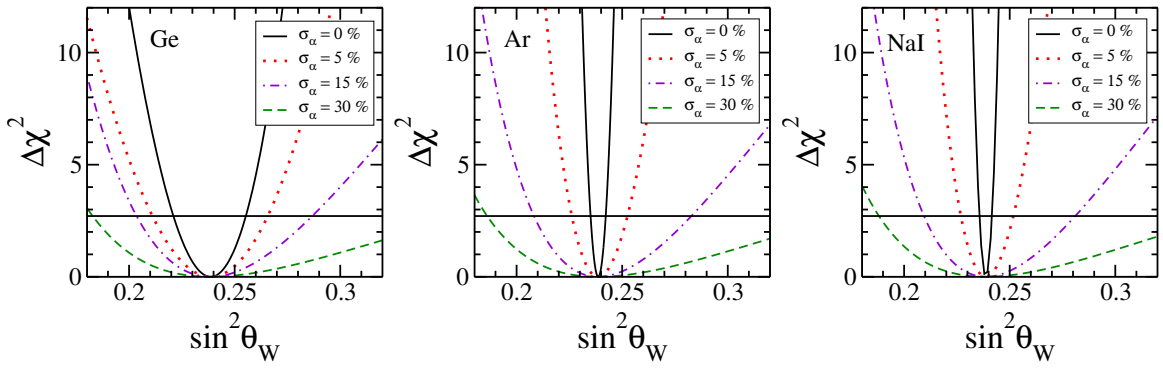

Figure 6.2: Expected sensitivity to $\sin^2\theta_W$ for the three future COHERRENT detectors: Ge (left panel), Argon (central panel), and NaI (right panel). The different curves are for a 100 % efficiency and no systematic errors (solid), for a systematic error of 15 % (dashed-dotted), and 30 % (dashed). Finally, the case of an efficiency of 50 % and 5% systematic error is also shown (dotted line) [113]. The horizontal line indicates the 90% C.L. sensitivity.

another with $\sigma_\alpha = 30\%$ and $\sigma_\beta = 10\%$, all of these cases assuming 100% of efficiency. To study the impact of the detectors efficiency in our results, we also show a case in which we assume a 50% of efficiency, while keeping the systematic uncertainties low, with $\sigma_\alpha = 5\%$ and $\sigma_\beta = 0\%$.

Although quite similar results, there are some notable differences when comparing the three panels shown in Fig. 6.2. We can see that the weak mixing angle is more constrained for the cases of LAr and NaI. The main reason is that the mass of these detectors is projected to be around two orders of magnitude larger than that of Ge, leading to a larger number of events, and thus, better statistics when considering the same experimental running time for all of the detectors. We can also explicitly recognize the importance of identifying and having the systematic errors under control, specially for the Ge detector, for which we also deal with low statistics and the restriction on the mixing angle value is wider than that from the other detectors.

6.1.2 Sensitivity to NSI parameters

We can also study the sensitivity that future detectors will have to physics beyond the SM through the NSI formalism. We start again by assuming only one of the NSI parameters in the cross-section to be different from zero at a time [113]. In particular, we will analyze the parameters ε_{ee}^{uV} and $\varepsilon_{\tau e}^{uV}$ under the same experimental assumptions used in the previous subsection for the study of the weak mixing angle. The results for $\varepsilon_{\tau e}^{uV}$, at a 90% C.L., are shown in Fig. 6.3 for Ge (left panel), LAr (central panel), and NaI (right panel). Again, for each case we show four different curves, each based on

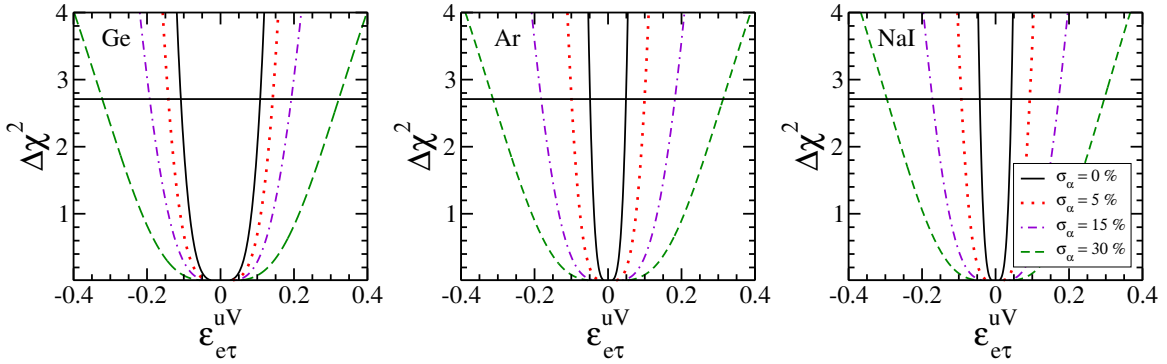

Figure 6.3: Expected sensitivity to flavor changing NSI for the three future COHERENT detectors: Ge (left panel), Ar (central panel), and NaI (right panel). We assume different combinations of efficiencies and systematic uncertainties as in Fig. 6.2 (see text for details) [113] The horizontal line indicates the 90% C.L. sensitivity.

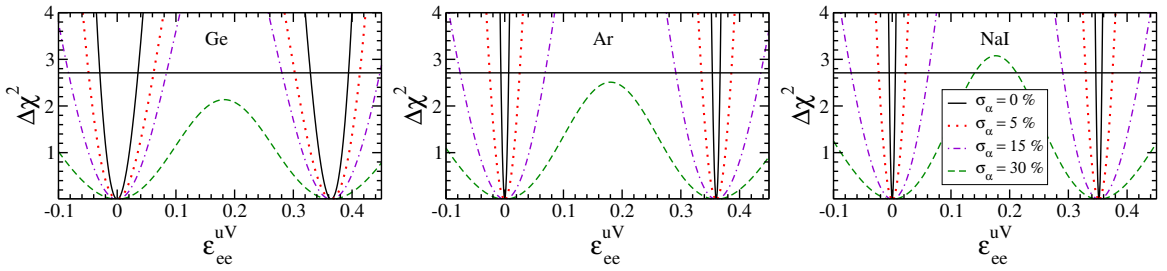

Figure 6.4: Expected sensitivity to non-universal NSI for the three future COHERENT detectors: Ge (left panel), Ar (central panel), and NaI (right panel). We assume different combinations of efficiencies and systematic uncertainties as in Fig. 6.2 (see text for details) [113]. The horizontal line indicates the 90% C.L. sensitivity.

specific assumptions regarding efficiency and systematic uncertainties just as in Fig. 6.2. Notice that, in contrast to the LAr results presented in chapter 5, in these cases we do not have a bump around zero. Instead, the minimum of the analyses are precisely located at zero. This is a consequence of assuming the experimental measurement to be the same as the SM prediction. Since the effect of the flavor-changing NSI is to contribute in a positive way to the expected number of events, then we can not have less events than those predicted by the SM, and then, we expect the minimum of the χ^2 function to be at a zero NSI value. Again, better constraints are obtained for NaI due to the better statistics that is expected for this detector because of its relatively large mass.

Regarding non-universal parameters, Fig. 6.4 shows the corresponding results for ε^{uV}_{ee} when considering Ge (left panel), Ar (central panel), and NaI (right panel) detectors. We can see that, in most of the cases, the parameters are constrained to be in two different intervals. The presence of two minima is a result of the linear and quadratic

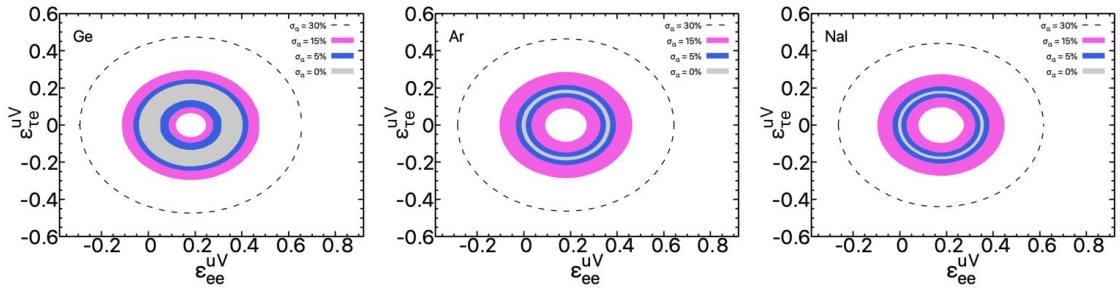

Figure 6.5: Expected sensitivity to NSI parameters at a 90% C. L. for the three future COHERENT detectors: Ge (left panel), Ar (central panel), and NaI (right panel). The different regions are for a 100 % efficiency and no systematic errors (gray), for a systematic error of 15 % (magenta), and 30 % (dashed contour). Finally, the case of an efficiency of 50 % and 5% systematic error is also shown (blue) [113].

dependence of the cross-section on the corresponding NSI parameter. We see that the expected constraints for both NSI parameters are competitive with the current values shown in Table 3.4.

As a final step, we can study the correlation between NSI by assuming both of the analyzed parameters to be different from zero at a time. The results are shown in Fig. 6.5 for the same configurations of systematic uncertainties as in the previous analysis. We see a degeneracy for these parameters that is not broken in the pessimistic case of $\sigma_\alpha = 30\%$, which corresponds to the region enclosed by a dashed contour. For all the other results, we see that the degeneracy is broken and the results can be expected to be better than those shown in the case of LAr and CsI measurements.

6.2 SNS and reactor experiments

In addition to spallation neutron sources, there are other experimental collaborations that aim to measure the CEvNS process by using reactors as a neutrino source. Among the main candidates we have CONUS [111], CONNIE [112], NUCLEUS [114], MINER [115], and RICOCHET [116]. An important progress on the detection mechanism has been achieved, but for now there is not a confirmed measurement. The main problem when dealing with reactor sources comes from the very low energy thresholds needed for the detection. Moreover, the quenching factor uncertainties at such thresholds are high, and the characterization of backgrounds is difficult. Nonetheless, we can study the implications that future reactor experiments can have within different physics scenarios. In this section, we show how the combination of experiments, that are different in nature (source and detection), could be used to study the interplay between NSI and nuclear

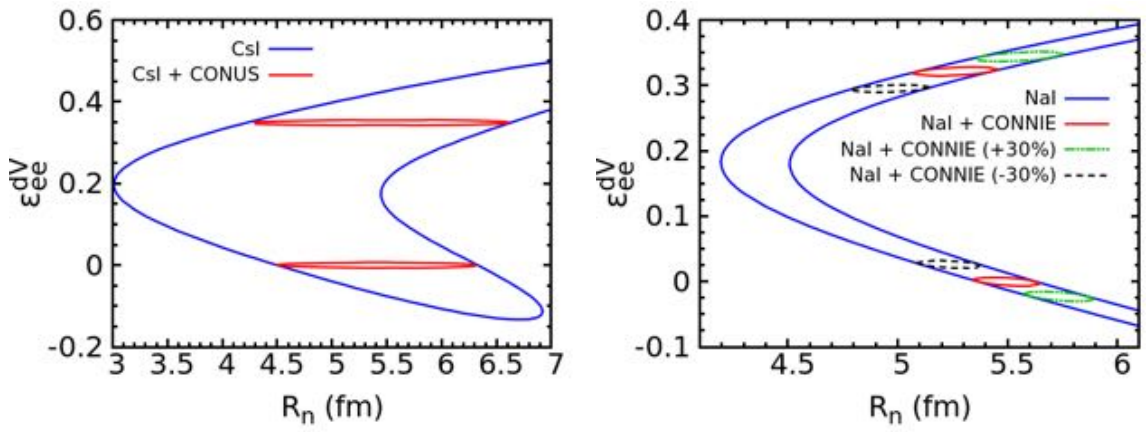

Figure 6.6: Left panel: Blue contour shows the 1σ level allowed region in the $(\epsilon_{ee}^{dV}, R_n)$ parameter space consistent with the CsI COHERENT data. The red contour shows the expected results when combining the CsI analysis with the expected sensitivity from the CONUS experiment. Right panel: Blue contour shows the expected sensitivity from an NaI detector at the SNS. The inner regions represents the combination of this experiment with the expected results from the CONNIE experiment [105].

physics parameters.

Let us first recall the results from section 5.2, specifically Fig. 5.7, where we have given constraints that are consistent with COHERENT data in the parameter space $(\varepsilon_{ee}^{dV}, R_n)$. We can see that the introduction of NSI induces a degeneracy on the parameter space that opens the possibility for nonphysical values of the neutron rms radius for Cs and I nuclei. By non-physical, we mean that the radius is too large (or too small) for what we expect by comparing with heavier (or lighter) nuclei for which these parameters are known. These effects are a consequence of the dependence of the cross-section on the nuclear distribution, which is not thoroughly understood, and which contributes as a major source of systematic uncertainties. Fortunately, the form factor sources of systematic errors can be avoided by using reactor neutrinos, for which the energy regime is such that we have $F_N^V(q^2) \to 1$ (see Fig. 3.11). This means that reactor neutrinos are not sensitive to nuclear information. Then, the analysis on NSI parameters from reactor sources, when combined with the SNS results, will help to remove some of the degeneracies present in the parameter space $(\varepsilon_{ee}^{dV}, R_n)$ [105].

For our analysis, we will study the expectations from future reactor neutrino ex-

	T_{thres}	Baseline	Z/N	Det. Tec.	Fid. Mass
CONNIE	28 eV	30 m	1.0	CCD (Si)	$0.1 - 1$ kg
CONUS	100 eV	10 m	0.79	HPGe	$4 - 100$ kg

Table 6.2: Experimental proposals to detect CEvNS from reactor neutrinos.

periments. In particular, we consider experiments with the characteristics of CONUS and CONNIE, which are listed in Table 6.2, and we assume a reactor antineutrino spectrum given by the Huber model. In Ref. [105], we have studied the sensitivity of these experiments to NSI parameters in the $(\varepsilon_{ee}^{dV}, \varepsilon_{ee}^{uV})$ parameter space by performing a χ^2 analysis as that in Eq. (5.6), by using the information in Table 6.2 to compute the expected number of events and using the SM prediction as the experimental measurement. Since there are no correlations between reactor experiments and the SNS, then we can combine the results by adding the two independent χ^2 functions. That is, we combine the results from the current CsI measurement presented in the previous section with the expectation from the future analyses using reactors. The results for the combination of a CONUS-like detector, and the CsI data, at a 1σ level, are shown in the left panel of Fig. 6.6. The blue contour shows the results of the CsI analysis alone, and the red contour shows the combined analysis. Notice that the allowed region has been significantly reduced, and that we have recovered mainly physical values of R_n when allowing for the presence of new physics through NSI. Our analysis can be extended to other combinations of future experiments. For instance, we consider the case of CONNIE as a reactor anti-neutrino experiment, in combination with the future NaI detector at the SNS, which contains iodine nuclei in the same rate as the CsI detector. The results, at a 1σ level, are shown in the right panel of Fig. 6.6, where the blue contour corresponds to the NaI detector alone, and the red contour shows the results for the combined analysis.

For our last futuristic combination, we have the freedom to study the impact on the parameter space of an hypothetical scenario in which one of the experiments reports a measurement that is significantly deviated from the SM prediction. For instance, in Fig. 6.6 we also show the impact that a measurement 30% above (green line), and 30% below (dashed line) the SM prediction from the CONNIE experiment would have in our results. This assumption is only illustrative and can be interpreted in the following manner: a reactor neutrino experimental measurement that significantly differs from the SM prediction would result in a displacement of the central value of the χ^2 analysis in the parameter space, but with the width of the allowed region unchanged. If in a reactor experiment it is measured an excess above the SM prediction, then the NSI contribution would be responsible for this excess, and for the data to be consistent with the SNS result, we would need larger values of the neutron rms radius. In contrast, when the measured number of events in the reactor experiment is significantly lower than the SM prediction, the neutron radius would need lower values to compensate the observed deficit in a reactor experiment. This analysis illustrates the interplay that

we have between the measurement of CEvNS in reactors and SNS experiments when exploring the effects of nuclear physics and NSI together.

6.3 Use of isotopically enriched detectors

Currently, the status of CEvNS reduces to two experiments that have successfully achieved a measurement of this process. For the more skeptical, these measurements would not be enough to corroborate the most characteristic feature of CEvNS, which at leading order, is the quadratic dependence of its cross-section on the number of neutrons, N, of the scatter material. Unfortunately, with current data it is not sufficient to observe this behavior since two measurements are not enough to unambiguously establish a correlation between the cross-section and N^2. Then, a third experiment with another target material that differs in the number of neutrons from the previous two is needed. Indeed, there are many experimental collaborations that aim to achieve another measurement by using detection technologies that include xenon, germanium, and silicon nuclei, among others. The main issue with this approach of using materials that are so different in nature is that systematic uncertainties are different for each detector, and there are no correlations between them. Recently, several advances have been made to have these uncertainties under control but, eventually, this may hide the effect of the quadratic dependence that we want to see.

Rather than using detectors of different materials, in this section we propose a feasible low time-scale experiment that could improve the CEvNS accuracy in the near future with the help of a detectors array of the same element, but different isotopes, taking data at the same time [117]. We show in Fig. 6.7 a graphical sketch that illustrates our experimental proposal, where we have a neutrino source, and three detectors of different isotopes located at the same distance from the source. It is true that the setup can be generalized to a number of detectors as large as the different isotopes, but three are enough to illustrate our point. The idea is to set the three detectors simultaneously, all with the same fiducial mass, and to compare the measured relative number of events between detectors after a certain amount of time. Under these conditions, any variation on the neutrino flux through the running time of the experiment will be common to all detectors and, more importantly, there will be a strong correlation between systematic errors, which can be of different nature. For instance, systematic uncertainties can be originated from quenching and form factors of target materials, as well as from the neutrino flux itself, having an impact on the relative expected number of events between detectors.

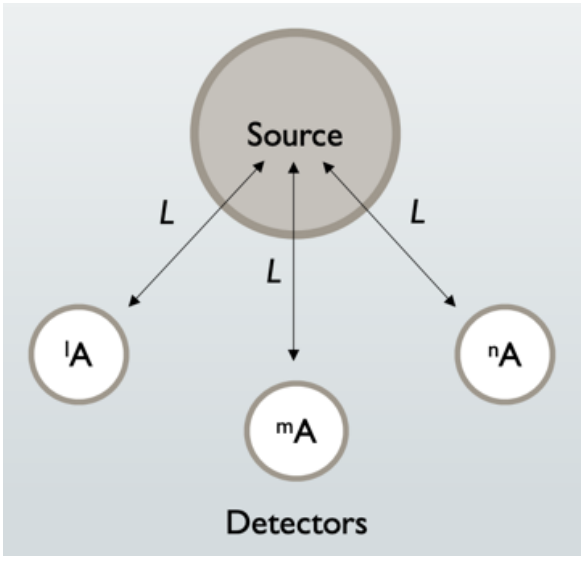

Figure 6.7: Array of detectors of the same element A, but different isotopes, located at the same distance, L, from a neutrino source.

For illustration, we perform our computations assuming a set of Ge detectors, which is an ideal candidate since it has five known stable isotopes: ^{70}Ge, ^{72}Ge, ^{73}Ge, ^{74}Ge, and ^{76}Ge. Certainly, the analysis can be extended to other target materials that also have stable isotopes such as silicon and nickel. However, germanium seems to be the most feasible option since the technology of enriching Ge detectors to a desired isotope has seen a lot of progress in recent years. In fact, highly enriched ^{76}Ge detectors have been used for neutrino physics in the searches of processes like neutrinoless double beta decay [118]. We will compare the results for two different neutrino sources: a π-DAR source like the SNS, and a hypothetical anti-neutrino reactor flux characterized by the Huber model above the 2 MeV neutrino energy threshold.

Before getting into the analysis, we discuss some kinematic features that can be exploited in our further computations when considering this kind of array. As we have pointed out, the CEvNS cross-section has a characteristic dependence on the quadratic number of neutrons of the target material. Then, it can be expected that an isotope with more neutrons will measure a larger number of events than one which has less. However, due to kinematic effects, this is only true if we consider the whole spectrum of kinetic recoil energy, which is difficult for actual detectors due to their different thresholds and efficiencies. For instance, Fig. 6.8 shows the expected differential rate as a function of the recoil energy, T, for ^{70}Ge and ^{76}Ge, where we assumed a one year data taking ($N_{POT} = 1.5 \times 10^{23}$) and a 100% efficiency, for a 10 kg fiducial mass in the case of an SNS source (left panel) and 1 kg for reactor neutrinos (right panel). In both

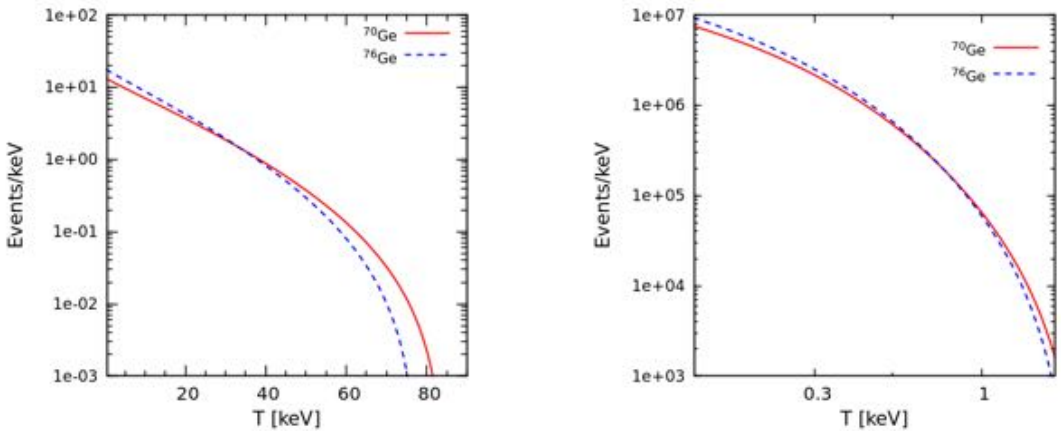

Figure 6.8: Differential event rate for Ge isotopes assuming one year data taking for SNS neutrinos (left panel) and reactor antineutrinos (right panel).

panels, there is a point close to the tail of the spectrum where the differential rates of the different isotopes intercept, which is expected since, the heavier the nucleus, the lower kinetic energy limit it can reach. In consequence, there will be recoil energy regions for which, despite the N^2 dependence, a target with less neutrons would measure more events. As we will see, this does not have a significant impact for an experiment with SNS neutrinos, but will be important for a nuclear reactor source experiment, where, experimentally, very low energy thresholds are not easily achieved, and we can mainly study the high energy part of the spectrum.

In the following sections, we introduce some of the applications that such an experimental array with three detectors can have. Since we are dealing with stable detector materials that only differ in the number of neutrons, then it is expected that there will be correlations between the different systematic uncertainties, which needs to be considered in our different analyses. We will do this by following the covariant matrix approach, where, instead of using Eq. (5.6), we minimize the squared function

$$\chi^2 = \sum_{ij} (N_i^{theo} - N_i^{exp})[\sigma_{ij}^2]^{-1}(N_j^{theo} - N_j^{exp}), \tag{6.1}$$

where σ_{ij}^2 is the covariant matrix. The indexes i, j run over the different detectors used during the analysis, and the total number of events is calculated in the same way as in our previous analyses. We will use this method to explore the sensitivity of our proposed experiment to different parameters that involve SM and NSI parameters, assuming in all cases the experimental measurement to be the SM prediction.

6.3.1 Testing the N^2 dependence

We begin by using the proposed array to test the quadratic dependence of the cross-section on the number of neutrons. From now, we consider an array of three different isotopes, $^{\ell}$Ge, ^{m}Ge, and ^{n}Ge, with $\ell \neq m \neq n$ indicating the total number of nucleons. To test the sensitivity to the quadratic dependence on the number of neutrons, we now express the expected number of events for each detector in the form

$$\begin{aligned} N_i^{th} = N_i'^2 \left(g_V^{n^2} N_D \frac{G_F^2 M}{\pi} \int_T A(T) dT \int_{E_{min}}^{E_{Max}} dE \left[1 - \frac{MT}{2E_\nu^2} \right] \phi(E) F_N^2(q^2) \right) \\ + N_i' \left(Z g_V^p g_V^n N_D \frac{G_F^2 M}{\pi} \int_T A(T) dT \int_{E_{min}}^{E_{Max}} dE \left[1 - \frac{MT}{2E_\nu^2} \right] \phi(E) F_Z(q^2) F_N(q^2) \right) \\ + Z^2 g_V^{p^2} N_D \frac{G_F^2 M}{\pi} \int_T A(T) dT \int_{E_{min}}^{E_{Max}} dE \left[1 - \frac{MT}{2E_\nu^2} \right] \phi(E) F_Z^2(q^2), \end{aligned} \tag{6.2}$$

where we use the index $i = \ell, m, n$ to distinguish between the different detectors. Notice that Eq. (6.2) is the same as Eq. (5.5), but we have explicitly expanded the SM cross-section, and we have also replaced the number of neutrons for the ith detector, N_i, by a factor N_i' that will quantify the deviation of an experimental measurement from the expected quadratic dependence. For a given neutrino source, we can now calculate the expected number of events N_i^{th} as a function of the N_i' factor for each detector, and we can perform a χ^2 analysis using Eq. (6.1), where correlations between detectors are considered. For a general analysis, we assume that the systematic uncertainties will be dominated by two different sources, which we denote as A and B, each with a contribution to the total systematic uncertainty of σ_i^A, and σ_i^B, respectively. These can refer to uncertainties coming, for instance, from quenching factors, form factors, or the neutrino flux itself, among others. Since we are considering three different detectors, and two main sources of systematic errors, the covariance matrix has the form

$$\sigma^2 = \begin{pmatrix} \sigma_l^{stat\,2} + \sigma_l^{A\,2} + \sigma_l^{B\,2} & \sigma_l^A \sigma_m^A + \sigma_l^B \sigma_m^B & \sigma_l^A \sigma_n^A + \sigma_l^B \sigma_n^B \\ \sigma_l^A \sigma_m^A + \sigma_l^B \sigma_m^B & \sigma_m^{stat\,2} + \sigma_m^{A\,2} + \sigma_m^{B\,2} & \sigma_m^A \sigma_n^A + \sigma_m^B \sigma_n^B \\ \sigma_l^A \sigma_n^A + \sigma_l^B \sigma_n^B & \sigma_m^A \sigma_n^A + \sigma_m^B \sigma_n^B & \sigma_n^{stat\,2} + \sigma_n^{A\,2} + \sigma_n^{B\,2} \end{pmatrix}, \tag{6.3}$$

with σ_i^{stat} the statistical error of the ith detector. When no correlations are present, then the non-diagonal matrix elements are set to zero. However, for this proposed array we expect a strong correlation between systematic uncertainties since we are dealing with detectors from stable nuclei that only differ in the number of neutrons. Calculating the inverse of Eq. (6.3), and substituting in Eq. (6.1), we can test the sensitivity of

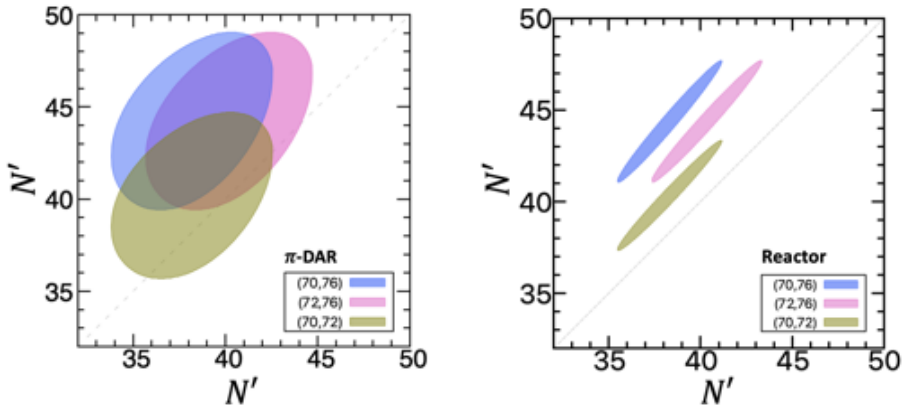

Figure 6.9: Allowed values of the N' factor at a 90% C. L. , for the three different detectors using neutrinos from SNS (left panel) and reactor (right panel) sources. We compare the results by pairs, labeling each detector by the number of nucleons of the corresponding isotope. The contours show the different projections after marginalizing the information over the third detector and the heavier isotope is shown on the vertical axis. [117].

such an array to the quadratic dependence on the number of neutrons. To do so, we vary the $N_i^{'}$ factors for each of the isotopes and compare with the experimental result, which we assume as the SM prediction, obtained when the $N_i^{'}$ factors coincide with the corresponding number of neutrons. We perform the analysis by using neutrinos from both SNS and reactor sources.

For the case of an SNS source, we take ^{70}Ge, ^{72}Ge, and ^{76}Ge detectors, each with a mass of 10 kg, and a one year data taking. Regarding systematic uncertainties, the main contributions for current SNS experiments come from quenching and form factors. As discussed in [96], several progress has been made for CsI detection technology such that these uncertainties have been lowered within 5%. Similar advances are expected in the case of Ge detectors, and we consider a realistic case in which both form factors and quenching factors have a contribution of 5% to systematic uncertainties. In addition, we consider a scenario in which background measurements contribute to the statistical error with 10% of the SM prediction. The results assuming a nuclear recoil energy region from 5 to 30 keV are shown in left panel of Fig. 6.9, where we show the allowed three different projections, at a 90% C.L., that result after marginalizing the information of the missing component on each panel. For instance, the green region shows the allowed values of N' for ^{70}Ge (x-axis) and ^{72}Ge (y-axis) that are compatible with a quadratic dependence on the number of neutrons at a 90% C.L., after marginalizing over ^{76}Ge. The allowed region corresponds to an ellipse that is separated from the diagonal according to the ratio between the isotopes that are compared, being the major and minor axis determined by the systematic uncertainties. Similar regions are

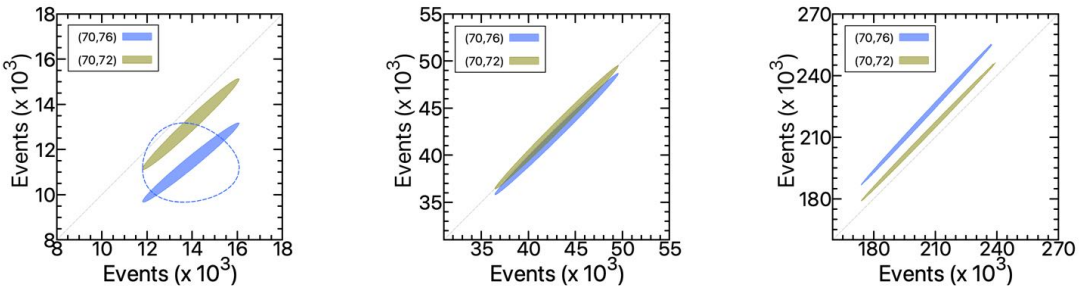

Figure 6.10: Expected number of events, for the three different Ge detectors, consistent with an N^2 dependence of the CEvNS cross-section at a 90% C.L. We compare the results by pairs, labeling each detector by the number of nucleons of the corresponding isotope. The rate from the heavier isotope is shown on the vertical axis. We assume a one year data taking, using a reactor source, for three different thresholds: 1 - 2 keV (left), 0.7 - 1 keV (central), and 0.4 -0.8 keV (right). For reference, the dashed contour shows the results for the pair (70,76) when no correlations between detectors are considered [117].

shown in blue and magenta for the pairs (^{70}Ge, ^{76}Ge) and (^{72}Ge, ^{76}Ge), respectively. Since the sensitivity of the array is limited, then we can see that in this case, the ellipses are not well separated.

We now analyze the case of nuclear reactors as a neutrino source, for which we consider the same Ge isotopes, with a mass of 1 kg each, and a recoil energy range from 1 to 2 keV, which is above the crossing point of the spectra shown in Fig. 6.8. Here the main contributions to systematic uncertainties are considered from quenching factors and the neutrino flux, each contributing with a 5%. We show the results of the analyses in the right panel of Fig. 6.9, at a 90% C.L., and with the same color code used for the SNS case. Again, we can see elliptical regions for which the minor and major axes are governed by systematic and statistical uncertainties. In contrast to the SNS case, and because of the very large statistics, here we can see three regions that are completely separated from one another, a feature that we can exploit for a more complete analysis. Clearly, the ultimate goal of an experiment can not be the determination of the parameters $N_i^{'}$ since, after all, these are not physical observables. Instead, we want to examine whether a counting experiment like this would measure a number of events that is consistent with the quadratic dependence on the number of neutrons, of the CEvNS cross-section, by comparing the relative measurements between detectors. Indeed, our previous analysis can be mapped into regions that show this number of events. Left panel in Fig. 6.10 shows the number of events obtained by varying the parameters $N_i^{'}$ for reactor neutrinos as in Fig. 6.9. For clarity we only show the corresponding blue and green regions. From this figure, we conclude that a relative measurement between detectors, that is consistent at a 90% C. L. with a

cross-section that goes as N^2, will fall on each of the well separated contour regions. We can explicitly see that, even if the quadratic dependence in the number of neutrons of the cross-section holds, we expect to have more events from the lighter isotope in the analyzed recoil energy region. For comparison, we also show as a dashed contour, the case corresponding to the blue region when no correlations are taken into account. We conclude that the effects of the correlations allow us to have these well separated regions.

So far, we have used for the analysis a conservative case in which we assume a threshold of 1 keV for the nuclear recoil energy. As a next step, and to see the quadratic dependence effects, we can consider a more optimistic case in which we assume a lower threshold and perform the same analysis from this lower threshold to 2 keV. In contrast, we can get more information by exploiting the shape of the recoil energy spectrum discussed above, and computing the predicted number of events in convenient regions of this spectrum. We choose the intermediate region from 0.7 to 1 keV, and the very low energy region that goes from 0.4 to 0.8 kev. The results are shown in the central and right panels of Fig. 6.10, respectively. For the intermediate region we see that the ellipses come together, which is expected since we are in a neighborhood of the intersection point of the differential rates from the isotopes (see Fig. 6.8), which means that the three detectors will measure a very similar number of events. In the case of the low energy region we see that the order of the ellipses is now inverted with respect to the high energy region counterpart, which means that in this region, the quadratic dependence in the number of neutrons becomes dominant. This comparison at different recoil energy ranges provides a clear signature of the SM CEvNS cross-section by taking advantage of systematic correlations, which can not be achieved when using different detectors.

6.3.2 Neutron rms radius

The proposed experiment can also be used to study other parameters, with different sensitivities depending on the neutrino source. To illustrate this, we study the effect of systematic correlations in the determination of the neutron rms radius of the germanium isotopes, which is only accessible for SNS neutrinos. This analysis will be important not only for the field of high energy and nuclear physics, but also for some areas like in Dark Matter (DM) searches, where Ge detectors are widely used. For instance, a correct characterization of these detectors is needed for a complete understanding of backgrounds that constitute the so called neutrino floor [119]. The results for the corresponding analyses, under the same assumptions as in the previous SNS scenario,

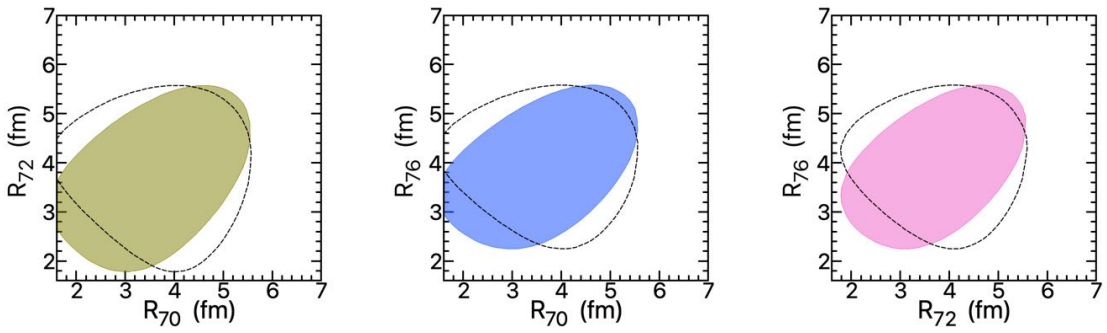

Figure 6.11: Allowed projections at a 90% C. L. for the neutron rms radius of the three Ge isotopes. Colored regions show the results when correlations between detectors are considered. For reference, the regions enclosed by dashed contours show the case when no correlations are considered [117].

are shown in the three panels of Fig. 6.11, where we display the results by pairs (at a 90% C. L.), after marginalizing the information from the detector that is not shown. We can see the pairs (^{70}Ge, ^{72}Ge) , (^{70}Ge, ^{76}Ge), and (^{72}Ge, ^{76}Ge) in the left, central, and right panels, respectively. For comparison, we also show the projection corresponding to the case where no correlations are considered. Although the sensitivity is not the best, the effects of the correlations are present, and the resulting contours can be reduced by having more statistics, which can be achieved either with a larger fiducial mass, or by means of a larger running time of the experiments.

6.3.3 NSI

We also discuss on the applicability of the intended experiment for the study of NSI by showing how this approach can help to remove typical degeneracies that appear when we introduce new physics scenarios. An example of interest is that of the degeneracy for the weak mixing angle value. For the analysis we will assume nuclear reactors as a neutrino source under the same assumptions as when we studied the N^2 dependence of the cross-section. The results of the χ^2 analysis when varying the SM weak mixing angle and the non-universal parameter ε_{ee}^{dV} are shown in the left chart of Fig. 6.12, where we have considered the contribution from the two main sources of systematic errors as 5% each. Dashed contours represent the results when systematic correlations are not considered, and we can see a clear degeneracy in both parameters under study. However, this degeneracy can be reduced by introducing the correlation effects between systematic uncertainties. These are illustrated by colored regions in the same figure, where we display the results for the three different recoil energy regions used to test the N^2 dependence of the SM cross-section. The magenta, blue and gray regions correspond

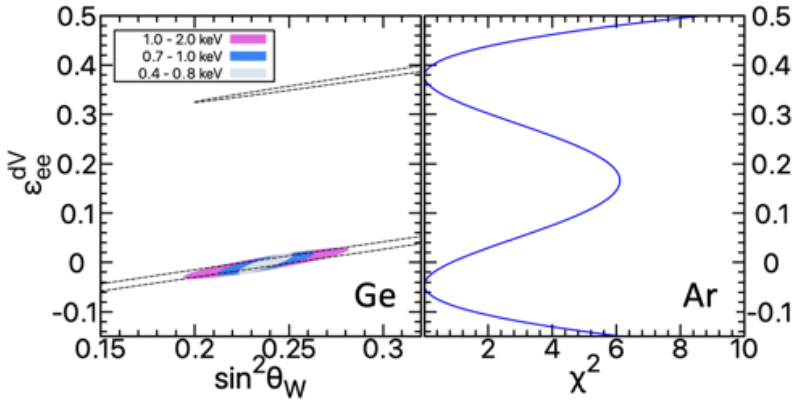

Figure 6.12: Allowed values at a 90% C.L. in the $(\sin^2\theta_W, \varepsilon_{ee}^{dV})$ parameter space for an array of three Ge detectors of different isotopes. Colored regions indicate the results when correlations between detectors are considered for three different nuclear recoil energy thresholds: 1 - 2 keV (magenta), 0.7 - 1 keV (blue), and 0.4 - 0.8 keV (gray). We show between dashed contours the result when no correlations are considered for 1 - 2 keV [117]. For reference we also show the current limits obtained from the LAr measurement when analyzing the NSI for a fixed value of $\sin^2\theta_W$ [103].

to 0.4 keV - 0.8 keV, 0.7 keV - 1 keV, and 1 keV - 2 keV, respectively. Notice that the upper band is removed in the three cases, making clear the advantage of this approach when studying this kind of degeneracies. For comparison, we show in the right chart the current result of the analysis for the LAr detector when only varying the NSI parameter while fixing the weak mixing angle to the standard best fit value at low energies. Notice that in this analysis the degeneracy on the NSI parameter is also present, meaning that with current data we can not restrict the value of ε_{ee}^{dV} around a single value.

To end this section, we explore the case when we study two NSI parameters at a time, where we can also use our method to break some degeneracies. The results of the analysis are shown in Fig. 6.13 for the case of the the parameter space $(\varepsilon_{ee}^{dV}, \varepsilon_{\tau e}^{dV})$. Again, the region between dashed contours represent the case where no systematic correlations are considered, giving as a result the characteristic ring found in many analyses for the specific case of these NSI parameters. In contrast, colored regions represent the correlated case according to the same color code as in the previous analysis. In the remaining charts we show the current status from the LAr data when varying only one of the NSI parameters. When comparing, we see that our proposed method can help to remove the degeneracy present in the case of ε_{ee}^{dV} around ≈ 0.38.

For all of our previous analyses, we assumed a 5% contribution from each of the dominant systematic uncertainties. This was motivated by the progress that the COHERENT collaboration has made for other detection technologies like in the case of CsI. In Ref. [117] we have also studied the more pessimistic case in which the main

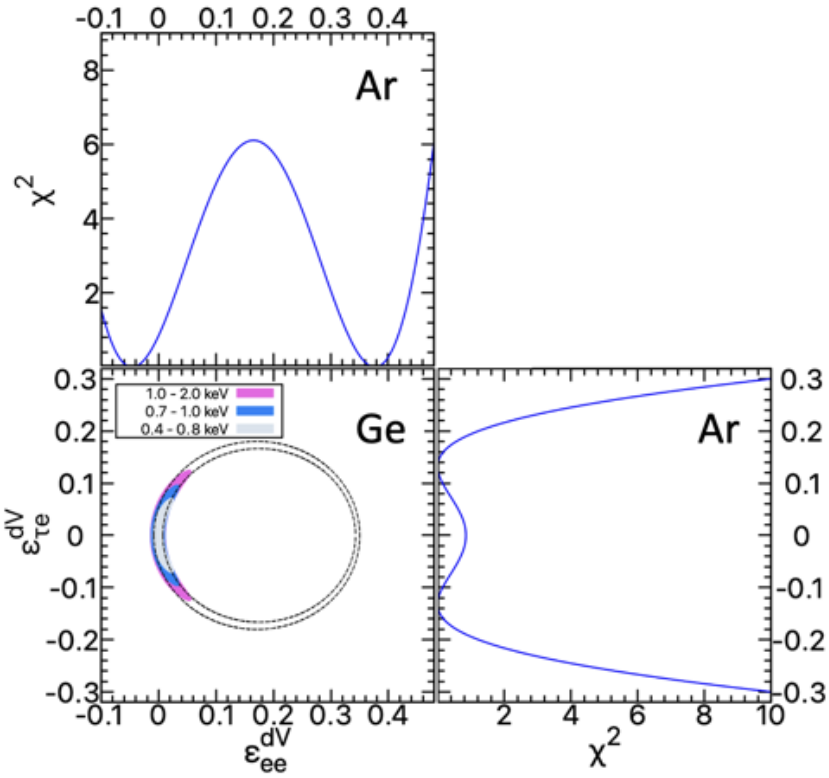

Figure 6.13: Allowed NSI values at a 90% C.L. for an array of three Ge detectors of different isotopes. Colored regions indicate the results when correlations between detectors are considered for three different nuclear recoil energy thresholds: 1 - 2 keV (magenta), 0.7 - 1 keV (blue), and 0.4 - 0.8 keV (gray). We show between dashed contours the result when no correlations are considered for 1 - 2 keV [117]. For reference we also show the current limits obtained from the LAr measurement when analyzing one of the parameters at a time [103].

systematic contributions are of 25% and 10%. Qualitatively the results are the same as presented here, the only difference being that the obtained regions were a little less constrained but the effects of the correlations are still present and they still have a significant impact on the results.

Chapter 7

Neutrino electromagnetic properties

After discussing the general formalism of NSI, we now focus on neutrino electromagnetic interactions. These interactions can be present when considering theories on which neutrinos are massive and, in general, can not be described through NSI. In this chapter, we mainly discuss the theory and phenomenology of what we call the neutrino magnetic moment. In particular, we will focus on the minimal extension of the SM where only three massive neutrino states are considered. However, as we have seen from the discussion in section 3.5, the symmetries of the SM allow for a more general case in which N right-handed neutrinos, and hence N massive states, are introduced.

7.1 Electromagnetic form factors

In the SM, the interaction of a charged fermion, f, with the electromagnetic field, A^μ, is described through the Hamiltonian:

$$H_{em} = q\bar{f}\gamma_\mu f A^\mu, \tag{7.1}$$

where q is the fermion charge. Within the SM, an interaction of the form in Eq. (7.1) is not possible for neutrinos because they have no electric charge. However, when right-handed neutrino states are introduced, an electromagnetic coupling is possible for them at quantum loop levels. In this case, the interaction of a massive neutrino with the photon can be described through an effective matrix operator Λ_μ such that

$$H^\nu_{em} = \sum_{k,j=1}^{3} \overline{\nu_k}\Lambda^{kj}_\mu \nu_j A^\mu, \tag{7.2}$$

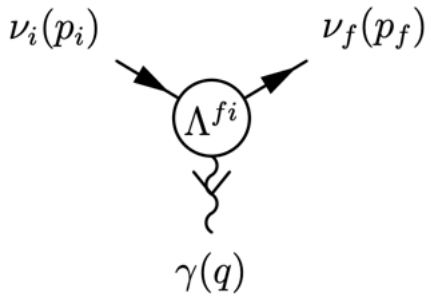

Figure 7.1: Feynman diagram representing the coupling of a neutrino with the electromagnetic field. The bubble in the diagram accounts for quantum loop effects responsible of the interaction.

where ν_i denotes massive states. Notice that, in general, Eq. (7.2) allows for transitions between different massive states, so the states before and after the interaction can be different. Loop effects are represented by the bubble in the Feynman diagram of Fig. 7.1. In general, the matrix operator Λ_μ must respect Lorentz symmetries and the electromagnetic current gauge invariance. Then, the most general form of Λ_μ, consistent with these symmetries, can be parametrized through four form factor matrices F_Ω [120]:

$$\Lambda_\mu^{fi} = \left(\gamma_\mu - q_\mu \not{q}/q^2\right)\left(\mathrm{F}_{\mathrm{Q}}^{fi}(q^2) + \mathrm{F}_{\mathrm{A}}^{fi}(q^2)q^2\gamma_5 - i\sigma_{\mu\nu}q^\nu\left[\mathrm{F}_{\mathrm{M}}^{fi}(q^2) + i\mathrm{F}_{\mathrm{E}}^{fi}(q^2)\gamma_5\right]\right), \quad (7.3)$$

where $\mathrm{F_Q}$, $\mathrm{F_A}$, $\mathrm{F_M}$, and $\mathrm{F_E}$ are 3×3 matrices in the massive neutrino states space. When $q^2 = 0$, the electromagnetic form factors can be identified as the neutrino charge, the magnetic dipole moment, the electric dipole moment, and the anapole moment, respectively. This can be done by taking the classical limit of the different operators and identifying the corresponding Hamiltonian with the associated physical quantity in this limit [121]. In the literature, it is common to denote the magnetic and the electric dipole moments as $\mu \equiv \mathrm{F}_M(0)$ and $\epsilon \equiv \mathrm{F}_E(0)$, respectively. On the other hand, while in the SM neutrinos have no charge, there are many extensions where neutrinos acquire a milicharge, and in general, $\mathrm{F_Q}(q^2) \neq 0$ [122]. Notice that the form factors introduced in Eq. (7.3) are different in nature from those used in the CEvNS cross-section. Here the form factors parametrize information of higher orders in scattering theory, while the form factors in CEvNS contain information of the internal structure of the nucleus. Also, it is important to insist on the fact that, as fundamental particles, the origin of electromagnetic properties of neutrinos comes from quantum loop effects. This is exactly the same origin as, for instance, the magnetic moment of the electron

and muon, and it is different from the magnetic moment origin for composite particles like neutrons, for which electric and magnetic form factors are a consequence of their internal quark structure.

The properties of the form factor matrices are different depending on the neutrino mass nature. For example, in the case of Dirac neutrinos we have [122]

$$\mathrm{F}_\Omega = \mathrm{F}_\Omega^\dagger \qquad (\Omega = Q, M, E, A), \tag{7.4}$$

which means that diagonal moments are real. For the corresponding anti-neutrinos, the form factors are denoted as $\overline{\mathrm{F}}_\Omega$, and they can be expressed in terms of the neutrino form factors [122]:

$$\overline{\mathrm{F}}_\Omega = -\mathrm{F}_\Omega^* \qquad (\Omega = Q, M, E) \ , \tag{7.5}$$

$$\overline{\mathrm{F}}_\mathrm{A} = \mathrm{F}_\mathrm{A}^* \ ,$$

which means that, for diagonal moments, the theoretical neutrino charge, as well as the electric and magnetic moments have the same strength but opposite sign.

For the case of Majorana neutrinos, particle and antiparticle states are the same and the degrees of freedom are reduced so, by equating Eqs. (7.4) and (7.5), we conclude that in this case

$$\mathrm{F}_\Omega = -\mathrm{F}_\Omega^T \qquad (\Omega = Q, M, E) \ , \tag{7.6}$$

$$\mathrm{F}_\mathrm{A} = \mathrm{F}_\mathrm{A}^T.$$

We see that for Majorana neutrinos, the charge, dipole electric, and dipole magnetic form factors are anti-symmetric matrices, which means that diagonal moments are zero. In contrast, the anapole moment matrix is symmetric and the diagonal moments are constrained to be real. Here we will focus on the phenomenology of magnetic and electric dipole moments, which interaction form can not be directly translated into the NSI formalism presented in the previous section. The cases of electric charge and anapole moments have been widely studied in Ref. [123].

7.2 Neutrino magnetic moment

From the above discussion we see that, by considering electromagnetic properties of neutrinos, we are now introducing a huge number of free parameters to the theory. This can be seen from Eq. (7.3), where each matrix element is in general a complex number described by a modulus and a phase. The good news are that not all the parameters are independent. In addition, for the particular case of the electric and magnetic dipole

moments we can reduce all these parameters to a single effective coupling, which can be studied in a phenomenological approach.

As shown on appendix A, in the presence of electric and magnetic dipole moments, the differential cross-section for neutrino-electron scattering can be parametrized in terms of one single coupling μ_{ν_l}:

$$\frac{d\sigma_{\mu_{\nu_\ell}}}{dT} = \frac{\pi\alpha^2\,\mu_{\nu_l}^2}{m_e^2}\left(\frac{1}{T} - \frac{1}{E_\nu}\right) , \tag{7.7}$$

where α is the fine structure constant. The quantity μ_{ν_l}, parametrized in units of the Bohr magneton, μ_B, is called the *effective neutrino magnetic moment,* and it has been widely studied from a phenomenological and experimental point of view. In terms of the fundamental parameters, the expression for μ_{ν_l} is different depending on the neutrino source, and hence the sub-index l in the notation. In fact, from Appendix A we have [122]

$$\mu_{\nu_l}^2 = \sum_j \left| \sum_k U_{lk}^* e^{-i\Delta m_{kj}^2 L/2E_\nu} \lambda_{jk}^{'} \right|^2 , \tag{7.8}$$

where we have used the notation $\lambda_{ij}^{'} = \mu_{ij} - i\epsilon_{ij}$. The matrix λ' is usually called the neutrino magnetic moment matrix. However, notice that it contains information of both magnetic and electric dipole moments. The corresponding effective magnetic moment for anti-neutrinos can be obtained by taking the complex conjugate of the exponential in Eq. (7.8) [122]. We summarize in Table 7.1 the current experimental limits for μ_{ν_l}, which have been obtained through accelerator, reactor, and solar neutrino sources.

The effective coupling μ_{ν_l} in Eq. (7.8) has been obtained assuming neutrino massive states (see appendix A). Then, the operator $\lambda^{'}$ in the same equation is written in the mass basis. However, it is sometimes useful to express the magnetic moment operator, and hence the effective coupling, in the flavor basis. The transformation rule between mass and flavor basis for $\lambda^{'}$ can be obtained from the interaction Hamiltonian when rotating the neutrino fields, and we have [124]

$$\lambda^{'} = U^T \lambda U, \tag{7.9}$$

where λ is the magnetic moment matrix in the flavor basis. In the following sections, we study the relationship between the effective coupling and the fundamental parameters for the specific cases of short baseline (SBL) and solar neutrinos, in the two different bases, for both Majorana and Dirac neutrinos.

Considering that the maximum squared mass difference of neutrinos is very small,

Type	Experiment	μ_{ν_l}	90% C.L.	Reference
Reactor	GEMMA	μ_{ν_e}	$< 2.9 \times 10^{-11}$	[125]
Accelerator	LSND	μ_{ν_μ}	$< 6.8 \times 10^{-10}$	[126]
Accelerator	DONUT	μ_{ν_τ}	$< 3.9 \times 10^{-7}$	[127]
Solar	Borexino	$\mu_{\nu_{e,\mathrm{sol}}}$	$< 2.8 \times 10^{-11}$	[128]
Solar	XENON1T	$\mu_{\nu_{e,\mathrm{sol}}}$	(1.4, 2.9) $\times 10^{-11}$	[129]

Table 7.1: Experimental limits for the effective neutrino magnetic moments from experiments with different neutrino sources [122].

for short baseline neutrinos we can approximate the argument of the exponential in Eq. (7.8) to zero, so the exponential itself can be approximated to unity. Since the only difference between the effective coupling for neutrinos and anti-neutrinos comes from the phase of the exponential, then both are equal in this case, and we can write

$$\mu^2_{\nu_l} = \mu^2_{\overline{\nu}_l} \simeq \sum_j \left| \sum_k U^*_{lk} \lambda'_{jk} \right|^2 = \left(U \cdot \lambda'^{\dagger} \cdot \lambda' \cdot U^{\dagger} \right)_{ll} \qquad \text{(SBL mass basis)}, \tag{7.10}$$

where we have used the matrix notation in the last equality, which results more convenient when transforming between different bases. Applying the basis transformation rule in Eq. (7.10), in the flavor basis we have

$$\mu^2_{\nu_\alpha} = \left(\lambda^{\dagger} \cdot \lambda \right)_{\alpha\alpha} \qquad \text{(SBL flavor basis)}. \tag{7.11}$$

On the other hand, for solar neutrinos, Eq. (7.8) needs to be modified to take into account matter effects in neutrino propagation. To this end, it is enough to replace $U_{lk} \to U^M_{lk}$, with U^M denoting the leptonic mixing matrix in matter, described by an effective mixing angle that takes into account matter effects as discussed in section 3.4. As a result, oscillations, and the effective coupling itself, become energy dependent. Then, for solar neutrinos we have

$$\mu^2_{\nu_l} = \sum_j \left| \sum_k (U^M_{lk})^* e^{-i\Delta m^2_{kj} L/2E_\nu} \lambda'_{jk} \right|^2 . \tag{7.12}$$

In this equation, L corresponds to the Earth-Sun distance, so $L/E \gg 1$ and, in contrast to the short baseline case, the phases of the exponential can not be considered small. Instead, we can consider the finite energy resolution of the detector and average over

L/E. This can be done by assuming a smearing function given by a Gaussian distribution with median $\langle L/E\rangle$ and averaging over the propagation phases. The effect of this average is [124]

$$\left\langle e^{\pm i(\Delta m^2_{ij}/2)(L/E_\nu)}\right\rangle = e^{\pm(\Delta m^2_{ij}/2)\langle L/E_\nu\rangle} e^{-\Delta m^4_{ij}\langle L/E_\nu\rangle^2/8}\ , \tag{7.13}$$

which implies that interference terms are exponentially suppressed and can be ignored. Then, for solar neutrinos in the mass basis we have

$$\mu^2_{\nu_e} = \sum_k \left|U^M_{ek}\right|^2 \sum_j \left|\lambda^{'}_{jk}\right|^2 = \sum_{k=1}^{3} \left|U^{\rm M}_{\alpha k}\right|^2 \left(\lambda'^{\dagger}\cdot\lambda'\right)_{kk} \qquad \text{(Solar mass basis)}, \tag{7.14}$$

where, according to the discussion of neutrino oscillations in matter, the elements of the lepton mixing matrix in matter are given by:

$$|U_{e1}|^2 = c^2_{13}P^{2\nu}_{e1}, \qquad |U_{e2}|^2 = c^2_{13}P^{2\nu}_{e2}, \qquad |U_{e3}|^2 = s^2_{13}, \tag{7.15}$$

with $P^{2\nu}_{ei} = P^{2\nu}_{ei}(E_\nu)$ denoting the two-flavor approximation probability of observing the i-th mass eigenstate ν_i at the scattering point. Applying the transformation rule for the λ' matrix, in the flavor basis we have

$$\mu^2_{\nu_\alpha} = \sum_{k=1}^{3} |U^{\rm M}_{\alpha k}|^2 \left(U^{\dagger}\cdot\lambda^{\dagger}\cdot\lambda\cdot U\right)_{kk} \qquad \text{(Solar flavor basis)}. \tag{7.16}$$

7.3 Majorana neutrinos

From the discussion in section 7.1, we know that for Majorana neutrinos the matrices μ_{ij} and ϵ_{ij} are anti-symmetric, and hence the matrix $\lambda^{'}$ is also anti symmetric. Then, to simplify the computations we can use the notation

$$\Lambda_i = \varepsilon_{ijk}\lambda^{'}_{jk}, \tag{7.17}$$

where ε_{ijk} denotes the Levi-Civita symbol and $\Lambda_i = |\Lambda_i|e^{i\varphi_i}$, with φ_i magnetic moment CP phases. However, only two phases are physical [130]. Then, under this parametrization, the magnetic moment matrix in the mass basis explicitly reads

$$\lambda^{'}_M = \begin{pmatrix} 0 & |\Lambda_3|e^{i\varphi_3} & -|\Lambda_2| \\ -|\Lambda_3|e^{i\varphi_3} & 0 & |\Lambda_1|e^{i\varphi_1} \\ |\Lambda_2| & -|\Lambda_1|e^{i\varphi_1} & 0 \end{pmatrix}. \tag{7.18}$$

Neutrino Magnetic Moment short baseline Majorana neutrinos	
	Mass Basis
$\mu^2_{\nu_e}$	$\begin{aligned}&\left\|\Lambda_1\right\|^2+\left\|\Lambda_2\right\|^2+\left\|\Lambda_3\right\|^2-\left\|\Lambda_1\right\|^2 c_{13}^2c_{12}^2-\left\|\Lambda_2\right\|^2 c_{13}^2s_{12}^2-\left\|\Lambda_3\right\|^2 s_{13}^2\\&-2c_{12}c_{13}^2s_{12}\left\|\Lambda_1\right\|\left\|\Lambda_2\right\|\cos(-\varphi_1)-2c_{13}s_{12}s_{13}\left\|\Lambda_2\right\|\left\|\Lambda_3\right\|\cos(\varphi_3-\delta)\\&-2c_{12}c_{13}s_{13}\left\|\Lambda_1\right\|\left\|\Lambda_3\right\|\cos(\varphi_3-\varphi_1-\delta)\end{aligned}$
$\mu^2_{\nu_\mu}$	$\begin{aligned}&\left\|\Lambda_1\right\|^2\left(c_{12}^2c_{23}^2+s_{23}^2(c_{13}^2+s_{12}^2s_{13}^2)-2c_{12}c_{23}s_{12}s_{13}s_{23}\cos(\delta)\right)\\&+\left\|\Lambda_2\right\|^2\left(c_{23}^2s_{12}^2+s_{23}^2(c_{13}^2+c_{12}^2s_{13}^2)+2c_{12}c_{23}s_{12}s_{13}s_{23}\cos(\delta)\right)\\&+\left\|\Lambda_3\right\|^2(c_{23}^2+s_{13}^2s_{23}^2)+2\left\|\Lambda_1\Lambda_2\right\|(c_{12}^2c_{23}s_{13}s_{23}\cos(-\varphi_1-\delta)\\&\quad-c_{23}s_{12}^2s_{13}s_{23}\cos(-\varphi_1+\delta)+c_{12}s_{12}(c_{23}^2-s_{13}^2s_{23}^2)\cos(-\varphi_1))\\&+2\left\|\Lambda_1\right\|\left\|\Lambda_3\right\|(c_{13}s_{23}(c_{12}s_{13}s_{23}\cos(\varphi_3-\varphi_1-\delta)+c_{23}s_{12}\cos(\varphi_3-\varphi_1)))\\&+2\left\|\Lambda_2\right\|\left\|\Lambda_3\right\|(c_{13}s_{23}(s_{12}s_{13}s_{23}\cos(\varphi_3-\delta)-c_{12}c_{23}\cos(\varphi_3)))\end{aligned}$
$\mu^2_{\nu_\tau}$	$\begin{aligned}&\left\|\Lambda_1\right\|^2(c_{23}^2(c_{13}^2+s_{12}^2s_{13}^2)+c_{12}^2s_{23}^2+2c_{12}c_{23}s_{12}s_{13}s_{23}\cos(\delta))\\&+\left\|\Lambda_2\right\|^2(c_{23}^2(c_{13}^2+c_{12}^2s_{13}^2)+s_{12}^2s_{23}^2-2c_{12}c_{23}s_{12}s_{13}s_{23}\cos(\delta))\\&+\left\|\Lambda_3\right\|^2(s_{23}^2+c_{23}^2s_{13}^2)+2\left\|\Lambda_2\right\|\left\|\Lambda_3\right\|c_{23}c_{13}(c_{12}s_{23}\cos(\varphi_3)+c_{23}s_{12}s_{13}\cos(\varphi_3-\delta))\\&-2\left\|\Lambda_1\right\|\left\|\Lambda_3\right\|c_{13}c_{23}(s_{12}s_{23}\cos(\varphi_3-\varphi_1)-c_{12}c_{23}s_{13}\cos(\varphi_3-\varphi_1-\delta))\\&-2\left\|\Lambda_1\right\|\left\|\Lambda_2\right\|(c_{12}s_{12}(c_{23}^2s_{13}^2-s_{23}^2)\cos(-\varphi_1)+c_{12}^2c_{23}s_{13}s_{23}\cos(-\varphi_1-\delta)\\&\quad-c_{23}s_{12}^2s_{13}s_{23}\cos(-\varphi_1+\delta))\end{aligned}$

	Flavor Basis
$\mu^2_{\nu_e}$	$\left\|\Lambda_\mu\right\|^2+\left\|\Lambda_\tau\right\|^2$
$\mu^2_{\nu_\mu}$	$\left\|\Lambda_\tau\right\|^2+\left\|\Lambda_e\right\|^2$
$\mu^2_{\nu_\tau}$	$\left\|\Lambda_\mu\right\|^2+\left\|\Lambda_e\right\|^2$

Table 7.2: Magnetic moments in terms of fundamental parameters for short baseline neutrinos in the mass and flavor bases for Majorana neutrinos.

After applying the mass to flavor transformation rule, the anti-symmetry of the λ' matrix in the mass basis is preserved in the flavor basis. Then, in the flavor basis we denote

$$\lambda_M=\begin{pmatrix}0 & |\Lambda_\tau|e^{i\phi_\tau} & -|\Lambda_\mu|\\ -|\Lambda_\tau|e^{i\phi_\tau} & 0 & |\Lambda_e|e^{i\phi_e}\\ |\Lambda_\mu| & -|\Lambda_e|e^{i\phi_e} & 0\end{pmatrix}. \tag{7.19}$$

Explicit expressions for $\mu^2_{\nu_l}$ can then be obtained by substituting Eqs. (7.18), and (7.19) in Eq. (7.8), and they are summarized in Table 7.2, where we can see the explicit dependence of the effective coupling on the different physical phases in the mass basis.

Some interesting properties of the effective coupling can also be explored for Majo-

rana neutrinos in the mass basis if we define the vectors:

$$\vec{\mathbf{\Lambda}} = \sum_{j=1}^{3} |\Lambda_j| \widehat{e}_j, \tag{7.20}$$

$$\vec{\mathbf{\Lambda}}_\alpha = \sum_{j=1}^{3} |U_{\alpha j}| \, |\Lambda_j| \, \widehat{e}_{j\alpha}, \tag{7.21}$$

with $\widehat{e}_j$ the rectangular coordinates unitary vectors and $\widehat{e}_{j\alpha}$ unit vectors such that

$$\widehat{e}_{i\alpha} \cdot \widehat{e}_{j\beta} = \delta_{\alpha\beta} \cos\left[- \arg\left(U_{\alpha i}\right) + \arg\left(U_{\beta j}\right) - \varphi_i + \varphi_j \right] \ . \tag{7.22}$$

Then, the neutrino magnetic moment can be expressed as the difference between the moduli of the two vectors:

$$\mu^2_{\nu_\alpha} = \left| \vec{\Lambda} \right|^2 - \left| \left(\sum_{j=1}^{3} |U_{\alpha j}| \, |\Lambda_j| \, \widehat{e}_{j\alpha} \right) \right|^2 . \tag{7.23}$$

Several analyses have been done in the literature to set bounds for the fundamental parameters $|\Lambda_i|$ by assuming specific values for the different magnetic moment phases [131]. However, we now show that these phases can have a significant impact on the order of magnitude of the fundamental couplings given a specific limit for the effective coupling. To simplify our computations, we now set the Dirac CP phase $\delta = \pi$, which is consistent with the current global analyses as reported in [53]. Similar results can be obtained for a different value of δ but this will clarify our point.

7.3.1 Reactor neutrinos

Within the formalism given in Eq. (7.23), for the case of electron (anti)neutrinos, the presence of magnetic moment CP phases can be interpreted as a misalignment between the three defined $\widehat{e}_{je}$ vectors, as visualized in Fig. 7.2. We can then study the effect of these magnetic moment CP phases in the following way: for fixed values of $|\Lambda_i|$, we calculate the critical points with respect to the phases φ_i in Eq. (7.23). We find a total of five critical points, four of which are trivial (when $\cos\varphi_i = \pm 1$), and are listed in Table 7.3. In addition, a non-trivial critical point is given when the phases satisfy:

$$\cos(\varphi_1) = \frac{-c^2_{12}c^2_{13}|\Lambda_1|^2 - s^2_{12}c^2_{13}|\Lambda_2|^2 + s^2_{13}|\Lambda_3|^2}{2c_{12}c^2_{13}s_{12}|\Lambda_1||\Lambda_2|}, \tag{7.24}$$

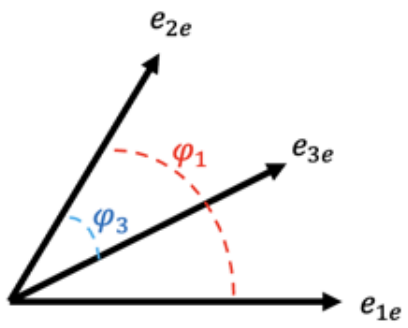

Figure 7.2: Graphical representation of the vectors defined in Eq. (7.21) for reactor neutrinos. The misalignment can be interpreted as a consequence of electromagnetic CP phases.

(φ_1, φ_2)	**Critical Point**	**Condition for max or min**	η
(0,0)	max/saddle	$s_{13}\|\Lambda_3\| > c_{12}c_{13}\|\Lambda_1\| + c_{13}s_{12}\|\Lambda_2\|$	$c_{12}c_{13}\|\Lambda_1\| + c_{13}s_{12}\|\Lambda_2\| - s_{13}\|\Lambda_3\|$
(0, π)	min	Always	$c_{12}c_{13}\|\Lambda_1\| + c_{13}s_{12}\|\Lambda_2\| + s_{13}\|\Lambda_3\|$
(π, 0)	max/saddle	$c_{13}s_{12}\|\Lambda_2\| > c_{12}c_{13}\|\Lambda_1\| + s_{13}\|\Lambda_3\|$	$c_{12}c_{13}\|\Lambda_1\| - c_{13}s_{12}\|\Lambda_2\| + s_{13}\|\Lambda_3\|$
(π, π)	max/saddle	$c_{12}c_{13}\|\Lambda_1\| > c_{13}s_{12}\|\Lambda_2\| + s_{13}\|\Lambda_3\|$	$c_{12}c_{13}\|\Lambda_1\| + c_{13}s_{12}\|\Lambda_2\| - s_{13}\|\Lambda_3\|$

Table 7.3: Effective magnetic moment critical points in the case of reactor neutrinos for fixed $|\Lambda_i|$.

$$\cos(\varphi_3) = \frac{-c_{12}^2 c_{13}^2 |\Lambda_1|^2 - s_{12}^2 c_{13}^2 |\Lambda_2|^2 + s_{13}^2 |\Lambda_3|^2}{2 c_{13} s_{12} s_{13} |\Lambda_2||\Lambda_3|}. \tag{7.25}$$

Among all the critical points, one and only one will be a maximum, one a minimum, and the others will be saddle points depending on the relative values between the different $|\Lambda_i|$. For instance, the non-trivial critical point determined by Eqs. (7.24) and (7.25), corresponds to a maximum when the $|\Lambda_i|$ are such that in these equations we have the condition $|\cos(\varphi_i)| < 1$. If this is the case, the second term in Eq. (7.23) vanishes and the effective coupling has a maximum value given by

$$\mu_{\nu_e}^2|_{\max} = |\Lambda|^2 \equiv |\Lambda_1|^2 + |\Lambda_2|^2 + |\Lambda_3|^2. \tag{7.26}$$

If this is not the case, then, depending on the relationship between the $|\Lambda_i|$, the maximum will be located at one of the trivial critical points listed in Table 7.3, where the condition for each combination to be a maximum point is also indicated. Only one of the conditions among the maximum point candidates can be satisfied at once, and the other critical points will become saddle points. In the case of the trivial critical

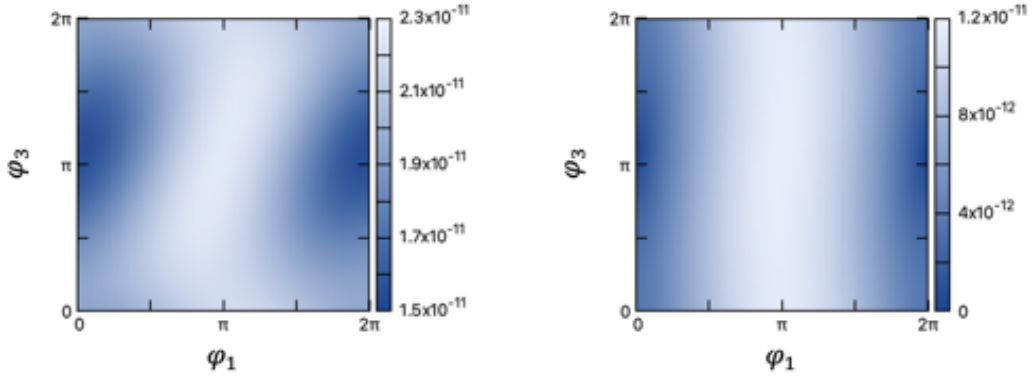

Figure 7.3: Contour regions for the effective neutrino magnetic moment (in units of μ_B) for reactor neutrinos as a function of the electromagnetic CP phases for fixed $|\Lambda_i|$. Left panel shows the results for $|\Lambda_1| = |\Lambda_2| = 1 \times 10^{-11}\mu_B$ and $|\Lambda_3| = 1.7 \times 10^{-11}\mu_B$. Right panel shows the contour for $|\Lambda_1| = 1 \times 10^{-11}\mu_B, |\Lambda_2| = 6.8 \times 10^{-12}\mu_B$, and $|\Lambda_3| = 1.8 \times 10^{-12}$, a combination for which the relations in Eq. (7.28) are satisfied and the effective coupling can vanish.

points, the maximum (or minimum) will take the value:

$$\mu^2_{\nu_e}|_{\max\,/\,\min} = |\Lambda|^2 - \eta^2, \tag{7.27}$$

with η also given in Table 7.3 for each case. We can see that there is a different relative sign for the effective coupling value among all the maximum candidates. A more interesting feature arises from the minimum, which, regardless of the relative values between $|\Lambda_i|$, it will always be located at $(0, \pi)$. The value of the effective coupling at this point is also given by Eq. (7.27), with its corresponding η defined in Table 7.3. In general, this minimum will be different from zero. For instance, the contour plot in the left panel of Fig. 7.3 shows the effective coupling as a function of the magnetic moment phases for $|\Lambda_1| = |\Lambda_2| = 1 \times 10^{-11}\mu_B$ and $|\Lambda_3| = 1.7 \times 10^{-11}\mu_B$. Dark regions show that, indeed, the minimum is at $(0, \pi)$, with a value for the effective coupling of $1.5 \times 10^{-11}\mu_B$. In addition, bright regions show that the maximum is near one of the trivial critical points, which is consistent with our previous discussion. An important feature comes when the moduli satisfy the relations:

$$|\Lambda_2| = \frac{s_{12}}{c_{12}}|\Lambda_1|, \qquad\qquad |\Lambda_3| = \frac{s_{13}}{c_{12}c_{13}}|\Lambda_1|. \tag{7.28}$$

Under these conditions, $\eta^2 = |\Lambda|^2$ in Eq. (7.27), and the effective coupling vanishes. The contour plot in the right panel of Fig. 7.3 shows the case where $|\Lambda_1| = 1 \times 10^{-11}\mu_B, |\Lambda_2| = 6.8 \times 10^{-12}\mu_B$, and $|\Lambda_3| = 1.8 \times 10^{-12}$, a combination that satisfies the

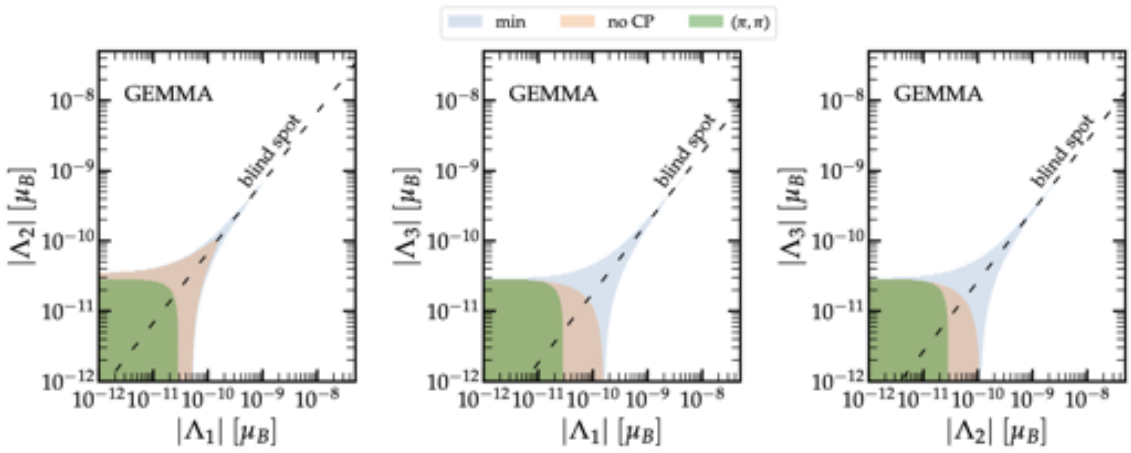

Figure 7.4: Projections in the fundamental parameter space that are consistent with current limits of the effective magnetic moment coupling for reactor neutrinos (GEMMA). Blue regions show the results for $\varphi_1 = 0$, $\varphi_3 = \pi$, with the dashed line indicating the blind spot region. Green regions show the case $\varphi_1 = \pi$, $\varphi_3 = \pi$ and brown regions show the case for which there are no CP phases, $\varphi_1 = 0$, $\varphi_3 = 0$ [124].

relations in Eq. (7.28), and hence the minimum possible effective coupling is zero.

From the previous analysis, we conclude that there are some directions in the parameter space on which the fundamental couplings $|\Lambda_i|$ can be different from zero but the effective coupling μ_{ν_e} vanishes and, in that case, we can not have a measurable electromagnetic effect in neutrino interactions. We refer to these directions in the parameter space as *blind spots* [124, 132]. To illustrate this, we show in Fig. 7.4 the different values of $|\Lambda_i|$ that are consistent with the GEMMA limit for different combinations of phases (φ_1, φ_3). The panels in the figure show the three different projections in the $(|\Lambda_i|, |\Lambda_j|)$ parameter space. The blue regions on each panel correspond to the pair of phases $(0, \pi)$, with the dashed line indicating the direction of blind spots, where the effective magnetic moment is zero. We also show in brown the case where the two phases are zero, and in green the combination (π, π), where there are no blind spot effects.

The property of blind spots can equivalently be seen in the flavor basis. From Table 7.2, notice that for the electron neutrino case in the flavor basis, the effective coupling only depends on two of the independent moduli that parametrize the Majorana magnetic moment matrix. This means that the effective coupling can be zero even in the case when $|\Lambda_e|$ has a relatively large value. Actually, it can take any value and the effects of the effective coupling will remain zero!

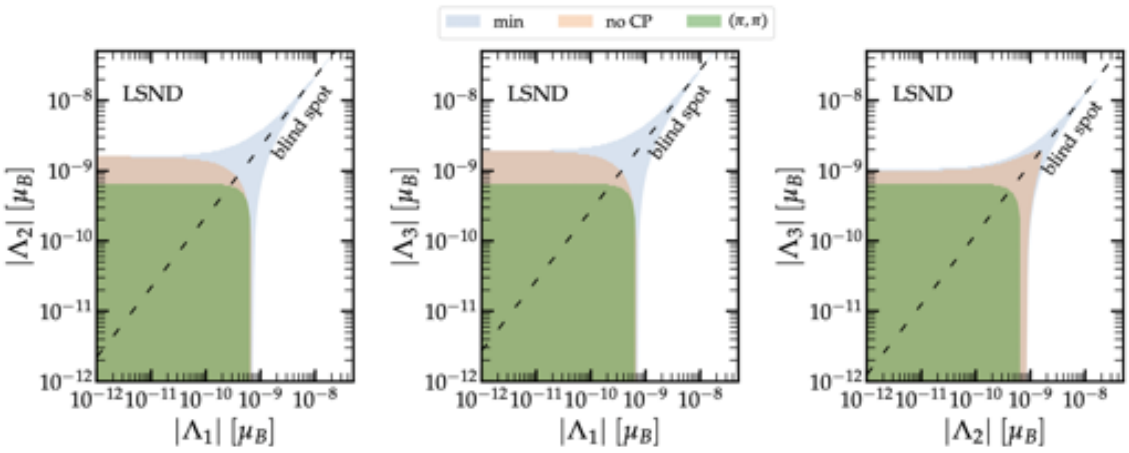

Figure 7.5: Projections in the fundamental parameter space that are consistent with current limits of the effective magnetic moment coupling for accelerator neutrinos (LSND). Blue regions show the results for $\varphi_1 = \pi$, $\varphi_3 = 0$, with the dashed line indicating the blind spot region. Green regions show the case $\varphi_1 = \pi$, $\varphi_3 = \pi$ and brown regions show the case for which there are no CP phases, $\varphi_1 = 0$, $\varphi_3 = 0$ [124].

7.3.2 Accelerator neutrinos

Now we focus on the neutrino magnetic moment for muon neutrinos, which can be studied from accelerator sources, where we have the production of both muon neutrinos and anti-neutrinos. Explicit expressions for $\mu^2_{\nu_\mu}$ can be obtained from Eqs. (7.10) and (7.11), and they are shown in Table 7.2. The most stringent bound for this coupling comes from the LSND experiment as indicated in Table 7.1.

We performed a similar analysis as that for electron neutrinos; the most important result being that in this case the minimum is now located at the point $(\pi, 0)$, where we have access to what we defined as blind spots, and hence, for relatively large values of $|\Lambda_i|$ that still satisfy the experimental bounds. We show in Fig. 7.5 the different values of $|\Lambda_i|$ that are consistent with current LSND bounds for different values of electromagnetic CP phases. On each panel, the blue region shows the allowed parameters for $(\pi, 0)$, with the dashed line indicating the blind spot region. Again, the brown region shows the projections when both electromagnetic phases are zero and the green region for (π, π). Notice that the blind spot regions for $\mu^2_{\nu_e}$ and $\mu^2_{\nu_\mu}$ can not be accessed simultaneously because each of them appears for different combination of phases. This means that it is possible to have a large signal of one of these couplings, while the other remains zero. In the next section we will come back to this point.

Considering now the operator λ in the flavor basis, for muon neutrinos we are again only sensitive to the moduli of two fundamental parameters. In fact, from Table 7.2, we see that in this case, the effective coupling is sensitive to $|\Lambda_e|$ and $|\Lambda_\tau|$. The absence of

the term $|\Lambda_\mu|$ tells us that it can take any value, no matter how large, and the effective coupling can still satisfy the corresponding limit, allowing for a consistent result with the electron (anti)neutrino case.

7.3.3 Tau neutrinos

For completeness, we also show the effective coupling expressions for the case of tau (anti)neutrinos in Table 7.2, for both mass and flavor bases. As in the case of the $\mu^2_{\nu_\mu}$ coupling, the minimum here is also found at the physical phases $(\pi, 0)$, so the conclusions are basically the same for these two flavors. The experimental bound for this effective coupling comes from the DONUT experiment, which is less restrictive with respect to the other flavors and we do not show here. Future experiments like Faser will be also sensitive to this neutrino flavor [133].

7.3.4 Solar neutrinos

By using Eq. (7.14), the explicit form of the neutrino magnetic moment in the mass basis, for Majorana neutrinos reads

$$\mu^2_{\nu_{e,\mathrm{sol}}} = |\Lambda_1|^2 + |\Lambda_2|^2 + |\Lambda_3|^2 - c^2_{13}\,|\Lambda_2|^2 + (c^2_{13} - 1)\,|\Lambda_3|^2 + c^2_{13} P^{2\nu}_{e1}(|\Lambda_2|^2 - |\Lambda_1|^2). \quad (7.29)$$

As discussed in section 3.4, the oscillation probabilities introduce an energy dependence on the effective coupling. For the particular case of electron-neutrino scattering experiments, that dependence is to a large degree determined by the energy range of the solar *pp* flux, while for CEvNS by the energy range of the ^{8}B one. Since these processes peak at $\sim 0.4\,\mathrm{MeV}$ and $\sim 10\,\mathrm{MeV}$, respectively, one can then evaluate the probability for those energies and then map into parameter space. Notice that in this case the effective coupling does not depend on the physical phases. Moreover, it only depends on terms that are proportional to $|\Lambda_i|^2$ and the only way to have a vanishing magnetic moment is through the trivial solution $|\Lambda_i| = 0$, which means that we do not have blind spot regions and, in order to satisfy the experimental limits, $|\Lambda_i|$ can not be arbitrarily large. Currently, the most stringent bound for the neutrino magnetic moment in solar neutrinos comes from Borexino. In addition, the XENON1T experiment has reported an excess on the number of events for electron recoils in the low energy part of the spectrum. Among many possibilities, the excess can be justified by magnetic moment effects, constraining its value to the range indicated in Table 7.1. The magenta regions in the top panels of Fig. 7.6 show the mapping of XENON1T limits into the funda-

mental parameter space for fixed values of $|\Lambda_3|$. We can notice that for low values of $|\Lambda_3|$, the allowed region for the other two moduli results on a defined band.

Regarding the flavor basis, the explicit form of the effective coupling for solar neutrinos is lengthy and we do not show it here.

7.3.5 Consistency between short baseline and solar measurements

From the previous analysis, we have found that it can be possible to have a large magnetic moment effect for reactor neutrinos and, at the same time, have no signal for accelerator neutrinos. This makes us wonder whether there are combinations of fundamental parameters that reconcile the different experimental limits for SBL and solar neutrinos. With current measurements, it is easy to see that there are different values of $|\Lambda_i|$ in the parameter space for which the three experimental limits (reactor, accelerator and solar neutrinos) are consistent. However, in the case of future measurements, the presence of blind spots may be necessary to reconcile all the results. To see this, we take the limits given by GEMMA and LSND, and we consider that the XENON1T excess is due to neutrino magnetic moments. We know that this has not been confirmed yet but it will help to illustrate our point.

In the top panels of Fig. 7.6, we show the allowed values in the $(|\Lambda_1|, |\Lambda_2|)$ parameter space (for $|\Lambda_3|$ fixed), that satisfy the current limits of the effective magnetic moment coupling for GEMMA (reactor), LSND (accelerator), and XENON1T (solar) as given in Table 7.1. The blue and gray regions correspond to allowed values for reactor and accelerator bounds, respectively, when electromagnetic CP phases are fixed to $(0, \pi)$, a combination of phases that activates the blind spots for reactor neutrinos. In addition, the magenta region corresponds to the solar bound, which is phase independent. The intersection of these three regions represents the parameter space for which the three measurements are consistent. We can see that in the three different panels (different values of $|\Lambda_3|$) it is easy to reconcile the three measurements since the solar (magenta) region is totally contained in the reactor (blue) region, which in turn is totally contained in the accelerator (grey) region. As a second scenario, the regions behind dashed and dash-dotted contours represent the allowed values for accelerator and reactor bounds when the CP phases are fixed to (π, π), a combination of phases that hides the blind spot effects of reactor neutrinos. To reconcile the three measurements we look for the intersection of these two regions with the solar (magenta) region, which is phase independent. We can see that, again, it is easy to reconcile the measurements since

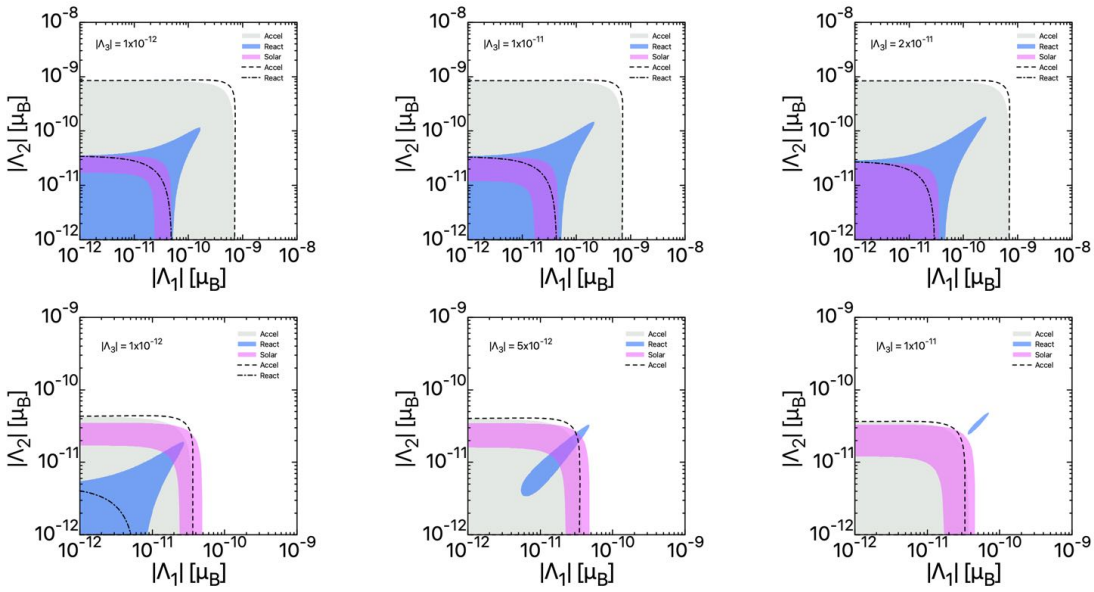

Figure 7.6: Allowed values in the $(|\Lambda_1|, |\Lambda_2|)$ parameter space that are consistent with experimental limits of reactor, accelerator, and solar experimental limits for a fixed $|\Lambda_3|$ and two different combinations of CP phases. Colored regions assume $\varphi_1 = 0$, $\varphi_3 = \pi$, while the regions under dashed contours assume $\varphi_1 = \pi$, $\varphi_3 = \pi$. Top panels show the results assuming current limits for the effective magnetic moment coupling while bottom panels assume future limits for reactor and accelerator neutrinos.

in the three cases the reactor (dash-dotted) region is contained in the solar (magenta) region, which in turn is contained within the accelerator (dashed) region. We conclude that, independently of the value of $|\Lambda_3|$, blind spots are not necessary to reconcile current magnetic moment limits.

To illustrate how blind spots may be useful to reconcile the three measurements, now we assume a future scenario on which the effective coupling limits for reactor and accelerator sources are reduced by one order of magnitude, lets say, $\mu_{\nu_e} = 4 \times 10^{-12}\mu_B$, and $\mu_{\nu_\mu} = 3.5 \times 10^{-11}\mu_B$, while the solar measurement remains the same. The corresponding regions in the parameter space $(|\Lambda_1|, |\Lambda_2|)$ that satisfy these limits are shown in the bottom panels of Fig. 7.6, under the same color code used for the top panels. This means that blue and grey regions correspond to reactor and accelerator limits for fixed phases of $(0, \pi)$, for which blind spots for reactor neutrinos are activated. To reconcile the three measurements, we need again the blue, grey, and magenta regions to intersect, which can be achieved in the left and central panels, when $|\Lambda_3|$ has a relatively small value. The overlap in these cases is a consequence of blind spots since they allow for large values of $|\Lambda_1|$ and $|\Lambda_2|$ while keeping the effective coupling small. However, the overlap is lost for a large value of $|\Lambda_3|$ since, for the reactor coupling to remain small, we need even larger values of $|\Lambda_1|$ and $|\Lambda_2|$, that eventually exceed the

allowed ones for the other effective coupling limits.

On the other hand, the regions behind dashed and dash-dotted contours represent again the allowed values for accelerator and reactor limits, respectively, for fixed phases of (π, π), when blind spots for reactor magnetic moment are not present. To reconcile the three measurements we need these regions to overlap with the solar (magenta) region. In the left panel, we see that this is not possible since the reactor region falls bellow the solar band. This happens because for this particular combination of phases, the effects of blind spots are hidden, and the $(|\Lambda_1|, |\Lambda_2|)$ allowed values fall below the assumed effective coupling limit. The situation is even worse for the central and right panels, where the allowed regions for reactor fall bellow $10^{-12}\mu_B$ and are not visible in the figures. We conclude that in this case, where blind spots are not accessed, it is impossible to reconcile the three measurements.

7.4 Dirac diagonal-mass basis

We now comment on the form of the effective coupling $\mu^2_{\nu_l}$ for Dirac neutrinos, where the $\lambda^{'}$ matrix is completely general. Again, some of the phases are not physical [130], but still, the number of free parameters becomes very large. Because of this, we limit ourselves to the particular case where we only have diagonal couplings, which contrasts with the Majorana case. Then, for Dirac neutrinos in the mass basis we can express

$$\lambda'_D = \begin{pmatrix} \lambda_{11} & 0 & 0 \\ 0 & \lambda_{22} & 0 \\ 0 & 0 & \lambda_{33} \end{pmatrix}, \tag{7.30}$$

where $\lambda_{ii} = |\lambda_{ii}|e^{i\phi_{ii}}$, being ϕ_{ii} the electromagnetic CP phases in this case. Applying the transformation rule to $\lambda^{'}$, we conclude that in the flavor space the matrix is not diagonal. However, it is a symmetric matrix and takes the form

$$\lambda_D = \begin{pmatrix} \lambda_{ee} & \lambda_{e\mu} & \lambda_{e\tau} \\ \lambda_{e\mu} & \lambda_{\mu\mu} & \lambda_{\mu\tau} \\ \lambda_{e\tau} & \lambda_{\mu\tau} & \lambda_{\tau\tau} \end{pmatrix}. \tag{7.31}$$

However, not all the matrix elements in Eq. (7.31) are independent since the number of degrees of freedom needs to be the same upon a change of basis. Had we assumed a diagonal flavor mass matrix, then the mass basis would not be diagonal, but would be a symmetric matrix. For short baseline sources, Eq. (7.10) is again valid, and the

Neutrino Magnetic Moment short baseline Dirac neutrinos diagonal		
	Mass	**Flavor**
$\mu^2_{\nu_e}$	$c^2_{12}c^2_{13}\left\|\lambda_{11}\right\|^2 + c^2_{13}s^2_{12}\left\|\lambda_{22}\right\|^2 + s^2_{13}\left\|\lambda_{33}\right\|^2$	$\left\|\lambda_{ee}\right\|^2 + \left\|\lambda_{\mu e}\right\|^2 + \left\|\lambda_{\tau e}\right\|^2$
$\mu^2_{\nu_\mu}$	$\left\|\lambda_{11}\right\|^2 (c^2_{23}s^2_{12} + c^2_{12}s^2_{13}s^2_{23} + 2c_{12}c_{23}s_{12}s_{13}s_{23}\cos(\delta))$ $+ \left\|\lambda_{22}\right\|^2 (c^2_{12}c^2_{23} + s^2_{12}s^2_{13}s^2_{23} - 2c_{12}c_{23}s_{12}s_{13}s_{23}\cos(\delta))$ $+ \left\|\lambda_{33}\right\|^2 c^2_{13}s^2_{23}$	$\left\|\lambda_{e\mu}\right\|^2 + \left\|\lambda_{\mu\mu}\right\|^2 + \left\|\lambda_{\mu\tau}\right\|^2$
$\mu^2_{\nu_\tau}$	$\left\|\lambda_{11}\right\|^2 (c^2_{12}c^2_{23}s^2_{13} + s^2_{12}s^2_{23} - 2c_{12}c_{23}s_{12}s_{13}s_{23}\cos(\delta))$ $+ \left\|\lambda_{22}\right\|^2 (c^2_{23}s^2_{12}s^2_{13} + c^2_{12}s^2_{23} + 2c_{12}c_{23}s_{12}s_{13}s_{23}\cos(\delta))$ $+ \left\|\lambda_{33}\right\|^2 c^2_{13}c^2_{23}$	$\left\|\lambda_{e\tau}\right\|^2 + \left\|\lambda_{\mu\tau}\right\|^2 + \left\|\lambda_{\tau\tau}\right\|^2$

Table 7.4: Magnetic moments in terms of fundamental parameters for short baseline neutrinos in the mass and flavor bases for Dirac neutrinos assuming only diagonal matrix elements.

corresponding explicit expressions for μ_{ν_l} in the mass and flavor bases are given in Table 7.4.

We can see that, in the mass basis, these expressions only depend on the moduli of the three different complex elements of the magnetic moment matrix. In consequence, the only trivial solution that allows for a vanishing magnetic moment is when $|\lambda_{ii}| = 0$, and we do not have the presence of blind spots in the mass basis. This can be seen in Fig. 7.7, where we have used the experimental limits in Table 7.1 for μ_{ν_l} to set bounds for the fundamental parameters. Notice that in each case, the maximum for each $|\lambda_{ii}|$ is just above the corresponding limit for the effective coupling.

In the case of solar neutrinos, from Eq. (7.14), for the mass basis we have the expression

$$\mu^2_{\nu_{e,\mathrm{sol}}} = c^2_{13}P^{2\nu}_{e1}\left|\lambda_{11}\right|^2 + c^2_{13}(1 - P^{2\nu}_{e1})\left|\lambda_{22}\right|^2 + s^2_{13}\left|\lambda_{33}\right|^2, \tag{7.32}$$

depending again on the three moduli of the magnetic moment parameters. The mapping of the experimental limit from XENON1T is also shown in Fig. 7.7. Notice that the regions corresponding to GEMMA and XENON1T are entirely overlapped, which is expected since their expressions for the effective coupling are very similar (see Eq. (7.32) and first row in Table 7.4). The analogue in the flavor basis can be obtained from Eq. (7.16), which is lengthy and we do not show it here.

In conclusion, a Majorana neutrino nature allows for couplings in fundamental parameter space that are larger than one of the limits for the effective coupling. This effect can help to reconcile measurements from different experiments if the limits differ in several orders of magnitude, as it is the case for present limits. In contrast, for the case of Dirac diagonal neutrinos, the fundamental couplings are only allowed to be just

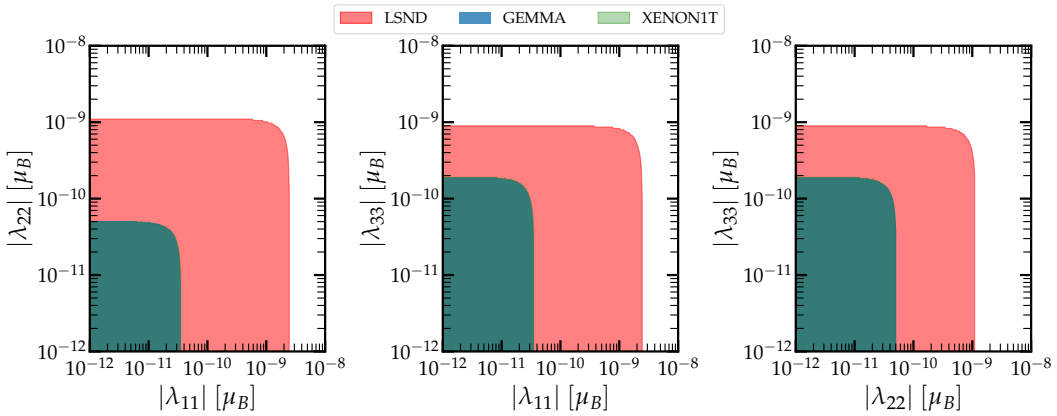

Figure 7.7: Allowed values for diagonal neutrino magnetic moments in the mass basis for Dirac neutrinos consistent with LSND (magenta), GEMMA (blue) and XENON1T (green) experimental limits. The regions for GEMMA and XENON1T are entirely overlapped, and hence the dark-green color in the figure [124].

above the limits of the effective coupling.

7.5 NMM from solar neutrinos in Dark Matter experiments

We have seen in previous sections that neutrino magnetic moment effects can be parametrized by one single effective coupling, and that the different bounds on this parameter can be used to constrain the more fundamental parameters of the theory. This has been done, for instance, in the case of neutrino-electron scattering, and more recently in the context of CEvNS [131] by using SBL neutrinos. In this section we explore the feasibility of using experiments sensitive to solar neutrinos to constrain the effective neutrino magnetic moment.

Among active solar neutrino experiments, we only have the case of Super-Kamiokande, for which electromagnetic properties were studied in [134]. Here we focus our attention on the sensitivity of future direct detection Dark Matter (DM) experiments to neutrino electromagnetic properties. As their name suggest, these experiments have the search of DM signals as their main purpose. However, as they reach lower energy thresholds, they will eventually become sensitive to solar neutrinos that produce nuclear and electron recoils as backgrounds in their measurements. Among these experiments we have current detectors as XENON1T [135] and future proposals like XENONnT [136] and DARWIN [137]. These experiments share the property of being xenon based scintillating detectors, and they will have the technology capable of distinguishing between

electron and nuclear recoils [135]. In the case of XENON1T, the collaboration has already reported low recoil energy thresholds of 1 keV, which are enough to detect recoil backgrounds coming from CEvNS and neutrino-electron scattering produced by solar neutrinos. This will allow to probe physics beyond the SM in the neutrino sector at very low energies. In fact, the same collaboration has reported an excess on the electron recoil channel at the edge of this low energy threshold [129]. Among the possible explanations for this excess we have a tritium contamination, or indeed the presence of physics beyond the SM such as the signature from axion particles, or neutrino electromagnetic properties from which the limit in Table 7.1 is obtained.

The concept of neutrino magnetic moment as an effective coupling was introduced in section 7.2. Since the associated cross-section has a dependence on T^{-1}, its effects become dominant at low energies, so we can exploit the DM detector low thresholds to study this new physics scenario separately in electron and nuclear recoils. Here we study the sensitivity to magnetic moment effects when considering current and future expected thresholds for the XENON1T experiment [138], which consists of a 1-ton Xe detector. In addition, we will consider experimental arrays representative of its future upgrade XENONnT (10 ton), and the DARWIN proposal [139], which will be a 40-ton Xe based experiment.

7.5.1 NMM from CEvNS

We begin by studying the effective neutrino magnetic moment for solar neutrinos, $\mu_{\nu_{e,\mathrm{sol}}}$, through CEvNS. The corresponding cross-section can be obtained through the neutrino-electron scattering one in Eq. (7.7) by adding the form factor to account for the nucleus distribution and weighting to the number of protons inside the target nucleus. Then, the magnetic moment cross-section for CEvNS is given by [140]

$$\frac{d\sigma_{\mu_{\nu_\ell}}}{dT} = \frac{\pi\alpha^2 Z^2\,\mu_{\nu_l}^2}{m_e^2}\left(\frac{1}{T}-\frac{1}{E_\nu}\right)F_Z^2(q^2)\ . \tag{7.33}$$

We use this cross-section to test the sensitivity of DM experiments to the effective neutrino magnetic moment. To this end, we compare experimental data with the predicted *differential rate* by minimizing the squared function

$$\chi^2 = \sum_{i=1}^{n}\frac{\left(\frac{\mathrm{d}R_i}{\mathrm{d}T}\Big|_{exp}-\frac{\mathrm{d}R_i}{\mathrm{d}T}\Big|_{th}\right)^2}{\sigma_i^2}, \tag{7.34}$$

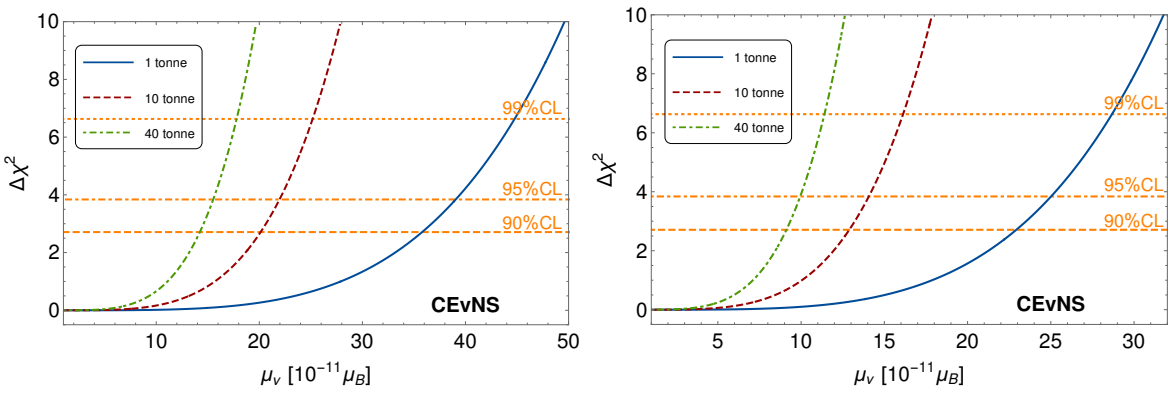

Figure 7.8: CEvNS sensitivity to the effective neutrino magnetic moment coupling in 1, 10 and 40 tons active volume detectors during a one-year data taking. The result assumes a 1 keV (left) and 0.3 keV (right) thresholds, 100% detector efficiency and backgrounds for XENON1T, XENONnT and DARWIN experiments, respectively [143].

where the index i is running over the number of bins, and σ_i is the statistical uncertainty. Notice that Eq. (7.34) compares the differential rate rather than the total number of events. We perform the analysis in this form since it is common for direct detection experiments to present their results in units of events/(ton·keV·year). This rate corresponds to the quantity obtained before performing the integral over T in Eq. (5.5).

The predicted differential rate is obtained by adding the cross-section in Eq. (7.33) to the SM one and varying $\mu_{\nu_{e,\mathrm{sol}}}$ while fixing all the other parameters of the theory to their best fit values. For the analysis, we assume the experimental measurement to be the one predicted by the SM and a bin width of 0.3 keV. Regarding backgrounds, several studies for our considered experiments have been performed in Refs. [141] and [142]. We use these data to incorporate background contributions to the expected statistical uncertainty for each bin. We also assume a one year data taking, with an efficiency given by a step function delimited by the corresponding threshold. In addition, we consider two different thresholds, one at 1 keV and the other at 0.3 keV [143]. For these thresholds, the main contribution for the cross-section is driven by the solar neutrino ^{7}Be line. We consider a detector mass of 1, 10 and 40 tons, representative of XENON1T, XENONnT, and DARWIN, respectively.

The results for each of the experiments are shown at different confidence levels in Fig. 7.8. Left panel in the figure corresponds to 1 keV threshold and the right panel to 0.3 keV. We can see that experiments with a 40-ton fiducial mass, representative of DARWIN, will be sensitive to experimental values of an effective neutrino magnetic moment of the order $10^{-10}\mu_B$. We also conclude that achieving lower thresholds has a significant impact on the expected sensitivity, giving an enhancement of a factor of

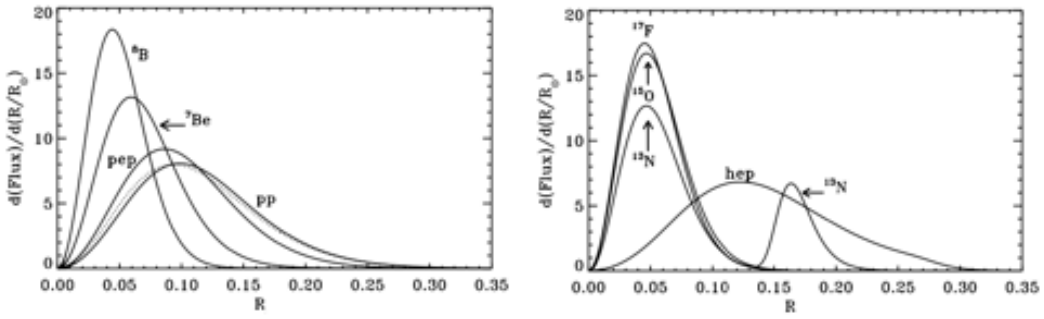

Figure 7.9: Neutrino production distribution in the sun as a function of the distance from its center (and normalized to its radius) under the BSB(GS98) model. Left panel shows the the *pp* chain and the right panel shows the CNO cycle fluxes [8].

two for the future 0.3 keV projection when compared to the 1 keV case. This result is remarkable since it shows that if a 0.3 keV threshold is attainable, experiments with characteristics as those like DARWIN, will be able to explore regions in parameter space comparable to those currently explored by Borexino (see Table 7.1), but now using nuclear recoil signals rather than neutrino-electron scattering. Furthermore, it demonstrates that even in its nuclear recoil data sets, DARWIN will be able to test regions close to those not yet ruled out, for instance, by astrophysical arguments [144].

7.5.2 NMM from neutrino-electron scattering

We have mentioned that future DM experiments will be able to distinguish between nuclear and electron recoils in their measurements. Then, we can also explore the sensitivity to neutrino magnetic moments for the case of neutrino-electron scattering in these experiments by following a similar method as that used in the previous section. To calculate the predicted differential rate, this time the total cross-section will be given by the sum of the SM neutrino-electron scattering presented in Eq. (3.18), and the magnetic moment contribution given in Eq. (7.7). For the SM contribution, we need to account for the transition probability since neutrino-electron scattering depends on the neutrino flavor as explained in section 3.2.1. In general, to account for neutrino oscillations, we need to consider the three neutrino mixing case. However, in the special case of Δm^2_{31} dominance, and active Δm^2_{21}, the problem can be effectively described by two-neutrino mixing. For solar neutrinos both conditions are satisfied [8], which means that we can use the results from section 3.4. Then, the survival probability can be calculated in terms of a two neutrino mixing scenario, and we have

$$P^{eff}_{\nu_e\to\nu_e} = \cos^4\theta_{13} P^{(1,2)}_{\nu_e\to\nu_e} + \sin^4\theta_{13}, \tag{7.35}$$

with $P^{(1,2)}_{\nu_e\to\nu_e}$ the survival probability in the case of two-neutrino mixing. As the matter density in the sun varies slowly, we can assume an adiabatic approximation and $P^{(1,2)}_{\nu_e\to\nu_e}$ will be given as discussed in section 3.4:

$$P_{\nu_e\to\nu_e}(E_\nu, R) = \frac{1}{2}\left(1 + \cos 2\theta \cos 2\theta_M(E_\nu, R)\right) \tag{7.36}$$

Where we explicitly wrote the dependence of θ_M on the neutrino energy E_ν and the production point, R, measured from the center of the Sun and normalized to its radius. This is important to consider since neutrino production regions are not fixed. Instead, there is a production distribution as a function of R, as illustrated in Fig. 7.9, where the left panel shows the distributions corresponding to the *pp* chain, and the right panel those of the CNO cycle. For very low thresholds, as it is the case of our experimental scenarios, the number of events will be sensitive to all the solar neutrino contributions. Then, by using the solar neutrino fluxes, Φ_α, as well as the production distributions, $\rho_\alpha(R)$, we can average over all the contributions to obtain the effective survival probability

$$\langle P_{\nu_e\to\nu_e}\rangle = \frac{\sum_\alpha \Phi_\alpha(E_\nu)\int_0^1 dR \rho_\alpha(R) P_{\nu_e\to\nu_e}(E_\nu, R)}{\sum_\alpha \Phi_\alpha(E_\nu)}, \tag{7.37}$$

where the index α runs over the different solar neutrino spectra. Then, having calculated the effective probability, and since the cross-section for muon and tau neutrinos is the same, the final recoil spectrum for solar neutrinos will be given by

$$\frac{\mathrm{d}R}{\mathrm{d}T} = N_e \int_{E_{min}}^{E_{max}} \sum_\alpha \frac{\mathrm{d}\Phi_\alpha}{\mathrm{d}E_\nu}\left[\langle P_{\nu_e\to\nu_e}\rangle \frac{\mathrm{d}\sigma_{\nu_e}}{\mathrm{d}T} + (1 - \langle P_{\nu_e\to\nu_e}\rangle)\frac{\mathrm{d}\sigma_{\nu_a}}{\mathrm{d}T} + \frac{\mathrm{d}\sigma_{\mu_{\nu_\ell}}}{\mathrm{d}T}\right], \tag{7.38}$$

where we have denoted $\mathrm{d}\sigma_{\nu_e}/\mathrm{d}T$ as the SM cross-section for an incoming electron neutrino and similarly $\mathrm{d}\sigma_{\nu_a}/\mathrm{d}T$ for either an incoming muon or tau neutrino. We perform the χ^2 analysis under the same assumptions as in the case of CEvNS, where we assume the experimental measurement to be the one obtained through the SM prediction. The results for each of the experimental setups are shown in Fig. 7.10. Notice that the expected sensitivities are competitive with current bounds of magnetic moment. We conclude that future DM experiments will be sensitive to neutrino magnetic moment effects in both neutrino-electron scattering and CEvNS. Then, if electromagnetic effects are measured in one of the two channels, we will have the sensitivity to see these effects

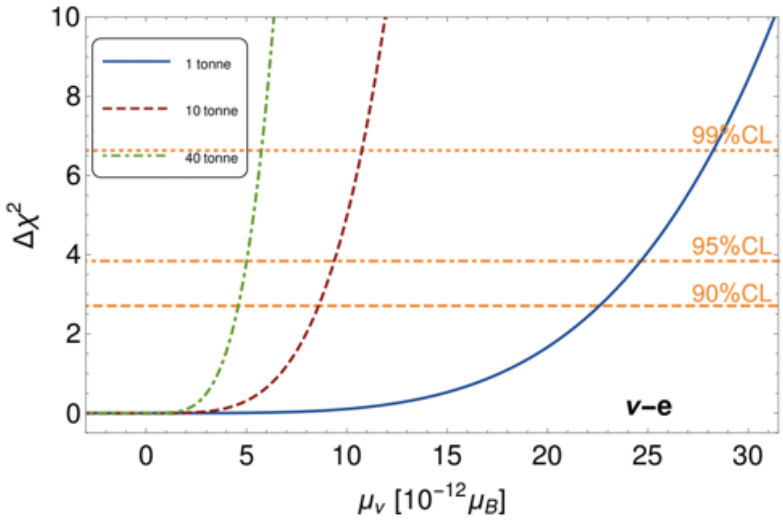

Figure 7.10: Electron recoil sensitivities to the effective neutrino magnetic moment coupling in 1, 10 and 40 tons active volume detectors during a one-year data taking. The result assumes a 0.3 keV threshold, 100% detector efficiency and backgrounds for XENON1T, XENONnT and DARWIN experiments, respectively [143].

on the other and the measurement would be unambiguously determined.

Chapter 8

Conclusions

Along this thesis, we studied how neutrino interactions can be used to search for signals that can give a hint of physics beyond the SM. During the first part, we discussed how NSI terms could arise from theoretical models that intend to explain neutrino masses. In particular, we studied the type II seesaw mechanism, where the induced NSI are related to Yukawa couplings and the triplet scalar mass. We analyzed the impact that current limits on lepton flavor violation processes have on the expected size of these NSI. The applied method can be adapted to different mass generation mechanisms. Our results show that the expected NSI from the type II seesaw are below current experimental sensitivities [77]. However, we showed how neutrino properties, characteristic of the type II seesaw, can also be studied in particle colliders [77, 93].

In the second part, we studied how data from the recently observed CEvNS interactions can be used to test SM parameters and nuclear physics and to constrain NSI parameters [103]. We show in Table 8.1 a summary of the results obtained for NSI by using the COHERENT data from CsI and LAr detectors when assuming only one parameter to be different from zero at a time. The allowed regions when considering two parameters to be different from zero were also given in chapter 5. In addition, we studied the interplay between NSI and nuclear parameters like the neutron rms radius, which uncertainties can be responsible for discrepancies between experimental data and theoretical predictions for CEvNS interactions. We also studied the expected sensitivity of future CEvNS experiments to NSI parameters [113]. We focused on experiments that will be developed by the COHERENT collaboration, which include an enhanced LAr detector, together with Ge and NaI-based detectors. As a future perspective, similar analyses can be done by using the second data set of CsI from the COHERENT collaboration [145], as well as different future proposals like the ESS [146], where detectors with different technologies like Xe, Si, and C_3F_8 aim to be used.

	Current	
NSI	CsI	LAr (24 kg)
ε_{ee}^{dV}	(-0.12, 0.47)	(-0.11, 0.05) ∪ (0.28, 0.44)
$\varepsilon_{\mu\mu}^{dV}$	(-0.07, 0.10) ∪ (0.24, 0.42)	(-0.06, 0.02) ∪ (0.31, 0.39)
$\varepsilon_{e\mu}^{dV}$	(-0.18, 0.18)	(-0.15, 0.15)
$\varepsilon_{e\tau}^{dV}$	(-0.25, 0.25)	(-0.22, 0.22)
$\varepsilon_{\mu\tau}^{dV}$	-0.15, 0.15	(-0.13, 0.13)

Table 8.1: Current NSI bounds from CEvNS experiments.

	Future		
Magnetic Moment	Xenon 1T	Xenon nT	Darwin
μ_ν^{sol}	$< 2.29 \times 10^{-10}\mu_B$	$< 1.29 \times 10^{-10}\mu_B$	$< 9.18 \times 10^{-11}\mu_B$

Table 8.2: Expected NMM bounds for solar neutrinos from CEvNS.

Apart from neutrinos produced at spallation neutron sources, there are many experimental proposals that aim to measure CEvNS in the upcoming years but using reactor anti-neutrino sources. As for August 2022, the release date of this thesis, there is a strong evidence suggesting that the detection of CEvNS from reactor detectors can be achieved soon. In this sense, we have seen that the combination of experiments from different sources can be used to reduce some degeneracies that appear when studying parameters related to nuclear physics and NSI [105]. In line with these searches, we have proposed an experimental array that can take advantage of correlations between systematic uncertainties and which can help to get a cleaner measurement of CEvNS, as well as to break some degeneracies that are characteristic when introducing NSI effects [117].

Regarding the electromagnetic properties of neutrinos, in the last part of this work, we mainly studied the effective magnetic moment coupling and its relation to more fundamental parameters of the theory. We illustrated how measurements from different experiments could be reconciled to be consistent with this scenario of new physics [124]. In addition, we explored the expected limits for the effective coupling that can be achieved through neutrino-electron scattering and CEvNS in future experiments whose main purpose is the detection of DM. The expected sensitivities we found for CEvNS are listed in Table 8.2 [143]. We found that we can achieve better constraints for neutrino-electron scattering than in current neutrino-dedicated experiments. In the case of CEvNS, the limits are not that competitive, but we will be able to explore

regions that have been achieved only through neutrino-electron scattering.

Overall we can say that neutrino physics will still be one of the main fields in searching for physics beyond the SM in the upcoming years. Particularly for CEvNS, we have shown only a part of the potential that this process has for this purpose. We can find many other physics scenarios in the literature that can be explored through this interaction. Therefore, we expect this relatively new process to continue giving important hints to answer some of the main questions that govern neutrino physics. We insist that a correct understanding of CEvNS has a lot of interest not only from the particle physics point of view but also in other physics fields such as DM searches, where the corresponding detectors will measure CEvNS as an important contribution to their backgrounds. These backgrounds constitute the famous neutrino floor, which has been proven sensitive to NSI effects, hence the importance of having robust constraints for these parameters. In addition, there has also been explored the possibility of using CEvNS for practical purposes as nuclear safeguards and for reactor monitoring. With all of these, we can say that the future of CEvNS, and in general neutrino physics, is bright and surely will lead us to a better understanding of nature, which is eventually the main goal of physics.

Appendix A

Magnetic moment effective coupling

In this appendix we show that the magnetic moment cross-section can be described by one single parameter which we have called the effective neutrino magnetic moment. From the Feynman diagram in Fig. 7.1 we have the scattering amplitude:

$$M = -ig_e \sum_{k=1}^{3} \frac{1}{q^2} \overline{u}_j(p_3)\sigma_{\mu\nu}q^\nu \lambda_{jk} U^*_{\ell k} e^{-i\frac{\Delta m^2_{kj} L}{2E_\nu}} u_k(p_1)\overline{u}(p_4)\gamma^\mu u(p_2). \tag{A.1}$$

Taking the squared modulus of Eq. (A.1), we have

$$|M|^2 = g_e^2 \sum_{k=1}^{3}\sum_{m=1}^{3} \frac{1}{q^4} \lambda_{jk}\lambda^*_{jm} e^{-i\frac{\Delta m^2_{kj} - \Delta m^2_{mj}}{2E_\nu} L} U^*_{\ell k} U_{\ell m} \left[\overline{u}_j(p_3)\sigma_{\mu\nu}q^\nu u_k(p_1)\right] \left[\overline{u}_j(p_3)\sigma_{\rho\tau}q^\tau u_m(p_1)\right]^* \times \left[\overline{u}(p_4)\gamma^\mu u(p_2)\right] \left[\overline{u}(p_4)\gamma^\mu u(p_2)\right]^* . \tag{A.2}$$

We now need to sum over the all possible spin orientations. Then, we can use Casimir's trick to express the spinor products in the form:

$$A \equiv \left[\overline{u}_j(p_3)\sigma_{\mu\nu}q^\nu u_k(p_1)\right] \left[\overline{u}_j(p_3)\sigma_{\rho\tau}q^\tau u_m(p_1)\right]^* = \mathrm{Tr}\left[\sigma_{\mu\nu}q^\nu \not{p}_1 \sigma_{\rho\tau}q^\tau \not{p}_3\right], \tag{A.3}$$

$$B \equiv \left[\overline{u}(p_4)\gamma^\mu u(p_2)\right] \left[\overline{u}(p_4)\gamma^\mu u(p_2)\right]^* = \mathrm{Tr}\left[\gamma^\mu \left(\not{p}_2 + m_e\right) \gamma^\rho \left(\not{p}_4 + m_e\right)\right], \tag{A.4}$$

where we have neglected the neutrino masses. Using trace techniques to calculate the right hand side of the previous equations we have:

$$\begin{aligned} A = 4(&-q^2 p_{1\mu}p_{3\rho} + (p_3\cdot q)p_{1\mu}q_\rho - q^2 p_{1\rho}p_{3\mu} + (p_1\cdot q)p_{3\mu}q_\rho \\ &- (p_1\cdot q)(p_3\cdot q)g^{\mu\rho} + (p_1\cdot q)p_{3\rho}q_\mu - (p_1\cdot p_3)q_\rho q_\mu + q^2(p_1\cdot p_3)g^{\mu\rho} \\ &- (p_3\cdot q)(p_1\cdot q)g^{\mu\rho} + (p_3\cdot q)p_{1\rho}q^\mu), \end{aligned} \tag{A.5}$$

$$B = 4(p_{2\mu}p_{4\rho} + p_{2\rho}p_{4\mu} - (p_2 \cdot p_4)g^{\mu\rho} + m_e^2 g^{\mu\rho}). \tag{A.6}$$

Multiplying the two quantities, and using properties of the metric tensor we have

$$\begin{aligned} AB = 32(p_1 \cdot p_3)[&(p_1 \cdot p_2)(p_3 \cdot p_4) + (p_1 \cdot p_2)(p_1 \cdot p_4) - (p_1 \cdot p_3)(p_2 \cdot p_4) \\ &+ (p_1 \cdot p_4)(p_2 \cdot p_3) + (p_2 \cdot p_3)(p_3 \cdot p_4) + m_e^2(p_1 \cdot p_3)]. \end{aligned} \tag{A.7}$$

Expanding the dot products, we end with the expression:

$$AB = 128E^2 m_e^3 T\left(1 - \frac{T}{E}\right). \tag{A.8}$$

Substituting in Eq. (A.2) and summing over the three neutrino mass states we have

$$|M|^2 = \sum_{j=1}^{3} \frac{32e^2E^2m_e}{T} \sum_{k=1}^{3}\sum_{m=1}^{3} \lambda_{jk}\lambda_{jm}^* e^{-i\frac{\Delta m_{kj}^2 - \Delta m_{mj}^2}{2E_\nu}L} U_{\ell k}^* U_{\ell m}, \tag{A.9}$$

$$|M|^2 = \sum_{j=1}^{3} \frac{32e^2E^2m_e}{T} \left|\sum_{k=1}^{3} U_{\ell k}^* e^{-i\frac{m_k^2 L}{2E_\nu}} \lambda_{jk}\right|^2. \tag{A.10}$$

On the other hand, the cross-section for a two body process where the mass of one of them is negligible is given by

$$\frac{\mathrm{d}\sigma}{\mathrm{d}T} = \frac{|M|^2}{32\pi m_e E^2}. \tag{A.11}$$

Then, using Eq. (A.10), and rearranging terms we have

$$\frac{\mathrm{d}\sigma}{\mathrm{d}T} = \sum_{j=1}^{3} \left|\sum_{k=1}^{3} U_{\ell k}^* e^{-i\frac{m_k^2 L}{2E_\nu}} \lambda_{jk}\right|^2 \frac{\pi\alpha^2}{m_e^2\mu_B^2}\left(\frac{1}{T} - \frac{1}{E}\right). \tag{A.12}$$

We notice that the information of the magnetic moment couplings has been factored out from the last expression. Then, we can define an effective neutrino magnetic moment, weighted by the Bohr magneton, as

$$\mu_\nu^2 \equiv \sum_{j=1}^{3} \left|\sum_{k=1}^{3} U_{\ell k}^* e^{-i\frac{m_k^2 L}{2E_\nu}} \lambda_{jk}\right|^2, \tag{A.13}$$

so that we now recover the cross-section given in section 7.2

$$\frac{d\sigma}{dT} = \frac{\pi\alpha^2\,\mu_\nu^2}{m_e^2}\left(\frac{1}{T} - \frac{1}{E_\nu}\right), \tag{A.14}$$

which shows that, regardless of the neutrino mass nature, the dipole magnetic and electric moment effects can be parametrized by a single effective coupling.

List of publications

1. Sanjoy Mandal, O.G. Miranda, G. Sanchez Garcia, J.W.F. Valle, and Xun-Jie Xu
Toward deconstructing the simplest seesaw mechanism. (2022)
DOI: 10.1103/PhysRevD.105.095020 | arXiv:2203.06362

2. Sanjoy Mandal, O.G. Miranda, G. Sanchez Garcia, J.W.F. Valle, and Xun-Jie Xu
High-energy colliders as a probe of neutrino properties. (2022)
DOI: 10.1016/j.physletb.2022.137110 | arXiv:2202.04502

3. D. Aristizabal Sierra, O. G. Miranda, D.K. Papoulias, and G. Sanchez Garcia
Neutrino magnetic and electric dipole moments: From measurements to parameter space. (2021)
DOI: 10.1103/PhysRevD.105.035027 | arXiv:2112.12817

4. A. Galindo-Uribarri; O. G. Miranda; and G. Sanchez Garcia
Novel approach for the study of coherent elastic neutrino-nucleus scattering. (2021)
DOI: 10.1103/PhysRevD.105.033001 | arXiv:2011.10230

5. D. Aristizabal Sierra, R. Branada, O. G. Miranda, and G. Sanchez Garcia
Sensitivity of direct detection experiments to neutrino magnetic dipole moments. (2020)
DOI: 10.1007/ JHEP12(2020)178 | arXiv:2008.05080

6. O. G. Miranda, D. K. Papoulias, G. Sanchez Garcia, O. Sanders, M. Tortola, and J. W. F. Valle
Implications of the first detection of coherent elastic neutrino-nucleus scattering (CEvNS) with Liquid Argon. (2020)
DOI: 10.1007/JHEP05(2020)130 | arXiv:2003.12050

7. B. Canas, E. Garces, O. G. Miranda, A. Parada, and G. Sanchez Garcia
Interplay between nonstandard and nuclear constraints in coherent

elastic neutrino-nucleus scattering experiments (2020)
DOI: 10.1103/PhysRevD.101.035012 | arXiv:1911.09831

8. O. G. Miranda, G. Sanchez Garcia, and O. Sanders
Coherent elastic neutrino-nucleus scattering as a precision test for the Standard Model and beyond: the COHERENT proposal case (2019)
DOI: 10.1155/2019/3902819 (Adv.High Energy Phys.) | arXiv:1902.09036

Proceedings

1. G. Sanchez Garcia
17th International Conference on Topics in Astroparticle and Underground Physics (2021 Virtual Conference)
Using isotopically enriched detectors to perform CEvNS measurements.
DOI: 10.1088/1742-6596/2156/1/012207

2. B. Canas, E. Garces, O. G. Miranda, A. Parada, and G. Sanchez Garcia
International Conference on High Energy Physics (2020 Virtual Conference)
Constraints on nonstandard interactions and the neutron radius from coherent elastic neutrino-nucleus scattering experiments.
DOI: 10.22323/1.390.0168

Bibliography

[1] F. Reines and C. L. Cowan, "Detection of the free neutrino," *Phys. Rev.*, vol. 92, pp. 830–831, 1953.

[2] F. Reines and C. L. Cowan, "The neutrino," *Nature*, vol. 178, pp. 446–449, 1956.

[3] S. L. Glashow, "Partial Symmetries of Weak Interactions," *Nucl. Phys.*, vol. 22, pp. 579–588, 1961.

[4] S. Weinberg, "A Model of Leptons," *Phys. Rev. Lett.*, vol. 19, pp. 1264–1266, 1967.

[5] A. Salam, "Weak and Electromagnetic Interactions," *Conf. Proc. C*, vol. 680519, pp. 367–377, 1968.

[6] C. N. Yang and R. L. Mills, "Conservation of isotopic spin and isotopic gauge invariance," *Phys. Rev.*, vol. 96, pp. 191–195, Oct 1954.

[7] D. Griffiths, *Introduction to elementary particles*. 2008.

[8] C. Giunti and C. W. Kim, *Fundamentals of Neutrino Physics and Astrophysics*. 2007.

[9] P. W. Higgs, "Broken symmetries, massless particles and gauge fields," *Phys. Lett.*, vol. 12, pp. 132–133, 1964.

[10] P. W. Higgs, "Broken Symmetries and the Masses of Gauge Bosons," *Phys. Rev. Lett.*, vol. 13, pp. 508–509, 1964.

[11] S. M. Bilenky and S. T. Petcov, "Massive Neutrinos and Neutrino Oscillations," *Rev. Mod. Phys.*, vol. 59, p. 671, 1987. [Erratum: Rev.Mod.Phys. 61, 169 (1989), Erratum: Rev.Mod.Phys. 60, 575–575 (1988)].

[12] S. L. Glashow, J. Iliopoulos, and L. Maiani, "Weak Interactions with Lepton-Hadron Symmetry," *Phys. Rev. D*, vol. 2, pp. 1285–1292, 1970.

[13] W. Pauli, "Dear radioactive ladies and gentlemen," *Phys. Today*, vol. 31N9, p. 27, 1978.

[14] E. Fermi, "An attempt of a theory of beta radiation. 1.," *Z. Phys.*, vol. 88, pp. 161–177, 1934.

[15] G. Danby, J. M. Gaillard, K. A. Goulianos, L. M. Lederman, N. B. Mistry, M. Schwartz, and J. Steinberger, "Observation of High-Energy Neutrino Reactions and the Existence of Two Kinds of Neutrinos," *Phys. Rev. Lett.*, vol. 9, pp. 36–44, 1962.

[16] M. L. Perl *et al.*, "Evidence for Anomalous Lepton Production in e+ - e- Annihilation," *Phys. Rev. Lett.*, vol. 35, pp. 1489–1492, 1975.

[17] K. Kodama *et al.*, "Observation of tau neutrino interactions," *Phys. Lett. B*, vol. 504, pp. 218–224, 2001.

[18] E. Vitagliano, I. Tamborra, and G. Raffelt, "Grand Unified Neutrino Spectrum at Earth: Sources and Spectral Components," *Rev. Mod. Phys.*, vol. 92, p. 45006, 2020.

[19] M. Ahlers and F. Halzen, "High-energy cosmic neutrino puzzle: a review," *Rept. Prog. Phys.*, vol. 78, no. 12, p. 126901, 2015.

[20] T. A. Mueller *et al.*, "Improved Predictions of Reactor Antineutrino Spectra," *Phys. Rev. C*, vol. 83, p. 054615, 2011.

[21] P. Huber, "On the determination of anti-neutrino spectra from nuclear reactors," *Phys. Rev. C*, vol. 84, p. 024617, 2011. [Erratum: Phys.Rev.C 85, 029901 (2012)].

[22] G. Gamow, "Zur Quantentheorie des Atomkernes," *Z. Phys.*, vol. 51, pp. 204–212, 1928.

[23] J. N. Bahcall, A. M. Serenelli, and S. Basu, "10,000 standard solar models: a Monte Carlo simulation," *Astrophys. J. Suppl.*, vol. 165, pp. 400–431, 2006.

[24] N. Grevesse and A. J. Sauval, "Standard Solar Composition," *Space Sci. Rev.*, vol. 85, pp. 161–174, 1998.

[25] M. Asplund, N. Grevesse, and J. Sauval, "The Solar chemical composition," *ASP Conf. Ser.*, vol. 336, p. 25, 2005.

[26] Y. Takahashi, "The fierz identities—a passage between spinors and tensors," *Journal of Mathematical Physics*, vol. 24, no. 7, pp. 1783–1790, 1983.

[27] D. Akimov *et al.*, "Observation of Coherent Elastic Neutrino-Nucleus Scattering," *Science*, vol. 357, no. 6356, pp. 1123–1126, 2017.

[28] D. Z. Freedman, "Coherent effects of a weak neutral current," *Phys. Rev. D*, vol. 9, pp. 1389–1392, Mar 1974.

[29] A. Drukier and L. Stodolsky, "Principles and Applications of a Neutral Current Detector for Neutrino Physics and Astronomy," *Phys. Rev. D*, vol. 30, p. 2295, 1984.

[30] D. K. Papoulias and T. S. Kosmas, "Standard and Nonstandard Neutrino-Nucleus Reactions Cross Sections and Event Rates to Neutrino Detection Experiments," *Adv. High Energy Phys.*, vol. 2015, p. 763648, 2015.

[31] J. Barranco, O. G. Miranda, and T. I. Rashba, "Probing new physics with coherent neutrino scattering off nuclei," *JHEP*, vol. 12, p. 021, 2005.

[32] O. Tomalak, P. Machado, V. Pandey, and R. Plestid, "Flavor-dependent radiative corrections in coherent elastic neutrino-nucleus scattering," *JHEP*, vol. 02, p. 097, 2021.

[33] J. Lewin and P. Smith, "Review of mathematics, numerical factors, and corrections for dark matter experiments based on elastic nuclear recoil," *Astroparticle Physics*, vol. 6, no. 1, pp. 87–112, 1996.

[34] M. Caddedu, "Average csi neutron density distribution from coherent data," 2018.

[35] G. A. Jones, "The nuclear surface," *Reports on Progress in Physics*, vol. 33, pp. 645–689, may 1970.

[36] M. Cadeddu, C. Giunti, Y. Li, and Y. Zhang, "Average CsI neutron density distribution from COHERENT data," *Phys. Rev. Lett.*, vol. 120, no. 7, p. 072501, 2018.

[37] B. T. Cleveland, T. Daily, R. Davis, Jr., J. R. Distel, K. Lande, C. K. Lee, P. S. Wildenhain, and J. Ullman, "Measurement of the solar electron neutrino flux with the Homestake chlorine detector," *Astrophys. J.*, vol. 496, pp. 505–526, 1998.

[38] P. Anselmann *et al.*, "Solar neutrinos observed by GALLEX at Gran Sasso.," *Phys. Lett. B*, vol. 285, pp. 376–389, 1992.

[39] M. Altmann *et al.*, "Complete results for five years of GNO solar neutrino observations," *Phys. Lett. B*, vol. 616, pp. 174–190, 2005.

[40] J. N. Abdurashitov *et al.*, "Solar neutrino flux measurements by the Soviet-American Gallium Experiment (SAGE) for half the 22 year solar cycle," *J. Exp. Theor. Phys.*, vol. 95, pp. 181–193, 2002.

[41] Y. Fukuda *et al.*, "Solar neutrino data covering solar cycle 22," *Phys. Rev. Lett.*, vol. 77, pp. 1683–1686, 1996.

[42] Y. Fukuda *et al.*, "Measurements of the solar neutrino flux from Super-Kamiokande's first 300 days," *Phys. Rev. Lett.*, vol. 81, pp. 1158–1162, 1998. [Erratum: Phys.Rev.Lett. 81, 4279 (1998)].

[43] B. Aharmim *et al.*, "Electron energy spectra, fluxes, and day-night asymmetries of B-8 solar neutrinos from measurements with NaCl dissolved in the heavy-water detector at the Sudbury Neutrino Observatory," *Phys. Rev. C*, vol. 72, p. 055502, 2005.

[44] S. N. Ahmed *et al.*, "Measurement of the total active B-8 solar neutrino flux at the Sudbury Neutrino Observatory with enhanced neutral current sensitivity," *Phys. Rev. Lett.*, vol. 92, p. 181301, 2004.

[45] B. Pontecorvo, "Inverse beta processes and nonconservation of lepton charge," *Zh. Eksp. Teor. Fiz.*, vol. 34, p. 247, 1957.

[46] B. Pontecorvo, "Neutrino Experiments and the Problem of Conservation of Leptonic Charge," *Zh. Eksp. Teor. Fiz.*, vol. 53, pp. 1717–1725, 1967.

[47] L. Wolfenstein, "Neutrino oscillations in matter," *Phys. Rev. D*, vol. 17, pp. 2369–2374, May 1978.

[48] S. P. Mikheyev and A. Y. Smirnov, "Resonance Amplification of Oscillations in Matter and Spectroscopy of Solar Neutrinos," *Sov. J. Nucl. Phys.*, vol. 42, pp. 913–917, 1985.

[49] E. Majorana, "Teoria simmetrica dell'elettrone e del positrone," *Nuovo Cim.*, vol. 14, pp. 171–184, 1937.

[50] S. Weinberg, "Baryon and Lepton Nonconserving Processes," *Phys. Rev. Lett.*, vol. 43, pp. 1566–1570, 1979.

[51] P. Zyla *et al.*, "Review of Particle Physics," *PTEP*, vol. 2020, no. 8, p. 083C01, 2020. and 2021 update.

[52] W. Rodejohann and J. W. F. Valle, "Symmetrical Parametrizations of the Lepton Mixing Matrix," *Phys. Rev. D*, vol. 84, p. 073011, 2011.

[53] P. F. de Salas, D. V. Forero, S. Gariazzo, P. Martínez-Miravé, O. Mena, C. A. Ternes, M. Tórtola, and J. W. F. Valle, "2020 global reassessment of the neutrino oscillation picture," *JHEP*, vol. 02, p. 071, 2021.

[54] G. Bellini *et al.*, "Precision measurement of the 7Be solar neutrino interaction rate in Borexino," *Phys. Rev. Lett.*, vol. 107, p. 141302, 2011.

[55] K. Abe *et al.*, "Solar neutrino results in Super-Kamiokande-III," *Phys. Rev. D*, vol. 83, p. 052010, 2011.

[56] S. Abe *et al.*, "Precision Measurement of Neutrino Oscillation Parameters with KamLAND," *Phys. Rev. Lett.*, vol. 100, p. 221803, 2008.

[57] Y. Farzan and M. Tortola, "Neutrino oscillations and Non-Standard Interactions," *Front. in Phys.*, vol. 6, p. 10, 2018.

[58] D. Adey *et al.*, "Measurement of the Electron Antineutrino Oscillation with 1958 Days of Operation at Daya Bay," *Phys. Rev. Lett.*, vol. 121, no. 24, p. 241805, 2018.

[59] G. Bak *et al.*, "Measurement of Reactor Antineutrino Oscillation Amplitude and Frequency at RENO," *Phys. Rev. Lett.*, vol. 121, no. 20, p. 201801, 2018.

[60] Y. Abe *et al.*, "Improved measurements of the neutrino mixing angle θ_{13} with the Double Chooz detector," *JHEP*, vol. 10, p. 086, 2014. [Erratum: JHEP 02, 074 (2015)].

[61] J. Hosaka *et al.*, "Solar neutrino measurements in super-Kamiokande-I," *Phys. Rev. D*, vol. 73, p. 112001, 2006.

[62] S. Adrian-Martinez *et al.*, "Measurement of Atmospheric Neutrino Oscillations with the ANTARES Neutrino Telescope," *Phys. Lett. B*, vol. 714, pp. 224–230, 2012.

[63] M. G. Aartsen *et al.*, "Determining neutrino oscillation parameters from atmospheric muon neutrino disappearance with three years of IceCube DeepCore data," *Phys. Rev. D*, vol. 91, no. 7, p. 072004, 2015.

[64] K. Abe *et al.*, "Combined Analysis of Neutrino and Antineutrino Oscillations at T2K," *Phys. Rev. Lett.*, vol. 118, no. 15, p. 151801, 2017.

[65] P. Adamson *et al.*, "Combined analysis of ν_μ disappearance and $\nu_\mu \to \nu_e$ appearance in MINOS using accelerator and atmospheric neutrinos," *Phys. Rev. Lett.*, vol. 112, p. 191801, 2014.

[66] M. A. Acero *et al.*, "New constraints on oscillation parameters from ν_e appearance and ν_μ disappearance in the NOvA experiment," *Phys. Rev. D*, vol. 98, p. 032012, 2018.

[67] O. G. Miranda, M. A. Tortola, and J. W. F. Valle, "Are solar neutrino oscillations robust?," *JHEP*, vol. 10, p. 008, 2006.

[68] A. Bolanos, O. G. Miranda, A. Palazzo, M. A. Tortola, and J. W. F. Valle, "Probing non-standard neutrino-electron interactions with solar and reactor neutrinos," *Phys. Rev. D*, vol. 79, p. 113012, 2009.

[69] M. C. Gonzalez-Garcia, M. Maltoni, and J. Salvado, "Testing matter effects in propagation of atmospheric and long-baseline neutrinos," *JHEP*, vol. 05, p. 075, 2011.

[70] M. G. Aartsen *et al.*, "Search for Nonstandard Neutrino Interactions with IceCube DeepCore," *Phys. Rev. D*, vol. 97, no. 7, p. 072009, 2018.

[71] S. Davidson, C. Pena-Garay, N. Rius, and A. Santamaria, "Present and future bounds on nonstandard neutrino interactions," *JHEP*, vol. 03, p. 011, 2003.

[72] M. Deniz *et al.*, "Constraints on Non-Standard Neutrino Interactions and Unparticle Physics with Neutrino-Electron Scattering at the Kuo-Sheng Nuclear Power Reactor," *Phys. Rev. D*, vol. 82, p. 033004, 2010.

[73] J. Schechter and J. W. F. Valle, "Neutrino masses in su(2) $\bigotimes$ u(1) theories," *Phys. Rev. D*, vol. 22, pp. 2227–2235, Nov 1980.

[74] R. N. Mohapatra and P. B. Pal, *Massive neutrinos in physics and astrophysics*, vol. 41. 1991.

[75] A. Arhrib, R. Benbrik, M. Chabab, G. Moultaka, M. C. Peyranere, L. Rahili, and J. Ramadan, "The Higgs Potential in the Type II Seesaw Model," *Phys. Rev. D*, vol. 84, p. 095005, 2011.

[76] G. 't Hooft, "Naturalness, chiral symmetry, and spontaneous chiral symmetry breaking," *NATO Sci. Ser. B*, vol. 59, pp. 135–157, 1980.

[77] S. Mandal, O. G. Miranda, G. Sanchez Garcia, J. W. F. Valle, and X.-J. Xu, "Toward deconstructing the simplest seesaw mechanism," *Phys. Rev. D*, vol. 105, no. 9, p. 095020, 2022.

[78] A. Gando *et al.*, "Search for Majorana Neutrinos near the Inverted Mass Hierarchy Region with KamLAND-Zen," *Phys. Rev. Lett.*, vol. 117, no. 8, p. 082503, 2016. [Addendum: Phys.Rev.Lett. 117, 109903 (2016)].

[79] S. Alam *et al.*, "Completed SDSS-IV extended Baryon Oscillation Spectroscopic Survey: Cosmological implications from two decades of spectroscopic surveys at the Apache Point Observatory," *Phys. Rev. D*, vol. 103, no. 8, p. 083533, 2021.

[80] N. Aghanim *et al.*, "Planck 2018 results. VI. Cosmological parameters," *Astron. Astrophys.*, vol. 641, p. A6, 2020. [Erratum: Astron.Astrophys. 652, C4 (2021)].

[81] M. Aker *et al.*, "First direct neutrino-mass measurement with sub-eV sensitivity," 5 2021.

[82] S. Andringa *et al.*, "Current Status and Future Prospects of the SNO+ Experiment," *Adv. High Energy Phys.*, vol. 2016, p. 6194250, 2016.

[83] N. Abgrall *et al.*, "The Large Enriched Germanium Experiment for Neutrinoless Double Beta Decay (LEGEND)," *AIP Conf. Proc.*, vol. 1894, no. 1, p. 020027, 2017.

[84] J. B. Albert *et al.*, "Sensitivity and Discovery Potential of nEXO to Neutrinoless Double Beta Decay," *Phys. Rev. C*, vol. 97, no. 6, p. 065503, 2018.

[85] Y. Cai, J. Herrero-García, M. A. Schmidt, A. Vicente, and R. R. Volkas, "From the trees to the forest: a review of radiative neutrino mass models," *Front. in Phys.*, vol. 5, p. 63, 2017.

[86] B. Aubert *et al.*, "Searches for Lepton Flavor Violation in the Decays tau+- —> e+- gamma and tau+- —> mu+- gamma," *Phys. Rev. Lett.*, vol. 104, p. 021802, 2010.

[87] P. S. B. Dev, C. M. Vila, and W. Rodejohann, "Naturalness in testable type II seesaw scenarios," *Nucl. Phys. B*, vol. 921, pp. 436–453, 2017.

[88] A. Abdesselam *et al.*, "Search for lepton-flavor-violating tau-lepton decays to $\ell\gamma$ at Belle," *JHEP*, vol. 10, p. 19, 2021.

[89] M. Aaboud *et al.*, "Search for doubly charged Higgs boson production in multi-lepton final states with the ATLAS detector using proton–proton collisions at $\sqrt{s} = 13\,\text{TeV}$," *Eur. Phys. J. C*, vol. 78, no. 3, p. 199, 2018.

[90] M. Aaboud *et al.*, "Search for doubly charged scalar bosons decaying into same-sign W boson pairs with the ATLAS detector," *Eur. Phys. J. C*, vol. 79, no. 1, p. 58, 2019.

[91] M. Lindner, M. Platscher, and F. S. Queiroz, "A Call for New Physics : The Muon Anomalous Magnetic Moment and Lepton Flavor Violation," *Phys. Rept.*, vol. 731, pp. 1–82, 2018.

[92] C. Dohmen *et al.*, "Test of lepton flavor conservation in mu —> e conversion on titanium," *Phys. Lett. B*, vol. 317, pp. 631–636, 1993.

[93] S. Mandal, O. G. Miranda, G. S. Garcia, J. W. F. Valle, and X.-J. Xu, "High-energy colliders as a probe of neutrino properties," *Phys. Lett. B*, vol. 829, p. 137110, 2022.

[94] E. J. Chun, K. Y. Lee, and S. C. Park, "Testing Higgs triplet model and neutrino mass patterns," *Phys. Lett. B*, vol. 566, pp. 142–151, 2003.

[95] D. Akimov *et al.*, "First Constraint on Coherent Elastic Neutrino-Nucleus Scattering in Argon," *Phys. Rev. D*, vol. 100, no. 11, p. 115020, 2019.

[96] D. Akimov *et al.*, "Measurement of the Coherent Elastic Neutrino-Nucleus Scattering Cross Section on CsI by COHERENT," 10 2021.

[97] D. Akimov *et al.*, "The COHERENT Experiment at the Spallation Neutron Source," 9 2015.

[98] R. Garoby *et al.*, "The European Spallation Source Design," *Phys. Scripta*, vol. 93, no. 1, p. 014001, 2018.

[99] D. Markoff, "Background studies for the coherent experiment at the spallation neutron source," *Journal of Physics: Conference Series*, vol. 888, p. 012152, 09 2017.

[100] B. J. Scholz, *First Observation of Coherent Elastic Neutrino-Nucleus Scattering*. PhD thesis, Chicago U., 2017.

[101] D. Akimov *et al.*, "First Measurement of Coherent Elastic Neutrino-Nucleus Scattering on Argon," *Phys. Rev. Lett.*, vol. 126, no. 1, p. 012002, 2021.

[102] D. Akimov *et al.*, "COHERENT Collaboration data release from the first observation of coherent elastic neutrino-nucleus scattering," 4 2018.

[103] O. Miranda, D. Papoulias, G. Sanchez Garcia, O. Sanders, M. Tórtola, and J. Valle, "Implications of the first detection of coherent elastic neutrino-nucleus scattering (CEvNS) with Liquid Argon," *JHEP*, vol. 05, p. 130, 2020.

[104] C. Horowitz *et al.*, "Weak charge form factor and radius of 208Pb through parity violation in electron scattering," *Phys. Rev. C*, vol. 85, p. 032501, 2012.

[105] B. Canas, E. Garces, O. Miranda, A. Parada, and G. Sanchez Garcia, "Interplay between nonstandard and nuclear constraints in coherent elastic neutrino-nucleus scattering experiments," *Phys. Rev. D*, vol. 101, no. 3, p. 035012, 2020.

[106] D. Akimov *et al.*, "COHERENT Collaboration data release from the first observation of coherent elastic neutrino-nucleus scattering," 4 2018.

[107] C. von Raesfeld and P. Huber, "Use of CEvNS to monitor spent nuclear fuel," *Phys. Rev. D*, vol. 105, no. 5, p. 056002, 2022.

[108] D. Akimov *et al.*, "The COHERENT Experiment at the Spallation Neutron Source," 9 2015.

[109] D. Baxter *et al.*, "Coherent Elastic Neutrino-Nucleus Scattering at the European Spallation Source," *JHEP*, vol. 02, p. 123, 2020.

[110] J. Colaresi, J. I. Collar, T. W. Hossbach, C. M. Lewis, and K. M. Yocum, "Suggestive evidence for Coherent Elastic Neutrino-Nucleus Scattering from reactor antineutrinos," 2 2022.

[111] M. Lindner, W. Rodejohann, and X.-J. Xu, "Coherent Neutrino-Nucleus Scattering and new Neutrino Interactions," *JHEP*, vol. 03, p. 097, 2017.

[112] A. Aguilar-Arevalo *et al.*, "Results of the Engineering Run of the Coherent Neutrino Nucleus Interaction Experiment (CONNIE)," *JINST*, vol. 11, no. 07, p. P07024, 2016.

[113] O. Miranda, G. Sanchez Garcia, and O. Sanders, "Coherent elastic neutrino-nucleus scattering as a precision test for the Standard Model and beyond: the COHERENT proposal case," *Adv. High Energy Phys.*, vol. 2019, p. 3902819, 2019.

[114] G. Angloher *et al.*, "Exploring CEνNS with NUCLEUS at the Chooz nuclear power plant," *Eur. Phys. J. C*, vol. 79, no. 12, p. 1018, 2019.

[115] G. Agnolet *et al.*, "Background Studies for the MINER Coherent Neutrino Scattering Reactor Experiment," *Nucl. Instrum. Meth. A*, vol. 853, pp. 53–60, 2017.

[116] J. Billard *et al.*, "Coherent Neutrino Scattering with Low Temperature Bolometers at Chooz Reactor Complex," *J. Phys. G*, vol. 44, no. 10, p. 105101, 2017.

[117] A. Galindo-Uribarri, O. G. Miranda, and G. S. Garcia, "Novel approach for the study of coherent elastic neutrino-nucleus scattering," *Phys. Rev. D*, vol. 105, no. 3, p. 033001, 2022.

[118] M. Gunther *et al.*, "Heidelberg - Moscow beta-beta experiment with Ge-76: Full setup with five detectors," *Phys. Rev. D*, vol. 55, pp. 54–67, 1997.

[119] D. Aristizabal Sierra, V. De Romeri, L. J. Flores, and D. K. Papoulias, "Impact of COHERENT measurements, cross section uncertainties and new interactions on the neutrino floor," *JCAP*, vol. 01, no. 01, p. 055, 2022.

[120] M. Nowakowski, E. A. Paschos, and J. M. Rodriguez, "All electromagnetic form-factors," *Eur. J. Phys.*, vol. 26, pp. 545–560, 2005.

[121] W. Greiner and J. Reinhardt, *Quantum electrodynamics*. 1992.

[122] C. Giunti and A. Studenikin, "Neutrino electromagnetic interactions: a window to new physics," *Rev. Mod. Phys.*, vol. 87, p. 531, 2015.

[123] I. B. Zel'dovich, "Electromagnetic interaction with parity violation," *Soviet Phys. JETP*.

[124] D. Aristizabal Sierra, O. G. Miranda, D. K. Papoulias, and G. S. Garcia, "Neutrino magnetic and electric dipole moments: From measurements to parameter space," *Phys. Rev. D*, vol. 105, no. 3, p. 035027, 2022.

[125] A. G. Beda, V. B. Brudanin, V. G. Egorov, D. V. Medvedev, V. S. Pogosov, M. V. Shirchenko, and A. S. Starostin, "The results of search for the neutrino magnetic moment in GEMMA experiment," *Adv. High Energy Phys.*, vol. 2012, p. 350150, 2012.

[126] L. B. Auerbach *et al.*, "Measurement of electron - neutrino - electron elastic scattering," *Phys. Rev. D*, vol. 63, p. 112001, 2001.

[127] R. Schwienhorst *et al.*, "A New upper limit for the tau - neutrino magnetic moment," *Phys. Lett. B*, vol. 513, pp. 23–29, 2001.

[128] M. Agostini *et al.*, "Limiting neutrino magnetic moments with Borexino Phase-II solar neutrino data," *Phys. Rev. D*, vol. 96, no. 9, p. 091103, 2017.

[129] E. Aprile *et al.*, "Observation of Excess Electronic Recoil Events in XENON1T," 6 2020.

[130] W. Grimus and T. Schwetz, "Elastic neutrino electron scattering of solar neutrinos and potential effects of magnetic and electric dipole moments," *Nucl. Phys. B*, vol. 587, pp. 45–66, 2000.

[131] O. G. Miranda, D. K. Papoulias, M. Tórtola, and J. W. F. Valle, "Probing neutrino transition magnetic moments with coherent elastic neutrino-nucleus scattering," *JHEP*, vol. 07, p. 103, 2019.

[132] B. C. Canas, O. G. Miranda, A. Parada, M. Tortola, and J. W. F. Valle, "New limits on neutrino magnetic moments from low energy neutrino data," *J. Phys. Conf. Ser.*, vol. 761, no. 1, p. 012043, 2016.

[133] A. Ariga *et al.*, "FASER: ForwArd Search ExpeRiment at the LHC," 1 2019.

[134] D. W. Liu *et al.*, "Limits on the neutrino magnetic moment using 1496 days of Super-Kamiokande-I solar neutrino data," *Phys. Rev. Lett.*, vol. 93, p. 021802, 2004.

[135] E. Aprile *et al.*, "Excess electronic recoil events in XENON1T," *Phys. Rev. D*, vol. 102, no. 7, p. 072004, 2020.

[136] E. Aprile *et al.*, "Projected WIMP sensitivity of the XENONnT dark matter experiment," *JCAP*, vol. 11, p. 031, 2020.

[137] J. Aalbers *et al.*, "DARWIN: towards the ultimate dark matter detector," *JCAP*, vol. 11, p. 017, 2016.

[138] E. Aprile *et al.*, "The XENON1T Dark Matter Experiment," *Eur. Phys. J. C*, vol. 77, no. 12, p. 881, 2017.

[139] J. Aalbers *et al.*, "DARWIN: towards the ultimate dark matter detector," *JCAP*, vol. 11, p. 017, 2016.

[140] P. Vogel and J. Engel, "Neutrino Electromagnetic Form-Factors," *Phys. Rev. D*, vol. 39, p. 3378, 1989.

[141] E. Aprile *et al.*, "Projected WIMP Sensitivity of the XENONnT Dark Matter Experiment," 7 2020.

[142] J. Aalbers *et al.*, "Solar Neutrino Detection Sensitivity in DARWIN via Electron Scattering," 6 2020.

[143] D. Aristizabal Sierra, R. Branada, O. G. Miranda, and G. Sanchez Garcia, "Sensitivity of direct detection experiments to neutrino magnetic dipole moments," *JHEP*, vol. 12, p. 178, 2020.

[144] G. G. Raffelt, "New bound on neutrino dipole moments from globular cluster stars," *Phys. Rev. Lett.*, vol. 64, pp. 2856–2858, 1990.

[145] O. Miranda, D. Papoulias, G. Sanchez Garcia, O. Sanders, M. Tórtola, and J. Valle, "New physics searches with CEvNS from the second COHERENT dataset with CsI," *Work in preparation.*

[146] S. Chatterjee, S. Lavignac, O. Miranda, and G. Sanchez Garcia, "Constraining Non-Standard Interactions with Coherent Elastic Neutrino-Nucleus Scattering at the European Spallation Source," *Work in preparation.*